A Statistical and Dynamical Study of Arctic Sea-Ice Variability

by

Mitchell Bushuk

A dissertation submitted in partial fulfillment

of the requirements for the degree of

Doctor of Philosophy

Department of Mathematics

Courant Institute of Mathematical Sciences

New York University

May 2015

Dimitrios Giannakis

Dedication

To my parents.

Acknowledgements

I would like to begin by thanking my PhD advisor, Dimitris Giannakis, for consistently providing inspiring problems to work on, for our frequent open and stimulating research discussions, and for sharing your deep knowledge of data analysis and predictability. It has been an honor and a pleasure to be your first PhD student. Thanks to David Holland for sharing your unique scientific approach and philosophy, the many wonderful discussions in the lab, and the incredible opportunity to participate in field work and laboratory experiments in Greenland, Antarctica and at CRREL. Thanks to Andy Majda for teaching me about research at the intersection of atmosphere-ocean science and modern applied mathematics, and for guidance and encouragement throughout our research projects. Also, thanks to Cecilia Bitz and Bruno Tremblay for serving on my thesis committee and providing valuable comments and suggestions.

I would like to thank my high school math teacher, Dave Long, and my grandfather, Walter Bushuk, for inspiring me to do this PhD in the first place.

Thanks to all those at the Courant Institute who helped create the community that made Courant a great place to come to work every day. In particular thanks to Olivier Pauluis, Shafer Smith, and Ed Gerber for your commitment to student development and pedagogy within CAOS. Thanks to the students and postdocs of CAOS for the countless discussions, lunches, and happy hours over the years, especially Alon Stern, Carl Gladish, Ray Yamada, Noah Brenowitz, Naftali Cohen, Louis-Phillipe Nadeau, and Irena Vankova. Also, thanks to all the members of *Xichen and the Li's*: Your music continues to inspire a generation. Thanks to the great friends in the math department, especially Steve Delong, Travis Askham, Andres Muñoz, Michael Lewis, Edgar Costa, Adam Stinchcombe, Giulio Triglia,

Sandra May, Dharshi Devendran, and Siddharth Krishna.

I gratefully acknowledge the graduate funding I received from the Natural Sciences and Engineering Research Council of Canada (PGS-M 393747, PGS-D 404213), the Office of Naval Research (DRI Grant N00014-14-1-0150 and MURI Grant 286 25-74200-F7112), and from the NYU Abu Dhabi Research Institute (Project G1204).

Thanks to all those in New York who allowed me to create a life outside the office. Thanks to Auntie Ole, Uncle Gordon, Myung Bae, and Heeae Bae for welcoming me to the city and making it feel like home. Thanks to Todd Martin, Tom Torre and all the players from the Coyotes and Psycho Jackpot of the Chelsea Piers hockey league–our late night games were always a highlight of my week. Thanks to Courant's Intramural Volleyball teams, Set Theory, Net Convergence and Bump Functions, and all the players who made it happen. Also, thanks to all the wonderful friends and family who came to visit, consistently providing something to look forward to: Dan Bushuk, Minhee Bae, Chris Heidebrecht, Kevin Chubey, Steph Warnez, Dan Ginsberg, Grandma and Grandpa Harri, Auntie Cap, Carli Mascitelli, Anthony Pranata, Diana Shaw, J.P. (ol') Barnabe, Jeffrey Wong, Trevor Shaw, Michael Tran, and Matt Balega. I would also like to thank Grandma Bushuk for her constant love and support.

To Minju: thank you for all the great memories we made in Manhattan, Brooklyn, Philly, and Newark and for being my rock throughout the entire grad school process. I love you.

Finally, I would like to thank my parents and my brother for the unwavering and incredible support that I have always counted on. This thesis is dedicated to you.

Abstract

Lagged correlation analysis of Arctic sea-ice area anomalies reveals that spring sea-ice anomalies tend to recur the following fall, and fall anomalies tend to recur the following spring. In this work, this phenomenon, termed sea-ice reemergence, is investigated in comprehensive climate models and observations. In Chapter 2, a novel multivariate data analysis technique, coupled nonlinear Laplacian spectral analysis (NLSA), is introduced. This approach is a generalization of the original NLSA algorithm, and allows for unit-independent analysis of multiple physical variables. In Chapter 3, coupled NLSA is applied to sea-ice concentration (SIC) and sea-surface temperature (SST) data in the North Pacific sector. In both models and observations, it is found that low-dimensional families of NLSA modes are able to reproduce the lagged correlation structure of the raw SIC data. These "reemergence families" provide an SST–SIC reemergence mechanism, in which persistent summer SST anomalies store the memory of spring SIC anomalies, allowing for reemergence of these anomalies in the fall season. These families are closely related to the North Pacific Gyre Oscillation (NPGO).

Chapter 4 investigates the co-variability of SIC, SST, and sea-level pressure (SLP) in the Arctic sector. Reemergence families are found to capture the SST–SIC mechanism, and additionally suggest an atmospheric role in reemergence. SLP patterns, resembling the Arctic Dipole Anomaly (DA) and Arctic Oscillation (AO), create large–scale teleconnections between different regions of sea-ice variability, providing communication via their geostrophic winds. Moreover, these SLP patterns suggest an SLP–SIC reemergence mechanism, via their winter-to-winter regime persistence. In Chapter 5, a hierarchy of climate models is studied to investigate the relative roles of the atmosphere and the ocean in producing sea-

ice reemergence. In models with ocean-to-atmosphere coupling, reemergence mode families display a pan-Arctic scale organization of SIC anomalies, related to SLP teleconnection patterns. In Chapter 6, we investigate fall-to-spring reemergence, finding that fall SIC anomalies reemerge the following spring due to persistent sea-ice thickness (SIT) anomalies in the central Arctic.

Contents

List of Figures

Chapter 1

Introduction

1.1 Contemporary climate science and the changing Arctic

Earth's climate is a remarkably rich nonlinear dynamical system involving interactions across spatial scales ranging from micrometers to thousands of kilometers and time scales ranging from seconds to millennia. The climate system involves coupling between the atmosphere, ocean, land, and cryosphere and incorporates a wide breadth of physics, including rotating and stratified fluid dynamics, thermodynamics, solid mechanics, and planetary orbits. The dynamics of this system are characterized by a wide-array of complex multiscale phenomena, such as monsoons and tropical oscillations, hurricanes, interannual and multidecadal variability of the ocean, ice-sheet evolution, and geophysical turbulence.

Since the industrial age, an additional element has been introduced into the climate system: human-produced carbon dioxide and other greenhouse gases from the burning of fossil fuels. Carbon dioxide levels have risen from 278 ± 2 parts-per

million (ppm) in 1750 to 390.5 ± 0.2 ppm in 2011 (Stocker et al., 2013), generally at an increasing rate (MacFarling Meure et al., 2006). Contemporaneous with this carbon dioxide increase, increases in global mean temperature and other related variables have also been observed, leading many to suggest that the warming and associated climate changes are human-induced. The Intergovernmental Panel on Climate Change (IPCC) was established as a formal body in 1988, with the objective of synthesizing current knowledge and identifying areas of uncertainty in climate science. The IPCC produces periodic assessment reports, which summarize observational data, modeling results, and theoretical understanding from research groups around the world. The observational datasets presented in the IPCC's latest assessment report (AR5; Stocker et al., 2013) provide unequivocal evidence of warming across a wide range of physical variables. Fig. 1.1 shows these observations for eight different climate variables, each of which contain multiple datasets. While any given dataset may have errors involving sparsity of observations in space and time (especially for earlier time periods), observation noise, and errors associated with processing algorithms, the agreement across all variables and datasets provides a striking message. The observations show increases in global land-surface air temperature, sea-surface temperature, marine air temperature, sea level, tropospheric air temperature, ocean heat content (upper 700m), and specific humidity, and decreases in summer Arctic sea-ice extent, Northern hemisphere snow cover, and glacier mass balance. The totality of evidence presented in this latest assessment report led the IPCC to conclude that: "Human influence on the climate system is clear. This is evident from the increasing greenhouse gas concentrations in the atmosphere, positive radiative forcing, observed warming, and understanding of the climate system" (Stocker et al., 2013).

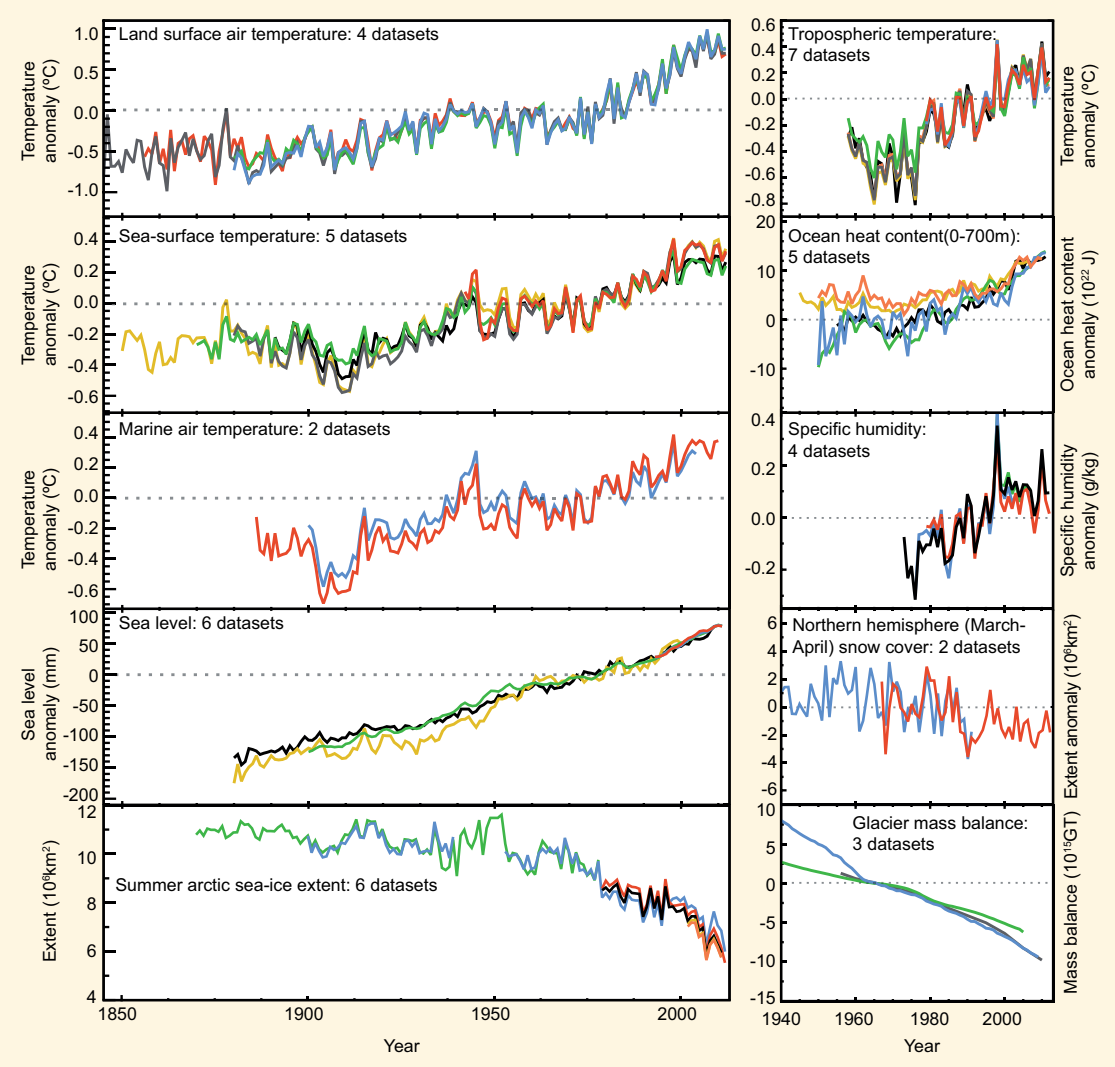

Figure 1.1: Climate change signals as reported by the 2013 IPCC report. Figure is modified from Stocker et al. (2013).

Contemporary climate science blends observations, theory, and modeling and depends crucially on the interplay between these approaches. The rise of computing power has led to increased use of, and confidence in, numerical climate models. Modern global climate models (GCMs) couple atmosphere, ocean, sea ice, and land components, numerically solving the corresponding set of coupled partial differential equations on a discrete grid. Typical grid spacing in a modern GCM is roughly 100km horizontally with approximately 50 vertical levels in the ocean and 20 vertical levels in the atmosphere. The resolution of GCMs necessitates the use of physical parameterizations to account for sub-grid scale processes, which cannot be directly resolved by the model. Despite model errors associated with incomplete physics, GCMs are quite effective at representing sufficiently coarse-grained fields. For example, Fig. 1.2, modified from IPCC report AR5, demonstrates the ability of GCMs to capture the observed changes of global temperature when forced by appropriate greenhouse gas forcings. In particular, the models of the coupled model intercomparison project (CMIP) agree well with temperature observations when forced with both natural and human forcings, and clearly disagree when only forced with natural forcings.

Climate change signals are not spatially uniform across the globe, owing to heat transport from large-scale circulation and climate feedback mechanisms. The Arctic stands out as a region that exhibits enhanced greenhouse-induced warming, likely due to changes associated with the loss of sea ice. This enhanced warming in the Arctic has been termed Arctic amplification (Holland and Bitz, 2003; Serreze and Francis, 2006; Screen and Simmonds, 2010). Since the beginning of the satellite era in 1979, Arctic sea-ice has exhibited a precipitous decline in areal extent (Serreze et al., 2007; Cavalieri and Parkinson, 2012; Stroeve et al., 2012).

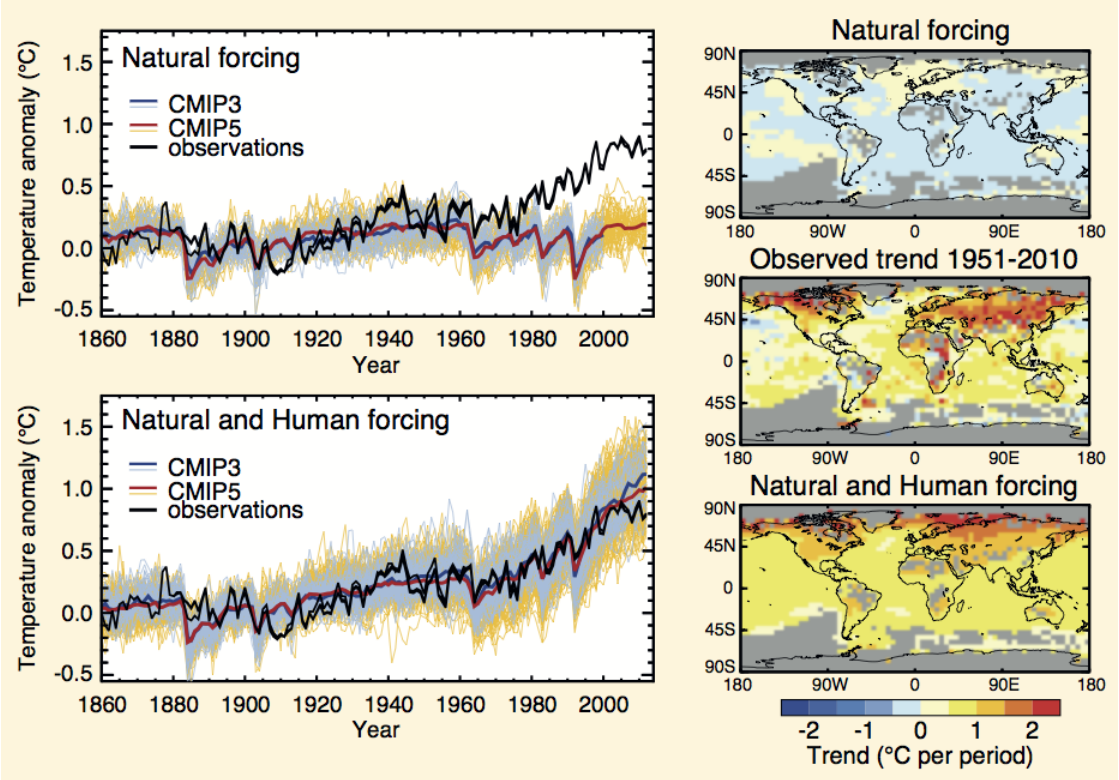

Figure 1.2: Climate response to natural and human forcings, as reported by the 2013 IPCC report. Figure is modified from Stocker et al. (2013).

This decline is observed over nearly all regions of the Arctic and for all months of the year, highlighted by the trend of -14% per decade for September Arctic sea-ice extent (Overland and Wang, 2013). There is also an observed thinning of Arctic sea ice; however, this is based on observations that are sparse in time (Rothrock et al., 1999; Kwok and Rothrock, 2009). Sea-ice thickness observations are based primarily on submarine observations and satellite observations beginning in 2003.

Arctic warming and sea-ice loss act as self-reinforcing processes via the sea-ice albedo feedback mechanism (Budyko, 1969; Curry et al., 1995), leading many to speculate on the possibility of a "tipping point" for the Arctic climate system (Lindsay and Zhang, 2005; Winton, 2006; Eisenman and Wettlaufer, 2009). Others

have shown that while ice-free summer conditions are a likely future possibility, the Arctic climate system does not exhibit hysteretic behavior, and recovery to states with higher ice cover is possible over time-scales of a few years (Tietsche et al., 2011; Serreze, 2011). Recently, there has also been a more controversial link made between decreased Arctic sea ice and extreme weather in the mid-latitudes (Francis and Vavrus, 2012; Screen and Simmonds, 2013; Barnes, 2013).

In addition to its impact on global climate, changes in Arctic sea ice influence a number of other stakeholders, including northern communities, Arctic wildlife, and industries that would benefit from the opening of new shipping routes in the Arctic (Stephenson et al., 2011). The rapid changes in the Arctic have motivated the creation of the Study of Environmental Arctic Change (SEARCH) Sea Ice Outlook (SIO), which is the first large-scale model intercomparison of seasonal Arctic sea-ice prediction skill. The SIO solicits forecasts for September Arctic sea-ice extent from a wide-range of research groups, based on dynamical, statistical and heuristic modeling approaches. The results of 309 individual contributions from 2008–2013 were summarized in the work of Stroeve et al. (2014), demonstrating success in years when the observed ice extent was close to the long-term trend and large errors in years that deviated significantly from the trend.

For longer timescale projections of Arctic sea ice, GCMs are the tool of choice. GCM simulations of 21st-century climate show rapid loss of summer sea ice (Holland et al., 2006b), with ice-free conditions emerging on average in the year 2070 (Overland and Wang, 2013). When compared to satellite observations, GCM simulations tend to underpredict the rate of sea-ice loss (Stroeve et al., 2007). This underprediction could either be the result of (1) systematic model error or (2) the fact that the observational record represents only a single realization of a com-

plex chaotic system. The chaotic nature of nonlinear dynamical systems has been well-known since the famous paper of Lorenz (1963). Recently, with advances in computational power, the chaotic nature of the climate system has begun to be studied in the context of GCM simulations. GCM ensembles, produced by repeatedly running the same model with slightly different initial conditions, display a striking amount of internal variability, especially when considering regional spatial scales (Deser et al., 2012a,b). This internal, or "natural", variability of the climate system imposes intrinsic limits on predictability, related to the manner in which infinitesimal errors grow in the system. Natural variability also poses challenges in attempting to separate a signal into a portion resulting from changes in external forcing and a portion corresponding to internally generated variability.

In the context of Arctic sea ice, studies have attributed roughly half of the observed trend in September sea-ice extent to anthropogenic forcing and the other half to internal variability (Kay et al., 2011; Stroeve et al., 2012). The task of disentangling the effects of external forcing, model error, and natural variability is formidable and will remain a challenge in climate science in the years ahead. A recent study by Swart et al. (2015) found that the spread in estimated sea-ice trends within a single model was comparable to the spread amongst a multi-model ensemble. This suggests that internal variability is of comparable importance to errors due to model physics and highlights the importance of performing long control integrations with fixed forcings. These long control integrations represent a unique testbed for sampling the internal variability of a given model.

Improving model physics and parameterizations represents one path to improving Arctic sea-ice prediction. Another route to improved prediction is the systematic study of sea-ice predictability, which we define here as the degree to which

accurate predictions of the Arctic climate system can be made. There has been a recent proliferation of sea-ice predictability studies (Koenigk and Mikolajewicz, 2009; Holland et al., 2011; Blanchard-Wrigglesworth et al., 2011a,b; Chevallier and Salas-Mélia, 2012; Holland et al., 2013; Tietsche et al., 2013; Day et al., 2014b; Guemas et al., 2014; Germe et al., 2014; Tietsche et al., 2014; Blanchard-Wrigglesworth and Bitz, 2014; Day et al., 2014a) and investigations focussed on seasonal sea-ice forecasts (Msadek et al., 2014; Chevallier et al., 2013; Sigmond et al., 2013; Wang et al., 2013; Schröder et al., 2014; Yuan et al., 2014). One promising avenue of this predictability work is the identification of physically-based mechanisms that could endow sea-ice with predictability. Earlier work has identified important roles of the atmosphere and the ocean in setting patterns of sea-ice variability (Chapman and Walsh, 1993; Fang and Wallace, 1994; Walsh et al., 1996; Deser et al., 2000, 2002; Bitz et al., 2005). Recent work has begun to place this knowledge in the context of sea-ice predictability.

The work of Blanchard-Wrigglesworth et al. (2011a) introduced a phenomenon termed *sea-ice reemergence*, which identified unexpected memory characteristics in Arctic sea-ice area anomalies. Sea-ice reemergence is a lagged correlation phenomenon that is observed in two forms: (1) spring sea-ice area anomalies tend to recur the following fall, despite a loss of correlation over the intervening summer months; and (2) fall sea-ice anomalies tend to recur the following spring, despite a loss of correlation over the intervening winter months. Blanchard-Wrigglesworth et al. (2011a) suggested that the spring-to-fall reemergence is the result of an SST–sea-ice interaction in which spring (melt season) sea-ice concentration (SIC) anomalies imprint anomalies of opposite sign in the surface ocean. These SST anomalies persist over the summer months, and when the SIC grows southward

in the fall (growth season) it interacts with the SST anomaly and reinherits its spring anomaly. SST is unable to participate in the fall-to-spring reemergence, as the regions where fall SIC anomalies occur become completely ice-covered over the winter months. Blanchard-Wrigglesworth et al. (2011a) suggested that the fall-to-spring reemergence occurred due to persistent sea-ice thickness (SIT) anomalies in the central Arctic. These SIT anomalies allow SIC anomalies to reemerge when the ice edge reaches a similar location the following spring. Sea-ice reemergence was examined in five GCMs by Day et al. (2014b), who found reemergence signals of varying strength across the five models. Day et al. (2014b) also corroborated the mechanisms of Blanchard-Wrigglesworth et al. (2011a) by performing correlation between SIC area anomalies and the spatially-varying SST and SIT anomaly fields.

Sea-ice reemergence represents a "predictability mechanism" for Arctic sea ice. Many unanswered questions regarding sea-ice reemergence remain, including the temporal and regional aspects of sea-ice reemergence, its relation to SIC, SST, SLP, and SIT variability, detailed understanding of the mechanisms for spring-to-fall and fall-to-spring reemergence, and the robustness of reemergence in simpler models. The goal of this thesis is to gain a deeper understanding of these, and related, questions. Next, we outline our research plan.

1.2 Research overview

The approach of this thesis is to investigate sea-ice "predictability mechanisms" using novel techniques for data analysis of high-dimensional multivariate time-series. We build upon the framework of nonlinear Laplacian spectral analysis (NLSA; Giannakis et al., 2012; Giannakis and Majda, 2012c,a, 2013, 2015), a

recently developed data analysis technique which is a nonlinear manifold generalization of linear projection-based approaches. The original NLSA algorithm is designed for analysis of a single scalar or vector-valued field. We seek a generalization of this algorithm that has two key features: (1) it is independent of the physical units of the multivariate input data and (2) it does not require any pre-normalization of this data. We term this new approach coupled NLSA.

In Chapter 2, we present the data analysis methods that form the basis for coupled NLSA. First, we introduce empirical orthogonal function (EOF) analysis, the standard data analysis technique in atmosphere-ocean science applications. Next, we introduce singular spectrum analysis (SSA; Broomhead and King, 1986; Vautard and Ghil, 1989; Sauer et al., 1991; Ghil et al., 2002; Groth and Ghil, 2011), which generalizes EOF analysis using the idea of time-lagged embedding. Subsequently, NLSA is introduced, which merges ideas from geometric data analysis and SSA. Finally, we introduce the coupled NLSA algorithm, which will be used extensively in the subsequent chapters. The work in Chapter 2 appeared previously as "Reemergence Mechanisms for North Pacific Sea Ice Revealed through Nonlinear Laplacian Spectral Analysis," in the *Journal of Climate*, **27**, pp 6265–6287, ©2014 AMS, in a paper by Mitchell Bushuk, Dimitrios Giannakis, and Andrew Majda.

In Chapter 3, we investigate the co-variability of SIC and SST in the North Pacific sector using coupled NLSA. We study the phenomenon of sea-ice reemergence in the North Pacific using coupled NLSA modes, finding that low-dimensional mode families form an efficient representation of sea-ice reemergence. In both comprehensive climate models and observations, these "reemergence families" reflect an SST-based reemergence mechanism, in which persistent summer SST anomalies store the memory of earlier SIC anomalies. These reemergence families are found

to be closely connected to the North Pacific Gyre Oscillation (NPGO, Di Lorenzo et al., 2008) pattern of SST variability. A second set of reemergence families, related to the Pacific Decadal Oscillation (PDO, Mantua and Hare, 2002), is found to capture North Pacific SST reemergence. The work presented in Chapter 3 appeared previously as "Reemergence Mechanisms for North Pacific Sea Ice Revealed through Nonlinear Laplacian Spectral Analysis," in the *Journal of Climate*, **27**, pp 6265–6287, ©2014 AMS, in a paper by Mitchell Bushuk, Dimitrios Giannakis, and Andrew Majda.

In Chapter 4, we extend our study of reemergence by considering an Arctic domain and adding SLP into our coupled analysis. This chapter focuses on the regional and temporal aspects of sea-ice reemergence, and the interplay between SIC, SST, and SLP. In both models and observations, we identify significant regional differences and temporal variability in the strength of reemergence. We find that reemergence families of NLSA modes are able to efficiently capture the SST–SIC reemergence mechanism identified in Chapter 3. These reemergence families display clear SIC phase relationships between geographically disconnected regions. The SLP patterns of these families provide an explanation for the corresponding SIC spatial patterns, as they provide a pan-Arctic scale organization of SIC anomalies via their geostrophic winds. The SLP patterns also suggest another plausible reemergence mechanism, via their winter-to-winter regime persistence. The content presented in Chapter 4 appeared previously as "Arctic Sea-Ice Reemergence: The Role of Large-Scale Oceanic and Atmospheric Variability," in the *Journal of Climate*, in press, ©2015 AMS, in a paper by Mitchell Bushuk, Dimitrios Giannakis, and Andrew Majda.

In Chapter 5, we further explore the results of Chapter 4, by studying a hi-

erarchy of models with active sea-ice components, but varying atmospheric and oceanic formulation. This hierarchy is designed to investigate the relative role of the atmosphere and the ocean in producing sea-ice reemergence. We find that dynamical feedback from the ocean to the atmosphere is essential in creating large-scale organized patterns of SIC–SLP co-variability. We also find that the ocean provides the key source of memory for reemergence, and the atmosphere provides the key source of variability. The work presented in Chapter 5 has been submitted to *Geophysical Research Letters*, in a manuscript entitled "Sea-Ice Reemergence in a Model Hierarchy," in a paper by Mitchell Bushuk and Dimitrios Giannakis.

In Chapter 6, we turn our focus to a study of the fall-to-spring reemergence by adding SIT into our coupled analysis. We find that a low-dimensional reemergence family of NLSA modes is able to efficiently capture an SIT–SIC mechanism, in which winter SIT anomalies store the memory of fall SIC anomalies. Using metrics for reemergence, we study the phase relationship of the SIT mechanism, and other reemergence mechanisms, with respect to the seasonal cycle.

Finally, we conclude in Chapter 7 by summarizing the main findings of this work and presenting a number of related problems which will form the basis for future work.

Chapter 2

Data Analysis Methods

2.1 Introduction

In this chapter we introduce a novel technique for unit-independent analysis of high-dimensional multivariate datasets. The approach, coupled nonlinear Laplacian spectral analysis (NLSA), generalizes a number of data analysis techniques, and we will incrementally assemble the building blocks of the method in this chapter. We begin by introducing empirical orthogonal function (EOF) analysis, the standard data analysis technique in atmosphere-ocean science applications. Next, we present singular spectrum analysis (SSA), a generalization of EOF analysis that provides superior time-scale separation and the ability to capture spatiotemporal patterns in data. Subsequently, we introduce the NLSA method, a recently developed nonlinear data analysis technique, which merges the concepts of time-lagged embedding from SSA and diffusion maps (Belkin and Niyogi, 2003; Coifman and Lafon, 2006) from the machine learning community. Finally, we present the coupled NLSA method, which is newly developed in this work, and is a multivariate

extension of NLSA.

2.2 Empirical Orthogonal Function Analysis

The most widely-used tool for data analysis and dimensionality reduction in atmosphere-ocean science is empirical orthogonal function (EOF) analysis (North et al., 1982; von Storch and Zwiers, 1999). EOF analysis seeks to decompose an input signal into a set of spatial patterns called EOFs and an associated set of temporal patterns called principal components (PCs). The EOFs represent the dominant spatial patterns of variability of the input signal, and the PCs encode the amplitude and sign of these patterns at each point in time. These "modes of variability" are ordered in terms of decreasing explained variance. In other contexts, EOF analysis is commonly referred to as Principal Component Analysis (PCA), the Karhunen-Loève transform (KLT), and the Proper Orthogonal Decomposition (POD).

EOF analysis is popular for a number of reasons: (1) it is "variance greedy", seeking patterns that capture the maximal variance of the input signal; (2) the spatial patterns identified often have a natural physical interpretation; and (3) the algorithm is simple and easy to implement. Many well-known patterns of climate variability are defined (or at least can be defined) via EOF analysis, including the North Atlantic Oscillation (NAO; Ambaum et al., 2001), the Pacific Decadal Oscillation (PDO; Mantua et al., 1997; Mantua and Hare, 2002), the Arctic Oscillation (AO; Thompson and Wallace, 1998), the North Pacific Gyre Oscillation (NPGO; Di Lorenzo et al., 2008), the Southern Annular Mode (SAM; Thompson and Wallace, 2000), and the El Niño Southern Oscillation (ENSO; Zhang et al.,

1997).

Next, we describe the operational implementation of EOF analysis. Suppose that we have a signal $y(t, \mathbf{r})$, where $\mathbf{r}$ is a position vector in the space in which our observable y is defined (for the geophysical applications in this work, this is a position on the 2-D surface of the earth). Suppose that we have an s-sample time series of y, which is sampled over d spatial gridpoints. Let the positions of these gridpoints be given by $\mathbf{r}_i$, where $i \in \{1, 2, \ldots, d\}$. Also, assume that this signal is sampled uniformly at time step δt, where $t_j = t_1 + (j-1)\delta t$ and $j \in \{1, 2, \ldots, s\}$.

First, as explained below, the data at each gridpoint is scaled by an appropriate area weighting factor $\sqrt{w_i}$, where w_i represents the area occupied by the ith spatial gridpoint. For example, if this data was defined on a regular latitude-longitude grid, the weighting factors would be $\sqrt{\cos(\phi)}$, where ϕ is the latitude. We define a new area-weighted timeseries $x(t, \mathbf{r})$, where $x(t, \mathbf{r}_i) = y(t, \mathbf{r}_i)\sqrt{w_i}$, $\forall i$. We use the notation $x_j \in \mathbb{R}^d$ to indicate a sample taken at time t_j over the d spatial gridpoints. Next, we form the $d \times s$ data matrix X,

$$X = \begin{bmatrix} x_1 & x_2 & \ldots & x_s \end{bmatrix}.$$

Entry X_{ij} in this matrix indicates the value of x at spatial gridpoint i and time t_j. Note that the data in this matrix has been pre-processed by subtracting the time mean from each spatial gridpoint. In other words, each row in X has mean zero. Next, we compute the temporal covariance function. The continuous version of this function is given by

$$C(t, t') = \int y(t, \mathbf{r}) y(t', \mathbf{r}) d\mathbf{r},$$

where $\mathbf{r}$ is a position vector in the space in which our observable $y(t, \mathbf{r})$ is defined.

Our observed signal y_j is an approximation to the continuous signal, sampled over d spatial gridpoints at time steps t_j. We would like to use this discrete data to compute an approximation to the temporal covariance function. Let w_i represent the area occupied by the ith gridpoint. Then, a discrete approximation to the temporal covariance function is given by:

$$C(t_j, t_{j'}) = \sum_{i=1}^{d} y(t_j, \mathbf{r}_i) y(t_{j'}, \mathbf{r}_i) w_i = \sum_{i=1}^{d} x(t_j, \mathbf{r}_i) x(t_{j'}, \mathbf{r}_i) = x_j^T x_{j'}.$$

Therefore, Euclidean inner products between area-weighted samples provide the temporal covariance between these samples. This is the reason that we use the area-weighted timeseries x. Next, we form the temporal covariance matrix $C = X^T X$ and solve the eigenvalue problem

$$C v_k = \lambda_k v_k.$$

C is a positive definite symmetric matrix, hence it is unitarily diagonalizable, and $\{v_k\}$ are an orthonormal set of vectors in $\mathbb{R}^s$. These are the principal components, or right singular vectors. We define the singular values σ_k as $\sigma_k = \sqrt{\lambda_k}$, and define the left singular vectors as:

$$u_k = \frac{X v_k}{\sigma_k}.$$

The $\{u_k\}$ are an orthonormal set of vectors with respect to the Euclidean inner product. These vectors define spatial patterns in $\mathbb{R}^d$. Upon division by the area-weighting factors $\sqrt{w_i}$, these are the EOFs. Note that if $\sigma_k = 0$, we simply choose

u_k as a unit vector that is orthogonal to the rest of the left singular vectors.

This decomposition of X is referred to as the Singular Value Decomposition (SVD), and can be written in the following matrix product form:

$$X = \begin{bmatrix} \uparrow & \uparrow & & \uparrow \\ u_1 & u_2 & \cdots & u_D \\ \downarrow & \downarrow & & \downarrow \end{bmatrix} \begin{bmatrix} \sigma_1 & 0 & \cdots & 0 \\ 0 & \sigma_2 & \cdots & 0 \\ \vdots & & \ddots & \vdots \\ 0 & \cdots & 0 & \sigma_D \end{bmatrix} \begin{bmatrix} \leftarrow & v_1 & \rightarrow \\ \leftarrow & v_2 & \rightarrow \\ & \vdots & \\ \leftarrow & v_D & \rightarrow \end{bmatrix},$$

where $D = \min(d, s)$. This decomposition, where $D = \min(d, s)$ and the matrix of singular values is square, is commonly referred to as the *reduced SVD*. It is also illuminating to write the decomposition as a sum of rank-one matrices:

$$X = \sum_{k=1}^{D} \sigma_k u_k v_k^T.$$

Here, each mode is represented by a rank one matrix. One can produce a reduced representation of the original data by choosing a subspace of modes, and summing up the appropriate rank one matrices. This concept of dimensionality reduction makes EOF analysis extremely powerful in explaining complex high-dimensional signals.

2.3 Singular Spectrum Analysis

Singular Spectrum Analysis (SSA) was introduced by Broomhead and King (1986) as a data analysis technique for dynamical systems with complex spatiotemporal data, and has been studied extensively since (Vautard and Ghil, 1989; Sauer et al., 1991; Ghil et al., 2002; Groth and Ghil, 2011). SSA is based upon the

idea of time-lagged embedding or "method of delays" introduced in the work of Takens (1981). Like EOF analysis, SSA seeks a decomposition of the input signal into modes of variability. However, instead of seeking spatial patterns (EOFs) and associated time series (PCs), SSA seeks spatiotemporal patterns and associated time series. The first step of the SSA algorithm is the choice of a parameter q, which specifies the time window $\Delta t = q\delta t$ that makes up each spatiotemporal pattern. As earlier, suppose that we have an area-weighted signal $x_j \in \mathbb{R}^d$, where $j \in \{1, 2, \ldots, s\}$. First, we embed our signal into the higher-dimensional space $\mathbb{R}^{qd}$, under the delay-coordinate mapping

$$x_j \mapsto X_j = (x_j, x_{j-1}, ..., x_{j-(q-1)}).$$

Each of these vectors, which we called time-lag embedded vectors, consists of q snapshots of our input signal. Next, we assemble the $qd \times s - q + 1$ lag-embedded data matrix, X, with these vectors placed along its columns:

$$X = \begin{bmatrix} X_q & X_{q+1} & \ldots & X_s \end{bmatrix}.$$

It is illuminating to also write the lag-embedded data matrix explicitly in terms of the input data, which illustrates the degree of data repetition in this matrix:

$$X = \begin{bmatrix} x_q & x_{q+1} & x_{q+2} & \ldots & x_{s-2} & x_{s-1} & x_s \\ x_{q-1} & x_q & x_{q+1} & \ldots & x_{s-3} & x_{s-2} & x_{s-1} \\ x_{q-2} & x_{q-1} & x_q & \ldots & x_{s-4} & x_{s-3} & x_{s-2} \\ \vdots & \vdots & \vdots & & \vdots & \vdots & \vdots \\ x_1 & x_2 & x_3 & \ldots & x_{s-q-1} & x_{s-q} & x_{s-q+1} \end{bmatrix}.$$

Note that the subdiagonals of X generically contain q copies of each data sample, except for the first $q-1$ and final $q-1$ samples in the time series. Next, analogous to EOF analysis, we compute the SVD of X, and write:

$$X = \sum_{k=1}^{D} \sigma_k u_k v_k^T,$$

where $D = \min(dq, s-q+1)$, $u_k \in \mathbb{R}^{qd}$, $\sigma_k \in \mathbb{R}_{\geqslant 0}$, and $v_k \in \mathbb{R}^{s-q+1}$. Here, $\{u_k\}$ are q-snapshot spatiotemporal patterns and $\{v_k\}$ are the principal components. Upon division by the area-weighting factors $\sqrt{w_i}$, the $\{u_k\}$ are known as extended empirical orthogonal functions (EEOFs). SSA is also commonly referred to EEOF analysis in the atmosphere-ocean science literature. Note that, in the case of $q = 1$, SSA reduces to EOF analysis.

Each of the $X^k = \sigma_k u_k v_k^T$ is a rank-one matrix that describes the temporal evolution of the mode u_k in lagged embedding space $\mathbb{R}^{qd}$. Often, we are interested in the evolution of this mode in physical space $\mathbb{R}^d$. To project back to physical space, we average along the appropriate subdiagonals (the diagonals with repeated entries; see lag-embedded data matrix above) and obtain a representation of x_j for all $j \in \{1, 2, \ldots, s\}$, which we call $\tilde{x}_j^k$. Specifically, let us denote the jth column of X^k by:

$$X_j^k = \begin{bmatrix} \hat{x}_{j,0}^k \\ \hat{x}_{j,1}^k \\ \vdots \\ \hat{x}_{j,q-1}^k \end{bmatrix}.$$

In this vector, $\hat{x}_{j,0}^k$ corresponds to x_j, $\hat{x}_{j,1}^k$ corresponds to x_{j-1}, *et cetera*. Ignoring

the first and last $q-1$ samples of the timeseries, there are q entries that correspond to x_j, specifically, $\hat{x}^k_{j,0}, \hat{x}^k_{j+1,1}, ..., \hat{x}^k_{j+q-1,q-1}$. To obtain $\tilde{x}^k_j$, we simply average these:

$$\tilde{x}^k_j = \frac{1}{q} \sum_{l=0}^{q-1} \hat{x}^k_{j+l,l}.$$

We call $\tilde{x}^k_j$ the reconstructed data. Upon division by the area-weighting factors $\sqrt{w_i}$, this gives a spatial reconstruction in the physical units of the input signal. This reconstructed data can be produced for a single mode, or for a mode subspace of the user's choosing. The user can either choose not to reconstruct the first and last $q-1$ samples of the timeseries (this is the approach we employ), or do the reconstruction for these samples by averaging the appropriate subdiagional, which will contain less than q entries that correspond to x_j.

2.4 Nonlinear Laplacian Spectral Analysis

The original nonlinear Laplacian spectral analysis (NLSA) algorithm, introduced in a series of papers in 2012 and 2013, is a nonlinear manifold generalization of SSA (Giannakis et al., 2012; Giannakis and Majda, 2012c,a, 2013, 2015). NLSA combines the concept of time-lagged embedding from SSA with Laplacian eigenmaps and diffusion maps, which are a class of nonlinear dimensionality reduction techniques from the machine learning and harmonic analysis community (Belkin and Niyogi, 2001, 2003, 2004; Coifman and Lafon, 2006; Jones et al., 2008). There is also another recently developed related approach, diffusion-mapped delay coordinates (DMDC), that merges time-lagged embedding and diffusion maps (Berry et al., 2013). As with SSA, NLSA operates on the time-lagged embedded data,

and also uses an SVD to extract spatiotemporal and temporal modes of variability from the data. The difference between the two algorithms is that NLSA adds an additional filtering step, in which the data is projected onto a natural set of temporal patterns that are derived via intrinsic similarity relationships of the data. Below, we present the steps of the NLSA algorithm.

Again, consider an area-weighted signal $x(t, \mathbf{r})$ sampled over d spatial gridpoints, with s time samples. Suppose the signal is sampled uniformly at time step δt. Following the techniques of SSA, we choose some time-lagged embedding window $\Delta t = q\delta t$, and we embed our data in the higher-dimensional space $H = \mathbb{R}^{dq}$ under the delay-coordinate mapping

$$x_j \mapsto X_j = (x_j, x_{j-1}, ..., x_{j-(q-1)}).$$

Next, we compute the phase space velocity, ξ_i, viz.

$$\xi_i = X_i - X_{i-1}.$$

These vectors have a natural geometric interpretation as the vector field on the data manifold driving the dynamics (Giannakis, 2015).

NLSA algorithms utilize a set of natural orthonormal basis functions on the nonlinear data manifold to describe temporal patterns analogous to PCs. These basis functions are eigenfunctions of a graph Laplacian operator computed from a pairwise kernel function K on the data. The graph Laplacian eigenfunctions form a complete basis on the data manifold and are ordered in terms of increasing eigenvalue. These eigenvalues can be interpreted as squared "wavenumbers" on the data manifold (Giannakis and Majda, 2015). Performing a spectral truncation

in terms of the leading l eigenfunctions acts as a filter for the data, which removes high wavenumber energy on the data manifold, while retaining the energy at low wavenumbers. This truncation penalizes highly oscillatory features on the data manifold, and emphasizes slowly varying ones.

We next introduce the pairwise kernel function K, which measures the similarity between different states in lagged embedding space. K is a Gaussian kernel and can be thought of as a local version of the temporal covariance matrix, which decays to zero outside of a given neighborhood. K_{ij} is defined as:

$$K_{ij} = \exp\left(-\frac{\|X_i - X_j\|^2}{\epsilon\|\xi_i\|\|\xi_j\|}\right).$$

Here, ϵ is a parameter that controls the locality of the Gaussian kernel, and $\|\cdot\|$ is the standard Euclidean norm. For typical climate datasets, ϵ is order 1, and is smaller for datasets with more time samples. Note that ϵ is order 1 due to the normalization by the phase velocities in the kernel. Heuristically, K_{ij} represents the likelihood of a random walker on the data manifold transitioning from state i to state j. Note that this random walk is introduced solely for the purpose of evaluating orthonormal basis functions on the discrete data manifold. In particular, the random walk has no relation to the actual dynamics of the system. This kernel depends on the phase velocity magnitude $\|\xi_i\|$ in the sense that states with a large (small) velocity magnitude have appreciable transition probability to a larger (smaller) number of states, due to the Gaussian having a larger (smaller) width. As a result, the algorithm has enhanced skill in capturing transitory events characterized by large $\|\xi_i\|$ (Giannakis and Majda, 2012c). Using the graph Laplacian approach of Coifman and Lafon (2006), we compute the Laplacian matrix L via

the following steps:

$$
\begin{aligned}
Q_i &= \sum_{j=1}^{s-q} K_{ij}, \\
\tilde{K}_{ij} &= \frac{K_{ij}}{Q_i^\alpha Q_j^\alpha}, \\
D_i &= \sum_{j=1}^{s-q} \tilde{K}_{ij}, \\
P_{ij} &= \frac{\tilde{K}_{ij}}{D_i}, \\
L &= I - P,
\end{aligned}
$$

where P is a transition matrix, I is the identity matrix, and α is a normalization parameter. Typical choices for this class of algorithms is $\alpha = 0$ and $\alpha = 1$.

Next, we solve the eigenvalue problem

$$L\phi_i = \lambda\phi_i,$$

and recover a set of discrete Laplacian eigenfunctions $\{\phi_1, \phi_2, \ldots, \phi_{s-q}\}$ defined on the data manifold. The transition matrix P also defines an invariant measure $\vec{\mu}$ on the discrete data manifold, given by

$$\vec{\mu}P = \vec{\mu},$$

where μ_i represents the volume occupied by the sample X_i on the data manifold.

Let $X : \mathbb{R}^{s-q} \mapsto \mathbb{R}^{qd}$ be the lagged-embedded data matrix for our s-sample data

set:

$$X = \begin{bmatrix} X_{q+1} & X_{q+2} & \dots & X_s \end{bmatrix}.$$

Note that this matrix begins with X_{q+1} rather than X_q, because the first sample was used in the computation of the phase velocities. Projecting X onto the leading l Laplacian eigenfunctions, we construct a linear map $A_l : \mathbb{R}^l \mapsto \mathbb{R}^{qd}$, given by

$$A_l = X\mu\Phi.$$

In the above, Φ is a matrix whose columns are the leading l Laplacian eigenfunctions, and μ is a diagonal matrix with entries $\vec{\mu}$ along the diagonal. SVD of the operator A_l yields sets of spatiotemporal modes u_k of dimension qd, analogous to extended EOFs, and temporal modes $v_k(t)$ of length $s - q$, analogous to PCs. Projecting the modes from lagged embedding space to physical space using the approach from SSA, we obtain reconstructed data $\tilde{u}_k(t)$ for the original field.

An important aspect of the NLSA algorithm is the selection of the temporal space dimension l. Ultimately, this is a choice that needs to made by the user of the algorithm. However this choice can be guided by a spectral entropy criterion (Giannakis and Majda, 2012a), which allows the user to systematically track changes in the singular value spectrum with changes in l. At large values of l, the singular values tend to saturate at a certain value. For small l, crucial features of the dataset are truncated. The spectral entropy criterion provides guidance to choosing a truncation level between these two limits.

First, given an l, we define a probability distribution p^l, with entries p^l_k given

by

$$p_k^l = \frac{(\sigma_k^l)^2}{\sum_{k=1}^{l}(\sigma_k^l)^2},$$

where σ_k^l is the kth singular value of A_l. The p_k^l values represent the variance distribution amongst the l modes. Now, we consider the values $\hat{\sigma}_k^l$, given by $\hat{\sigma}_k^l = \sigma_k^l$ for $k \leqslant l-1$ and $\hat{\sigma}_k^l = \sigma_{k-1}^l$ for $k = l$. We define a probability distribution π^l, given by

$$\pi_k^l = \frac{(\hat{\sigma}_k^l)^2}{\sum_{k=1}^{l}(\hat{\sigma}_k^l)^2}.$$

Next, we compute the relative entropy, D_l, between these two distributions:

$$D_l = \sum_{k=1}^{l} p_k^l \log \frac{p_k^l}{\pi_k^l}.$$

D_l exhibits a sequence of spikes at small to moderate values of l, eventually settling to smaller values (see Figure 1 of Chapter 3, ahead). The practical criterion used for truncation is to choose a value of l at which D_l begins to settle to these smaller values.

2.5 Coupled Nonlinear Laplacian Spectral Analysis

The original NLSA algorithm is designed for analysis of a high-dimensional time series from a single scalar or vector-valued variable. Here, we seek to modify the NLSA algorithm to allow for an analysis of multiple variables with, in general, different physical units. For example, the applications ahead will focus on the coupled variability of sea-ice concentration (measured in %) and sea-surface temperature (measured in K). Studying the coupled variability of these fields requires a method for normalizing each dataset. The coupled NLSA approach provides a natural method for "non-dimensionalizing" these datasets, which does not require any ad-hoc choices of normalization by the user.

Let $x^1(t, \mathbf{r})$ and $x^2(t, \mathbf{r})$ be two area-weighted signals, each sampled uniformly at time step δt. Let $x^1(t, \mathbf{r})$ be sampled over d_1 gridpoints and $x^2(t, \mathbf{r})$ be sampled over d_2 gridpoints. Following the techniques of SSA, we choose some time-lagged embedding window $\Delta t = q\delta t$, and we embed our data in the higher-dimensional spaces $\mathbb{R}^{d_1 q}$ and $\mathbb{R}^{d_2 q}$ under the delay-coordinate mappings

$$x_j^1 \mapsto X_j^1 = (x_j^1, x_{j-1}^1, ..., x_{j-(q-1)}^1),$$
$$x_j^2 \mapsto X_j^2 = (x_j^2, x_{j-1}^2, ..., x_{j-(q-1)}^2).$$

Next, for each variable we compute the phase space velocities, ξ_i^1 and ξ_i^2, viz.

$$\xi_i^1 = X_i^1 - X_{i-1}^1,$$
$$\xi_i^2 = X_i^2 - X_{i-1}^2.$$

Again, we seek to compute a pairwise kernel function K that measures similarity between states. In the coupled NLSA approach introduced here, this function is constructed using the idea of scale invariance. In particular, we compute the Gaussian kernel values K_{ij} so that physical variables are made dimensionless, allowing for direct comparison of different variables:

$$K_{ij} = \exp\left(-\frac{\|X_i^1 - X_j^1\|^2}{\epsilon\|\xi_i^1\|\|\xi_j^1\|} - \frac{\|X_i^2 - X_j^2\|^2}{\epsilon\|\xi_i^2\|\|\xi_j^2\|}\right).$$

As before, ϵ is a parameter that controls the locality of the Gaussian kernel, and $\|\cdot\|$ is the standard Euclidean norm. The phase velocities serve two key roles in this kernel: (1) as before, they provide a dynamical tuning of the kernel, emphasizing highly transitory states, and (2) division by the phase velocities nondimensionalizes the data, allowing for a natural comparison between X^1 and X^2. The coupled NLSA kernel is also constructed to emphasize the co-variability of the two input fields. The product form of this kernel implies that a large value of K_{ij} requires a high degree of similarity between both X_i^1 and X_j^1 and X_i^2 and X_j^2. If one of the fields does not have high similarity the value of K_{ij} will be significantly diminished.

Using the kernel values, we use the same approach as the NLSA algorithm to compute the Laplacian matrix L, solve the eigenvalue problem $L\phi_i = \lambda\phi_i$, and recover a set of discrete Laplacian eigenfunctions $\{\phi_1, \phi_2, \ldots, \phi_{s-q}\}$.

Next, we compute spatiotemporal and temporal patterns for each of the input fields. Let $X^1 : \mathbb{R}^{s-q} \mapsto \mathbb{R}^{qd_1}$ and $X^2 : \mathbb{R}^{s-q} \mapsto \mathbb{R}^{qd_2}$ be the data matrices for our

two s-sample data sets:

$$X^1 = \begin{bmatrix} X^1_{q+1} & X^1_{q+2} & \dots & X^1_s \end{bmatrix},$$
$$X^2 = \begin{bmatrix} X^2_{q+1} & X^2_{q+2} & \dots & X^2_s \end{bmatrix}.$$

Projecting X^1 and X^2 onto the leading l Laplacian eigenfunctions, we construct linear maps $A^1_l : \mathbb{R}^l \mapsto \mathbb{R}^{qd_1}$ and $A^2_l : \mathbb{R}^l \mapsto \mathbb{R}^{qd_2}$, given by

$$A^1_l = X^1 \mu \Phi, \quad A^2_l = X^2 \mu \Phi.$$

In the above, Φ is a matrix whose columns are the leading l Laplacian eigenfunctions, and μ is a diagonal matrix with entries $\vec{\mu}$ along the diagonal. As in the case of univariate NLSA, our choice of l is guided by a spectral entropy criterion. Singular value decomposition (SVD) of the operators A^1_l and A^2_l yields sets of spatiotemporal modes $\{u^1_k\}$ and $\{u^2_k\}$ of dimension qd_1 and qd_2, respectively, analogous to extended EOFs, and corresponding sets of length l vectors, $\{V^1_k\}$ and $\{V^2_k\}$. These length l vectors are the expansion coefficients in eigenfunction basis. Expanding using the first l eigenfunctions, we recover a set of temporal modes $\{v^1_k\}$ and $\{v^2_k\}$ of length $s - q$, where $v^1_k = \Phi_l V^1_k$ and $v^2_k = \Phi_l V^2_k$. These modes, indexed by k, are ordered by decreasing singular value. Forming products $\sigma^1_k u^1_k (v^1_k)^T$ and $\sigma^2_k u^2_k (v^2_k)^T$ and projecting from lagged embedding space to physical space using the standard approach from SSA, we obtain reconstructed fields $\tilde{u}^1_k(t)$ and $\tilde{u}^2_k(t)$.

It should be noted that, while the SVD is performed on each operator individually, the resulting spatiotemporal patterns $\{u^1_k\}$ and $\{u^2_k\}$, and principal components $\{v^1_k\}$ and $\{v^2_k\}$, are inherently coupled. This is because these operators are

constructed using the same l-dimensional set of eigenfunctions, which have been computed using the full multivariate dataset. Note that the variables used to construct the eigenfunctions do not necessarily need to coincide with the variables for which we compute the A_l operators. For example, we can use the eigenfunctions computed using X^1 and X^2 to filter any other variable of interest in our system.

Another natural possibility for performing coupled NLSA is to perform an initial normalization of each physical variable to unit variance, and subsequently perform the standard NLSA algorithm on the concatenated dataset. A problem with this approach is that we artificially impose the variance ratio of the two variables, without incorporating any information about their relative variabilities. An appealing feature of the coupled approach described above is that the variance ratio between variables is automatically chosen by the algorithm in a dynamically motivated manner. We term the approach outlined in this section "phase velocity normalization" and the normalization to unit variance "variance normalization." We will return to these issues in section 3a of Chapter 3. Another appealing aspect of the algorithm above is that it can be naturally generalized from two variables to many variables.

Chapter 3

Reemergence Mechanisms for North Pacific Sea Ice Revealed through Nonlinear Laplacian Spectral Analysis

3.1 Introduction

In this chapter, we utilize the coupled nonlinear Laplacian spectral analysis (NLSA) technique to investigate the coupled variability of sea ice and sea-surface temperature (SST) in the North Pacific Ocean. The dominant regions of North Pacific sea-ice variability are the Bering Sea and the Sea of Okhotsk. Empirical orthogonal function (EOF) analysis of North Pacific sea-ice observational data shows a leading mode which is a sea-ice dipole between the Okhotsk and Bering seas, and a second mode with spatially uniform ice changes over the domain (Deser

et al., 2000; Liu et al., 2007). Other authors have also found evidence of a Bering-Okhotsk dipole (Cavalieri and Parkinson, 1987; Fang and Wallace, 1994).

The primary hypothesis from earlier work on North Pacific sea ice is that atmospheric patterns such as the Aleutian low and the Siberian high drive sea ice variability (Parkinson, 1990; Cavalieri and Parkinson, 1987; Sasaki and Minobe, 2006). The study of Blanchard-Wrigglesworth et al. (2011a), hereafter BW, suggests that the ocean may also play an important role in sea-ice variability. BW found that Arctic sea ice has "memory", in which anomalies of a certain sign in the melt season (spring) tend to produce anomalies of the same sign in the growth season (fall). Additionally, they found that the intervening summer sea-ice cover was not strongly correlated with the spring anomalies. This phenomenon, termed sea-ice reemergence, was observed in the fall-spring variety described above, as well as a summer-summer reemergence. BW propose a mechanism for the spring-fall reemergence in which spring sea-ice anomalies induce an SST anomaly of opposite sign, which persists over the summer months. When the ice edge returns to this spatial location in the fall, the SST anomaly reproduces a sea-ice anomaly of the same sign as the spring. The phenomenon of reemergence has also been observed in North Pacific Ocean data (Alexander et al., 1999), in the form of a winter-to-winter SST reemergence.

In this work, we utilize the coupled NLSA technique (Chapter 2), which is a multivariate generalization of the original NLSA algorithm (Giannakis and Majda, 2012c,a, 2013). Given a time series of high-dimensional data, NLSA yields a set of spatiotemporal modes, analogous to extended EOFs, and a corresponding set of temporal patterns, analogous to principal components (PCs). In applications involving North Pacific SST from climate models (Giannakis and Majda, 2012a),

these include intermittent type modes not found in singular spectrum analysis (SSA) that carry low variance but are important as predictor variables in regression models (Giannakis and Majda, 2012b).

The coupled NLSA algorithm provides a unit-independent approach for analysis of multivariate datasets. Here, we investigate the phenomenon of sea-ice reemergence using the spatiotemporal modes of variability extracted through coupled NLSA of sea-ice concentration and SST from a 900-yr control integration of the Community Climate System Model version 3 (CCSM3, Collins et al., 2006), and in 34 years of sea ice and SST satellite observations from the Met Office Hadley Center Sea Ice and Sea Surface Temperature (HadISST, Rayner et al., 2003) dataset. We find that the sea-ice reemergence mechanism suggested by BW can be reproduced in both model output and observations using low-dimensional families of NLSA modes, with the intermittent modes playing a crucial role in this mechanism. Moreover, we find that the reemergence of correlation, in both sea ice and SST, is significantly strengthened by conditioning on certain low-frequency modes being active. These low-frequency modes reflect the North Pacific SST variability of the North Pacific Gyre Oscillation (NPGO, Di Lorenzo et al., 2008) and the Pacific Decadal Oscillation (PDO, Mantua and Hare, 2002). We find that the NPGO is related to the sea-ice reemergence of BW, while the PDO is related to SST reemergence (Alexander et al., 1999).

The plan of this chapter is as follows. In section 2, we describe the CCSM3 and HadISST datasets. In section 3, we describe modes of variability captured by coupled NLSA when applied to North Pacific sea ice and SST from CCSM3. In section 4, we find reduced subsets of NLSA modes that are able to reproduce the lagged correlation structure of BW, and we provide a mechanism for the observed

sea-ice memory. We also investigate SST reemergence. In section 5, we compare the results from CCSM3 to observations, by performing similar analyses on the HadISST dataset. We conclude in section 6. Movies illustrating the dynamic evolution of modes are available as online supplementary material.

3.2 Dataset description

3.2.1 CCSM3 model output

This chapter analyzes model output from a 900-yr equilibrated control integration of CCSM3 (Collins et al., 2006). We use CCSM3 monthly averaged sea-ice concentration and SST data, which come from the Community Sea Ice Model (CSIM, Holland et al., 2006a) and the Parallel Ocean Program (POP, Smith and Gent, 2004), respectively. The model uses a T42 spectral truncation for the atmospheric grid (roughly $2.9^\circ \times 2.9^\circ$), and the ocean and sea ice variables are defined on the same grid, of 1° nominal resolution. This chapter focuses on the North Pacific sector of the ocean, which we define as the region 120°E–110°W and 20°N–65°N (Teng and Branstator, 2011). Note that the seasonal cycle has not been removed from this dataset.

Sea-ice concentration is only defined for the northern part of this domain, thus we have $d_1 = 3750$ sea ice spatial gridpoints, and $d_2 = 6671$ SST spatial gridpoints. Using an embedding window of $q = 24$ (Giannakis and Majda, 2012c), this yields lagged embedding dimensions of $qd_1 = 90{,}000$ and $qd_2 = 160{,}104$. The value of $q = 24$ months was used as the time lag because the resulting embedding window is longer than the seasonal cycle, which is a primary source of non-Markovianity in this dataset. A number of q values $\in [1, 48]$ were tested, including q's relatively

prime to 12. It was found that the results were qualitatively similar for sufficiently large q, i.e. $q \geqslant 12$, and sensitive to q for $q < 12$ (see also Giannakis and Majda, 2013).

3.2.2 Observational data

We also study the Met Office Hadley Center Sea Ice and Sea Surface Temperature (HadISST) dataset (Rayner et al., 2003), which consists of monthly averaged sea ice and SST data on a 1° latitude-longitude grid. We use the satellite era data from January 1979-August 2013. Note that all ice-covered gridpoints in the HadISST dataset were assigned an SST value of -1.8°C, the freezing point of salt water at a salinity of 35 parts per thousand. Moreover, the trend in the dataset was removed by computing a long-term linear trend for each month of the year, and removing the respective linear trend from each month.

3.3 Coupled sea ice-SST spatiotemporal modes of variability in CCSM3

We apply the coupled NLSA algorithm described in Chapter 2 to the CCSM3 sea ice and SST datasets, using an embedding window of $\Delta t = 24$ months, and choosing the parameter ϵ, which controls the locality of the Gaussian kernel, as $\epsilon = 1.4$. We include a discussion of the of the robustness of results with respect to changes in ϵ in section 4a. Note that the time mean at each gridpoint has been subtracted from the dataset, but the seasonal cycle has not been subtracted. Utilizing the spectral entropy criterion outlined in Giannakis and Majda (2012a, 2013), we choose a truncation level of $l = 22$, and express the lagged embedding matrices

X^{ICE} and X^{SST} in the basis of the leading 22 Laplacian eigenfunctions, yielding the operators A_l^{ICE} and A_l^{SST}. Singular value decomposition of A_l^{ICE} produces a set of l temporal patterns, v_k^{ICE}, of length $s-q$, analogous to PCs and l corresponding spatiotemporal patterns, u_k^{ICE}, of dimension qd_1, analogous to extended EOFs. Similarly, SVD of A_l^{SST} produces temporal patterns, v_k^{SST}, and corresponding spatiotemporal patterns u_k^{SST}, of dimension qd_2. Each variable has its own set of principal components, but we find that each sea ice PC is strongly correlated with a particular SST PC. Therefore, it is natural to consider the corresponding spatiotemporal patterns as a pattern of coupled SST-sea ice variability.

Figure 3.1a shows the singular values of the operators A_l^{ICE} and A_l^{SST} using the phase velocity normalization approach outlined in Chapter 2 and the variance normalization approach mentioned at the end of Chapter 2. Also shown are the singular values from SSA performed on the unit variance normalized dataset. Note that the SST singular values decay much more rapidly than the sea-ice singular values, indicating that the SST signal has more variability stored in its leading modes than the sea-ice signal.

Figure 3.1b shows a plot of the normalized relative entropy vs truncation level l, computed using the approach of Giannakis and Majda (2012a, 2013). As $l \to \infty$, and in the case of uniform measure $\vec{\mu}$ and phase velocity ξ, the results of NLSA converge to SSA. The spectral entropy criterion provides a heuristic guideline for choosing l, designed to select l large-enough to reproduce the crucial features of the data, but small-enough to filter out highly oscillatory features of the data (Giannakis and Majda, 2015). The latter would be present in the SSA limit mentioned above. In the normalized relative entropy plot, spikes represent the addition of qualitatively new features to the data, and suggest possible truncation levels.

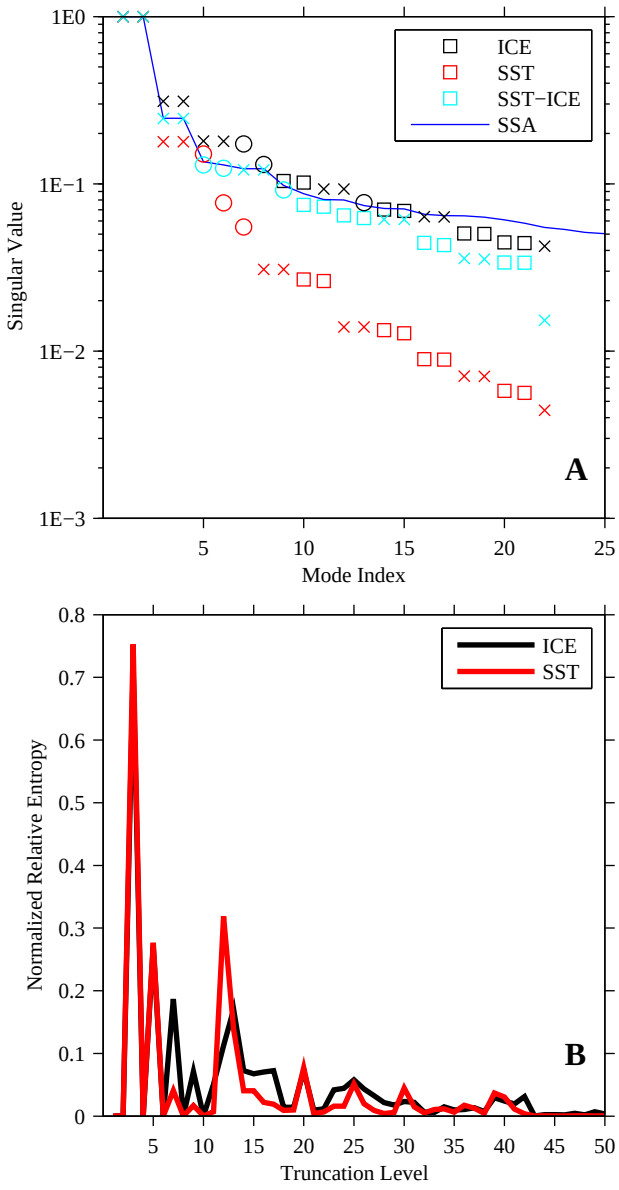

Figure 3.1: (a) Singular values from coupled NLSA with phase velocity normalization (black and red markers show ice and SST singular values, respectively), variance normalization (cyan markers), and SSA (blue line). The singular values have been normalized so that $\sigma_1 = 1$. Low-frequency modes are indicated by "◯", periodic modes by "×", and intermittent modes by "□". (b) Normalized relative entropy for A_l^{ICE} and A_l^{SST} vs truncation level l. Spikes in the relative entropy curve indicate possible candidates for the choice of truncation level.

Here, seeking a parsimonious description of the data, we select a truncation level of $l = 22$.

3.3.1 Temporal modes and sea ice-SST coupling

Coupled NLSA yields three distinct families of of modes: periodic, low-frequency, and intermittent modes. Figures 3.2 and 3.3 summarize the temporal patterns v_k^{ICE} and v_k^{SST}, respectively, showing snapshots of the v_k^{ICE} and v_k^{SST} time series, power spectral densities, and autocorrelation functions. We use the letters P, L, and I to designate periodic, low-frequency, and intermittent modes, respectively.

The periodic modes exist in doubly degenerate pairs with temporal patterns $v_k(t)$ that are sinusoidal with a relative phase of $\pi/2$, and with frequencies of integer multiples of 1 yr^{-1}. The leading two pairs of periodic modes carry more variance than any of the low-frequency or intermittent modes, and represent annual and semiannual variability, respectively. The low-frequency modes carry the majority of their spectral power over interannual to decadal timescales, and have a typical decorrelation time of 3–4 years.

The intermittent modes are characterized by broadband spectral power centered on a base frequency of oscillation with some bias towards lower frequencies. Similar to the periodic modes, these modes come in nearly degenerate pairs. The temporal behavior of the intermittent modes resembles a periodic signal modulated by a low frequency envelope. In the spatial domain, they are characterized by a bursting-type behavior with periods of quiescence followed by periods of strong activity. The intermittent modes carry lower variance than their low-frequency and periodic counterparts (see Fig. 3.1a), however they play a crucial role in explaining the sea-ice reemergence mechanism, as will be demonstrated in the fol-

lowing sections of this chapter. Elsewhere (Giannakis and Majda, 2012b), it has been demonstrated that this class of modes has high significance in external-factor regression models for low-frequency modes, in which the intermittent modes are used as prescribed external factors (forcings). Intermittent type modes highlight the main difference between SSA and NLSA: NLSA captures low-variance patterns of potentially high dynamical significance using a small set of modes, while classical SSA does not.

The sea-ice PCs, v_k^{ICE}, are certainly not independent of the SST PCs, v_k^{SST}. We find that each sea-ice PC is strongly correlated with a certain SST PC. In Fig. 3.4, we show correlations between selected sea ice and SST PCs. Motivated by these correlations, we define the following coupled modes of sea ice-SST variability: $\mathbf{P}_1 = (P_1^{\mathrm{ICE}}, P_1^{\mathrm{SST}})$, $\mathbf{P}_2 = (P_2^{\mathrm{ICE}}, P_2^{\mathrm{SST}})$, $\mathbf{P}_3 = (P_3^{\mathrm{ICE}}, P_3^{\mathrm{SST}})$, $\mathbf{P}_4 = (P_4^{\mathrm{ICE}}, P_4^{\mathrm{SST}})$, $\mathbf{L}_1 = (L_1^{\mathrm{ICE}}, L_2^{\mathrm{SST}})$, $\mathbf{L}_2 = (L_3^{\mathrm{ICE}}, L_1^{\mathrm{SST}})$, $\mathbf{I}_1 = (I_1^{\mathrm{ICE}}, I_3^{\mathrm{SST}})$, $\mathbf{I}_2 = (I_2^{\mathrm{ICE}}, I_4^{\mathrm{SST}})$, $\mathbf{I}_3 = (I_3^{\mathrm{ICE}}, I_2^{\mathrm{SST}})$, $\mathbf{I}_4 = (I_4^{\mathrm{ICE}}, I_1^{\mathrm{SST}})$, $\mathbf{I}_5 = (I_5^{\mathrm{ICE}}, I_8^{\mathrm{SST}})$, $\mathbf{I}_6 = (I_6^{\mathrm{ICE}}, I_7^{\mathrm{SST}})$, $\mathbf{I}_7 = (I_7^{\mathrm{ICE}}, I_6^{\mathrm{SST}})$, and $\mathbf{I}_8 = (I_8^{\mathrm{ICE}}, I_5^{\mathrm{SST}})$. Note that the mode pairs $\{\mathbf{P}_1, \mathbf{P}_2\}$, $\{\mathbf{P}_3, \mathbf{P}_4\}$, $\{\mathbf{I}_1, \mathbf{I}_2\}$, $\{\mathbf{I}_3, \mathbf{I}_4\}$, $\{\mathbf{I}_5, \mathbf{I}_6\}$, and $\{\mathbf{I}_7, \mathbf{I}_8\}$ are degenerate modes with a relative phase of $\pi/2$.

A number of different values of ϵ, the locality parameter of the Gaussian kernel, were tested to examine the robustness of these results. We find that the modes are very similar for values of $\epsilon \in [1, 2]$. For values of ϵ outside this interval, we observe a less clean split between $\mathbf{L}_2$ and certain intermittent modes, resulting in modes with power spectra that resemble a combination of the low-frequency and intermittent modes. We find that the periodic modes and modes $\{\mathbf{L}_1, \mathbf{I}_1, \mathbf{I}_2, \mathbf{I}_5, \mathbf{I}_6\}$, which will be important later in the chapter, are much more robust with respect to changes in ϵ. These modes are very similar for values of $\epsilon \in [0.5, 5]$.

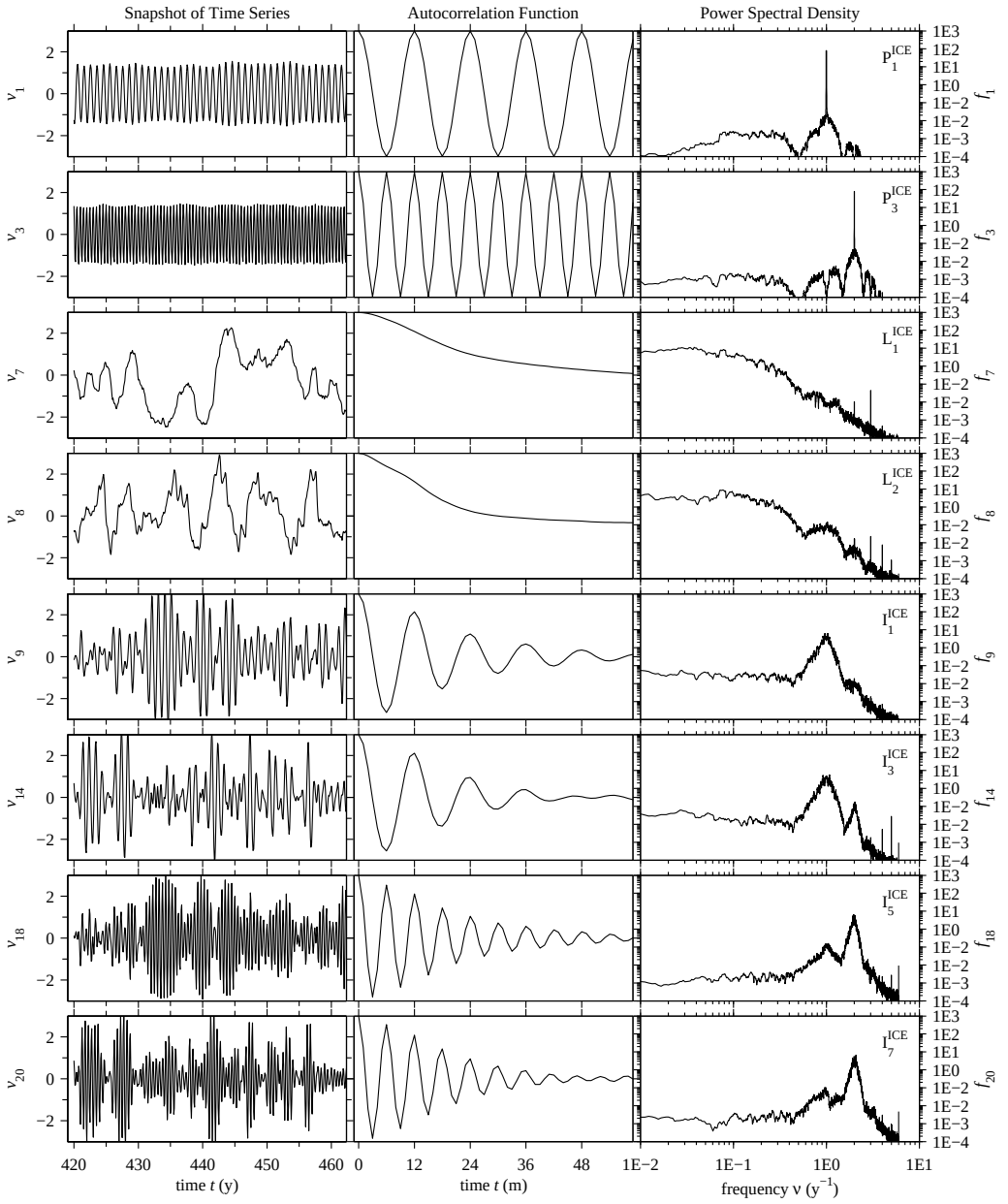

Figure 3.2: Snapshots of the time series, power spectral density, and autocorrelation functions for the sea-ice PCs (v_k) from coupled NLSA. Shown here are the annual periodic (P_1^{ICE}) and semiannual periodic (P_3^{ICE}) modes, the NPGO mode (L_1^{ICE}), the PDO mode (L_2^{ICE}), annual intermittent modes (I_1^{ICE} and I_3^{ICE}), and semiannual intermittent modes (I_5^{ICE} and I_7^{ICE}). The autocorrelation vertical scale is [-1,1]. The power spectral densities (f_k) were estimated over the full 900 year timeseries via the multitaper method with time-bandwidth product $p = 6$ and $K = 2p - 1 = 11$ Slepian tapers.

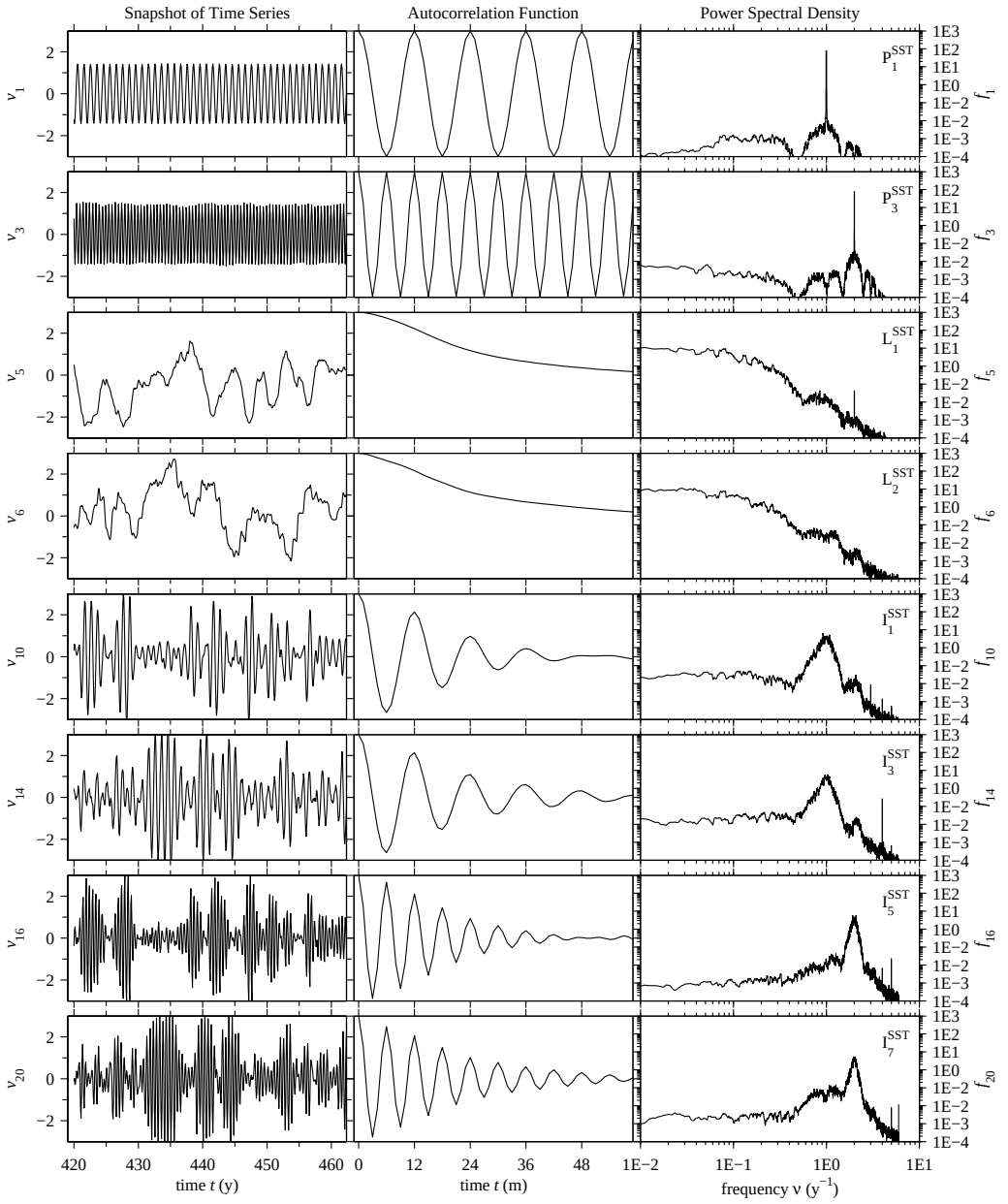

Figure 3.3: Snapshots of the time series, power spectral density, and autocorrelation functions for the SST PCs (v_k) from coupled NLSA. Shown here are the annual periodic (P_1^{SST}) and semiannual periodic (P_3^{SST}) modes, the PDO mode (L_1^{SST}), the NPGO mode (L_2^{SST}), annual intermittent modes (I_1^{SST} and I_3^{SST}), and semiannual intermittent modes (I_5^{SST} and I_7^{SST}). The autocorrelation vertical scale is [-1,1]. The power spectral densities (f_k) were estimated over the full 900 year timeseries via the multitaper method with time-bandwidth product $p = 6$ and $K = 2p - 1 = 11$ Slepian tapers.

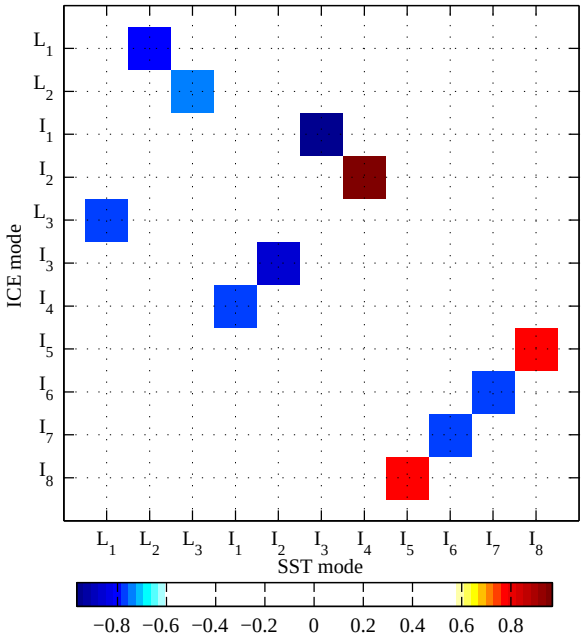

Figure 3.4: Correlations between selected SST and and sea-ice principal components. Note that each SST PC can be associated with a single sea-ice PC.

3.3.2 Spatiotemporal modes

Figure 3.5 shows the spatial patterns of the coupled modes defined above at a snapshot in time. Movie 1, showing the evolution of these spatial patterns, is available in the online supplementary material, and is much more illuminating.

Periodic modes

The pair of annual periodic modes, $\{\mathbf{P}_1, \mathbf{P}_2\}$, have a sea-ice pattern which involves spatially uniform growth in the Bering and Okhotsk Sea from October to March and spatially uniform melt from April to September. The SST pattern is intensified in the western part of the basin and along the West Coast of North America. Moreover, it is relatively uniform zonally, and out of phase with the

annual periodic sea-ice anomalies. The semiannual pair of modes, $\{\mathbf{P}_3, \mathbf{P}_4\}$, have a sea-ice pattern with strong amplitude in the southern part of the Bering and Okhotsk seas and much weaker amplitude in the northern part of these seas. The SST pattern of these modes is, again, relatively uniform zonally and intensified in the western part of the basin. The higher-frequency periodic modes have more spatial structure and zonal variability, as well as smaller amplitude.

Low-frequency modes

The leading low-frequency mode, $\mathbf{L}_1$, has an SST pattern that resembles the NPGO (Di Lorenzo et al., 2008), which is the second leading EOF of seasonally detrended Northeast Pacific (180°W – 110°W and 25°N – 62°N) SST. Computing pattern correlations between EOFs of Northeast Pacific SST and the q SST spatial patterns of $\mathbf{L}_1$, we find a maximum pattern correlation of 0.94 with EOF 2, the NPGO mode. If we consider basin-wide SST patterns, we find that the SST pattern of $\mathbf{L}_1$ has a maximum pattern correlation of 0.82 with EOF 3 of North Pacific (120°E – 110°W and 20°N – 65°N) SST. EOF 3 has a pattern correlation of 0.91 with the NPGO, thus this mode seems to reflect the basin-wide pattern of variability corresponding to the NPGO mode of the Northeast Pacific. In light of these correlations, we call $\mathbf{L}_1$ the NPGO mode. Note that these SST EOFs were computed using SST output from the CCSM3 model. The NPGO mode has its dominant sea-ice signal in the Bering Sea, and its amplitude is largest in the southern part of the Bering Sea. Its SST pattern has a strong anomaly of opposite sign, spatially coincident with the sea-ice anomaly, as well as a weaker anomaly extending further southward and eastward in the domain.

The second low-frequency mode, $\mathbf{L}_2$, has a spatial pattern resembling the PDO,

which is the leading EOF of seasonally detrended North Pacific SST data (Mantua and Hare, 2002). Computing pattern correlations between EOF 1 of North Pacific SST (the PDO) and the SST pattern of $\mathbf{L}_2$, we find a maximum pattern correlation of 0.99. Also, EOF 1 of Northeast Pacific SST (which has a 0.99 pattern correlation with the PDO) has a maximum pattern correlation of 0.98 with the SST pattern of $\mathbf{L}_2$. In light of these correlations, we call $\mathbf{L}_2$ the PDO mode. The sea-ice component of the PDO mode consists of sea-ice anomalies along the Kamchatka Peninsula, and in the southern and eastern parts of the Sea of Okhotsk. The SST pattern consists of a large-scale SST anomaly along the Kuroshio extension region, and an anomaly of the opposite sign along the west coast of North America.

Intermittent modes

The leading pair of intermittent modes, $\{\mathbf{I}_1, \mathbf{I}_2\}$, have a base frequency of 1 yr^{-1} and are characterized by a strong pulsing sea-ice anomaly in the southern Bering Sea and a weaker anomaly of opposite sign in the Sea of Okhotsk. The SST pattern consists of a strong pulsing dipole anomaly in the Bering Sea and weaker small-scale temperature anomalies that propagate eastward along the Kuroshio extension region. The next pair of annual intermittent modes, $\{\mathbf{I}_3, \mathbf{I}_4\}$, have sea-ice anomalies that originate in the Bering Sea and propagate along the Kamchatka peninsula into the Sea of Okhotsk. The SST pattern is a basin-wide signal, with strong intermittent anomalies along the Kuroshio extension region, as well as in the Sea of Okhotsk and Bering Sea. The semiannual intermittent mode pairs $\{\mathbf{I}_5, \mathbf{I}_6\}$ and $\{\mathbf{I}_7, \mathbf{I}_8\}$, are active in similar parts of the domain as $\{\mathbf{I}_1, \mathbf{I}_2\}$ and $\{\mathbf{I}_3, \mathbf{I}_4\}$, respectively, and have finer spatial structure compared with their annual counterparts.

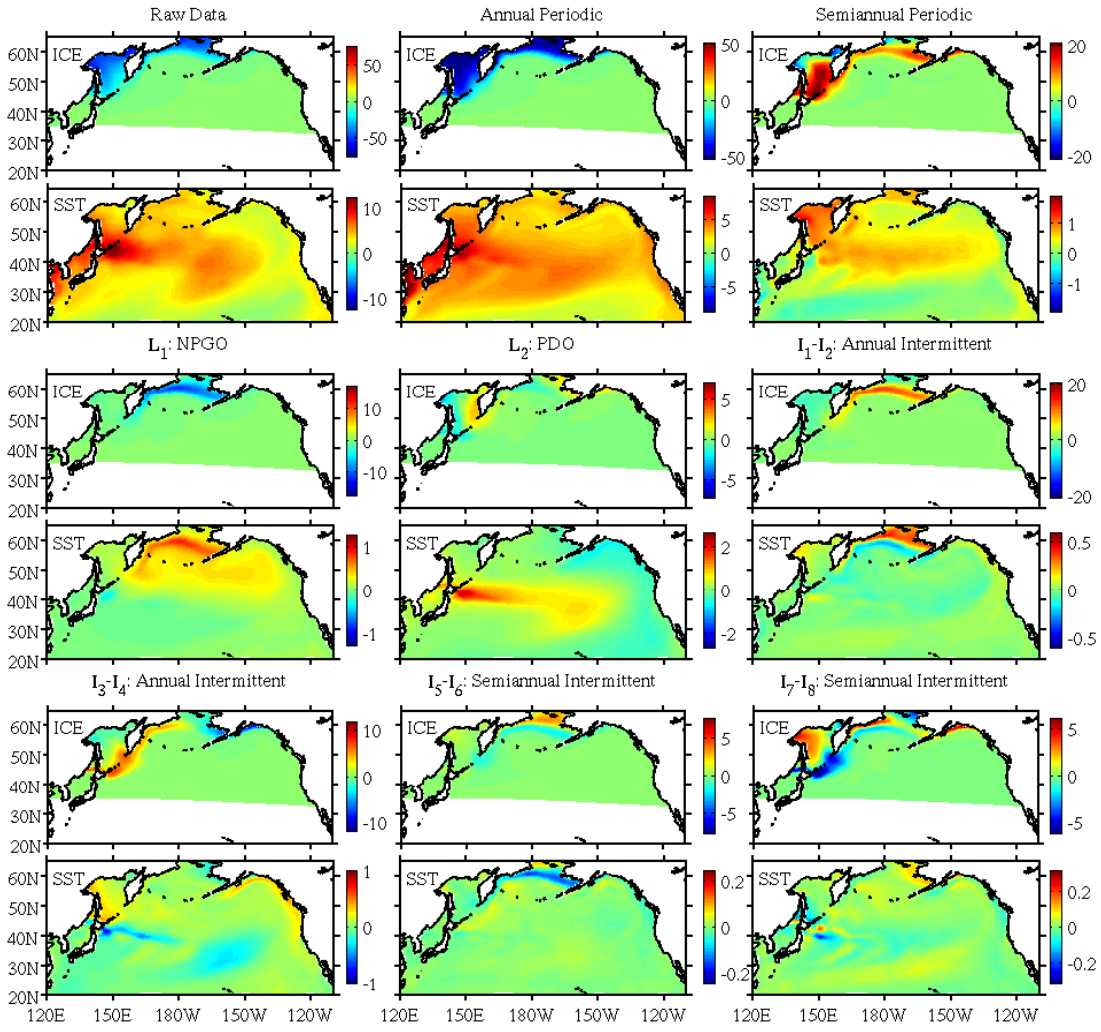

Figure 3.5: Snapshots of raw data and spatiotemporal modes from coupled NLSA. See movie 1 for the dynamic evolution of these modes.

3.3.3 Connection between low-frequency and intermittent modes

The intermittent modes have time series which appear to be a periodic mode modulated by a low-frequency signal. What low-frequency signal is modulating these modes? It turns out that most intermittent modes can be directly associated with a certain low-frequency mode from NLSA. Figure 3.6 shows time series snapshots for the annual and semiannual intermittent SST modes, I_1^{SST}, I_3^{SST}, I_5^{SST}, and I_7^{SST}, and low-frequency envelopes defined by L_1^{SST} (the PDO mode) and L_2^{SST} (the NPGO mode). We observe that I_3^{SST} and I_7^{SST} fit inside the NPGO envelope, and do not fit inside the PDO envelope. Similarly, I_1^{SST} and I_5^{SST} fit inside the PDO envelope and not the NPGO envelope. Despite clearly being modulated by a certain low-frequency mode, the intermittent modes are not simply products of a periodic mode and a low-frequency mode. The sea-ice modes also share a similar relationship between the low frequency and intermittent modes. $\{I_1^{\mathrm{ICE}}, I_2^{\mathrm{ICE}}\}$, and $\{I_5^{\mathrm{ICE}}, I_6^{\mathrm{ICE}}\}$ are clearly modulated by L_1^{ICE} (the NPGO mode). $\{I_3^{\mathrm{ICE}}, I_4^{\mathrm{ICE}}\}$, and $\{I_7^{\mathrm{ICE}}, I_8^{\mathrm{ICE}}\}$ are not as clearly modulated by a certain low-frequency mode, but they are most closely associated with L_3^{ICE} (the PDO mode).

The intermittent modes have important phase relationships with their corresponding periodic modes. We find that the intermittent modes tend to either phase lock such that they are in phase or out of phase with the periodic mode, and this phase locking is determined by the sign of the low-frequency signal that modulates the intermittent mode. However, the intermittent modes also experience other phase relationships with the periodic modes, particularly during transitions between the two phase-locked regimes. In Fig. 3.7 we show three characteristic phase

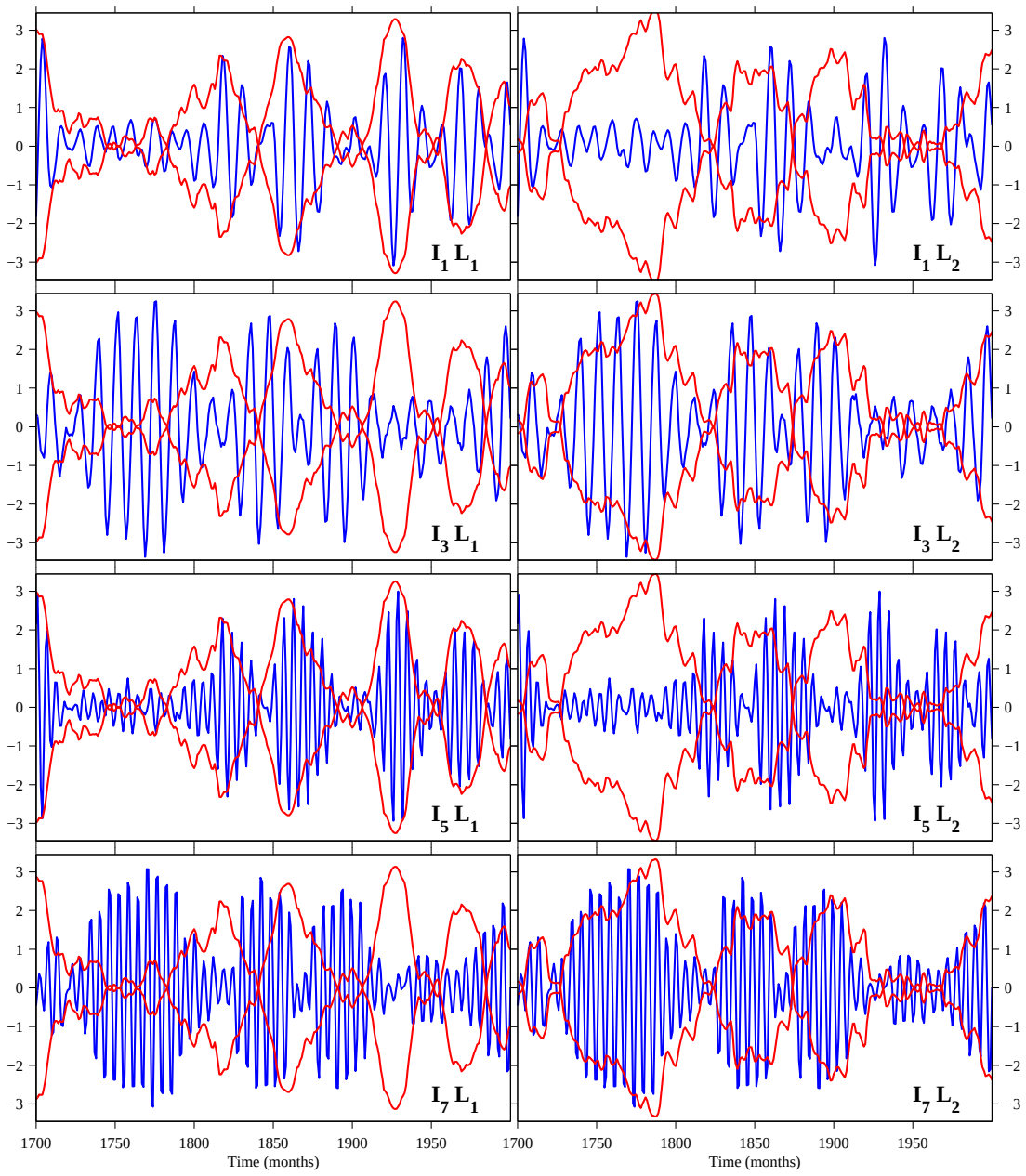

Figure 3.6: Time series of intermittent modes $I_1^{\mathrm{SST}}, I_3^{\mathrm{SST}}, I_5^{\mathrm{SST}}, I_7^{\mathrm{SST}}$ plotted in blue, and low-frequency envelopes defined by L_1^{SST} (PDO) and L_2^{SST} (NPGO) plotted in red.

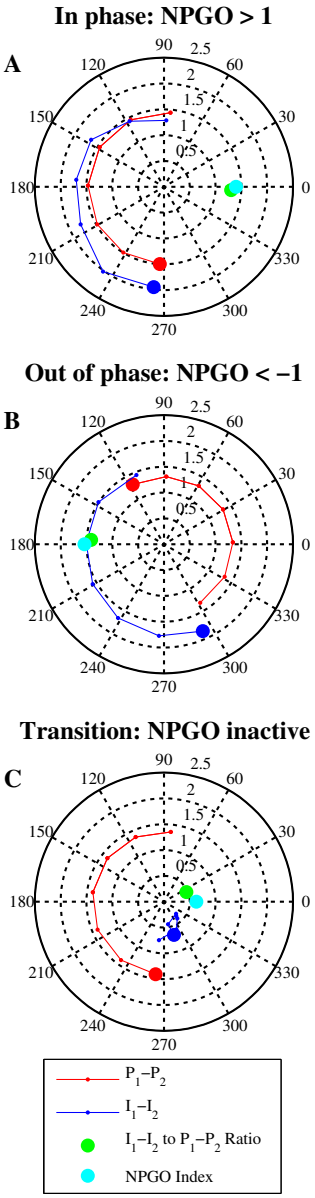

Figure 3.7: Phase evolution of intermittent modes $\{I_1^{\text{ICE}}, I_2^{\text{ICE}}\}$ in the $I_1^{\text{ICE}} - I_2^{\text{ICE}}$ plane (blue dots) and periodic modes $\{P_1^{\text{ICE}}, P_2^{\text{ICE}}\}$ in the $P_1^{\text{ICE}} - P_2^{\text{ICE}}$ plane (red dots), where the present value is shown with the larger dot and the smaller dots show the previous six values. The cyan dot shows the value of L_1^{ICE} plotted along the real axis, and the green dot shows the ratio of $\{I_1^{\text{ICE}}, I_2^{\text{ICE}}\}$ to $\{P_1^{\text{ICE}}, P_2^{\text{ICE}}\}$, a test for how close the intermittent modes are to being a product of periodic and low-frequency modes. (A) shows an in phase regime, (B) shows and out of phase regime and (C) shows a transition regime. See movie 2 for a more illuminating time evolution.

relationships between the intermittent and periodic modes. These plots, as well as the corresponding visualization in movie 2, show evolution of the intermittent modes $\{I_1^{\mathrm{ICE}}, I_2^{\mathrm{ICE}}\}$ in the $I_1^{\mathrm{ICE}} - I_2^{\mathrm{ICE}}$ complex plane (blue dots) and the periodic modes $\{P_1^{\mathrm{ICE}}, P_2^{\mathrm{ICE}}\}$ in the $P_1^{\mathrm{ICE}} - P_2^{\mathrm{ICE}}$ plane (red dots). The periodic modes trace a circle in the $P_1^{\mathrm{ICE}} - P_2^{\mathrm{ICE}}$ complex plane, and the intermittent modes trace out a more complicated trajectory. Also, plotted in cyan along the real axis is the value of L_1^{ICE}, the NPGO mode. We find that $\{I_1^{\mathrm{ICE}}, I_2^{\mathrm{ICE}}\}$ is in phase with $\{P_1^{\mathrm{ICE}}, P_2^{\mathrm{ICE}}\}$ when $L_1^{\mathrm{ICE}} > 0$ and out of phase when $L_1^{\mathrm{ICE}} < 0$. Finally, the green dot is the ratio of $\{I_1^{\mathrm{ICE}}, I_2^{\mathrm{ICE}}\}$ to $\{P_1^{\mathrm{ICE}}, P_2^{\mathrm{ICE}}\}$, where the ratio is taken by first writing these points in complex polar form. If $\{I_1^{\mathrm{ICE}}, I_2^{\mathrm{ICE}}\}$ were indeed the product of $\{P_1^{\mathrm{ICE}}, P_2^{\mathrm{ICE}}\}$ and L_1^{ICE}, we would expect this green dot to be perfectly coincident with the cyan dot for L_1^{ICE}. We observe that the intermittent mode is close to being a product of these two, yet is not an exact product (e.g., Fig. 3.7b). A similar phase behavior is observed for most other intermittent modes, but in some cases the near product relationship does not apply. For instance, $\{I_1^{\mathrm{SST}}, I_2^{\mathrm{SST}}\}$ are near products of $\{P_1^{\mathrm{SST}}, P_2^{\mathrm{SST}}\}$ and L_1^{SST}, but the corresponding ice modes, $\{I_3^{\mathrm{ICE}}, I_4^{\mathrm{ICE}}\}$, deviate significantly from the product of $\{P_1^{\mathrm{ICE}}, P_2^{\mathrm{ICE}}\}$ and L_3^{ICE}. In section 5 ahead, we will see that the phase relationships between the intermittent and periodic modes have important implications for explaining reemergence.

3.3.4 Comparison with SSA

In addition to NLSA, we also performed SSA on the coupled sea ice-SST dataset. These calculations were done by normalizing both variables to unit variance, and then performing SSA on the concatenated dataset. SSA produces periodic and low-frequency modes, and also two modes whose temporal patterns

loosely resemble the intermittent modes of NLSA, with a broadband power spectrum around a certain base frequency and a bias towards lower frequencies. The periodic modes of SSA are very similar to the periodic modes of NLSA, but we observe a number of differences in the non-periodic modes. NLSA produces two low-frequency modes, which correlate strongly with the NPGO and PDO, respectively. SSA, on the other hand, produces a large number of low-frequency modes, most of which correlate most strongly with the PDO. For example, if we consider EOFs of North Pacific SST, we find that the leading eight low-frequency modes of SSA all correlate most strongly with the PDO (EOF 1). If we consider EOFs from the Northeast Pacific, we find that low-frequency modes 1, 2, 4, 5, 7, and 8 all correlate most strongly with the PDO (EOF 1) and modes 3 and 6 correlate most strongly with the NPGO (EOF 3). Low-frequency mode 3 has pattern correlations of 0.83 and 0.87 with the PDO and NPGO, respectively, and its spatial pattern looks like a mixed PDO-NPGO signal. The NLSA modes cleanly split low-frequency SST patterns between different modes, whereas SSA tends to mix these patterns over a large number of low-frequency modes. A consequence of this is that NLSA may be more effective at capturing patterns of variability using a small subset of modes. The two SSA modes that have a broadband power spectrum centered on a base frequency are different from the intermittent modes of NLSA in that their temporal patterns are not modulated by any of the the low-frequency SSA modes. Rather, these time series evolve independently of the other SSA modes. Figure 3.8 shows temporal patterns of selected SSA modes, and the spatiotemporal evolution of these modes in shown in Movie 7 of the supplementary material.

We also performed NLSA on the unit variance dataset as a comparison with

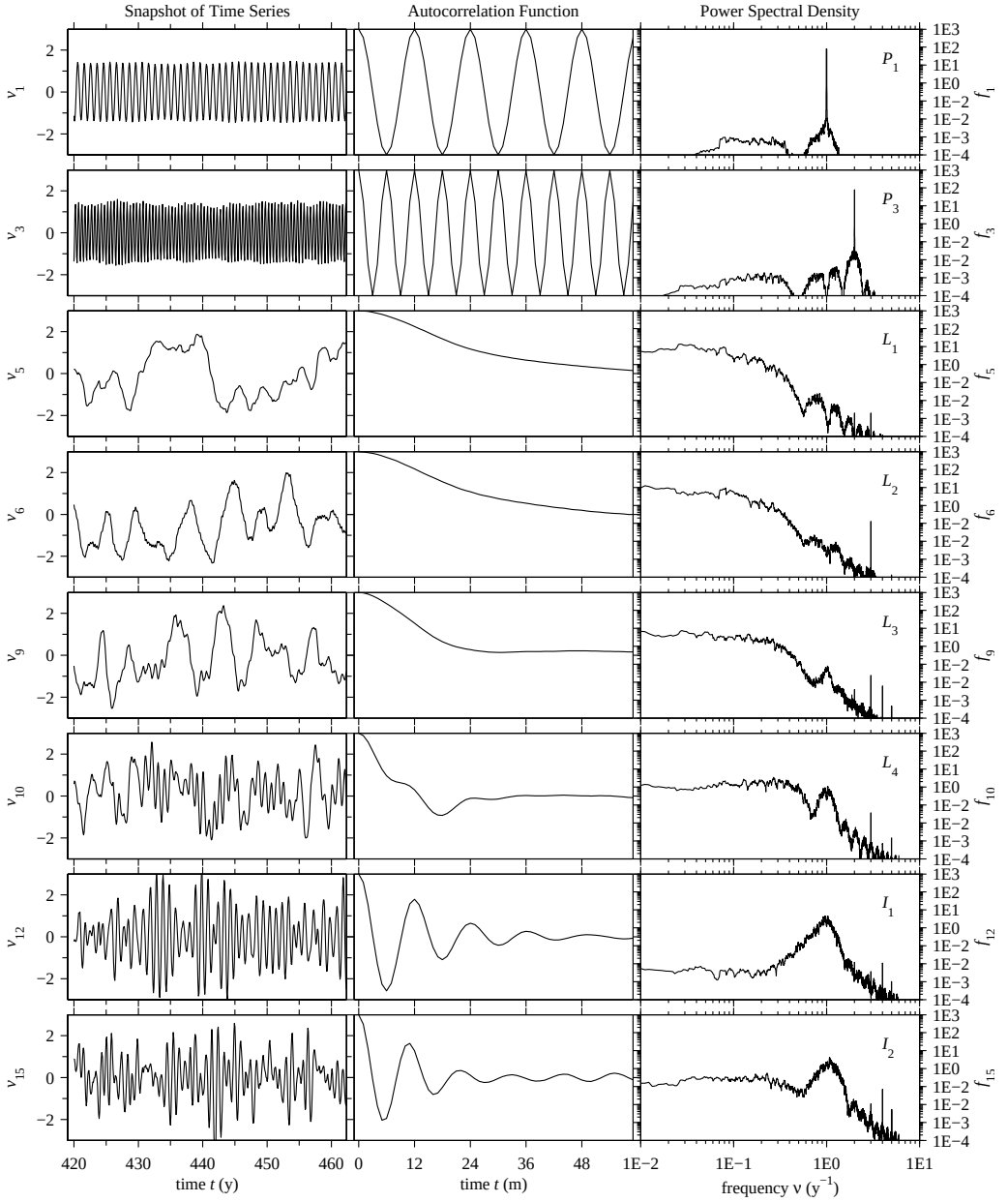

Figure 3.8: Snapshots of the time series, power spectral density, and autocorrelation functions for PCs obtained via SSA on the unit-variance normalized SST-sea ice dataset from CCSM3. Shown here are the annual periodic (P_1) and semiannual periodic (P_3) modes, the leading four low-frequency modes (L_1,L_2,L_3,L_4), and two modes which resemble annual intermittent modes (I_1,I_2).

the phase velocity normalization presented above. We find three low-frequency modes, and pairs of annual and semiannual intermittent modes associated with these modes. A primary difference is that, unlike the phase velocity results above, the low-frequency modes do not cleanly split into patterns associated with the NPGO and PDO. Rather, low-frequency modes 1 and 2 correlate most strongly with the PDO (this is true for both North Pacific and Northeast Pacific EOFs). Low-frequency mode 3 has correlations of 0.81 and 0.89 with the PDO and NPGO (defined using Northeast Pacific EOFs), respectively, and has a spatial pattern that reflects a mixed NPGO-PDO signal.

3.4 Sea-ice reemergence via NLSA

3.4.1 Sea-ice reemergence in the North Pacific

Inspired by the sea-ice reemergence mechanism put forward by BW, we study time lagged correlations of sea ice in the North Pacific sector of the ocean. We focus on the Bering and Okhotsk seas, the two primary areas of sea-ice variability in the North Pacific. BW observe a spring-fall sea-ice reemergence, in which sea-ice anomalies of a certain sign in spring tend to produce anomalies of the same sign in the fall, despite lagged correlations dropping to near zero in the intervening summer months. The authors propose that spring sea-ice anomalies create an anomaly of opposite sign in SST, and this SST imprint is retained over the summer months as the sea ice melts and the sea-ice edge moves northwards. In the fall, the sea-ice edge begins to move southward and when it reaches the SST anomaly it reinherits an ice anomaly of the same sign as the spring. It is by this proposed mechanism that SST stores the memory of melt season sea-ice anomalies, allowing the same

anomaly to be reproduced in the growth season.

3.4.2 Correlation methodology

BW compute time-lagged correlations for total arctic sea-ice area as a method for examining sea-ice reemergence. One drawback to this approach is that dynamically relevant spatial structures, such as sea-ice dipoles, are integrated away when only considering total sea-ice area. In order to capture the memory in sea-ice spatial patterns, we perform time-lagged pattern correlations on the sea-ice concentration data.

Specifically, we compute time lagged pattern correlations using the following methodology. First, we define $\bar{a}_m(x, y)$, the average sea-ice concentration in a given month m, as a function of space. Let T be the number of samples of month m, and let m_k correspond to sample number $12(k-1)+m$, the mth month of the kth year. We set

$$\bar{a}_m(x, y) = \frac{\sum_{k=1}^{T} a_{m_k}(x, y)}{T}.$$

Next, we define the pattern correlation between times $m_k = 12(k-1)+m$ and $m'_j = 12(j-1)+m'$ as

$$P_{m_k m'_j} = \frac{\left\langle a_{m_k}(x, y) - \bar{a}_m(x, y), a_{m'_j}(x, y) - \bar{a}_{m'}(x, y) \right\rangle}{\|a_{m_k}(x, y) - \bar{a}_m(x, y)\| \|a_{m'_j}(x, y) - \bar{a}_{m'}(x, y)\|}.$$

In the above, $\langle \cdot, \cdot \rangle$ and $\| \cdot \|$ denote the Euclidean (area-weighted) inner product and two-norm with respect to the spatial gridpoints (x, y). Finally, we define the

time lagged pattern correlation between months m and $m+\tau$ as the time average of all pattern correlations:

$$C_{m,m+\tau} = \frac{\sum_{k=1}^{T-2} P_{m_k m'_j}}{T-2},$$

where $m_k = 12(k-1)+m$ and $m'_j = 12(j-1)+m' = m_k + \tau$. Note that time averaging is done over $T-2$ samples, because for lags up to 24 months there are only $T-2$ pairs of m_k and $m_k + \tau$.

3.4.3 Time lagged pattern correlations in the North Pacific sector

We compute time lagged pattern correlations in the North Pacific sector for all months and lags from 0 to 23 months, the results of which are shown in Fig. 3.9. In Fig. 3.9, the white boxes are not significant at the 95% level using a t–distribution statistic. All colored boxes are significant at the 95% level. Figure 3.9a shows time lagged total area correlations computed in the same way as BW, except being done for the North Pacific rather than the entire Arctic. We observe a similar correlation structure to that of BW, with one noteable difference. There is an initial decay of correlation over a 3–6 month timescale, after which, for the months of January–July, we observe an increase in correlation. This region of increased correlation is analogous to the "summer limb" of BW. In this summer limb, we can see natural pairings of spring months and the corresponding fall months in which the spring anomaly reemerges. These pairings are July-October, June-November, May-December, April-January, and March-January/February; they represent months at

which the sea-ice edge is similar in melt and growth seasons. A main difference between the North Pacific and the entire Arctic is that the North Pacific data does not contain a "winter limb" of anomalies produced in fall that are reproduced the following summer. This is because the North Pacific contains very little sea ice in the summer months. Figure 3.10 shows the monthly mean values plus/minus one standard deviation of North Pacific SST and sea-ice concentration in the CCSM3 dataset. We see that the sea-ice concentration is close to zero in the summer months and, moreover, there is significantly higher sea-ice variability in high sea ice months.

Figure 3.9b shows lagged pattern correlations for North Pacific sea ice. As expected, the correlations are significantly weaker than in the total area lagged correlation case, since having a pattern correlation in anomalies is a much more stringent test than simply having correlations in total area of anomalies. Despite being weaker, the pattern correlations still have the "summer limb" structure observed in Fig. 3.9a, and these correlations are significant at the 95% level. Most lagged pattern correlations besides the inital decay and the summer limb are not significant at the 95% level. Figures 3.9c and 3.9d show lagged pattern correlations for the Bering (165°E – 160°W and 55° – 65°N) and Okhotsk (135°E – 165°E and 42° – 65°N) Seas, respectively. Each of these seas has a similar lagged pattern correlation structure to the full North Pacific sector in Fig. 3.9b.

Next, we seek to reproduce the lagged pattern correlations seen in the raw sea-ice data using a low dimensional subset of coupled NLSA modes. We find that in each sea, a different set of modes is active, thus we choose to focus on the Bering and Okhotsk seas individually. In the Bering Sea, we find that modes $\{\mathbf{L}_1, \mathbf{I}_1, \mathbf{I}_2, \mathbf{I}_5, \mathbf{I}_6\}$ qualitatively reproduce the lagged pattern correlation structure

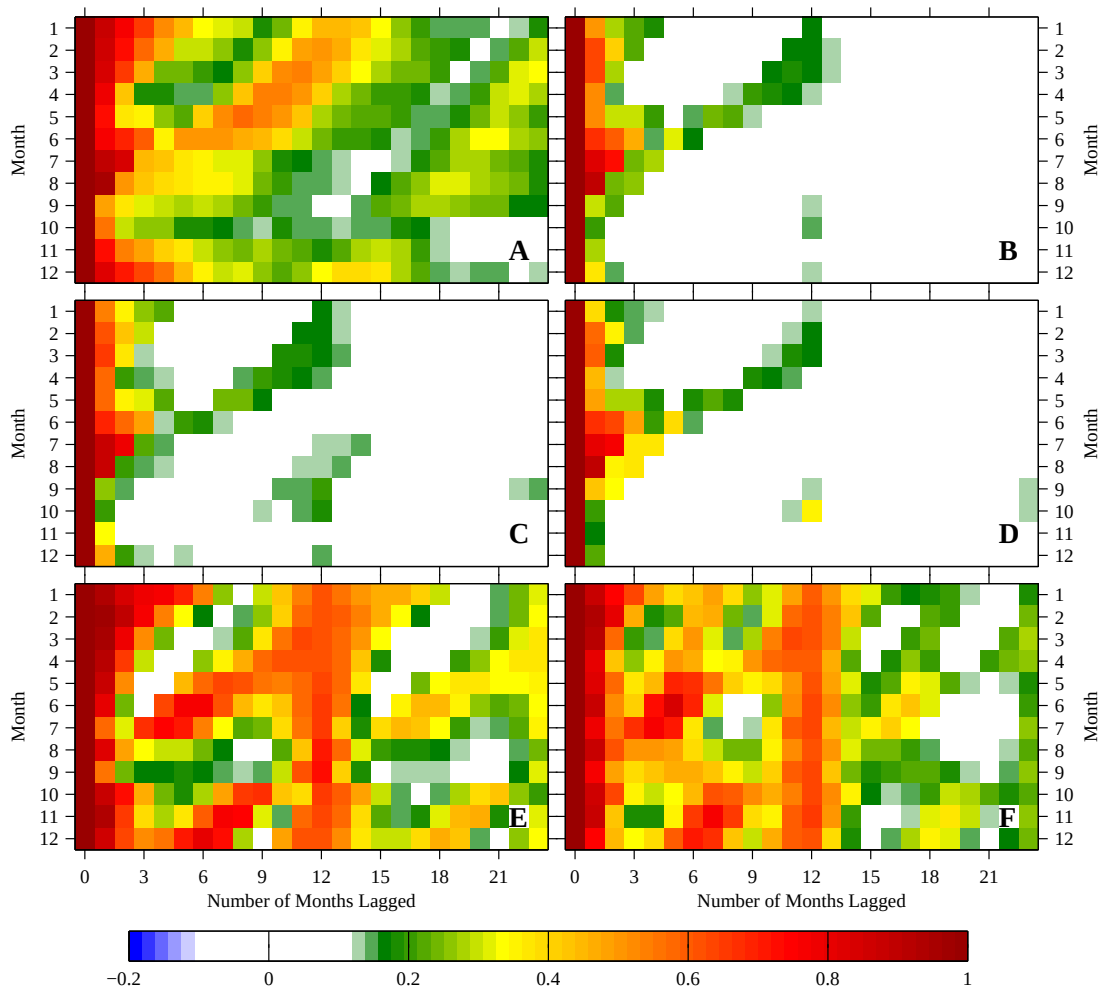

Figure 3.9: Lagged correlations for North Pacific sea ice for all months and lags from 0 to 23 months. (A) shows the lagged correlation structure in total arctic sea-ice area, computed following the methodology of BW. All other panels are lagged pattern correlations: (B) North Pacific with raw data; (C) and (D) are computed in the Bering and Okhotsk Seas, respectively, using raw data; (E) Bering Sea with modes $\{\mathbf{L}_1, \mathbf{I}_1, \mathbf{I}_2, \mathbf{I}_5, \mathbf{I}_6\}$; (F) Okhotsk Sea with modes $\{\mathbf{L}_2, \mathbf{I}_3, \mathbf{I}_4, \mathbf{I}_7, \mathbf{I}_8\}$. Colored boxes indicate correlations which are significant at the 95% level based on a t-test.

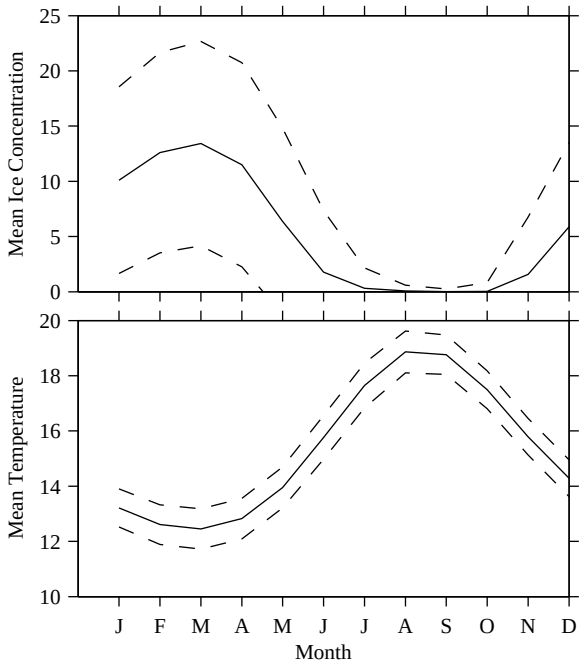

Figure 3.10: Monthly mean sea-ice concentration and SST from CCSM3, with the dashed line showing $\pm 1\sigma$. The SST variance is relatively uniform across all months, while the sea-ice variance is much larger in high concentration months.

seen in raw data. $\mathbf{L}_1$ is the NPGO mode and the other modes are the annual and semiannual intermittent modes which are modulated by the NPGO envelope. Moreover, this set appears to be the minimal subset, as smaller subsets of modes are unable to reproduce the correlation structure of the raw data. Figure 3.9e shows Bering Sea lagged pattern correlations computed using this three mode family, which we call the NPGO family. We see that this family has a very similar summer limb to the raw data, except with higher correlations, since this three–mode family decorrelates more slowly than the raw data.

Attempting a similar construction in the Okhotsk Sea, we find that modes $\{\mathbf{L}_2, \mathbf{I}_3, \mathbf{I}_4, \mathbf{I}_7, \mathbf{I}_8\}$ do the best job of reproducing the lagged pattern correlation structure. However, this mode family has clear deficiencies, as can be seen in

Fig. 3.9f. In particular, this mode family fails to reproduce the summer decorrelation that is observed in the raw data and also has a less contiguous summer limb. $\mathbf{L}_2$ is the PDO mode and these intermittent modes are the annual and semi-annual intermittent modes most closely associated to the PDO. Note that these intermittent modes are not perfectly modulated by the PDO, which may explain why this PDO family is unable to capture the sea-ice reemergence signal as well as the NPGO family. Instead, in section 5f ahead we will see that this PDO family is more closely related to SST reemergence (Alexander et al., 1999).

Many other NLSA mode subsets were tested, but were unable to reproduce the correlation structure of the raw data as well as the subsets above. Also, the same procedure was performed using SSA modes, and it was found that small subsets of SSA modes (fewer than 25 modes) were unable to reproduce the lagged correlation structure of the raw data.

3.4.4 A sea-ice reemergence mechanism revealed through coupled NLSA

Using the low-dimensional family of modes $\{\mathbf{L}_1, \mathbf{I}_1, \mathbf{I}_2, \mathbf{I}_5, \mathbf{I}_6\}$, active in the Bering Sea, to reconstruct patterns in the spatial domain, we observe sea ice and SST patterns which are remarkably consistent with the mechanism suggested by BW. Figure 3.11 shows the evolution of the three-mode family over the course of a year. These spatial patterns are composites, obtained by averaging over all years in which the NPGO is active in its positive phase (defined as $L_2^{\mathrm{SST}} > 1.5$). A very similar spatiotemporal pattern, with opposite sign, occurs in years when the NPGO is active in its negative phase. The dynamic evolution of this three-mode family is shown in movie 3. In January, there is a positive sea-ice anomaly and

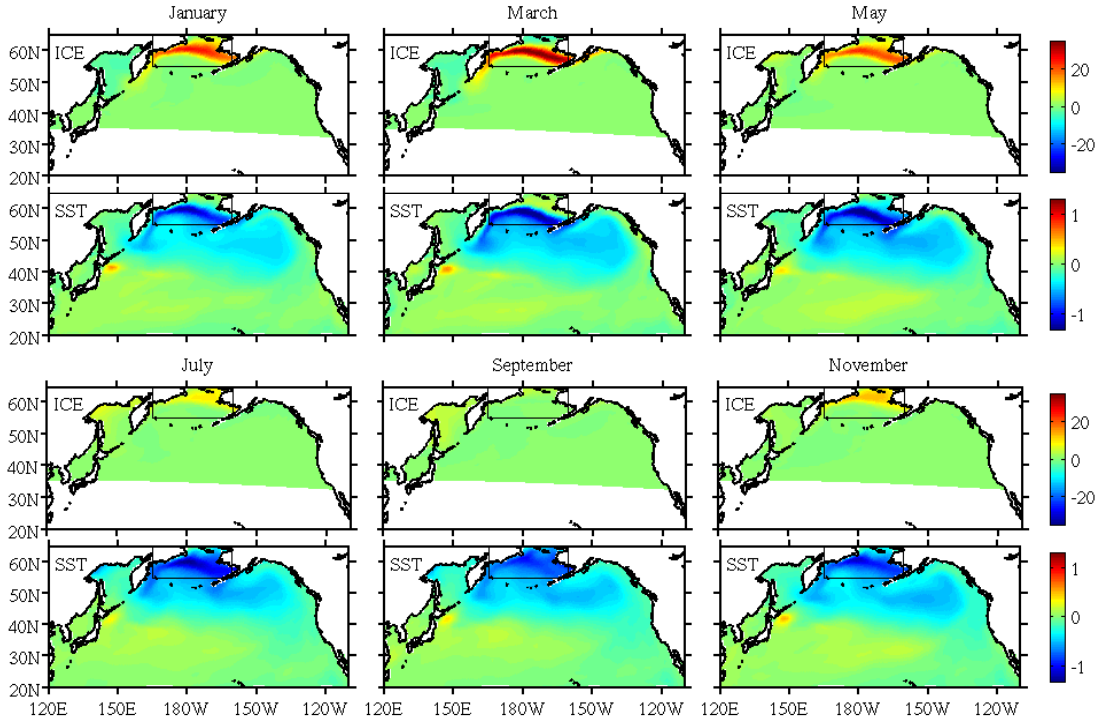

Figure 3.11: Sea Ice and SST patterns for different months of the year, reconstructed using $\{\mathbf{L}_1, \mathbf{I}_1, \mathbf{I}_2, \mathbf{I}_5, \mathbf{I}_6\}$. These spatial patterns are composites, obtained by averaging over all years in which the NPGO is active, in its positive phase (defined as $L_2^{\mathrm{SST}} > 1.5$). The Bering Sea (boxed) exhibits a spring-fall sea-ice reemergence. Positive spring sea-ice anomalies imprint negative SST anomalies as they move northward during the melt season. The SST anomalies persist through the summer months, and when the ice returns in the growth season, the positive sea-ice anomaly is reproduced. See movie 3 for the dynamic evolution of this mode family.

a negative SST anomaly in the southern part of the Bering Sea. The main SST anomaly extends slightly further south than the sea-ice anomaly, and there is also a weaker negative anomaly extending southward and eastward in the domain. The positive ice anomalies continue to move southward through the growth season, until reaching the maximum ice extent in March. The SST anomaly has not changed significantly from January and is primarily localized to the ice anomaly region. In particular, there is no SST anomaly in the northern part of the Bering Sea. The melt season begins in April, and in May we observe that the sea-ice anomaly has moved northward. The SST anomaly has also extended northward while maintaing its southern extent from March. In July the sea ice retreats further and only a weak positive anomaly remains in the Bering Sea. By September essentially no sea-ice anomaly remains in the Bering Sea. Despite the sea-ice anomaly being absent in September, the SST has a strong negative anomaly throughout the entire Bering Sea region. The northern Bering sea, previously free of SST anomalies, now has a negative anomaly, imprinted by the positive sea ice anomalies moving through the region during the melt season. As the sea ice returns to the domain in October–December, the ice interacts with the SST anomaly, using the cold SST to grow additional ice, and reproduces the positive ice anomaly that we observed in the spring. In November, part of the northern Bering Sea's negative SST anomaly has been wiped out, and the ice has begun to redevelop its positive anomaly. The ice continues to grow stronger positive anomalies as it moves southward and in January the cycle roughly repeats again. We observe this mechanism with the NPGO mode in both positive and negative phase.

As could be expected from Fig. 3.9f, the mode family $\{\mathbf{L}_2, \mathbf{I}_3, \mathbf{I}_4, \mathbf{I}_7, \mathbf{I}_8\}$ does not have a clear sea-ice reemergence in the Okhotsk Sea. This family does exhibit a

winter-winter persistence of ice anomalies, but the anomalies tend to unrealistically persist over the intervening summer months.

3.4.5 Reemergence conditioned on low-frequency modes

We earlier noted that the NPGO mode family $\{\mathbf{L}_1, \mathbf{I}_1, \mathbf{I}_2, \mathbf{I}_5, \mathbf{I}_6\}$ is able to reproduce the lagged correlation structure seen in sea-ice data in the Bering Sea. Additionally, we know that the intermittent modes within the mode families identified here are modulated by the low-frequency mode of that family. Thus, in order to determine whether a given mode family is active, we can simply assess whether or not the corresponding low–frequency mode is active. Given these observations, one would expect to see an enhanced reemergence structure if we performed lagged correlations on the raw sea-ice data, conditional on a certain low-frequency mode being active. Indeed, if we condition on the NPGO being active, we observe an enhanced summer limb in the lagged pattern correlation structure of the Bering Sea raw data. Similarly, if we condition on the NPGO being inactive, we find that the summer limb is significantly weakened. Figure 3.12 shows conditional lagged pattern correlations for these various cases. Note that the NPGO is defined as "active" over the time interval $[t, t + \Delta t]$ if $|L_2^{\mathrm{SST}}| > 1.5$. The NPGO index is defined for $t \in [1, s - q]$.

This summer limb strengthening has implications for regional sea-ice predictibility. In particular, tracking the NPGO index should help one predict whether a given spring anomaly in the Bering sea will return the following fall.

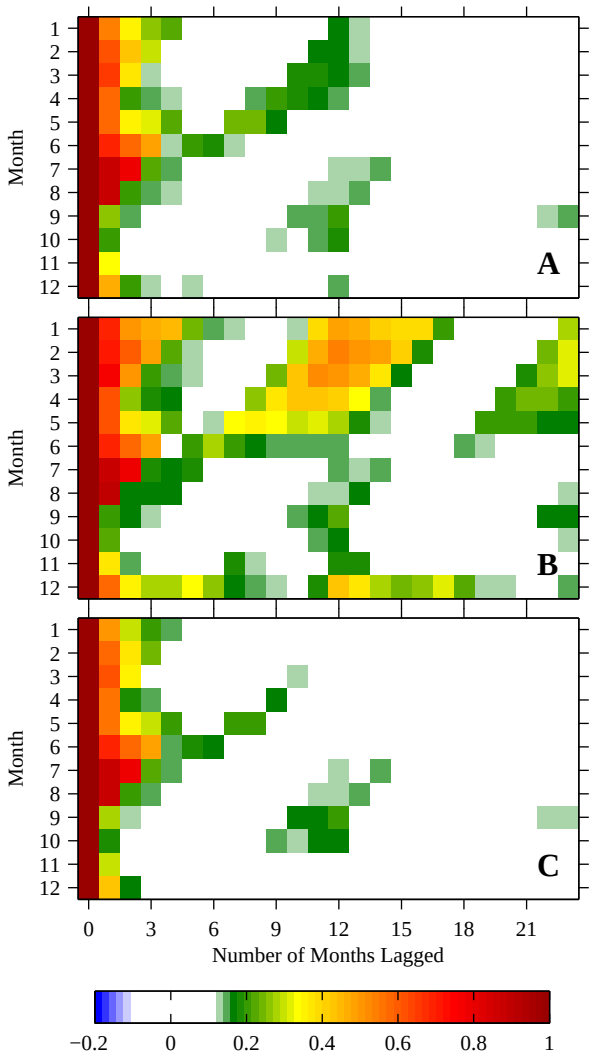

Figure 3.12: Lagged pattern correlations for raw sea-ice data in the Bering Sea, conditional on the NPGO principal component being active. (A) shows the Bering result with no conditioning. (B) and (C) show the Bering sea conditioned on $|L_2^{\mathrm{SST}}| > 1.5$ (all values above the 82nd percentile) and $|L_2^{\mathrm{SST}}| < 1$ (all values below the 65th percentile), respectively. Colored boxes indicate correlations which are significant at the 95% level based on a t-test.

3.4.6 Connection to other reemergence phenomena

BW also note a summer-to-summer reemergence in Arctic sea ice, which is connected to persistence in sea-ice thickness anomalies. This summer-to-summer reemergence is not seen in the North Pacific sector, since the North Pacific is essentially sea-ice free for the months of July through October (see Fig. 3.10).

Another reemergence phenomenon active in the North Pacific sector is the winter-to-winter SST reemergence studied by Alexander et al. (1999). This reemergence consists of the formation of an SST anomaly in winter months, a weakening of the anomaly over the summer due to the presence of a seasonal thermocline, and a subsequent re-strengthening the following winter. To investigate the presence of SST reemergence in the coupled NLSA modes, we perform a lagged correlation analysis analogous to the sea-ice study above.

We focus on the domains of active SST reemergence defined by Alexander et al. (1999): the central ($26^\circ - 42^\circ$N, $164^\circ - 148^\circ$W), eastern ($26^\circ - 42^\circ$N, $132^\circ - 116^\circ$W), and western ($38^\circ - 42^\circ$N, $160^\circ - 180^\circ$E) Pacific. For each of these domains, time lagged pattern correlations of SST were computed, including conditioning on certain low-frequency SST modes being active. It was found that correlations were significantly strengthened when the PDO mode ($\mathbf{L}_2$) was active, and were relatively unaffected by the state of the NPGO mode ($\mathbf{L}_1$). Figure 3.13 shows time-lagged pattern correlations for the central, eastern, and western Pacific domains, for both the raw SST data, and the raw SST data conditioned on an active PDO. In the central and eastern parts of the basin, we observe a strengthened reemergence signal when the PDO is active, as there is a clear drop in correlation over the summer months and a significantly stronger increase in correlation the following winter. In the western part of the basin, the reemergence signal is clear without any

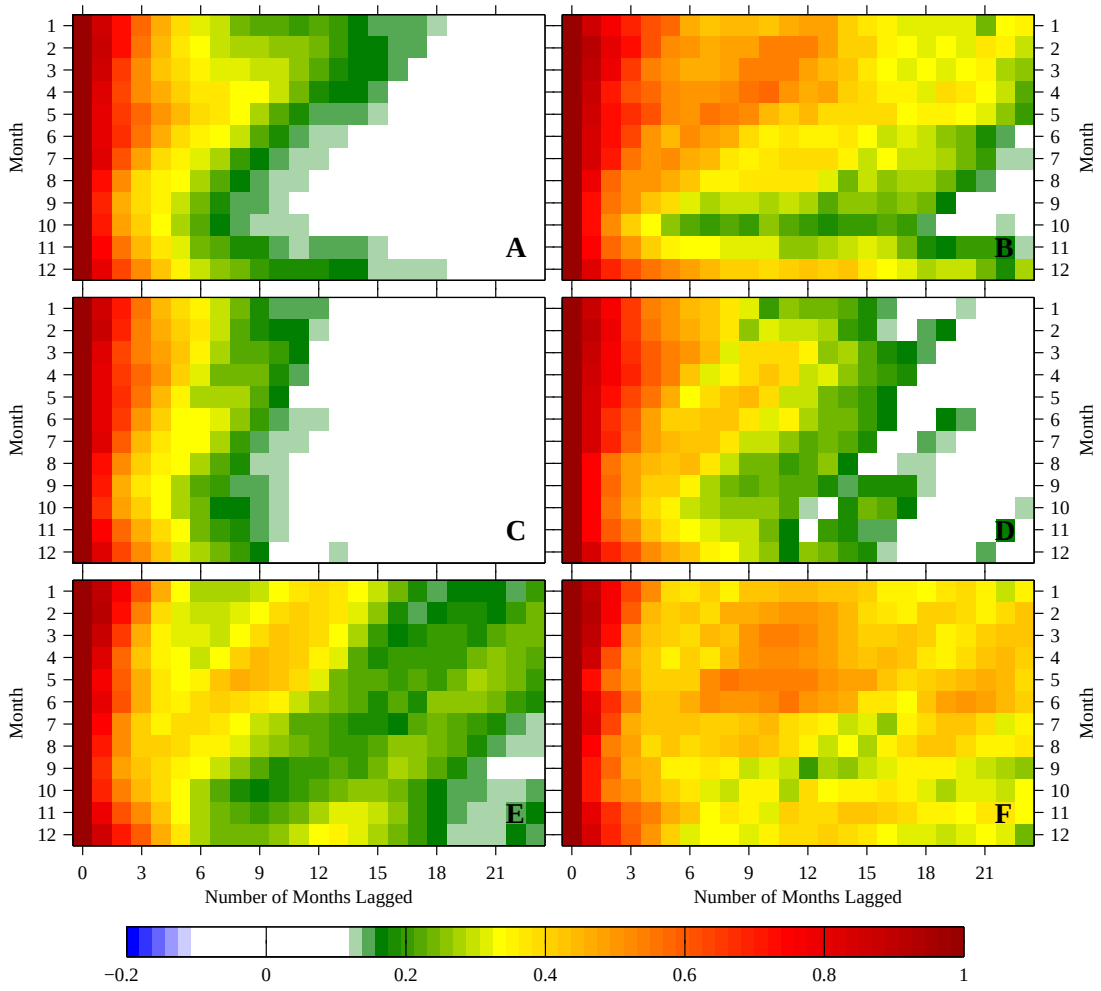

Figure 3.13: Lagged correlations for North Pacific SST for all months and lags from 0 to 23 months. (A), (C), and (E) show lagged correlations of raw SST data in the central, eastern, and western Pacific, respectively. (B), (D), and (F), show lagged correlations in the same domains, conditional on $|L_1^{\mathrm{SST}}| > 1.5$ (all values above the 82nd percentile). Colored boxes indicate correlations which are significant at the 95% level based on a t-test.

PDO conditioning. With an active PDO, the correlations become stronger, and the summer decorrelation remains visible. Note that, unlike North Pacific sea-ice reemergence, the SST correlations do not vanish over the summer months. Rather, they simply weaken over the summer and re-strengthen the following winter.

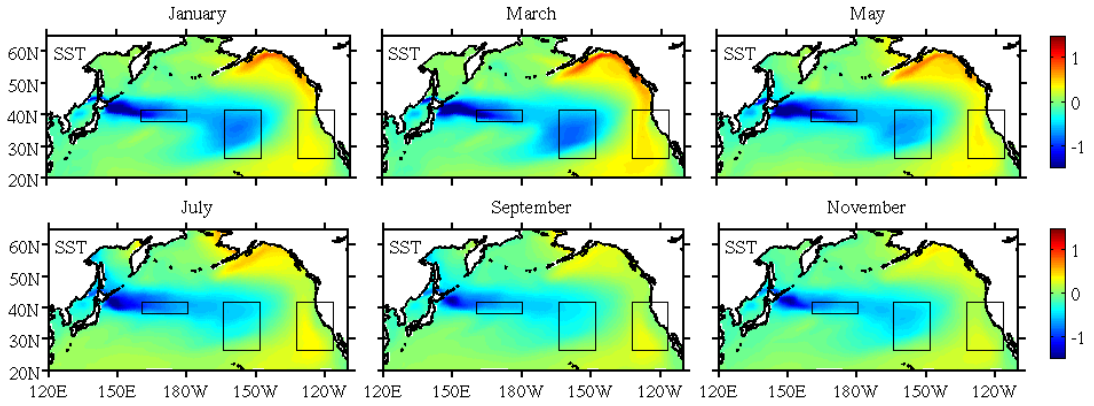

Figure 3.14: SST patterns for different month of the year, reconstructed using $\{\mathbf{L}_2, \mathbf{I}_3, \mathbf{I}_4, \mathbf{I}_7, \mathbf{I}_8\}$. These spatial patterns are composites, obtained by averaging over all years in which the PDO is active, in its positive phase (defined as $L_1^{\mathrm{SST}} > 1.5$). The central, eastern, and western Pacific domains are boxed. The central pacific exhibits a reemergence of SST anomalies, while weaker reemergences are present in the eastern and western Pacific. The dynamic evolution of this mode family is shown in Movie 4.

Following the sea-ice approach above, we seek a low-dimensional family of NLSA modes that reflect the lagged correlation structure of the raw data. We find that the PDO mode family, $\{\mathbf{L}_2, \mathbf{I}_3, \mathbf{I}_4, \mathbf{I}_7, \mathbf{I}_8\}$, has the highest skill in reproducing the observed correlations. Figure 3.14 shows a composite reconstruction of the SST patterns of the PDO family, where the composite is taken over years where the PDO index is high ($L_1^{\mathrm{SST}} > 1.5$). SST reemergence is most strikingly observed in the central Pacific. We observe a strong negative SST anomaly in January and March, which begins to decay in May, and is significantly weaker, yet still positive, in September. The anomaly begins to strengthen in November, and the pattern roughly repeats again the following year. As could be expected by the lagged correlations, we observe stronger SST persistence in the western Pacific, however a summer weakening and winter re-strengthening is nonetheless visible. The anomaly strength is significantly smaller in the eastern Pacific domain, but

a similar SST reemergence with positive anomalies can be observed, though the signal is poorly represented with the colorbar of Fig. 3.14 (chosen for the entire North Pacific). Note that there is also an active SST reemergence with positive anomalies along the Alaska-British Columbia coastline. When the PDO is active in its negative phase, a similar pattern is observed, with opposite sign. The dynamic evolution of the PDO mode family is shown in Movie 4. An interesting topic of future study would be to investigate whether the vertical structure of this reemergence mechanism can be captured by a low dimensional family of NLSA modes.

3.5 Comparison with Observations

3.5.1 Coupled NLSA on a short time series

To this point, all results have been derived from analysis of a 900-yr CCSM3 model integration. Given the relative shortness of most observational climate time series, a natural question is whether the coupled NLSA approach can be applied to a shorter time series for the purposes of exploratory data analysis. Given that NLSA is based upon sufficient exploration of a high-dimensional manifold, a short observational time series provides a stringent test for the algorithm. Nevertheless, it is plausible that certain coarse-grained nonlinear geometric features are adequately sampled (in particular, the periodic dimension associated with the seasonal cycle, which is crucial for reemergence). To test the feasibility of NLSA in this environment, we studied the HadISST dataset, which consists of 34 years of satellite observations of sea ice and SST.

We performed coupled NLSA on the HadISST dataset in a completely analo-

gous manner to the CCSM3 results above, using a value of $\epsilon = 0.8$, a truncation level of $l = 22$, and a lagged embedding window of $\Delta t = 24$ months. The resulting temporal modes have very similar characteristics to the temporal modes of the CCSM3 dataset, cleanly splitting into periodic, low-frequency and intermittent modes. We find that the periodic and intermittent modes come in doubly degenerate pairs, and that each intermittent mode is modulated by a certain low-frequency mode. Also, we find that each SST PC is highly correlated with a certain sea-ice PC, motivating the definition of coupled sea ice-SST modes of variability. For the sake of brevity, we only define the coupled modes that will be discussed in the following sections: $\mathbf{L}_1 = (L_1^{\mathrm{ICE}}, L_2^{\mathrm{SST}})$, $\mathbf{L}_2 = (L_2^{\mathrm{ICE}}, L_1^{\mathrm{SST}})$, $\mathbf{I}_1 = (I_1^{\mathrm{ICE}}, I_4^{\mathrm{SST}})$, $\mathbf{I}_2 = (I_2^{\mathrm{ICE}}, I_3^{\mathrm{SST}})$, $\mathbf{I}_3 = (I_3^{\mathrm{ICE}}, I_2^{\mathrm{SST}})$, $\mathbf{I}_4 = (I_4^{\mathrm{ICE}}, I_1^{\mathrm{SST}})$, $\mathbf{I}_5 = (I_5^{\mathrm{ICE}}, I_7^{\mathrm{SST}})$, $\mathbf{I}_6 = (I_6^{\mathrm{ICE}}, I_8^{\mathrm{SST}})$, $\mathbf{I}_7 = (I_7^{\mathrm{ICE}}, I_5^{\mathrm{SST}})$, $\mathbf{I}_8 = (I_8^{\mathrm{ICE}}, I_6^{\mathrm{SST}})$. Time series snapshots, autocorrelation functions, and power spectral densities for the leading low-frequency ice modes and an annual and semiannual intermittent mode are shown in Figure 3.15.

Similar to the CCSM3 results, the spatial patterns of these modes have correspondences with the NPGO and PDO. We find that $\mathbf{L}_1$ has a maximum pattern correlation of 0.65 with EOF 2 of Northeast Pacific SST, and $\mathbf{L}_2$ has a maximum pattern correlation of 0.90 with EOF 1 of North Pacific SST. Note that these EOFs were computed using SST output of HadISST. In light of these correlations, we call $\mathbf{L}_1$ the NPGO mode and $\mathbf{L}_2$ the PDO mode.

The sea-ice patterns of these modes have some notable differences from their CCSM3 counterparts. $\mathbf{L}_1$ has strong sea-ice anomalies in the Bering Sea, but also has strong anomalies of the opposite sign in the Sea of Okhotsk. This pattern of sea-ice variability is consistent with the leading sea-ice EOF found in Deser et al. (2000) and Liu et al. (2007). $\mathbf{L}_2$ consists of a strong sea-ice anomaly throughout

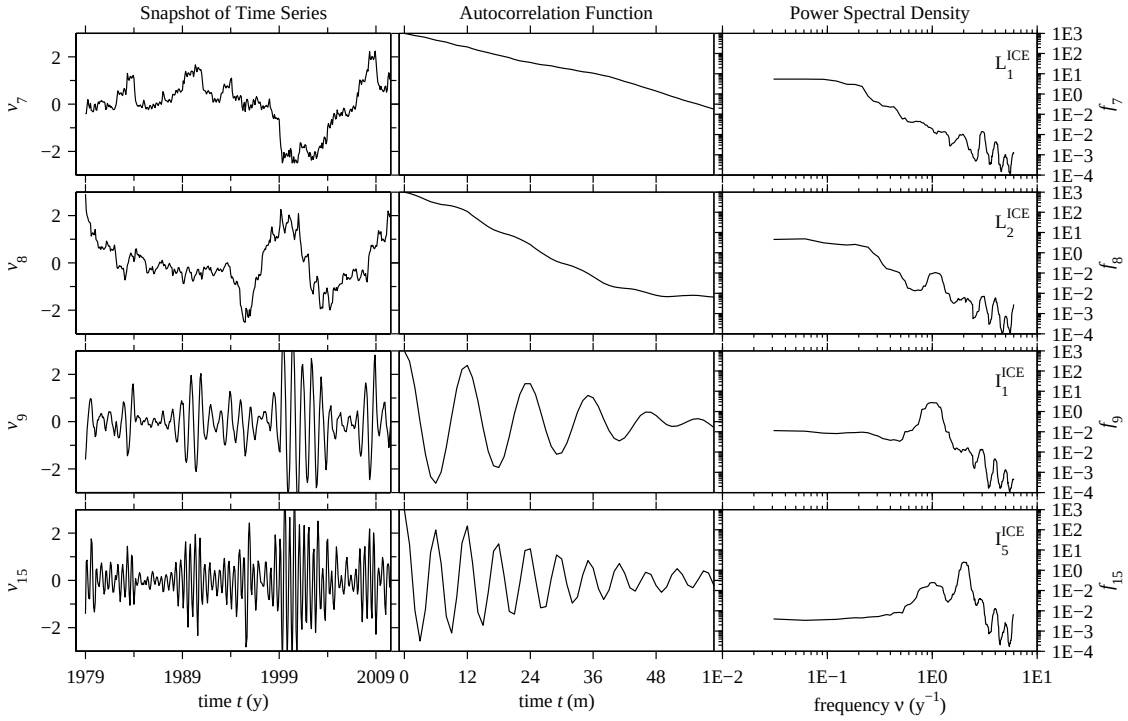

Figure 3.15: Snapshots of the time series, power spectral density, and autocorrelation functions for the sea-ice PCs (v_k) from coupled NLSA on the HadISST dataset. Shown here are two low-frequency modes (L_1^{ICE} and L_2^{ICE}), an annual intermittent mode (I_1^{ICE}) and a semiannual intermittent mode (I_5^{ICE}). The autocorrelation vertical scale is [-1,1]. The power spectral densities (f_k) were estimated over the 34 year record via the multitaper method with time-bandwidth product $p = 6$ and $K = 2p - 1 = 11$ Slepian tapers.

the Okhotsk Sea, and also an anomaly of the same sign in the southern part of the Bering Sea. Each of these low-frequency modes modulates a pair of annual and a pair of semiannual intermittent modes. These intermittent modes are active in similar parts of the domain as the low-frequency modes, and have finer spatial structures, as we also observed with the CCSM3 results.

3.5.2 Sea-ice reemergence in observations

With these coupled observational modes at our disposal, we now investigate North Pacific sea-ice reemergence in the observational record. First, we compute time lagged pattern correlations in the North Pacific sector, shown in Fig. 3.16a. We observe that there is no reemergence signal visible in these correlations. This is also the case for correlations computed over the Bering and Okhotsk Seas individually. Despite the lack of reemergence in the observational data, we examine a number of NLSA mode subsets for the presence of a reemergence signal. We find the strongest signal with the mode family $\{\mathbf{L}_1, \mathbf{I}_1, \mathbf{I}_2, \mathbf{I}_5, \mathbf{I}_6\}$, where the correlations are computed over the Bering Sea. The correlations are shown in Fig. 3.16b. This family also has signs of a reemergence signal in the Okhotsk Sea, except that the ice anomalies anti-correlate over the summer months, instead of simply decorrelating. Does this mode family have any explanatory power with regards to sea-ice reemergence? The answer appears to be yes. Fig. 3.16c shows North Pacific lagged pattern correlations, conditional on the NPGO mode, $\mathbf{L}_1$, being active. We observe an emphasized reemergence limb in years when the NPGO mode is active. A similar appearance of a summer limb is observed in the Bering Sea, but not in the Okhotsk, when conditioning on an active NPGO.

An sea ice-SST reconstruction for the year 2001, using the mode family $\{\mathbf{L}_1$,-$\mathbf{I}_1, \mathbf{I}_2, \mathbf{I}_5, \mathbf{I}_6\}$, is shown in Figure 3.17. This family shares some similarities to the NPGO mode family found in CCSM3, with the NPGO mode modulating the annual and semiannual intermittent modes, but also has many clear differences. In the winter months, we observe strong sea-ice anomalies of opposite sign in the Bering and Okhotsk seas. The Okhotsk anomalies were not present in the CCSM3 results. Spatially coincident with these ice anomalies, we observe SST anomalies

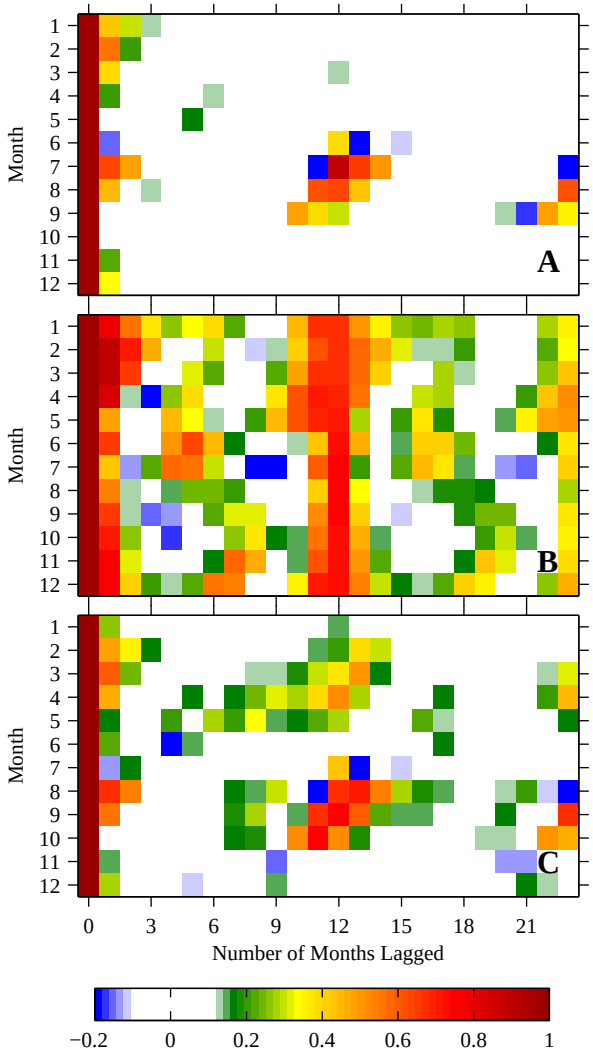

Figure 3.16: Lagged correlations for North Pacific Sea Ice from the HadISST dataset for all months and lags from 0 to 23 months. (A) Shows lagged correlation for raw North Pacific sea-ice data, (B) shows lagged correlations for the Bering Sea computed using the mode family $\{\mathbf{L}_1, \mathbf{I}_1, \mathbf{I}_2, \mathbf{I}_5, \mathbf{I}_6\}$, and (C) shows lagged correlations in the North Pacific for the raw data, conditional on $|L_2^{\mathrm{SST}}| > 1$ (all values above the 75th percentile). Colored boxes indicate correlations which are significant at the 95% level based on a t-test.

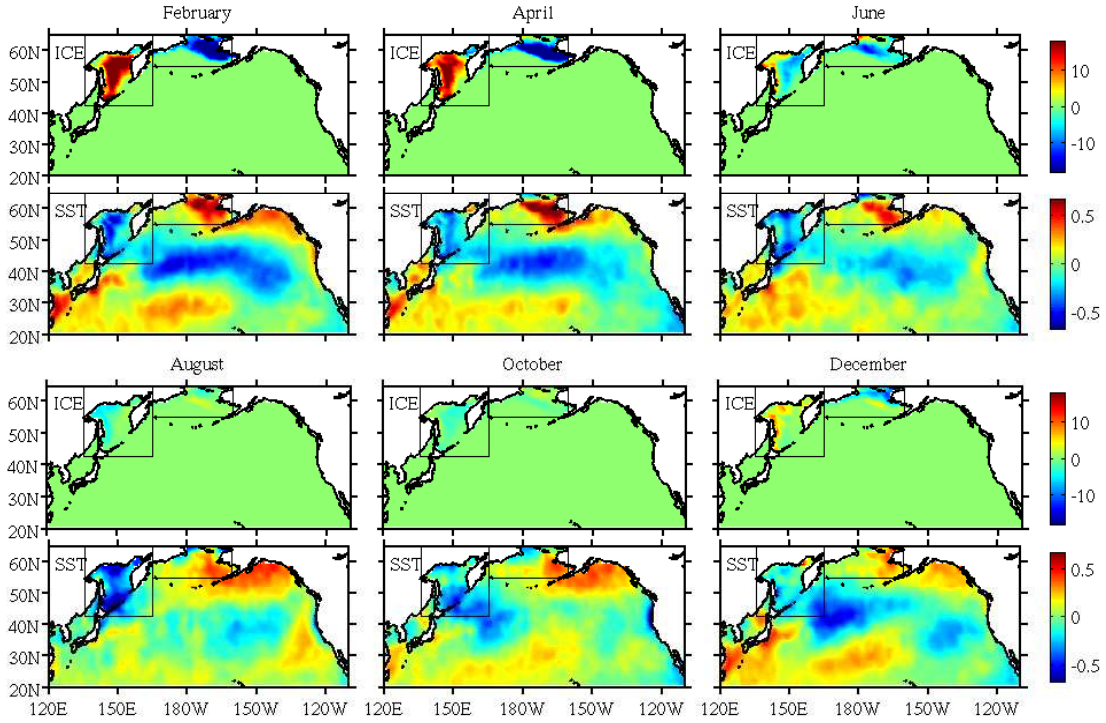

Figure 3.17: Sea ice and SST patterns for year 2001, reconstructed from the HadISST dataset using modes $\{\mathbf{L}_1, \mathbf{I}_1, \mathbf{I}_2, \mathbf{I}_5, \mathbf{I}_6\}$. The Bering and Okhotsk Seas (both boxed) exhibit a spring-fall sea-ice reemergence. See movie 5 for the dynamic evolution of this mode family.

of the opposite sign. We also observe strong SST anomalies throughout most of the North Pacific basin, especially along the Kuroshio extension region. This is different from the CCSM3 results, in which the SST anomalies of the NPGO family were primarily contained in the northern portion of the domain. During the months of July–October the Bering and Okhotsk Seas are relatively ice free, and we observe persistence of SST anomalies of opposite sign to the ice anomalies. Compared to CCSM3 results, the summer SST anomalies do not cover the Bering Sea as completely; there is a portion of the northwest Bering sea that remains anomaly-free over the summer. In the late fall and early winter, sea-ice anomalies reappear in the Bering and Okhotsk seas, adopting the same sign they had the

previous winter. This cycle roughly repeats itself the following winter. This family reflects the same SST-sea ice reemergence mechanism as seem in CCSM3, albeit in a slightly less clean manner.

Why is the North Pacific sea-ice reemergence signal significantly stronger in CCSM3 than in observations? One possibility is that the CCSM3 model overemphasizes the winter-to-winter persistence of the ice and SST anomalies associated with the NPGO. Another possibility is that the raw observational data, after linear detrending, contains a residual signal associated with a nonlinear trend. This nonlinear trend may act to obscure the reemergence signal in the raw data, though we find that the reemergence signal is sufficiently strong to be recoverable in the NPGO-conditioned data. Yet another possibility is that over the relatively short observational record, the low-frequency NPGO mode has been generally inactive, and a longer time series would reveal the reemergence signal.

To investigate the latter possibility, we divided the 900-year CCSM3 record into a number of 34 year datasets, analogous to the length of the observational record, and performed lagged correlations on each of these short timeseries. We found significant variation in the sea-ice reemergence signal over these different datasets, including some sets where the reemergence signal was absent, much like in observations. There were other 34 year datasets which contained a much stronger reemergence limb, quite similar to the conditional lagged correlations of Fig. 3.12b. Therefore, it is plausible that the record of satellite observations is simply too short to provide a sufficient sampling of low-frequency variability of the coupled ocean-sea ice system, and correlations computed using this dataset may not fully reflect the intrinsic variability of this system. We also computed lagged correlations of the sea-ice observations in other parts of the Arctic Ocean, and found strong

reemergence signals in the Barents and Kara Seas, the Labrador Sea, and the Greenland Sea.

3.5.3 SST reemergence in observations

We also investigate SST reemergence in the HadISST dataset by computing time lagged pattern correlations in the North Pacific. Fig. 3.18a shows lagged correlations of the raw SST data and Fig. 3.18b shows lagged correlations conditional on the PDO mode, $\mathbf{L}_2$, being active. We observe a strengthened winter-to-winter SST reemergence when the PDO is active. We also conditioned on other low-frequency modes, and found that the PDO produces the most prominent strengthening of correlation. Note that these correlations are computed over the entire North Pacific domain, rather than the smaller domains considered in section 5f. This choice was made because the conditional correlations were quite noisy when performed over the smaller domains, since the PDO is only "active" for about 25% of the observational record.

The coupled NLSA observational modes also have a mode family $\{\mathbf{L}_2, \mathbf{I}_3, \mathbf{I}_4, \mathbf{I}_7, \mathbf{I}_8\}$, which is analogous to the PDO family of CCSM3. In Fig. 3.19 we show an SST reconstruction for the year 2005 using this mode family. We observe an active SST reemergence in the central and eastern Pacific domains, but there is not a clear reemergence in the western Pacific. The reemergence in the central and eastern Pacific happens at different times of year, with weakest anomalies in September and November, respectively. Similar to the CCSM3 results, the observational PDO family has a large-scale anomaly along the Kuroshio extension region, and significant variability in the central Pacific. A primary difference is that the observational PDO family has much stronger anomalies along the west

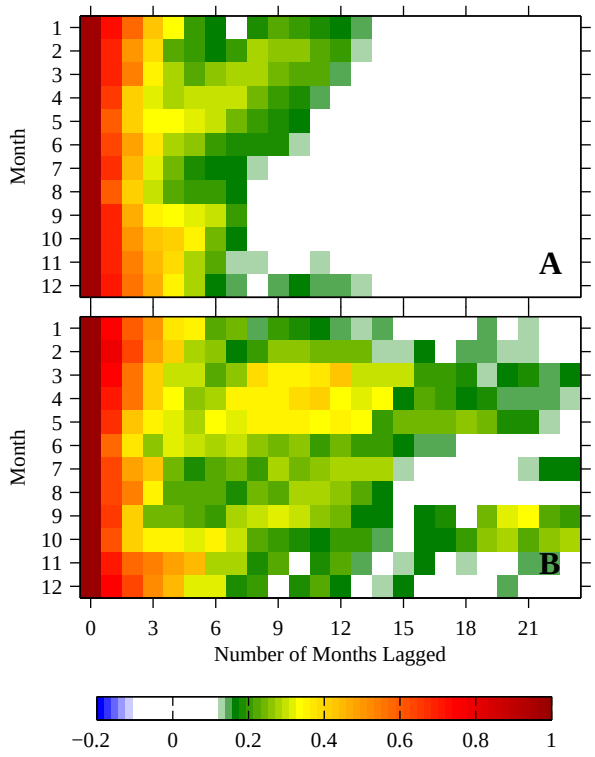

Figure 3.18: Lagged correlations for North Pacific SST from the HadISST dataset for all months and lags from 0 to 23 months. (A) Shows lagged correlation for raw North Pacific SST data, (B) shows lagged correlations in the North Pacific for the raw data, conditional on $|L_1^{\mathrm{SST}}| > 1.5$ (all values above the 75th percentile). Colored boxes indicate correlations which are significant at the 95% level based on a t-test.

coast of North America than the PDO family of CCSM3.

3.6 Conclusions

In this work, we have studied reemergence mechanisms for North Pacific sea ice in comprehensive climate model output and in satellite observations. We have utilized the newly developed coupled NLSA algorithm (Chapter 2), which allows for a scale-invariant coupled analysis of multiple variables in different physical units.

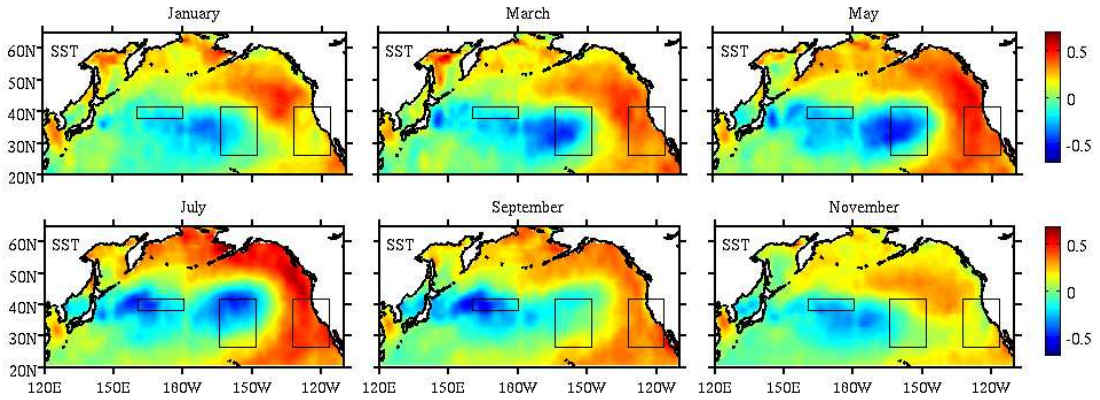

Figure 3.19: SST patterns for year 2005, reconstructed from the HadISST dataset using modes $\{\mathbf{L}_2, \mathbf{I}_3, \mathbf{I}_4, \mathbf{I}_7, \mathbf{I}_8\}$. The central, eastern, and western Pacific domains are boxed. The central and eastern Pacific exhibit a reemergence of SST anomalies. See movie 6 for the dynamic evolution of this mode family.

This algorithm computes a kernel matrix using the individual phase space velocities for each variable, simultaneously removing physical units from the analysis, as well as implicitly selecting the variance ratio between the two variables. The coupled NLSA algorithm was applied to North Pacific SST and sea-ice concentration data from a 900-year CCSM3 control integration, and a set of temporal patterns, analogous to PCs, and spatiotemporal patterns, analogous to extended EOFs, were obtained. The same analysis was performed on the 34 year record of sea ice and SST satellite observations. The modes recovered by coupled NLSA include periodic and low-frequency patterns of variability of sea ice and SST, as well as intermittent patterns not captured by SSA. The leading low-frequency modes correlate well with the familiar PDO and NPGO patterns of North Pacific SST variability. The intermittent modes have a base frequency of oscillation and are modulated by either the PDO or NPGO low-frequency signal, and tend to either be in phase or out of phase with their corresponding periodic cycle.

Using the modes obtained via coupled NLSA, we investigated the phenomenon of sea-ice reemergence suggested by BW, in the North Pacific region. In the CCSM3 data, it was found that the raw sea-ice data of the North Pacific exhibited a similar reemergence of correlation to that seen by BW, a notable difference being the lack of a "winter limb." Seeking a low-dimensional family of modes to explain this reemergence process, we found that the NPGO and its corresponding annual and semiannual intermittent modes were able to reproduce the lagged correlations seen in the Bering Sea. Moreover, reconstructing patterns in the spatial domain, we found that this low-dimensional family demonstrates a sea-ice reemergence mechanism, in which summer SST stores the memory of springtime sea-ice anomalies, remarkably well. It was also found that conditioning the raw sea-ice data on the NPGO being active, led to a significantly strengthened "summer limb" in the lagged correlations of the Bering Sea, which has implications for regional predictability of sea-ice reemergence. Also, the family of NLSA modes related to the PDO was able capture a winter-to-winter reemergence of SST anomalies, both in lagged correlations and in spatial reconstructions.

The raw observational sea-ice record does not contain a sea-ice reemergence signal in the North Pacific sector. However, when conditioned on the NPGO mode being active, a clear summer limb appears in the raw data lagged correlations. Additionally, an analogous NPGO family exists for the observations, and displays a similar SST-sea ice reemergence mechanism. An enhanced winter-to-winter SST reemergence was found when conditioning on an active PDO. Also, the observational modes have a PDO family, which exhibits SST reemergence in the North Pacific. In Chapter 4, we will add sea level pressure to our coupled analysis to gain insight into the variability of the coupled atmosphere-sea ice-ocean system.

Chapter 4

Arctic Sea-Ice Reemergence: The Role of Large-Scale Oceanic and Atmospheric Variability

4.1 Introduction

Satellite data shows that trends in sea-ice extent are negative for all months of the year and all Arctic regions except for the Bering Sea (Cavalieri and Parkinson, 2012). In addition to these strong trends, Arctic sea ice also exhibits large internal variability. Studies using comprehensive climate models have estimated that 50-60% of recent Arctic sea-ice changes can be attributed to externally forced trends, with the remainder resulting from internal variability in the climate system (Kay et al., 2011; Stroeve et al., 2012). Therefore, the challenge of making accurate projections of future Arctic sea-ice conditions crucially hinges on: (1) quantifying the sea-ice response to changes in external forcing (i.e., greenhouse gas forcing) and

(2) understanding the nature and magnitude of internal variability in the coupled ice-ocean-atmosphere system. The work of this chapter will focus on the latter.

The Arctic regions of interest in this study are shown in Fig. 4.1. The leading empirical orthogonal function (EOF) of observational Arctic sea-ice concentration (SIC) exhibits strong out-of-phase anomalies between the Labrador and Greenland-Barents Seas and weaker out-of-phase anomalies between the Bering Sea and Sea of Okhotsk (Deser et al., 2000). Regression of sea level pressure (SLP) onto the corresponding principal component (PC) yields a spatial pattern which closely resembles the Arctic Oscillation (AO, Thompson and Wallace, 1998), the leading pattern of SLP variability north of 20°N. Deser et al. (2000) observe a connection between the low-frequency (interannual to decadal) variability of the atmosphere and the low-frequency variability of sea-ice. In particular, they find that the AO and its associated geostrophic winds are physically consistent with the ice anomalies of the leading SIC mode, suggesting that atmospheric circulation anomalies force sea-ice anomalies. These winds have thermodynamic and dynamic effects on sea ice via advection of surface air temperature and ice advection. Many other studies have analyzed sea-ice variability in the context of the AO, finding that the AO affects sea ice on a wide range of time scales ranging from seasonal (Serreze et al., 2003) to decadal (Rigor et al., 2002; Rigor and Wallace, 2004; Zhang et al., 2004). These studies suggest that a "high-index" AO produces an Ekman divergence, leading to reductions in sea-ice thickness and concentration. This process has been proposed as a mechanism for the recent decline in Arctic sea ice.

Others have questioned the efficacy of the AO as a predictor for sea-ice changes (Maslanik et al., 2007), suggesting that other patterns of large-scale atmospheric variability may play a more important role. In particular, an SLP pattern known

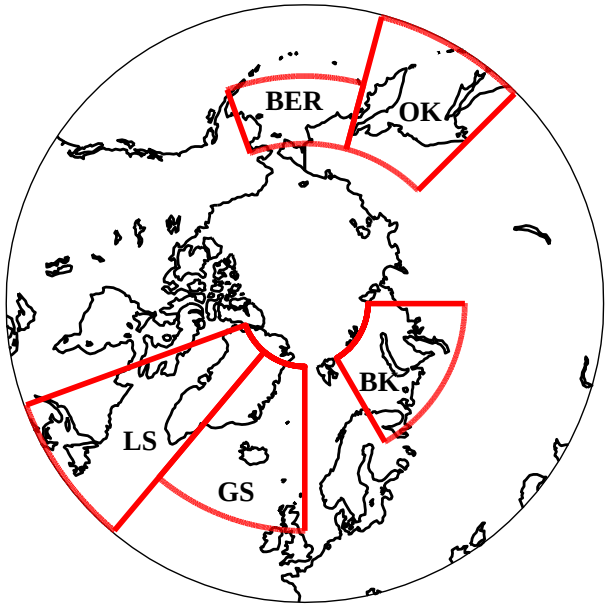

Figure 4.1: The regions of interest in this study: the Barents-Kara Seas (BK), the Labrador Sea (LS), the Greenland Sea (GS), the Bering Sea (BER), and the Sea of Okhotsk (OK). The Arctic domain is defined as all grid points north of 45°N.

as the Arctic Dipole Anomaly (DA) has drawn considerable recent attention (Wu et al., 2006; Wang et al., 2009; Tsukernik et al., 2010; Overland and Wang, 2005, 2010; Watanabe et al., 2006). The DA exhibits opposite-signed SLP anomalies between the Eastern and Western Arctic, which drive strong meridional winds. These winds act to enhance (reduce) sea-ice export from the Arctic basin through Fram Strait when the DA is in positive (negative) phase. Recent record lows in summer sea-ice extent generally correspond to years in which the DA index was positive (Wang et al., 2009). DA-like SLP patterns have also been associated with the large internal variability observed in the sea-ice component of the Community Climate System Model Version 3 (CCSM3, Collins et al., 2006; Wettstein and Deser, 2014). Other studies have suggested that the location and frequency of

storms (Screen et al., 2011), and the phase of the Pacific-North-America (PNA) pattern (L'Heureux et al., 2008) also play an important role in setting the summer sea-ice minimum.

The PCs corresponding to large-scale atmospheric patterns, such as the AO and DA, are quite noisy and contain significant spectral power at time scales ranging from monthly to decadal. A typical approach has been to initially low-pass filter the atmospheric component (by forming annual or winter means), as a way of smoothing out these PCs and emphasizing interannual-to-decadal variability. Besides the studies already cited, a large number of works have analyzed the impact of this low-frequency atmospheric variability on Arctic sea ice (Walsh et al., 1996; Proshutinsky and Johnson, 1997; Mysak and Venegas, 1998; Yi et al., 1999; Johnson et al., 1999; Deser et al., 2000; Polyakov and Johnson, 2000; Moritz et al., 2002). These studies emphasize that sea-ice regimes are modulated by low-frequency atmospheric circulation regimes.

The variability of Arctic sea ice is also strongly coupled to sea surface temperature (SST) variability (e.g., Francis and Hunter, 2007). Blanchard-Wrigglesworth et al. (2011a) proposed a mechanism for sea-ice–SST co-variability, in which sea-ice and SST anomalies trade off, allowing for unexpected "memory" effects in sea ice. These memory effects were termed "sea-ice reemergence", inspired by the similar North Pacific and North Atlantic SST phenomena (Alexander et al., 1999; Timlin et al., 2002; de Cotlogon and Frankignoul, 2003). Sea-ice reemergence is a lagged correlation phenomenon, in which spring sea-ice anomalies are positively correlated with fall sea-ice anomalies, despite a loss of correlation over the intervening summer months. There is also a similar, but weaker, reemergence between fall sea-ice anomalies and anomalies the following spring. The spring-fall mechanism

of Blanchard-Wrigglesworth et al. (2011a) suggests that spring sea-ice anomalies imprint SST anomalies of opposite sign, which persist over the summer months. During the fall, ice grows southward and interacts with these SST anomalies, reproducing ice anomalies of the same sign as the spring. This reemergence mechanism has been observed in the North Pacific sector in CCSM3 model output and observations (Chapter 3). Deser et al. (2002) note a similar winter-to-winter persistence of sea-ice anomalies in the Labrador Sea, and propose an atmospheric mechanism in which sea-ice anomalies persist due to persistent large-scale atmospheric circulation regimes.

Sea-ice reemergence may also have implications for sea-ice predictability. Day et al. (2014b) found that sea-ice forecast skill was strongly dependent on initialization month, with certain months exhibiting a slower decay of forecast skill than others. The authors suggested that this initialization month dependence was attributable to sea-ice reemergence mechanisms. Day et al. (2014b) also examined sea-ice reemergence in five global climate models (GCMs) and observations, finding robust reemergence signals, of varying strength, across all models and a weaker reemergence signal in the observational record.

In this study, we examine the coupled variability of Arctic SIC, SST, and SLP using coupled nonlinear Laplacian spectral analysis (NLSA; Chapter 2), a multivariate data analysis technique which provides scale-invariant analysis of multiple variables with different physical units. Coupled NLSA yields spatiotemporal modes, analogous to EEOFs, and temporal modes, analogous to PCs. These modes are constructed using a set of empirically derived Laplacian eigenfunctions on the nonlinear data manifold and, unlike linear approaches, do not maximize explained variance. Compared to linear techniques, NLSA (and other related non-

linear methods; Berry et al., 2013) provide superior time-scale separation and are able to effectively capture low-variance modes that may have important dynamical significance. These low-variance modes are known to be crucial in producing accurate representations of nonlinear dynamical systems (Aubry et al., 1993; Giannakis and Majda, 2012c), and in the present context, are efficient in explaining reemergence phenomena (Chapter 3).

We use coupled NLSA modes to study the basin-wide and regional characteristics of Arctic sea-ice reemergence in a comprehensive climate model and observations. We compute modes using CCSM3 model output from a 900-year equilibrated control integration. Modes are also obtained for the 34-year observational record, using SIC and SST data from the Met Office Hadley Center Sea Ice and Sea Surface Temperature (HadISST) dataset and Era-Interim SLP reanalysis data. No preprocessing of the data is required, enabling simultaneous extraction of interannual, annual, and semiannual patterns of variability. Using these modes, we identify low-dimensional families which efficiently describe sea-ice reemergence. These families capture a significant portion of the reemergence signal, and have the surprising property of being relatively low-variance. The families also reveal time-dependent aspects of reemergence, which were not accessible in previous studies. The SST and SIC modes of each family exhibit an SST–sea-ice reemergence mechanism consistent with that of Blanchard-Wrigglesworth et al. (2011a). Interannual components of large-scale SLP variability, which emerge objectively from this analysis, are found to be related to coherent sea-ice reemergence events in geographically distinct regions, and suggest an SLP–sea-ice reemergence mechanism.

This paper is organized as follows: In section 2, we briefly summarize the coupled NLSA algorithm. In section 3, we describe the CCSM3, HadISST, and

ERA-Interim datasets used in this study. In section 4, we study the SIC, SST, and SLP spatiotemporal modes obtained via coupled NLSA. In section 5, we examine the regional and temporal characteristics of sea-ice reemergence, and in section 6, we investigate oceanic and atmospheric reemergence mechanisms. We conclude in section 7. Movies, illustrating the spatiotemporal evolution of NLSA modes, are available as online supplementary material.

4.2 Coupled NLSA methodology

In this study, we apply the coupled NLSA approach, as developed in Chapter 2, to Arctic SIC, SST, and SLP. This technique is an extension of the recently developed NLSA algorithm (Giannakis and Majda, 2012c, 2013), and provides a scale-invariant approach for multivariate time series analysis. Unlike other multivariate data analysis approaches, coupled NLSA does not require initial normalization of the input fields to unit variance. Rather, the coupled NLSA algorithm implicitly selects the variance ratio between different physical fields, without requiring a choice of normalization by the user. Here, we refer the reader to the more thorough description of Chapter 2. In Fig. 4.2 we provide a schematic that summarizes the flow of data in the coupled NLSA algorithm.

4.3 Dataset description

4.3.1 CCSM3 model output

This chapter analyzes model output from a 900-yr equilibrated control integration (model run b30.004) of CCSM3 (Collins et al., 2006). This data was

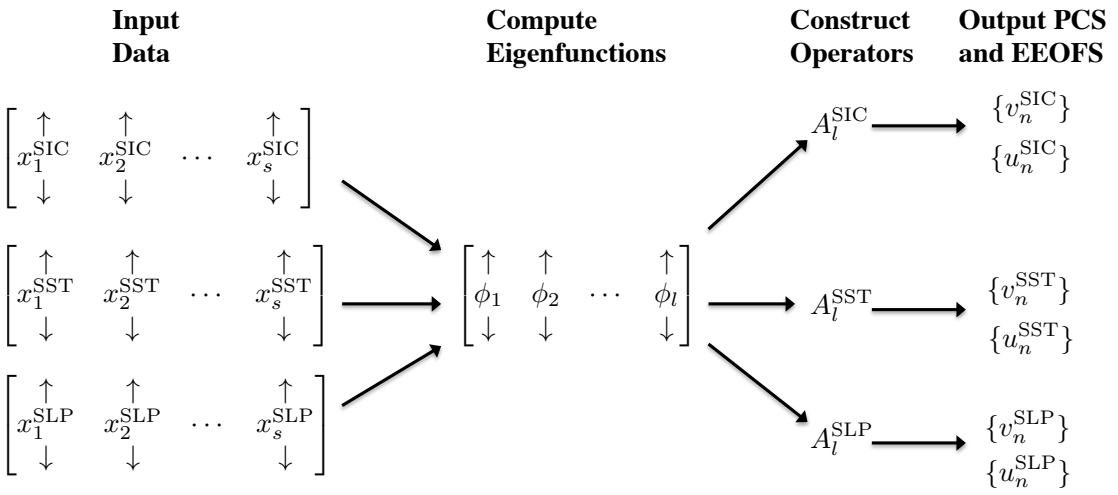

Figure 4.2: Schematic summarizing the flow of data in the coupled NLSA algorithm.

downloaded from the Earth System Grid website. We use monthly averaged data for SIC, SST, and SLP, which come from the Community Sea Ice Model (CSIM, Holland et al., 2006a), the Parallel Ocean Program (POP, Smith and Gent, 2004), and the Community Atmosphere Model version 3 (CAM3, Collins et al., 2004), respectively. The model uses a T42 spectral truncation for the atmospheric grid (roughly $2.8^\circ \times 2.8^\circ$), and the ocean and sea-ice variables are defined on the same grid, of 1° nominal resolution. This chapter focuses on a pan-Arctic domain, which we define as all gridpoints north of 45°N. Note that the seasonal cycle has not been removed from this dataset. This is crucial for capturing intermittent patterns associated with reemergence. In particular, intermittent modes, described ahead in section 4, are not recoverable in datasets that have been deseasonalized (Giannakis and Majda, 2013). As will be shown ahead in section 5, these modes are essential in low dimensional descriptions of sea-ice reemergence.

The spatial dimensions (number of spatial gridpoints) of these datasets are $d_{\mathrm{SIC}} = d_{\mathrm{SST}} = 13{,}202$ and $d_{\mathrm{SLP}} = 2{,}048$. Using a two-year embedding window with

$q = 24$ (Giannakis and Majda, 2012c, Chapter 3), this yields lagged embedding dimensions (the product of the number of spatial gridpoints and the embedding window) of $qd_{\text{SIC}} = qd_{\text{SST}} = 316{,}848$ and $qd_{\text{SLP}} = 49{,}152$. These data are monthly averaged, and consist of $s = 10{,}800$ time samples for the 900-yr simulation period. The value $\Delta t = 24$ months was used as the time lag because this embedding window is longer than the seasonal cycle, which is a primary source of non-Markovianity in this dataset. A number of different embedding windows were tested, yielding qualitatively similar results for $\Delta t \geqslant 12$ months, and qualitatively different results for $\Delta t < 12$ months.

4.3.2 HadISST observations

We also analyze the HadISST dataset (Rayner et al., 2003), which consists of monthly averaged SIC and SST data on a 1° latitude-longitude grid. The spatial dimension of the Arctic domain is $d_{\text{SIC}} = d_{\text{SST}} = 9{,}453$. As with the CCSM3 data, we use an embedding window of $\Delta t = 24$ months, which yields lagged-embedding dimensions of $qd_{\text{SIC}} = qd_{\text{SST}} = 226{,}872$. In this chapter we use the satellite era data from January 1979–August 2013. Note that all ice-covered gridpoints in the HadISST dataset were assigned an SST value of -1.8°C, the freezing point of salt water at a salinity of 35 parts per thousand. Also, the trend in the dataset was removed by computing a long-term linear trend for each month of the year, and removing the respective linear trend from each month. The seasonal cycle has not been removed from this dataset.

4.3.3 ERA-Interim reanalysis data

Finally, we also study monthly-averaged SLP data from the European Centre for Medium-Range Weather Forecasts (ECMWF) Interim Reanalysis project (ERA-Interim, Dee et al., 2011). These data are defined on a 0.75° latitude–longitude grid, of considerably higher resolution than the CCSM3 SLP data. The spatial dimension of the Arctic domain is $d_{\text{SLP}} = 29,280$, corresponding to a lagged-embedding dimension of $qd_{\text{SLP}} = 702{,}720$. These data have been detrended by subtracting the monthly trend from each month, but the seasonal cycle has not been subtracted.

4.4 Coupled SIC-SST-SLP spatiotemporal modes of Arctic variability

We utilize the coupled NLSA algorithm outlined in section 2 to study the spatiotemporal evolution of (i) SIC, SST, and SLP in CCSM3; and (ii) SIC and SST from HadISST, and SLP from ERA-Interim. Hereafter, we refer to the joint HadISST and ERA-Interim datasets as observations. For both the model and observational data, we use a lagged-embedding window of $\Delta t = 24$ months.

4.4.1 CCSM3 Modes

We choose ϵ, the Gaussian locality parameter, as $\epsilon = 0.90$. Using the spectral entropy criterion of Giannakis and Majda (2012a, 2013), we select a truncation level of $l = 27$ eigenfunctions, and express the data matrices X^{SIC}, X^{SST}, and X^{SLP} in this basis. SVD of the resulting operators (the A_l operators, as defined

in Chapter 2) yields a set of spatiotemporal patterns, $\{u_n^{\mathrm{SIC}}\}$, $\{u_n^{\mathrm{SST}}\}$, $\{u_n^{\mathrm{SLP}}\}$, and a set of temporal patterns, $\{v_n^{\mathrm{SIC}}\}$, $\{v_n^{\mathrm{SST}}\}$, $\{v_n^{\mathrm{SLP}}\}$, for each variable. The modes are ordered by decreasing singular value. In general, the temporal patterns for different variables need not be related. However, by virtue of the relatively low-dimensionality of the eigenfunction basis relative to the original temporal dimension ($l = 27 \ll s = 10{,}800$), and the fact that the eigenfunctions incorporate information from all three variables, we find strong correlations between the temporal patterns of different variables.

Temporal Modes

Figures 4.3, 4.4, and 4.5 show selected temporal patterns for SIC, SST, and SLP, respectively. For each variable, we observe three distinct types of temporal modes: periodic, low-frequency, and intermittent modes, indicated by P, L, and I in the figures.

The periodic temporal modes closely resemble sinusoids, with frequencies given by integer multiples of 1 yr^{-1}. These modes appear as doubly degenerate pairs, with a phase offset of $\pi/2$. The leading periodic modes, representing the annual and semiannual cycles, capture more variance than the low-frequency and intermittent modes of the system. Higher harmonic periodic modes are found later in the mode spectrum. The low-frequency modes are characterized by significant interannual variability, and have a typical decorrelation time of approximately 3 years. These modes carry significant spectral power at frequencies below 1 yr^{-1}, and exhibit a sharp decline in spectral power at frequencies above this.

The intermittent modes are characterized by periods of intense activity followed by periods of quiescence. Each intermittent mode has a base frequency of oscilla-

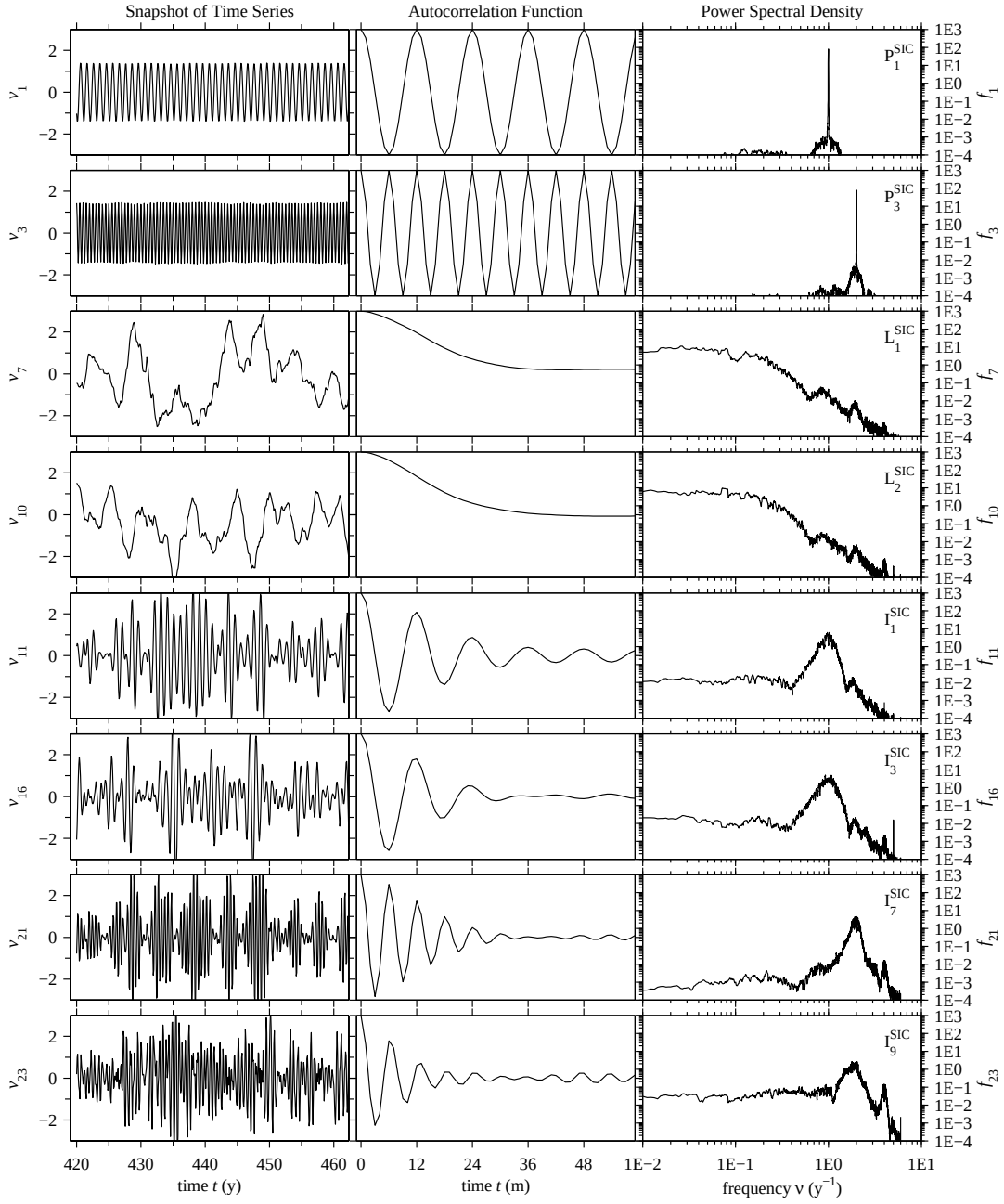

Figure 4.3: Snapshots of the time series, power spectral density, and autocorrelation functions for the CCSM3 SIC PCs (v_k) from coupled NLSA. Shown here for 50-year portions of the 900-yr time series are the annual periodic ($P_1^{\rm SIC}$) and semiannual periodic ($P_3^{\rm SIC}$) modes, low-frequency modes ($L_1^{\rm SIC}$ and $L_2^{\rm SIC}$), annual intermittent modes ($I_1^{\rm SIC}$ and $I_3^{\rm SIC}$), and semiannual intermittent modes ($I_7^{\rm SIC}$ and $I_9^{\rm SIC}$). The autocorrelation vertical scale is [-1,1].

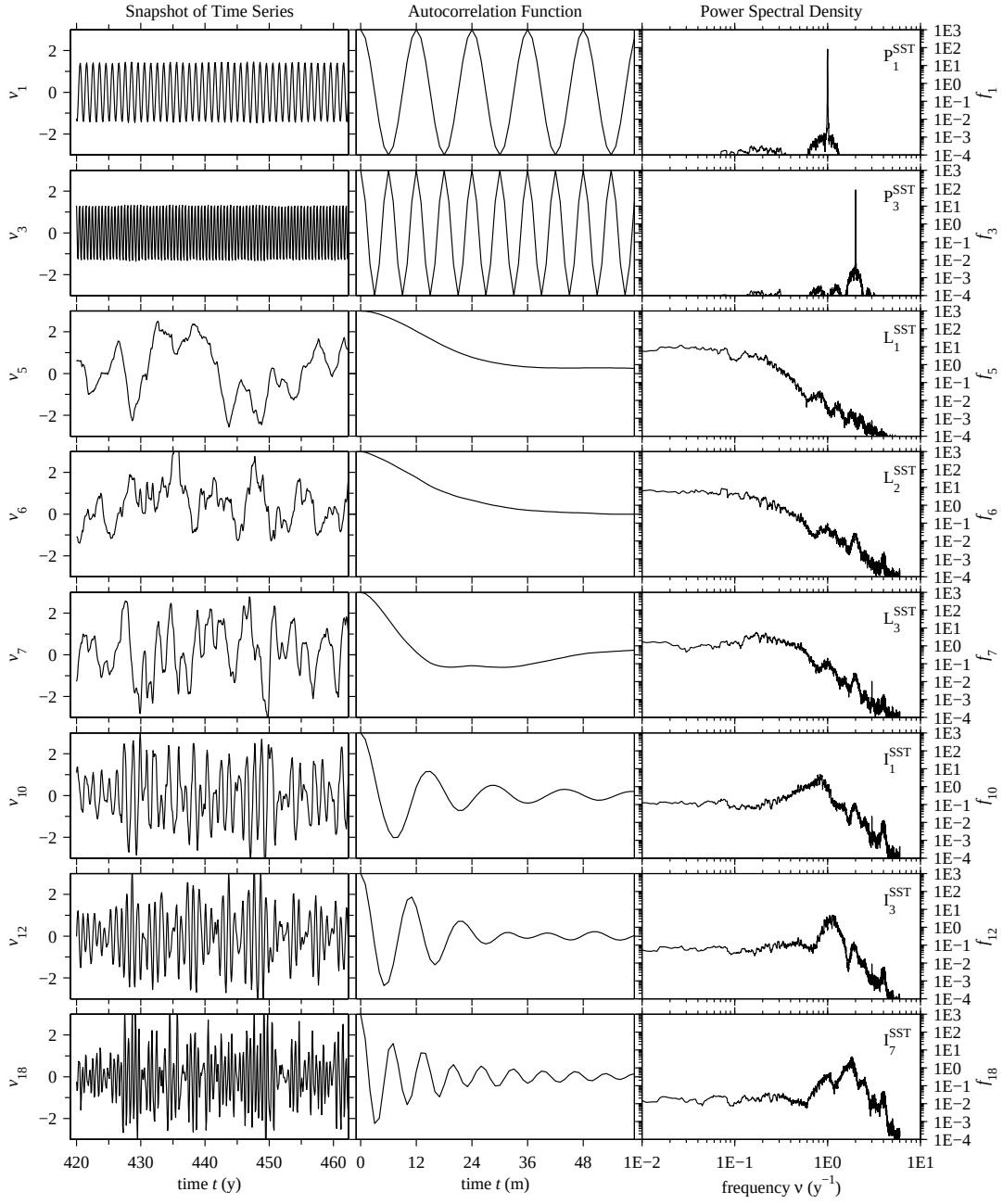

Figure 4.4: Snapshots of the time series, power spectral density, and autocorrelation functions for the CCSM3 SST PCs from coupled NLSA. Shown here are the annual periodic (P_1^{SST}) and semiannual periodic (P_3^{SST}) modes, low-frequency modes (L_1^{SST}, L_2^{SST}, and L_3^{SST}), annual intermittent modes (I_1^{SST} and I_3^{SST}), and semiannual intermittent modes (I_7^{SST}). The autocorrelation vertical scale is [-1,1].

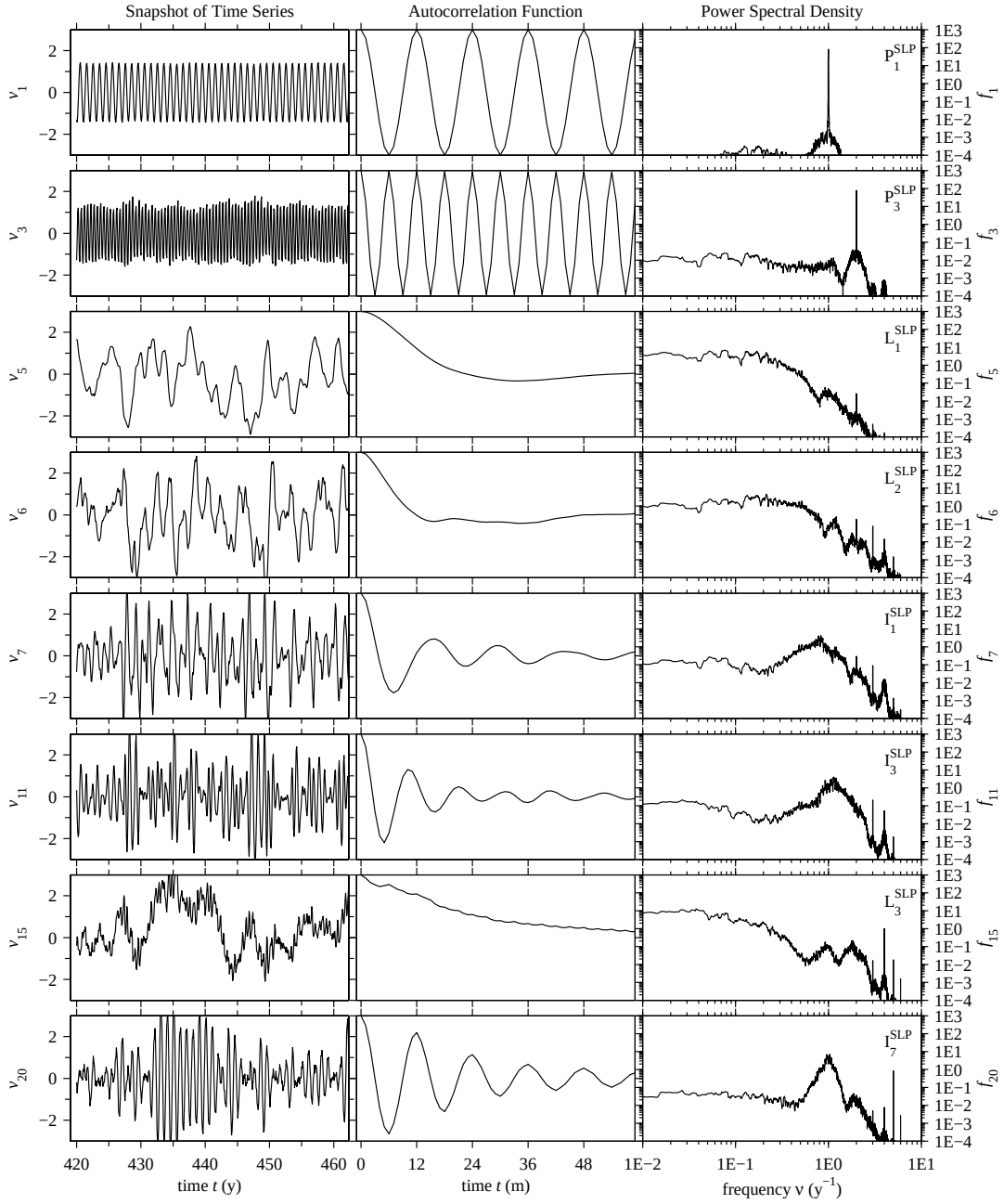

Figure 4.5: Snapshots of the time series, power spectral density, and autocorrelation functions for the CCSM3 SLP PCs from coupled NLSA. Shown here are the annual periodic (P_1^{SLP}) and semiannual periodic (P_3^{SLP}) modes, low-frequency modes (L_1^{SLP}, L_2^{SLP}, L_3^{SLP}), and intermittent modes (I_1^{SLP}, I_3^{SLP},I_7^{SLP}). The autocorrelation vertical scale is [-1,1].

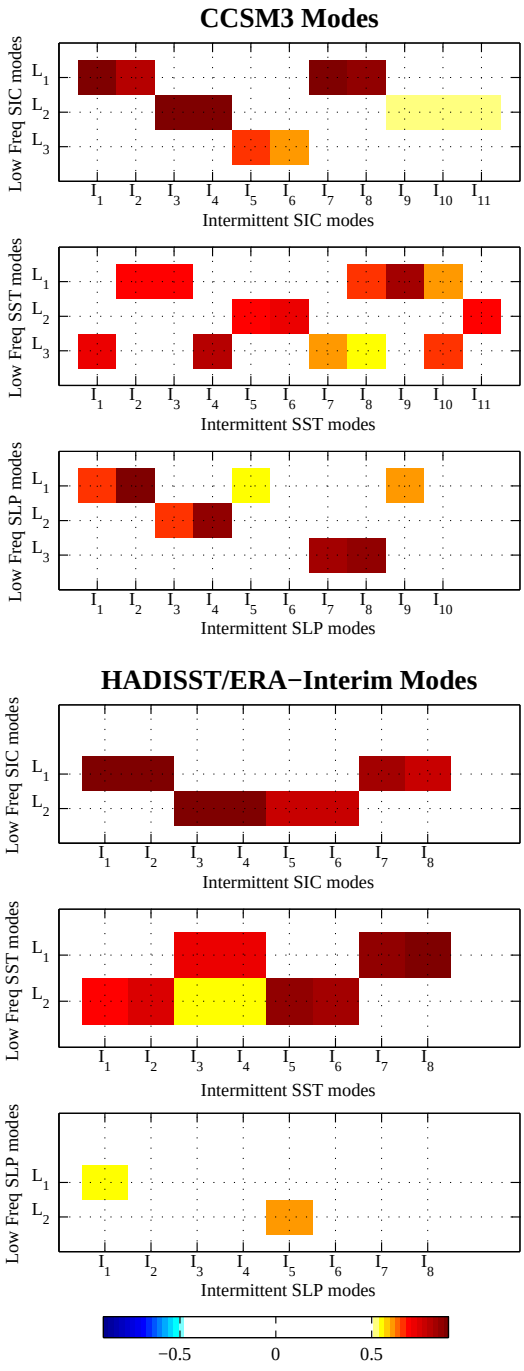

Figure 4.6: Correlations between low-frequency modes and envelope functions for intermittent modes. Mode pairs with large positive correlations indicate that the low-frequency mode provides the modulating envelope for the intermittent mode.

tion, and a broadband peak in spectral power centered upon this frequency. These modes carry lower variance than their periodic and low-frequency counterparts, yet have potentially high dynamical significance. For example, annual and semiannual intermittent modes are crucial components in low-dimensional descriptions of sea-ice reemergence phenomena (Chapter 3). Note that the leading low-frequency and intermittent modes are insensitive to truncation level, whereas increasing l will eventually disrupt the temporal character of some intermittent modes.

Intermittent modes closely resemble a periodic signal modulated by a low-frequency envelope. We find that nearly all intermittent modes can be directly associated with a particular low-frequency mode, which provides this modulating envelope (Chapter 3). To determine this association we compare the envelope function of the intermittent modes to the low-frequency modes. We find the envelope function via the Hilbert transform (von Storch and Zwiers, 1999). Let $I(t)$ be a given intermittent mode and let $H(I)(t)$ be the Hilbert transform of I. Then the envelope function, $e(t)$, is given by $e(t) = \sqrt{I(t)^2 + H(I)(t)^2}$. Next, we determine which low-frequency mode provides this modulating envelope by performing a correlation between $e(t)$ and $|L(t)|$, where $L(t)$ is a low-frequency mode. Fig. 4.6 shows these correlation values for intermittent and low-frequency modes of each variable, for both the model and observations. Note that the low-frequency-intermittent mode association is quite clear for most variables, except for the observational SLP, whose intermittent envelopes generally correlate weakly with the low-frequency modes.

As a comparison, we also performed SSA on the concatenated and unit-variance normalized SIC-SST-SLP dataset. Similar to the findings of Chapter 3, SSA produces periodic modes, many low-frequency modes, and some modes that loosely

resemble the intermittent modes of NLSA, with a spectral maximum at a certain base frequency. We find that the SSA modes do not share the same intermittent–low-frequency mode relationships as the NLSA modes. These relationships will be important for explaining reemergence, as they reflect the interaction of large-scale low-frequency modes of variability with the familiar annual and semiannual cycles in the climate system.

SIC Spatiotemporal Patterns

Figure 4.7 shows spatial patterns of selected modes at a snapshot in time. Movies 8 and 9, in the online supplementary material, show the spatiotemporal evolution of these modes and others. Below, we describe the prominent features of the spatiotemporal modes recovered for SIC, SST, and SLP.

The annual periodic SIC modes, $\{P_1^{\mathrm{SIC}}, P_2^{\mathrm{SIC}}\}$ (Fig. 4.7a), have spatially uniform anomalies throughout most of the Arctic, except at high-latitude gridpoints where there is year-round ice coverage, and in the marginal ice zones, where the anomalies are slightly weaker. These anomalies reach their maximum and minimum values in March and September, respectively. The higher-frequency periodic modes have increasingly finer spatial structure, and capture a decreasing portion of the variance.

The low-frequency modes closely resemble the leading EOFs of Arctic SIC in the CCSM3 model. L_1^{SIC} (Fig. 4.7d) exhibits anomalies in the Bering, Beaufort, and Labrador Seas, which are out-of-phase with the anomalies of the Barents, Kara, and Greenland Seas. Computing pattern correlations between the q spatial patterns of L_1^{SIC} and the different EOFs of deseasonalized Arctic SIC, we find a maximum pattern correlation of 0.97 with EOF 1. L_2^{SIC} (Fig. 4.7g) has strong anomalies in

the Bering and Labrador Seas, which are out-of-phase with one another. It also has weaker anomalies in the Sea of Okhotsk, Barents and Kara seas which are in-phase with the Bering Sea anomalies. This mode has a maximum pattern correlation of 0.77 with EOF 3.

Each intermittent mode has a natural association with a certain low-frequency mode, which acts as a modulating envelope for the intermittent mode. There is also a clear spatial connection, as the intermittent modes are active in the same parts of the domain as their low-frequency counterpart. The annual and semi-annual intermittent mode pairs, $\{I_1^{\mathrm{SIC}}, I_2^{\mathrm{SIC}}\}$ and $\{I_7^{\mathrm{SIC}}, I_8^{\mathrm{SIC}}\}$, are associated with L_1^{SIC} (see Fig. 4.6). These modes pulse with annual and semiannual frequency, respectively, and exhibit finer spatial structure than L_1^{SIC}. In regions where L_1^{SIC} has monopole anomalies, these intermittent modes have dipole and tripole anomalies, respectively. The annual and semiannual intermittent modes, $\{I_3^{\mathrm{SIC}}, I_4^{\mathrm{SIC}}\}$ and $\{I_9^{\mathrm{SIC}}, I_{10}^{\mathrm{SIC}}, I_{11}^{\mathrm{SIC}}\}$, are associated with L_2^{SIC}, and share similar spatial relationships.

SST Spatiotemporal Patterns

L_1^{SST} (Fig. 4.7e) has strong anomalies in the Bering Sea that extend southward into the Northeast Pacific, and anomalies of the opposite sign in the Barents and Kara Seas. There is also a North Atlantic signal with anomalies in the subpolar gyre region that are in-phase with the North Pacific anomalies. This mode has a maximum pattern correlation of 0.98 with EOF 1 of Arctic SST from CCSM3. L_2^{SST} (Fig. 4.7h) exhibits out-of-phase anomalies between the North Pacific and North Atlantic. The North Atlantic anomalies correspond to variability in the subpolar gyre, and the North Pacific anomalies are strongest in the Bering Sea, extending through most of the Pacific portion of the domain. This mode is most

similar to EOF 2, with 0.96 pattern correlation.

The intermittent modes associated with L_1^{SST} and L_2^{SST} are $\{I_1^{\mathrm{SST}}, I_2^{\mathrm{SST}}, I_8^{\mathrm{SST}}, I_9^{\mathrm{SST}}\}$ and $\{I_5^{\mathrm{SST}}, I_6^{\mathrm{SST}}, I_{11}^{\mathrm{SST}}\}$, respectively. As with the SIC modes, these modes are active in the same parts of the domain as their associated low-frequency mode, and have finer spatial structure. A primary difference is that these intermittent modes exhibit spatially propagating anomalies, as compared with their stationary SIC counterparts. This propagation is most evident in the subpolar gyre region of the North Atlantic.

SLP Spatiotemporal Patterns

L_1^{SLP} (Fig. 4.7f) has a similar SLP pattern to the AO, with an anomaly centered over the pole, and anomalies of opposite sign in the North Atlantic and North Pacific basins. The AO is defined as the leading EOF of SLP north of 20°N. Considering EOFs of CCSM3 SLP north of 20°N, we find a maximum pattern correlation of 0.98 with EOF 1. In light of this strong correlation, we call L_1^{SLP} the AO mode. L_2^{SLP} also closely resembles the AO, with a maximum pattern correlation of 0.98 with EOF 1. However, L_1^{SLP} and L_2^{SLP} have distinct temporal patterns and are non-degenerate modes.

L_3^{SLP} (Fig. 4.7i) has a strong resemblance to the DA, which consists of opposite-signed SLP anomalies between the Eastern and Western Arctic. Following Wu et al. (2006), we define the dipole anomaly as the second leading EOF of winter (October-March) SLP north of 70°N. Let PC 2 be the PC associated with EOF 2. To determine the corresponding spatial pattern over the Arctic domain (north of 45°N), we project winter Arctic SLP onto PC 2, and compare the resulting spatial pattern to L_3^{SLP}. We find a maximum pattern correlation of 0.78, and lower

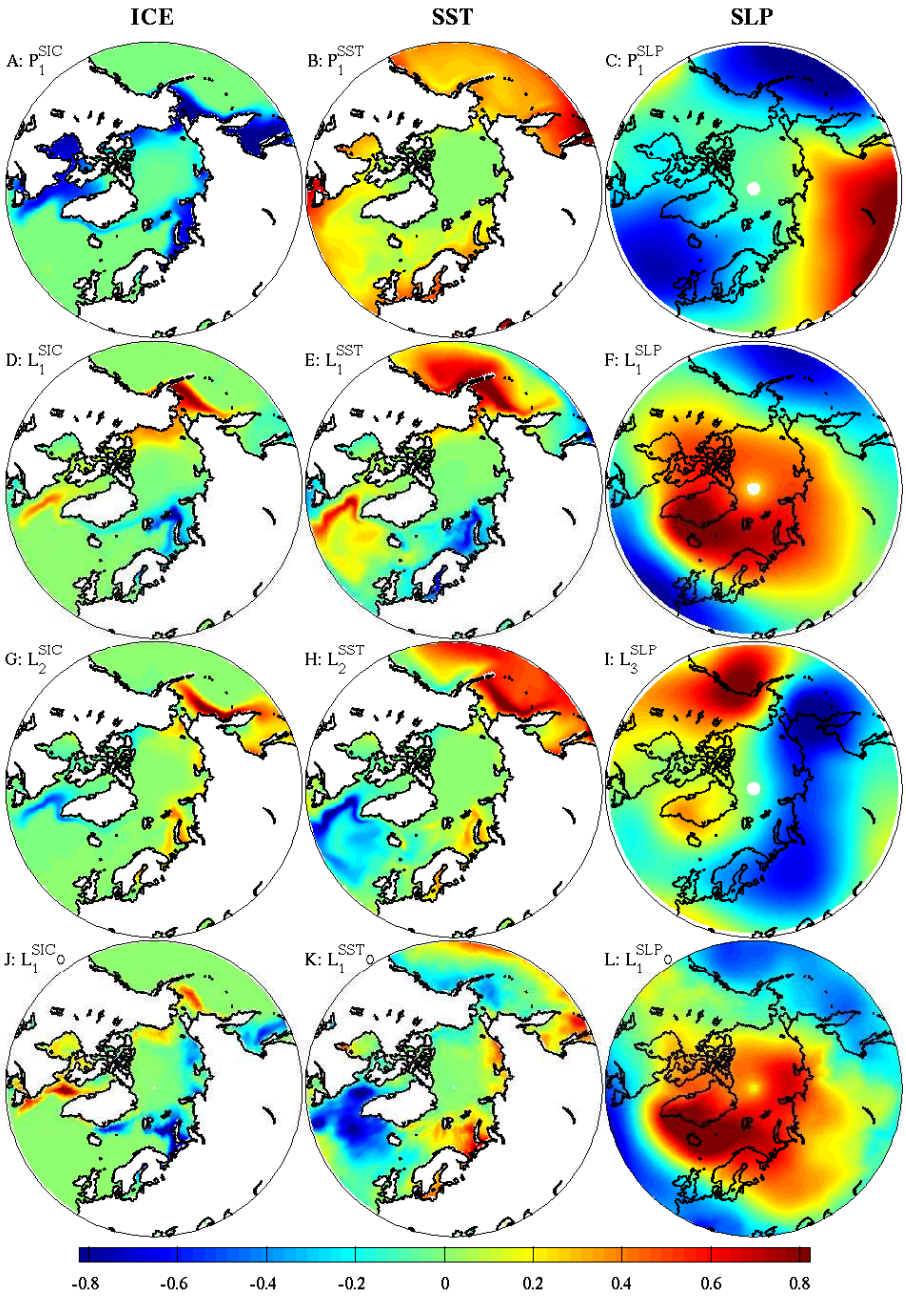

Figure 4.7: Spatial patterns of selected sea ice, SST, and SLP NLSA modes. For each mode, we plot the spatial pattern with largest variance (of the q spatial patterns that make up the spatiotemporal pattern). Rows 1-3 show CCSM3 modes and row 4 shows observational modes, indicated by an O subscript. The fields have been normalized to have a maximum absolute value of 1.

correlations when other PCs are used. Another possible technique for determining the Arctic SLP signal of the DA, as performed in Wu et al. (2006), is to perform a conditional composite, based on the months in which PC 2 is active. This yields a very similar pattern correlation of 0.77 with L_3^{SLP}. Wu et al. (2006) also perform a conditional composite in which the influence of the AO is removed via linear regression. We also computed a spatial pattern using this technique and found a pattern correlation of 0.78 with L_3^{SLP}. Based on these findings, we refer to L_3^{SLP} as the DA mode.

L_1^{SLP} has associated annual and semiannual intermittent modes $\{I_1^{\mathrm{SLP}}, I_2^{\mathrm{SLP}}$,-$I_9^{\mathrm{SLP}}, I_{10}^{\mathrm{SLP}}\}$. L_3^{SLP} is associated with a pair of annual intermittent modes $\{I_7^{\mathrm{SLP}}$,-$I_8^{\mathrm{SLP}}\}$, but not any semiannual intermittent modes.

4.4.2 Observational Modes

We compute the coupled NLSA observational modes using a locality parameter of $\epsilon = 1.20$ and a truncation level of $l = 21$ eigenfunctions. A primary difference between the observational modes and CCSM3 modes is the variables used for the eigenfunction computation. We find that computing SIC-SST-SLP eigenfunctions from the observational datasets yields temporal modes which are significantly noisier (more high-frequency power) than the corresponding modes from CCSM3. This corruption occurs due to the inclusion of the SLP data in the eigenfunction computation. We find that the eigenfunctions are substantially cleaner when computed using SIC and SST, and we use this as the base case for this chapter. On the other hand, the CCSM3 results are insensitive to the inclusion of SLP, with SIC-SST-SLP and SIC-SST eigenfunctions yielding very similar modes and conclusions regarding sea-ice reemergence. We obtain SLP observational modes by projecting

the SLP data onto the SIC-SST eigenfunctions and performing an SVD of the resulting operator. Note that the observational SLP data is roughly 4 times finer spatial resolution than the CCSM3 SLP data. This discrepancy in resolution may explain the corruption in observational modes compared with CCSM3 modes. An NLSA kernel that incorporates an initial spatial smoothing of the input data (making them comparable to the T42 resolution of the CCSM3 data) could alleviate these issues, but we elected not to carry out these calculations since we are able to identify reemergence families, ahead, using SIC and SST only as inputs to the kernel.

The observational temporal modes have a similar character to those obtained from CCSM3. For each variable, we find periodic, low-frequency, and intermittent modes, and in many cases the low-frequency modes act as modulating envelopes for the intermittent modes. The temporal modes for SIC, SST, and SLP are shown in Figs. 4.8, 4.9, and 4.10.

Next, we provide a brief description of the spatiotemporal modes that will be discussed later in the paper. Movies 10 and 11 of the supplementary material provide a more revealing spatiotemporal evolution of these modes and others. L_1^{SIC} (Fig. 4.7j) closely resembles the leading EOF of winter Arctic sea ice reported by Deser et al. (2000). In its positive phase, L_1^{SIC} has positive sea-ice anomalies in the Labrador and Bering seas and negative anomalies in the Greenland, Barents-Kara, and Okhotsk Seas. This mode has a maximum pattern correlation of 0.88 with EOF 1 of Arctic sea ice from HadISST. L_1^{SST} (Fig. 4.7k) is most similar to EOF 2 of Arctic SST, with a maximum pattern correlation of 0.70. In positive phase, this mode has positive anomalies in the Labrador Sea and subpolar gyre region, negative anomalies in the Barents-Kara Seas and positive anomalies in the

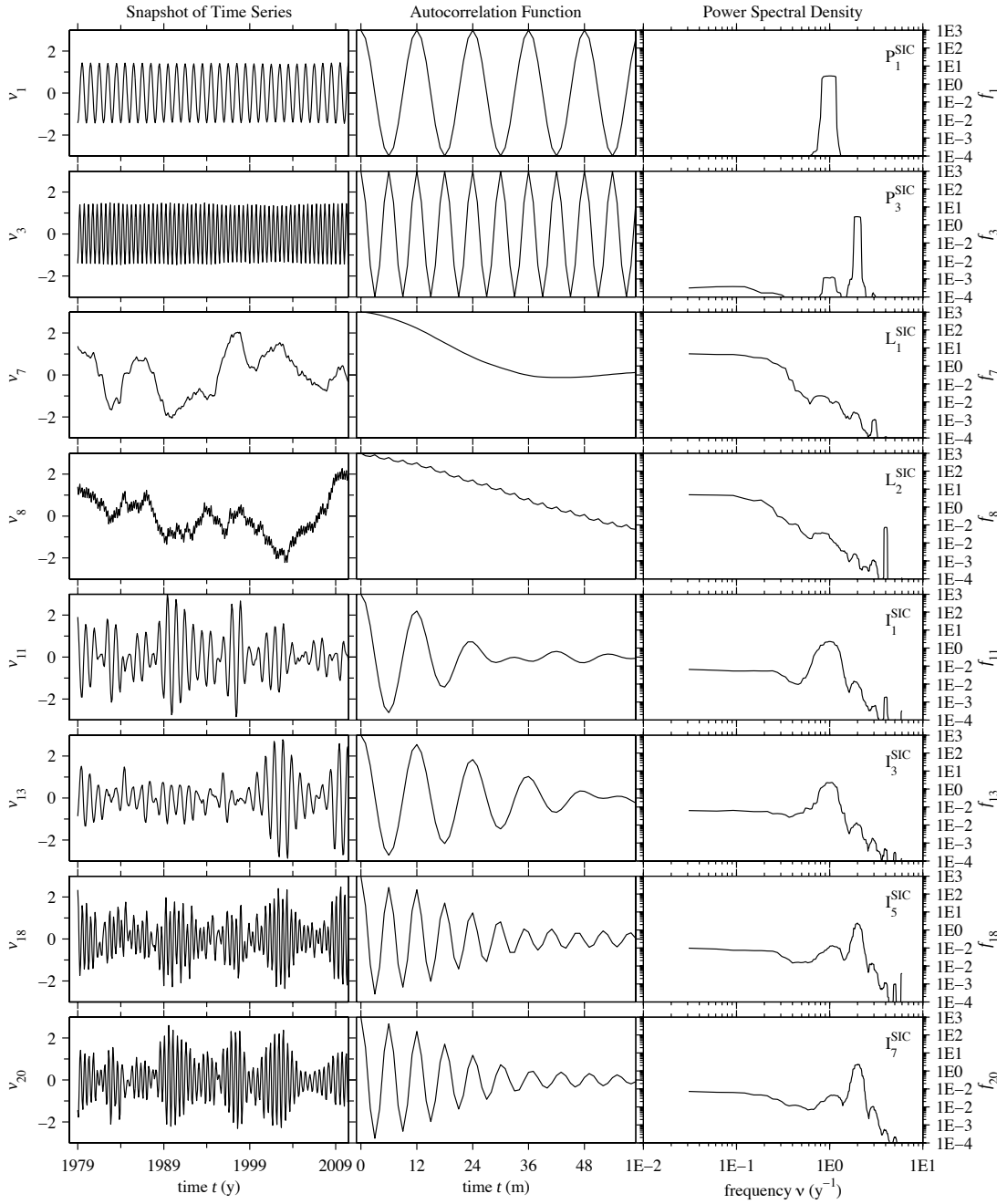

Figure 4.8: Snapshots of the time series, power spectral density, and autocorrelation functions for the HadISST SIC PCs (v_k) from coupled NLSA. Shown here are the annual periodic (P_1^{SIC}) and semiannual periodic (P_3^{SIC}) modes, low-frequency modes (L_1^{SIC} and L_2^{SIC}), annual intermittent modes (I_1^{SIC} and I_3^{SIC}), and semiannual intermittent modes (I_5^{SIC} and I_7^{SIC}). The autocorrelation vertical scale is [-1,1].

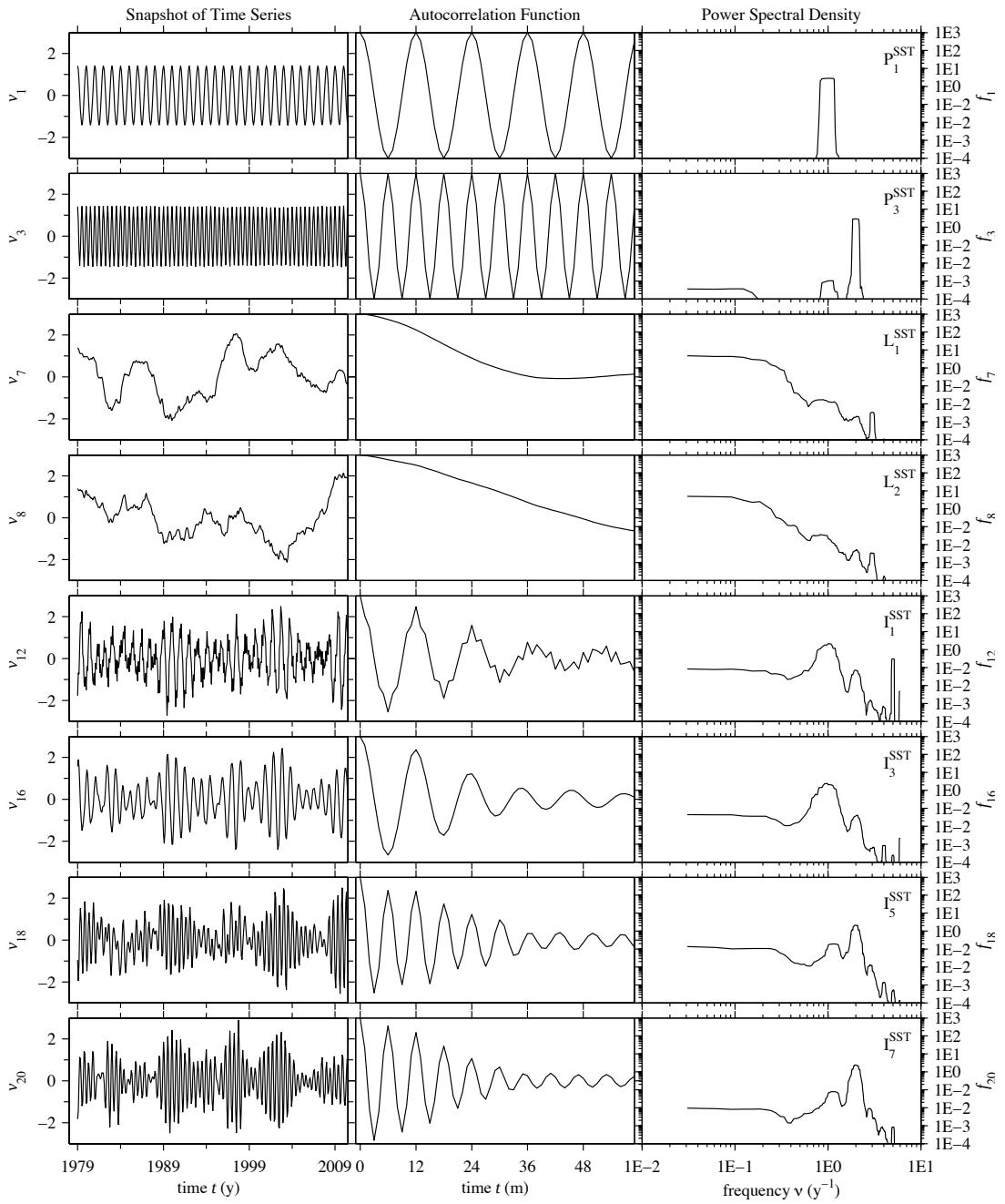

Figure 4.9: Snapshots of the time series, power spectral density, and autocorrelation functions for the HadISST SST PCs (v_k) from coupled NLSA. Shown here are the annual periodic (P_1^{SST}) and semiannual periodic (P_3^{SST}) modes, low-frequency modes (L_1^{SST} and L_2^{SST}), annual intermittent modes (I_1^{SST} and I_3^{SST}), and semiannual intermittent modes (I_5^{SST} and I_7^{SST}). The autocorrelation vertical scale is [-1,1].

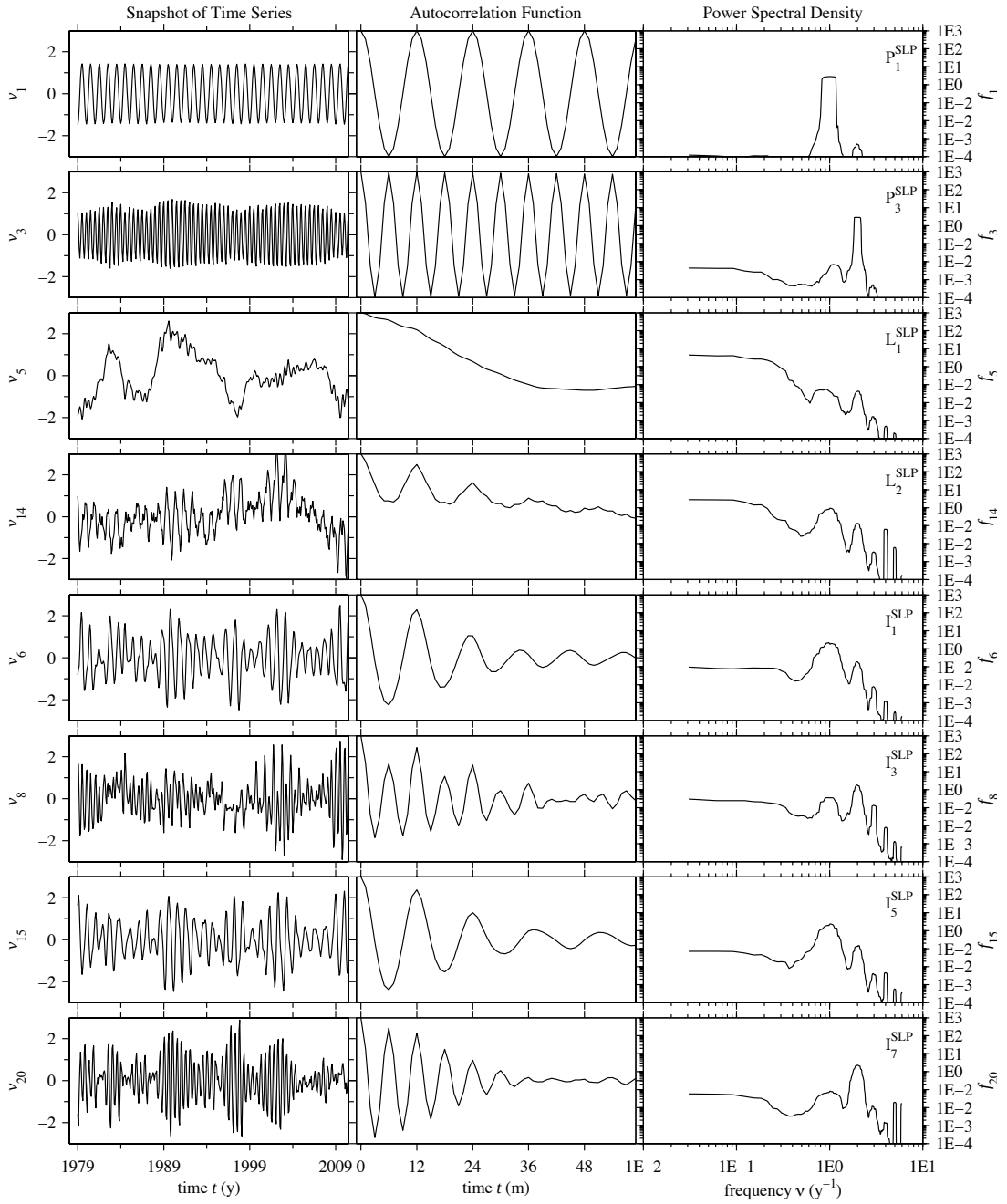

Figure 4.10: Snapshots of the time series, power spectral density, and autocorrelation functions for the Era-Interim SLP PCs (v_k) from coupled NLSA. Shown here are the annual periodic (P_1^{SLP}) and semiannual periodic (P_3^{SLP}) modes, low-frequency modes (L_1^{SLP} and L_2^{SLP}), annual intermittent modes (I_1^{SLP} and I_3^{SLP}), and semiannual intermittent modes (I_5^{SLP} and I_7^{SLP}). The autocorrelation vertical scale is [-1,1].

Bering Sea. L_1^{SLP} (Fig. 4.7l) strongly resembles the annular structure of the AO. Computing EOFs of ERA-Interim SLP north of 20°N, we find a maximum pattern correlation of 0.97 with EOF 1, the AO pattern. Similar to the CCSM3 results, the intermittent modes are generally associated with a low-frequency mode, are active in the same parts of the domain as this low-frequency mode, and display finer spatial structure.

One feature which is conspicuously absent from the observational SLP modes is a DA-like mode. Other fields, such as 850mb geopotential height and surface winds, and smaller domains were tested, but a low-frequency DA mode analogous to the CCSM3 results was not found. Certain modes obtained were quite transient, and resembled the DA pattern at certain snapshots in time, but not persistently.

4.4.3 Interpretation of low-frequency SLP modes

The low-frequency SLP modes have spatial patterns that closely resemble the familiar spatial patterns obtained via EOF analysis. However, their temporal behavior differs substantially. The low-frequency NLSA temporal modes have significant one-year autocorrelation and carry most of their power at frequencies below 1 yr^{-1}. This lies in sharp contrast to the PCs obtained via EOF analysis, which have a nearly white power spectrum and decorrelate very rapidly, losing all memory after 1-2 months. Despite these extremely different temporal characteristics, there is natural connection between the two: the low-frequency NLSA modes closely resemble a low-pass filtered version of the noisy PCs from EOF analysis.

This is illustrated in Fig. 4.11, which shows temporal behavior for L_1^{SLP}, the leading low-frequency NLSA mode from CCSM3, $\mathrm{PC}_1^{\mathrm{SLP}}$, the principal component corresponding to the leading EOF of SLP, and $\langle \mathrm{PC}_1^{\mathrm{SLP}} \rangle$, a low-pass filtered version

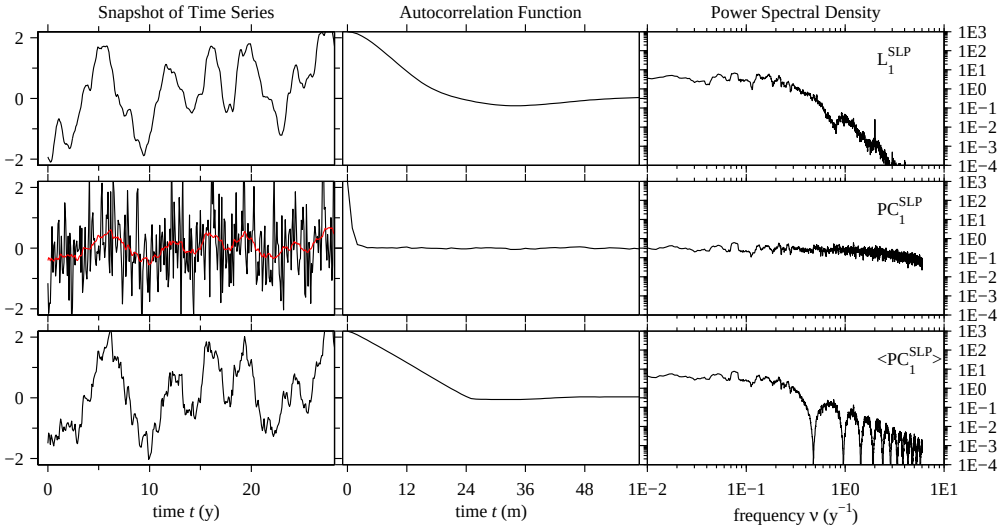

Figure 4.11: Snapshots of the time series, power spectral density, and autocorrelation functions for L_1^{SLP}, the leading low-frequency NLSA mode from CCSM3, $\mathrm{PC}_1^{\mathrm{SLP}}$, the principal component corresponding to the leading EOF of SLP, and $\langle \mathrm{PC}_1^{\mathrm{SLP}} \rangle$, a low-pass filtered version of $\mathrm{PC}_1^{\mathrm{SLP}}$, computed by taking a 24 month running mean. The red curve is $\langle \mathrm{PC}_1^{\mathrm{SLP}} \rangle$ plotted on top of $\mathrm{PC}_1^{\mathrm{SLP}}$. Note that the $\langle \mathrm{PC}_1^{\mathrm{SLP}} \rangle$ time series shown in the third row has been normalized to have a standard deviation of 1.

of $\mathrm{PC}_1^{\mathrm{SLP}}$, computed by taking a 24 month running mean. L_1^{SLP} has a relatively low correlation of 0.31 with $\mathrm{PC}_1^{\mathrm{SLP}}$, but a significantly higher correlation of 0.80 with the low-pass filtered PC, $\langle \mathrm{PC}_1^{\mathrm{SLP}} \rangle$. L_1^{SLP} and $\langle \mathrm{PC}_1^{\mathrm{SLP}} \rangle$ share qualitatively similar autocorrelation functions and power spectra, which are very different from the rapidly decaying autocorrelation and nearly white power spectrum of $\mathrm{PC}_1^{\mathrm{SLP}}$. These results suggest a natural interpretation of the low-frequency NLSA modes as low-pass filtered versions of the PCs from EOF analysis, which emphasize variability on interannual to decadal timescales and filter out higher-frequency variability. It is important to note that the low-frequency NLSA modes have weak sensitivity to the lag-embedding window Δt (as long as $\Delta t \geqslant 12$; see section 3). Also, a univariate NLSA analysis with only SLP was performed, and similar low-frequency

modes were recovered. This suggests that these low-frequency patterns describe an intrinsic component of SLP variability, which in this case can be reproduced by an ad-hoc running averaging of the data.

The observational SLP modes also display a similar correspondence, with a correlation of 0.83 between $\langle \mathrm{PC}_1^{\mathrm{SLP}} \rangle$ and L_1^{SLP}. This high correlation indicates that the SIC-SST eigenfunctions used for the observational data are able to capture important variability in the raw SLP data.

4.5 Arctic sea-ice reemergence in models and observations

Sea-ice reemergence is a time-lagged correlation phenomenon. SIC anomalies decorrelate over a 3-6 month timescale, however, at some time lag in the future, an increase in correlation occurs. Sea-ice reemergence is observed in two forms: a spring-fall reemergence, in which spring anomalies are reproduced the following fall, and a fall-spring reemergence, in which fall anomalies are reproduced the following spring. Both forms are observed in CCSM3 model output and HadISST observations, with the spring-fall reemergence being the significantly stronger signal in both cases.

We study sea-ice reemergence via the time-lagged pattern correlation methodology of Chapter 3. For each month of the year, pattern correlations are computed between the SIC anomaly field of the given month and the SIC field at lags of 0 to 23 months into the future. This is done for all (month, month+lag) pairs in the time series, and we report the average of these correlation values. Note that the pattern correlations are performed on anomalies from the seasonal cycle, are

area-weighted, and are uncentered (global mean has not been subtracted from the anomaly field). This differs from the approach of Blanchard-Wrigglesworth et al. (2011a), where the lagged correlations were performed using a time series of total sea-ice area. Performing correlations using the full SIC field, as opposed to its total area, allows for inclusion of the spatial distribution of sea ice. The pattern correlation approach is able to detect opposite-signed anomaly features, such as sea-ice dipoles, which would be integrated away in the total area approach. It also enforces a notion of locality, since anomalies must be spatially coincident in order to yield a significant pattern correlation. This ensures that a reported sea-ice reemergence signal represents recurrent anomalies at the same spatial location.

In this paper, we focus on the regions defined in Fig. 4.1: a pan-Arctic domain (0° – 360° and 45°N – 90°N), the Barents and Kara Seas (30°E – 90°E and 65°N – 80°N), the Labrador Sea and Baffin Bay (70°W – 40°W and 45°N – 80°N), the Greenland Sea (40°W – 0°E and 55°N – 80°N), the Bering Sea (165°E – 160°W and 55°N – 65°N), and the Sea of Okhotsk (135°E – 165°E and 45°N – 65°N).

4.5.1 Regional sea-ice reemergence in models and observations

We begin with a regional study of sea-ice reemergence using raw SIC data from HadISST observations and CCSM3 output, the results of which are shown in Fig. 4.12. This figure shows time-lagged pattern correlations, computed for all initial months and lags of 0 to 23 months. All correlations plotted in color are greater than 0.1 and are significant at the 95% level, based on a t-distribution statistic, which tests for the statistical significance of the time-mean pattern correlation values against a null hypothesis that there is no correlation.

Over a pan-Arctic domain, in both the model and observations, we observe a clear "summer limb" of positive correlations corresponding to sea-ice anomalies that originate in the melt season (March-August) and reemerge in the growth season (Fig. 4.12a,b). The "winter limb" of fall-spring reemergence, corresponding to anomalies originating in September-February, is weak over the Arctic domain, except for a small hint of the limb in the CCSM3 data. An interesting consequence of the time-lagged pattern correlation approach is the striking similarity of pan-Arctic lagged correlations in CCSM3 and observations. This lies in contrast to the total area lagged correlation methodology of previous studies, which reveal a clearly enhanced reemergence signal in the model relative to observations (Blanchard-Wrigglesworth et al., 2011a; Day et al., 2014b). This indicates that, despite differences in memory of total sea-ice area anomalies, the model and observations are quite similar in their memory of sea-ice spatial patterns.

The pan-Arctic reemergence signal is similar in the model and observations, however a regional analysis reveals significant differences between the two. Both CCSM3 and HadISST have strong summer limb signals in the Barents-Kara domain (Fig. 4.12g,h) and the Greenland Sea (Fig. 4.12k,l). The CCSM3 data also exhibits a winter limb in the Barents-Kara domain, which is not significant in observations. A striking difference is found in the Labrador Sea, with a strong summer limb and a significant winter limb in observations, neither of which are found in the model (Fig. 4.12i,j). Conversely, the strong summer limbs in the Bering and Okhotsk Seas found in the model data are absent in the observations (Fig. 4.12c,d,e,f). Note that the winter limb signal in the Bering and Okhotsk Seas should not be over-interpreted, as these domains are essentially sea-ice free during the summer and early fall. Therefore, the North Pacific winter limb lagged

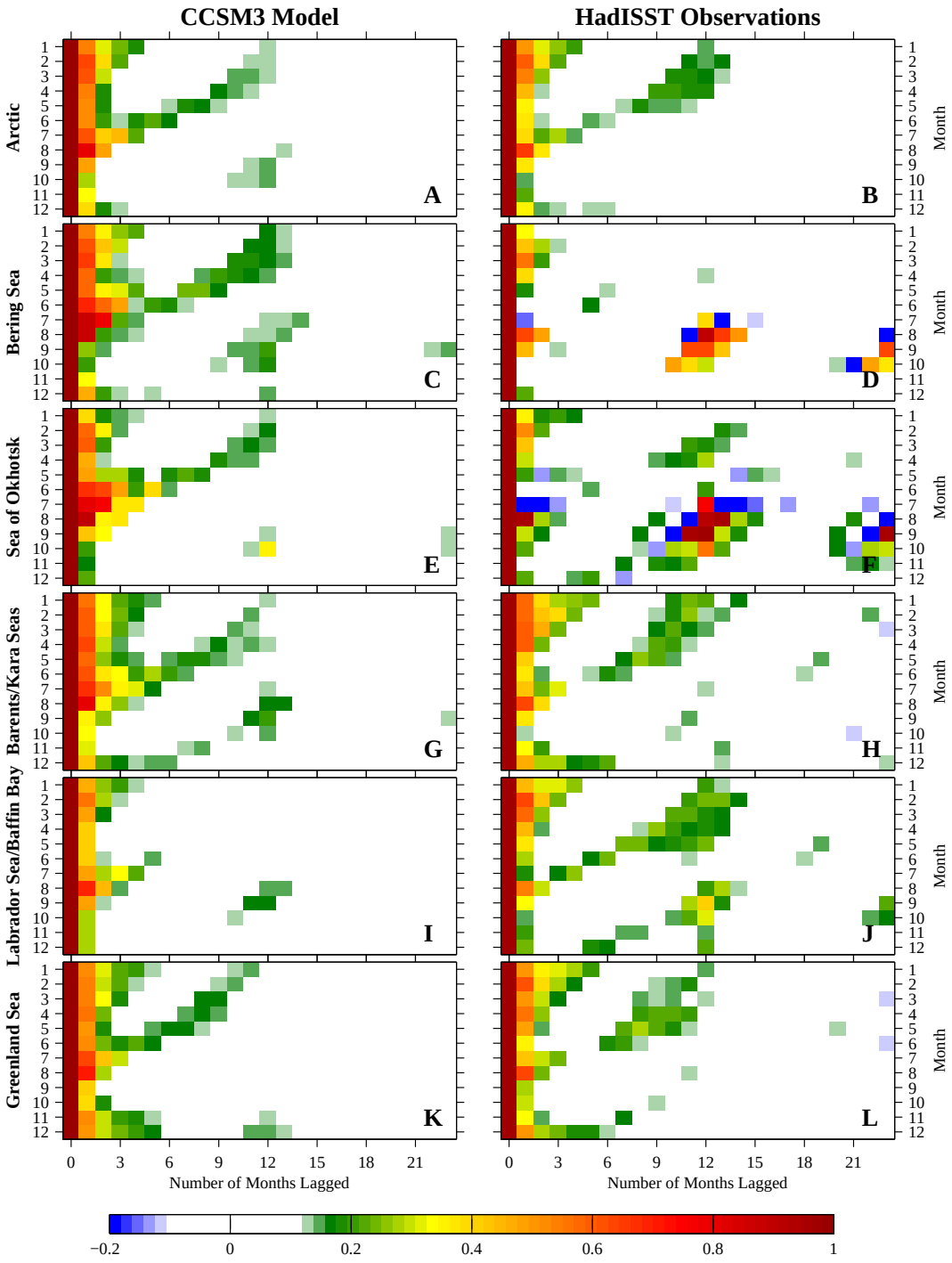

Figure 4.12: Time-lagged pattern correlations of Arctic sea ice in different regions. The left column shows results from CCSM3 model output, and the right column shows results from HadISST observations. All colored boxes are significant at the 95% level, based on a t-test.

correlations are performed using an extremely low-variance signal, and are not robust.

4.5.2 Sea-ice reemergence revealed via coupled NLSA

Given the non-trivial lagged correlation structures in the CCSM3 and HadISST sea-ice datasets, we seek a low-dimensional representation of sea-ice reemergence via the coupled NLSA modes obtained in Section 4. We aim to answer two main questions: (1) Can the reemergence signal of the raw data be efficiently reproduced by low-dimensional families of modes? (2) Can these mode families reveal possible mechanisms for Arctic sea-ice reemergence? To answer the former, we perform time-lagged pattern correlations using small subsets of reconstructed spatiotemporal fields from coupled NLSA. Our approach here is to first construct families of SIC modes, and then to augment these families with SST and SLP modes, based on correlations.

CCSM3 Reemergence Families

Based on the associations between low-frequency and intermittent modes identified in section 4a.1, we construct two families of SIC modes, each consisting of a low-frequency mode and annual and semiannual intermittent modes. These families, which we refer to as $\mathcal{F}_1^M$ and $\mathcal{F}_2^M$, are able to qualitatively reproduce the reemergence signal of the raw data. They are given by $\mathcal{F}_1^M = \{L_1^{\mathrm{SIC}}, I_1^{\mathrm{SIC}}, I_2^{\mathrm{SIC}},$-$I_7^{\mathrm{SIC}}, I_8^{\mathrm{SIC}}\}$ and $\mathcal{F}_2^M = \{L_2^{\mathrm{SIC}}, I_3^{\mathrm{SIC}}, I_4^{\mathrm{SIC}}, I_9^{\mathrm{SIC}}, I_{10}^{\mathrm{SIC}}, I_{11}^{\mathrm{SIC}}\}$. Here, the M superscript indicates that these families come from model output. Each family is particularly active in the Barents-Kara, Bering, and Labrador Seas, but shares different phase relationships between the different regions. Within each family, the low-frequency

and intermittent modes are closely related, in the sense that the low-frequency mode provides the modulating envelope for the intermittent modes. This means that all modes in a given family tend to be active or inactive at the same times. Note that similar envelope associations were observed in the reemergence families identified in Chapter 3, suggesting that this approach may be useful in a broader context. Many other mode subsets were tested, but were unable to reproduce the lagged correlation structure as effectively as these families, likely because they lack the envelope relationships that characterize the families. Moreover, $\mathcal{F}_1^M$ and $\mathcal{F}_2^M$ appear to be the minimal mode subsets, as smaller sets are unable to qualitatively reproduce the reemergence signal.

In Fig. 4.13d, we show time-lagged pattern correlations computed over the Arctic domain using NLSA family $\mathcal{F}_1^M$. Comparing with the time-lagged pattern correlation structure of the raw data, shown in Fig. 4.13a, we observe qualitatively similar features. The $\mathcal{F}_1^M$ correlations have a clear summer limb structure, with correlations that decay to near zero over the summer months and reemerge the following fall. They also have a slightly weaker winter limb, which may correspond to the weaker fall-spring reemergence seen in the raw data. The $\mathcal{F}_1^M$ correlations are substantially higher than the raw data correlations because the family's activity is primarily governed by L_1^{SIC}, which has a decorrelation time of 3 years.

This NLSA family has a qualitatively similar correlation structure to the raw data, yet it is natural to ask whether this family is capturing the portion of the signal responsible for the summer limb in the raw data. As a method for addressing this question, we compute time-lagged cross correlations between the raw data and the NLSA subspaces, shown in Fig. 4.13b and 4.13c. To explain panels b and c, we introduce $LC(A, B)$, a function that computes time-lagged pattern correlations,

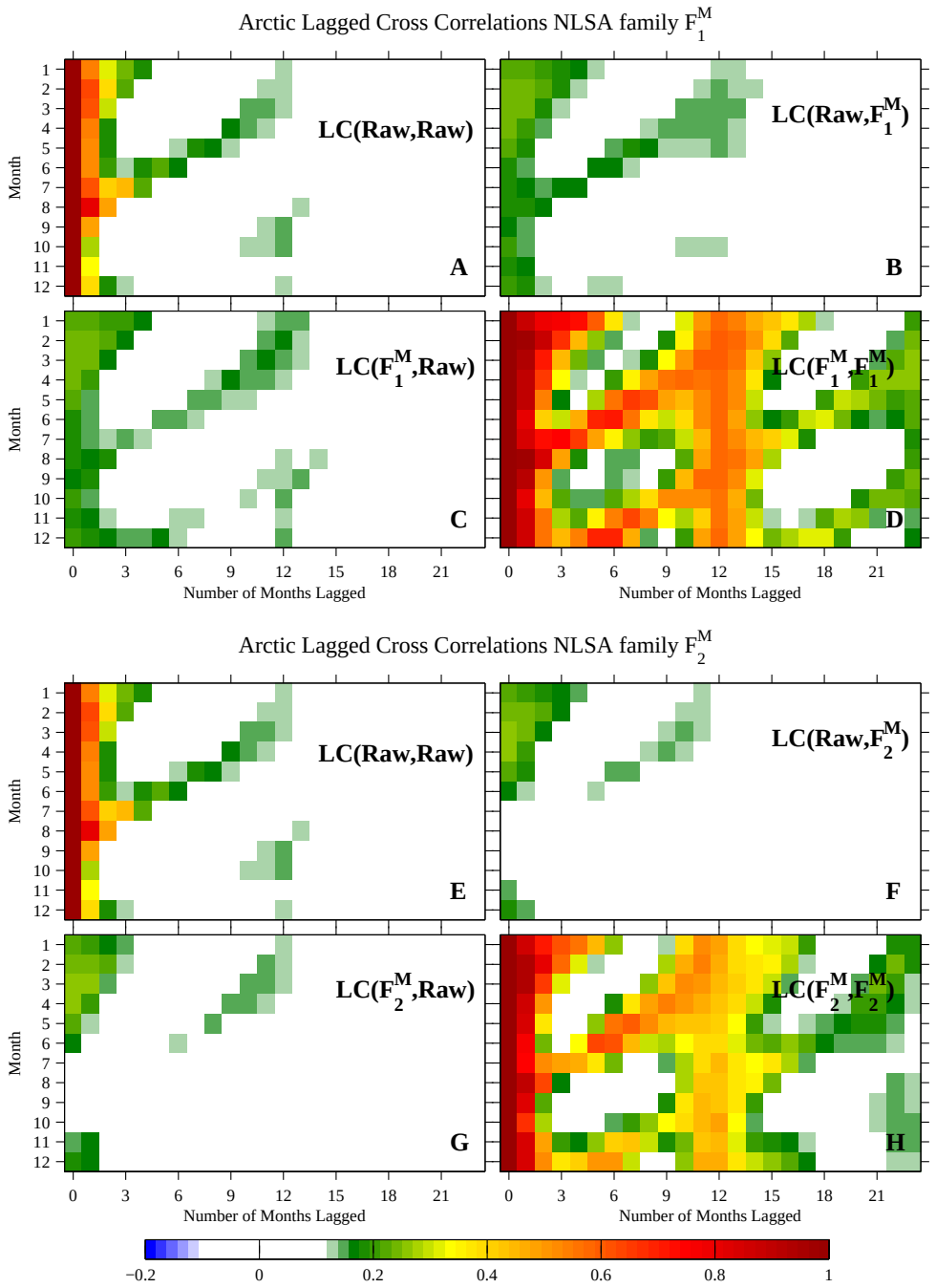

Figure 4.13: Time lagged pattern correlations of sea ice computed over the Arctic domain, using NLSA Familes $\mathcal{F}_1^M$ and $\mathcal{F}_2^M$. Panels (A) and (D) show correlations of the raw data and $\mathcal{F}_1^M$, respectively. Panels (B) and (C) show cross-correlations of $\mathcal{F}_1^M$ and the raw data, with the NLSA data lagging and leading, respectively. The same correlations for $\mathcal{F}_2^M$ are shown in panels (E)-(H). All colored boxes are significant at the 95% level.

with the dataset B lagging A. Using this notation, Fig. 4.13a shows $LC(\text{Raw}, \text{Raw})$ and Fig. 4.13d shows $LC(\mathcal{F}_1^M, \mathcal{F}_1^M)$. In Fig. 4.13b and 4.13c, we plot $LC(\text{Raw}, \mathcal{F}_1^M)$ and $LC(\mathcal{F}_1^M, \text{Raw})$, respectively.

If the reemergence signal of $\mathcal{F}_1^M$ is not representative of the signal in the raw data, one would expect these cross correlations to be small. However, we observe strong summer limbs in panels 4.13b and 4.13c, similar to the correlation structure of the raw data. The fact that these panels are similar to panel 4.13a, indicates that family $\mathcal{F}_1^M$ is capturing the portion of the data responsible for the sea-ice reemergence signal.

In Fig. 4.13e-h, we plot the same quantities as Fig. 4.13a-d, but for Family $\mathcal{F}_2^M$. $LC(\mathcal{F}_2^M, \mathcal{F}_2^M)$ also has a strong summer limb and a weaker winter limb, but each of these limbs is weaker than their respective counterparts in $LC(\mathcal{F}_1^M, \mathcal{F}_1^M)$. Also, $LC(\text{Raw}, \mathcal{F}_2^M)$ and $LC(\mathcal{F}_2^M, \text{Raw})$, plotted in Fig. 4.13f and 4.13g, shows partial summer limbs, but these correlations are weaker than the reemergence signal of the raw data. This indicates that family $\mathcal{F}_2^M$ is capturing some of the reemergence signal, but not as significant a portion as family $\mathcal{F}_1^M$.

HadISST Reemergence Families

The observational modes also admit a mode family which is able to reproduce the reemergence signal of the raw HadISST data. This family is given by $\mathcal{F}_1^O = \{L_1^{\text{SIC}}, I_1^{\text{SIC}}, I_2^{\text{SIC}}, I_5^{\text{SIC}}, I_6^{\text{SIC}}\}$, where the O indicates observational data. There is no clear second family which has non-trivial cross-correlations with the raw observational data. In Fig. 4.14 we plot time-lagged cross correlations for $\mathcal{F}_1^O$. $LC(\mathcal{F}_1^O, \mathcal{F}_1^O)$ has a clear summer limb and a weaker winter limb. We also find a strong summer limb structure in $LC(\text{Raw}, \mathcal{F}_1^O)$ and $LC(\mathcal{F}_1^O, \text{Raw})$, except for

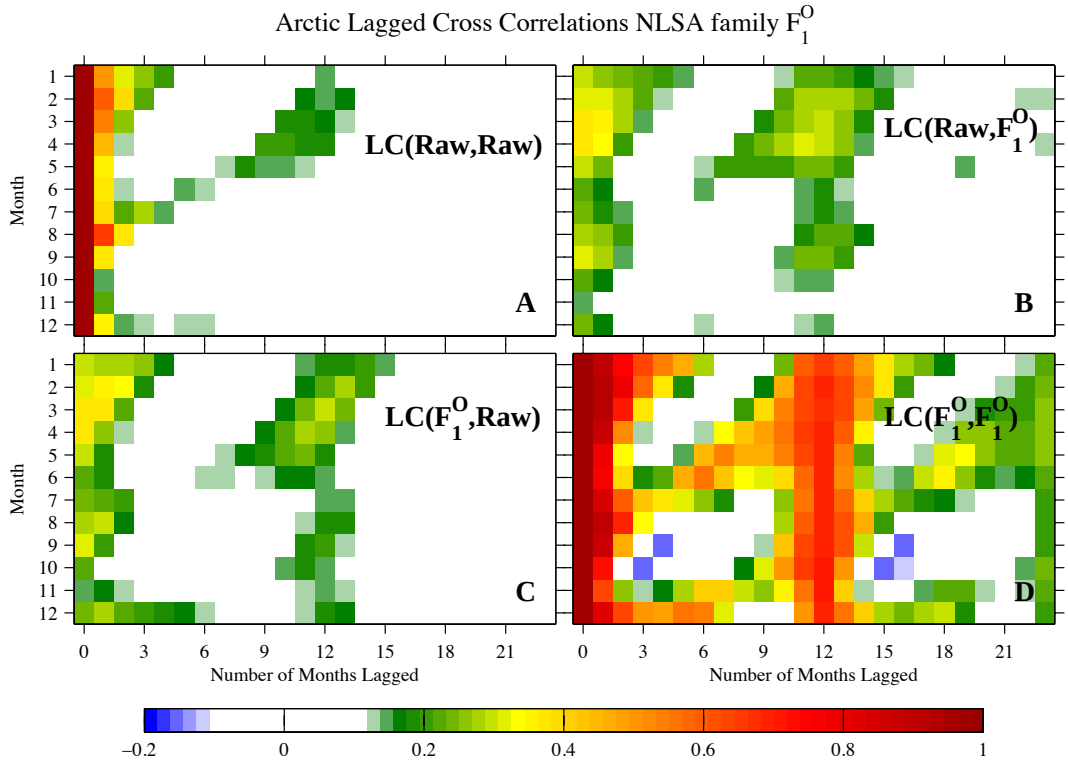

Figure 4.14: Time lagged pattern correlations of sea ice computed over the Arctic domain, using HadISST Family $\mathcal{F}_1^O$. Panels (A) and (D) show correlations of the raw data and NLSA Family $\mathcal{F}_1^O$, respectively. Panels (B) and (C) show cross-correlations of $\mathcal{F}_1^O$ and the raw data, with the NLSA data lagging and leading, respectively. All colored boxes are significant at the 95% level.

a small gap in the limb for anomalies beginning in July. This indicates that the family $\mathcal{F}_1^O$ is capturing a substantial portion of the reemergence signal in the raw data.

4.5.3 Variance explained by reemergence families

Another way to test the effectiveness of the families in capturing the reemergence signal is to directly subtract the families from the raw sea-ice data, and compute time-lagged pattern correlations on the resulting dataset. Fig. 5.3c shows

$LC(\text{Raw} - \mathcal{F}_1^M - \mathcal{F}_2^M, \text{Raw} - \mathcal{F}_1^M - \mathcal{F}_2^M)$, and Fig. 5.3d shows $LC(\text{Raw} - \mathcal{F}_1^O, \text{Raw} - \mathcal{F}_1^O)$. Each of these has a clearly reduced summer limb relative to $LC(\text{Raw}, \text{Raw})$, which are shown in Fig. 5.3a for CCSM3 and Fig. 5.3b for HadISST. This demonstrates that the reemergence families are capturing a substantial portion of the reemergence signal. In terms of total sea-ice area anomalies, family $\mathcal{F}_1^M$ explains 41%, 25%, and 8% of the variance in the Bering, Barents-Kara, and Labrador Seas, respectively. Similarly, $\mathcal{F}_2^M$ explains 18%, 1%, and 14% of the variance, and $\mathcal{F}_1^O$ explains 7%, 30%, and 18% of the variance, in these respective regions.

The variance explained by these families is lower if one considers the full (non-integrated) sea-ice anomaly field. Over the full Arctic domain family $\mathcal{F}_1^M$ explains 5% of the variance, $\mathcal{F}_2^M$ explains 3% and $\mathcal{F}_1^O$ explains 7%. While these values seem somewhat low, it is interesting to note that the leading two EOFs from CCSM3 capture 7% and 6% of the variance, respectively. These values are lower than those typically reported in EOF studies for three reasons: (1) the spatial domain is large; (2) there has been no temporal smoothing or averaging performed; and (3) the spatial resolution is relatively fine. For example, the leading EOF of Deser et al. (2000) captures 35% of the sea-ice variance in the Arctic, but this is based on a time series of winter mean sea-ice anomalies. This temporal averaging substantially smooths the data, and the leading EOF captures variance more efficiently in this time-filtered dataset. By contrast, the leading 10 EOFs of CCSM3 Arctic sea ice capture 38% of the variance.

The comparison with SSA, a variance greedy algorithm, is also illuminating. The leading two SSA modes capture 2.5% and 2% of the variance, respectively, and the leading 10 non-periodic SSA modes capture 14% of the variance. By comparison, the leading 10 non-periodic NLSA modes capture 10% of the variance,

which is modestly less than SSA. The main reason for this discrepancy is that the intermittent modes of NLSA carry less variance than low-frequency modes. Despite being low-variance, these intermittent modes are crucial components of the reemergence families and illustrate an important point: low-variance modes can play an important role in explaining dynamical phenomena.

4.5.4 Temporal variability of sea-ice reemergence

To this point, all reported lagged correlations have been time-mean values, computed over the full time series. Next, we consider the time-dependent aspects of sea-ice reemergence. Fig. 5.3e shows lagged correlations of the raw CCSM3 sea-ice data, conditional on the low-frequency modes of $\mathcal{F}_1^M$ or $\mathcal{F}_2^M$, L_1^{SIC} and L_2^{SIC}, being active. Specifically, we condition on all times for which $|L_1^{\mathrm{SIC}}(t)| > 2$ or $|L_2^{\mathrm{SIC}}(t)| > 2$ (which corresponds to 11% of the data). Similarly, Fig. 5.3f shows lagged correlations of the raw HadISST data conditional on the low-frequency mode of $\mathcal{F}_1^O$ being active ($|L_1^{\mathrm{SIC}}(t)| > 1.5$, which corresponds to 14% of the data). We observe a clearly enhanced reemergence signal (both summer and winter limbs) during times when these modes are active. Figs. 5.3g and 5.3h show lagged correlations conditional on these modes being inactive ($|L_1^{\mathrm{SIC}}(t)| < 1$ and $|L_2^{\mathrm{SIC}}(t)| < 1$ for CCSM3 and $|L_1^{\mathrm{SIC}}(t)| < 1$ for HadISST). This corresponds to 45% and 59% of the data, respectively. In both cases, particularly with CCSM3, we observe a diminished reemergence signal. These results indicate that reemergence events have significant temporal variability, characterized by regimes of quiescence and other regimes of intense activity. Another notable feature is the robust initial decay of correlation for lags of 0–3 months. The most significant differences between Figs. 5.3e,f and Figs. 5.3g,h occur at lags greater than 3 months, indicating that

reemergence events display more temporal variability than the initial decay of persistence. Note that due to the shortness of observational record, the conditional correlations from HadISST are less robust than those from CCSM3.

In CCSM3, about half of the record is characterized by a very weak reemergence signal (Fig. 5.3g), whereas other times exhibit strong reemergence (Fig. 5.3e). This may have important implications for sea-ice predictability, since predictability resulting from reemergence will have a strong temporal dependence, dependent on the strength of the reemergence signal at a given time. The results here also demonstrate the efficacy of certain low-frequency NLSA modes as predictors for the strength of reemergence events. Therefore, these modes could be a valuable addition to statistical sea-ice forecast models.

As another method to test the temporal variability of reemergence events, we measure the strength of the reemergence signal as a function of time. We define the reemergence strength as the sum of correlation values along the summer limb, compute this quantity for each year of the time series, and create a probability density function (PDF). The PDF (not shown here) is close to Gaussian, with a slight skew towards large reemergence events. If we let μ be the mean of the PDF, we find that 23% of reemergence events are less that 0.5μ and 23% of events are greater than 1.5μ. This spread in event distribution demonstrates that reemergence strength fluctuates strongly in time.

This temporal characterization of Arctic reemergence events is a new result of this study, which was inaccessible in previous studies of reemergence based on time-lagged total area correlations. In the time-lagged pattern correlation methodology, correlations are performed space, rather than time, which allows for the temporal variations of these correlations to be studied. The mode families also allow for an

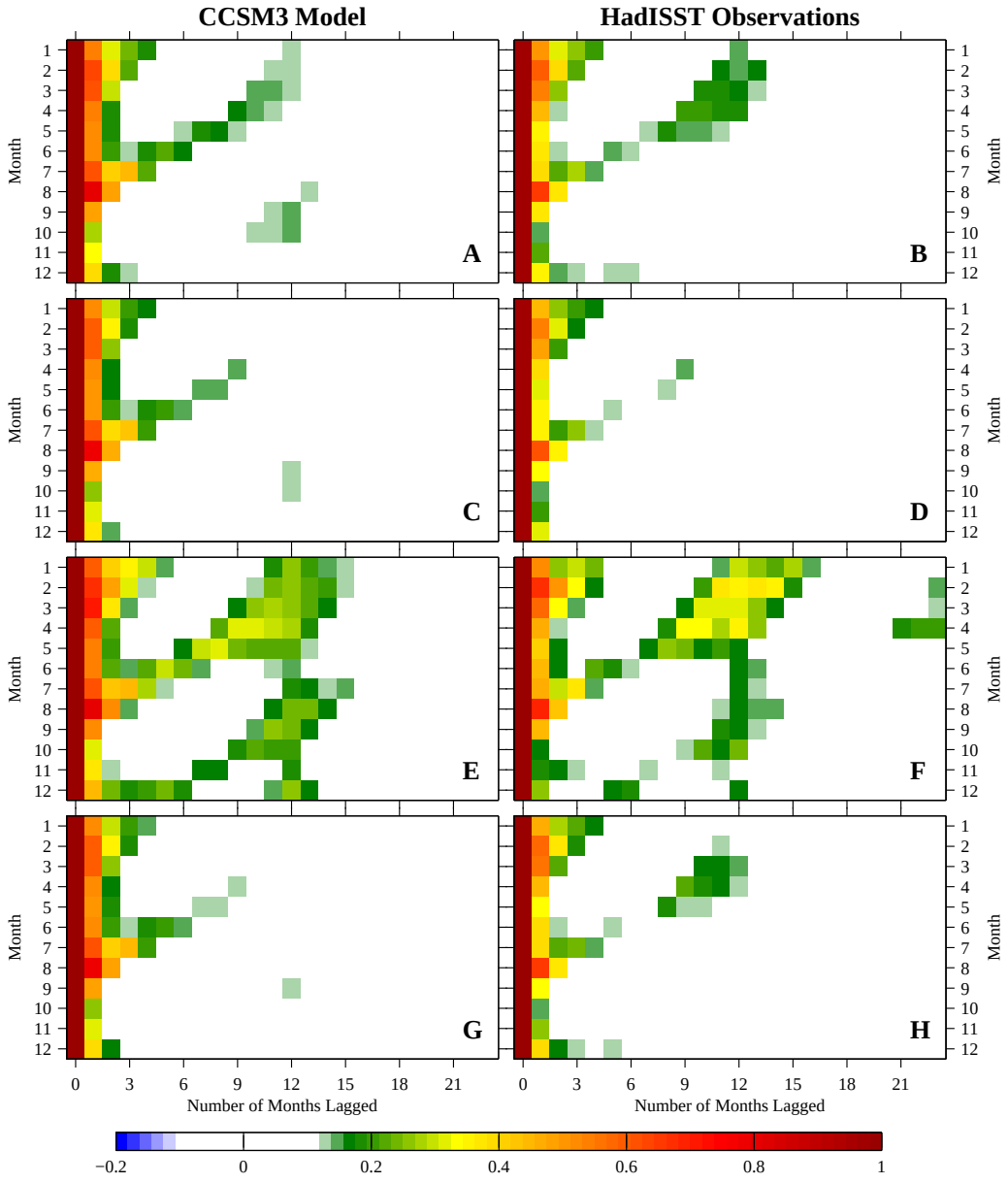

Figure 4.15: Time lagged patterns correlations of sea ice computed over the Arctic domain. Lagged correlations for CCSM3 data are shown for: (A) the raw data, (C) Raw $-\mathcal{F}_1^M - \mathcal{F}_2^M$, (E) conditional on $|L_1^{\text{SIC}}(t)| > 2$ or $|L_2^{\text{SIC}}(t)| > 2$ (which corresponds to 11% of the data) and (G) conditional on $|L_1^{\text{SIC}}(t)| < 1$ and $|L_2^{\text{SIC}}(t)| < 1$ (45% of the data). HadISST lagged correlations are shown for: (B) the raw data, (D) Raw $-\mathcal{F}_1^O$, (F) conditional on $|L_1^{\text{SIC}}(t)| > 1.5$ (which corresponds to 14% of the data) and (H) conditional on $|L_1^{\text{SIC}}(t)| < 1$ (59% of the data).

investigation of the temporal variability of reemergence events and mechanisms, and this will be returned to in section 6c, ahead.

4.5.5 SIC-SST-SLP reemergence families

We have identified families of coupled NLSA SIC modes which are able to reproduce the reemergence signal of the raw SIC data. Next, we focus on the spatiotemporal evolution of these families, and their associated SST and SLP patterns. As noted earlier, there are strong correlations between the temporal modes of SIC, SST, and SLP. We use this fact to augment the families $\mathcal{F}_1^M$, $\mathcal{F}_2^M$, and $\mathcal{F}_1^O$ with associated SST and SLP modes.

The low-frequency mode of $\mathcal{F}_1^M$ is L_1^{SIC}. Performing correlations between this mode and all low-frequency SST and SLP PCs, we find maximum correlations of -0.99 with L_1^{SST} and -0.69 with L_3^{SLP}. Similarly, for the L_2^{SIC} mode of $\mathcal{F}_2^M$, we find maximum correlations of -0.93 with L_2^{SST} and 0.64 with L_1^{SLP}. For the observational family, $\mathcal{F}_1^O$, we find that L_1^{SIC} has maximum correlations of 0.998 with L_1^{SST} and -0.81 with L_1^{SLP}. Note that the low-frequency mode correlations are higher between SIC and SST than between SIC and SLP, indicating that the temporal co-variability between SIC and SST is somewhat stronger.

Each family consists of a low-frequency mode and associated annual and semi-annual intermittent modes. In order to form the augmented families, we identify the intermittent modes associated with the low-frequency SST and SLP modes identified above. Based on the envelope correlations shown in Fig. 4.6, we define the following augmented families:

$$\mathcal{F}_1^M = \{L_1^{\mathrm{SIC}}, I_{\{1,2,7,8\}}^{\mathrm{SIC}}, L_1^{\mathrm{SST}}, I_{\{2,3,8,9\}}^{\mathrm{SST}}, L_3^{\mathrm{SLP}}, I_{\{7,8\}}^{\mathrm{SLP}}\},$$

$$\mathcal{F}_2^M = \{L_2^{\mathrm{SIC}}, I_{\{3,4,9,10,11\}}^{\mathrm{SIC}}, L_2^{\mathrm{SST}}, I_{\{5,6,11\}}^{\mathrm{SST}}, L_1^{\mathrm{SLP}}, I_{\{1,2,9,10\}}^{\mathrm{SLP}}\},$$
$$\mathcal{F}_1^O = \{L_1^{\mathrm{SIC}}, I_{\{1,2,5,6\}}^{\mathrm{SIC}}, L_1^{\mathrm{SST}}, I_{\{1,2,7,8\}}^{\mathrm{SST}}, L_1^{\mathrm{SLP}}, I_{\{1\}}^{\mathrm{SLP}}\}.$$

Here, the intermittent mode indices are given in braces for each variable.

4.6 Sea-ice reemergence mechanisms

4.6.1 SST–sea-ice reemergence mechanism

We now examine the sea-ice reemergence mechanisms suggested by the SIC-SST-SLP families defined above. Chapter 3 showed that low-dimensional families of NLSA modes produce an SST–sea-ice reemergence mechanism in the North Pacific sector which is consistent with that proposed by Blanchard-Wrigglesworth et al. (2011a). Can a similar mechanism be observed in Arctic NLSA modes? In both the model and observations, the answer is yes.

Figure 4.16 shows spatial reconstructions of SIC, SST, and SLP using family $\mathcal{F}_1^M$. These spatial patterns are composites, produced by averaging over all times where $L_1^{\mathrm{SIC}}(t) > 1$ (which corresponds to 17% of the data). Similar patterns, with opposite sign, are obtained by compositing over times when $L_1^{\mathrm{SIC}}(t)$ is in negative phase. This figure shows four months of the year, but the time evolution of $\mathcal{F}_1^M$, shown in Movie 12 of the supplementary material, is much more illuminating.

In the winter months of January–March, we observe strong negative sea-ice anomalies in the Barents Sea and strong positive anomalies in the Bering and Labrador Seas. These anomalies reach their maximum southerly extent in March. We observe SST anomalies of opposite sign, which are roughly spatially coincident with the sea-ice anomalies, but also extend further south in each of the three

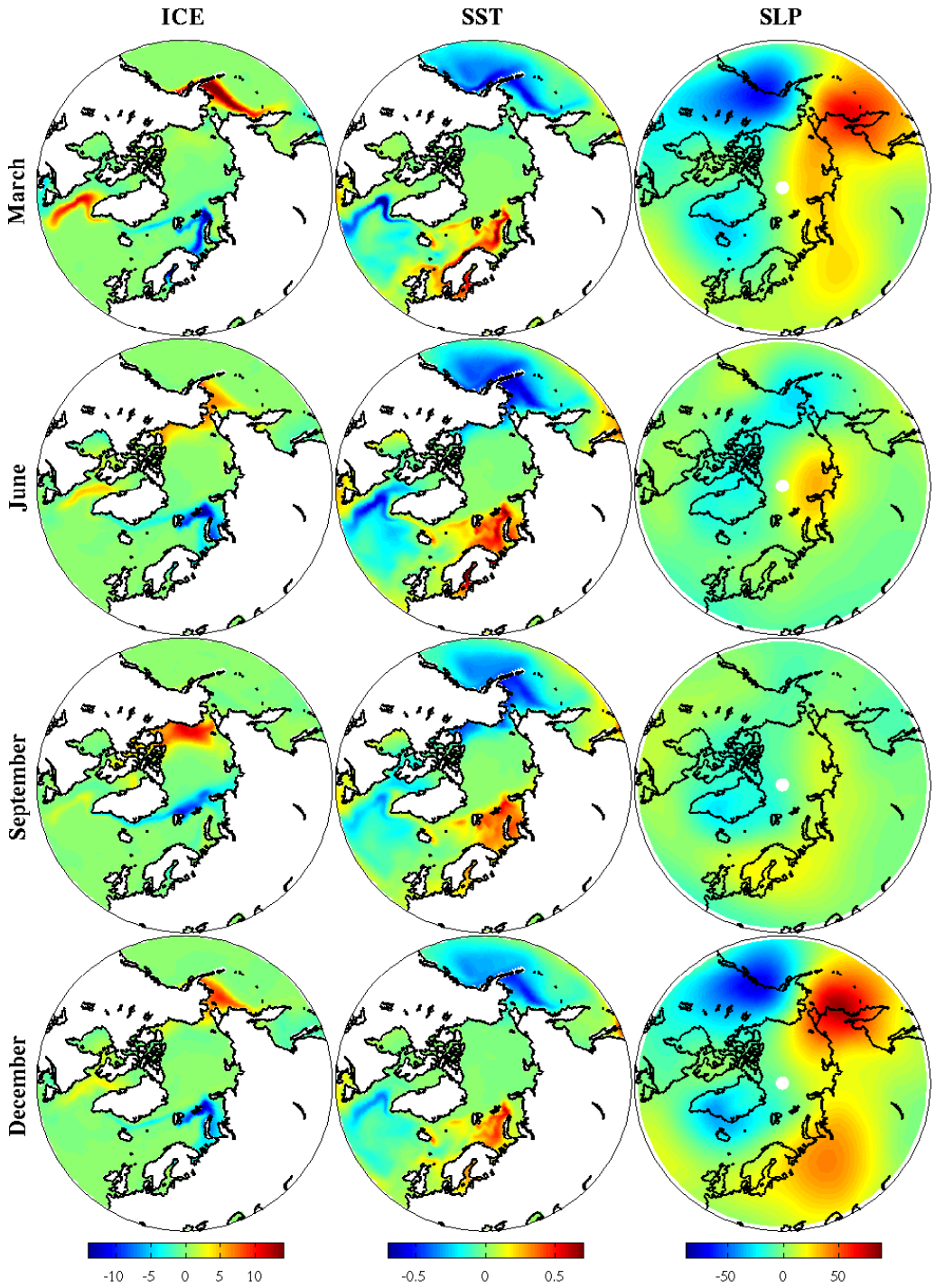

Figure 4.16: Sea ice, SST, and SLP patterns of CCSM3 reemergence Family $\mathcal{F}_1^M$ at different months of the year. These spatial patterns are composites, obtained by averaging over all years in which $L_1^{\text{SIC}} > 1$.

seas. Note that in March the Kara sea, the northern Bering Sea and the northern Labrador Sea are all SST anomaly-free. The ice anomalies move northward and weaken over the melt season, which begins in April. In June, the ice anomalies in the Barents-Kara region are located primarily in the Kara sea. Also, the Bering and Labrador anomalies have moved into the northern parts of these seas and weakened substantially.

As the ice anomalies move northward, they imprint an anomaly of opposite sign in the SST field. In particular, the previously anomaly-free Kara and northern Bering and Labrador Seas now have strong SST anomalies. The ice continues to retreat northwards over the melt season, reaching its minimum extent in September. In September the sea-ice anomalies are extremely weak in the Barents-Kara, Bering, and Labrador Seas, yet each of these seas has retained an SST anomaly. The SST anomaly retained in the Barents-Kara and Bering Seas is particularly strong, with a weaker anomaly in the Labrador Sea. As the growth season begins, the ice moves southward, interacts with the SST anomalies that have been stored over the summer months, and reinherits anomalies of the same sign as the previous spring. In December, we observe that most of the summer imprinted SST anomalies have disappeared, and the sea-ice anomalies have reemerged with the same sign as the spring anomalies. This reemergence family is typically active for a 2-8 year period, during which we observe reemerging sea-ice anomalies of a consistent sign (see Movie 12).

We observe a similar SST–sea-ice reemergence mechanism in family $\mathcal{F}_2^M$, shown in Fig. 4.17 and Movie 13 of the supplementary material. This figure is based on a composite over all times in which $L_2^{\mathrm{SIC}} > 1$ (which corresponds to 16% of the data). This family exhibits strong winter sea-ice anomalies in the Bering and Labrador

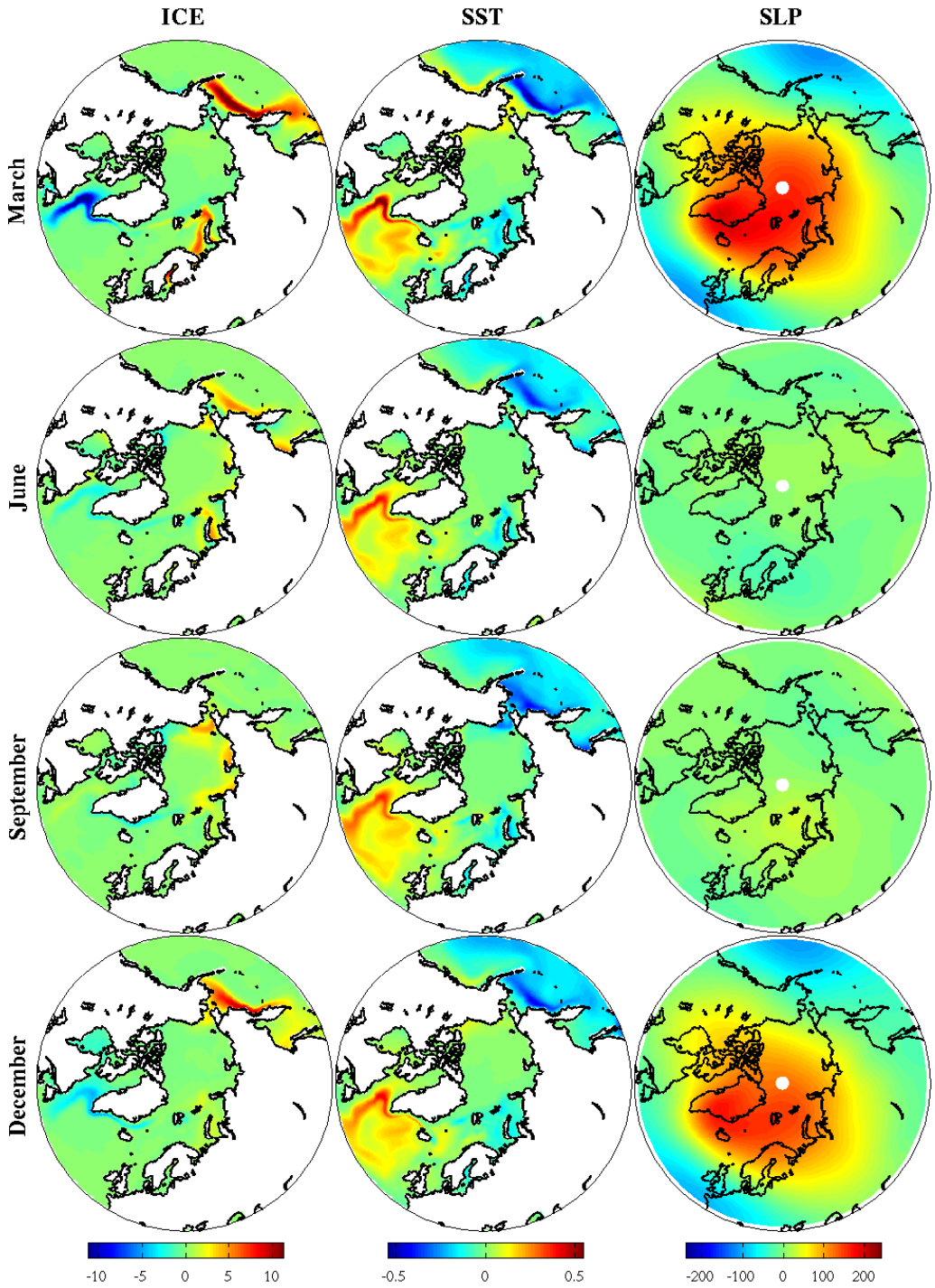

Figure 4.17: Sea ice, SST, and SLP patterns of CCSM3 reemergence Family $\mathcal{F}_2^M$ at different months of the year. These spatial patterns are composites, obtained by averaging over all years in which $L_2^{\text{SIC}} > 1$.

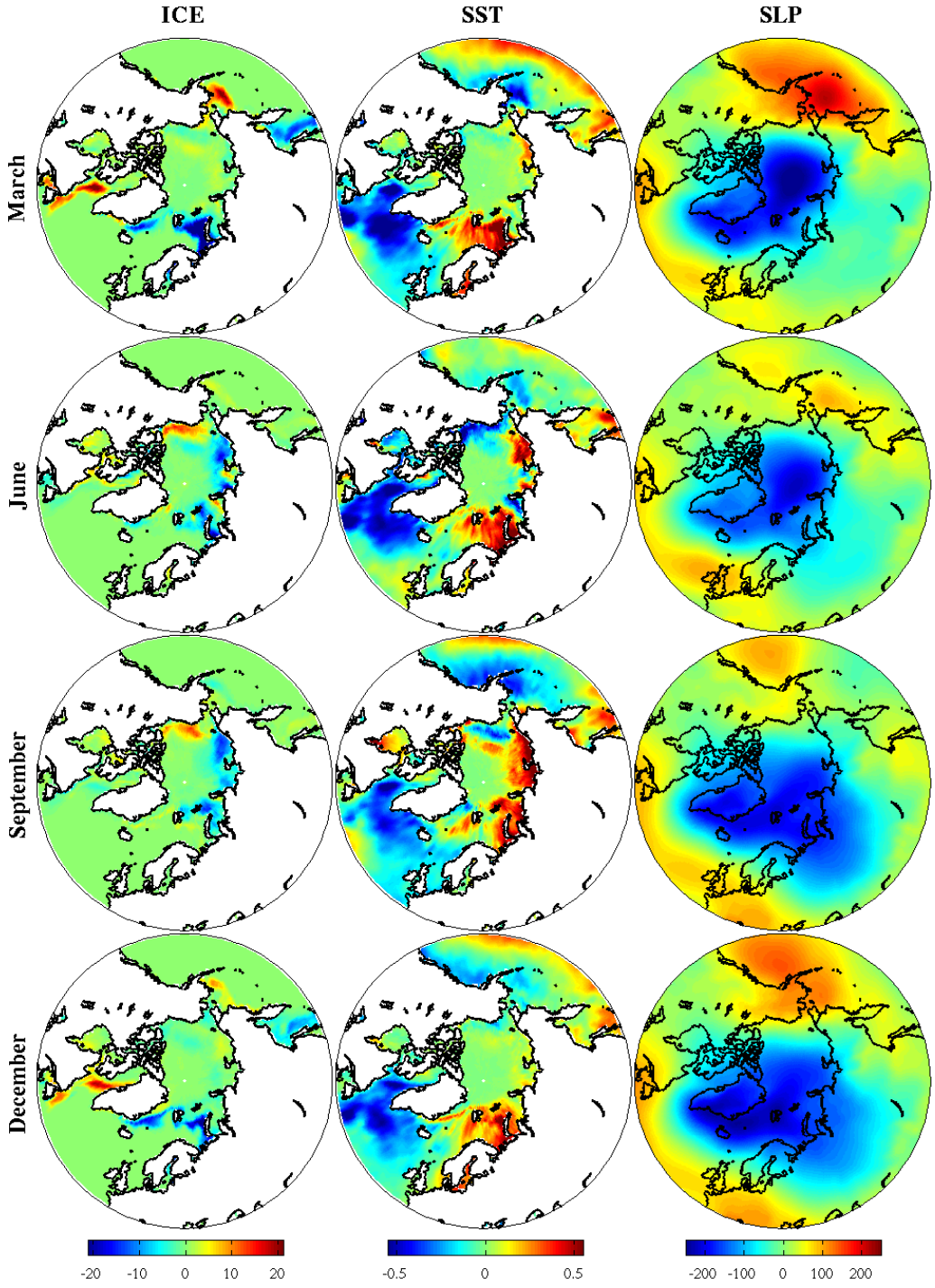

Figure 4.18: Sea ice, SST, and SLP patterns of HadISST reemergence Family $\mathcal{F}_1^O$ shown for different months of 1991.

Seas, which are out of phase with each other. These anomalies disappear over the melt season, leaving an SST imprint in the northern parts of these seas in June and September. We observe a sea-ice reemergence during the growth season, as the SST anomalies are converted into ice anomalies. This family does not have a strong signal in the Barents-Kara Seas.

The observational family, $\mathcal{F}_1^O$, displays a clear sea-ice reemergence, which is active primarily in the Barents-Kara, Bering, Okhotsk, Labrador, and Greenland Seas (Movie 14). This family, shown for the year 1991 in Fig. 4.18, also displays the SST–sea-ice reemergence mechanism, but in a slightly less clean manner than the model output. $\mathcal{F}_1^O$ has positive winter sea-ice anomalies in the Bering and Labrador Seas, and negative anomalies in the Barents-Kara, Greenland and Okhotsk Seas. The family has winter SST anomalies of opposite sign to these sea-ice anomalies, which extend southward of the sea-ice anomalies. Comparing the March panels to the June and September panels, an SST imprinting can be observed in the Barents-Kara Sea and, to a lesser extent, the Labrador and Bering Seas. Sea-ice anomalies of the same sign reappear in the fall, and this pattern roughly repeats the following year.

The reemergence families are able to capture the SST–sea-ice mechanism of Blanchard-Wrigglesworth et al. (2011a), previously only accessible via time correlation analysis of raw sea-ice and SST fields. This mode-based representation of reemergence allows one to track the temporal variability and strength of the SST–sea-ice reemergence mechanism, as will be done ahead in section 6c. Also, the low-dimensionality of these families has implications for predictability, since a small number of predictors (specifically, the low-frequency modes of the families) define the amplitude and sign of reemergence events.

4.6.2 Sea-ice teleconnections and reemergence via low-frequency SLP variability

Movies 12-14 reveal consistent phase relationships between sea-ice anomalies in the Barents-Kara, Bering, and Labrador Seas. The SST mechanism described above provides a local mechanism for sea-ice reemergence, but does not explain this phase-locking between geographically disconnected seas. We find that the SLP patterns of $\mathcal{F}_1^M$, $\mathcal{F}_2^M$, and $\mathcal{F}_1^O$ (shown in the third column of Figs. 4.16, 4.17, and 4.18) provide pan-Arctic scale teleconnections between these different regions.

We begin with family $\mathcal{F}_1^M$ (Fig. 4.16), which has an SLP pattern closely resembling the DA. This pattern is characterized by four main centers of action: pressure anomalies of the same sign over Greenland and Northwest North America and opposite-signed anomalies over Western Russia and Eastern Siberia. The geostrophic winds associated with this SLP pattern are primarily meridional, blowing across the Arctic from the Bering to the Barents-Kara Seas, or vice versa. We find that the ice advection and surface air temperature advection associated with these large-scale winds is consistent with the observed phase relationships in regional sea-ice anomalies.

From January–March, the dipole anomaly is very active, with strong northerly winds over the Bering Sea and strong southerly winds over the Barents-Kara Seas. The northerly winds advect cold Arctic air over the Bering Sea and also push the ice edge southwards and advect additional ice into the sea. Each of these effects encourages the formation of a positive sea-ice anomaly in the Bering Sea. Similarly, the Barents-Kara Seas experience warm southerly winds, which melt additional ice, and also push the ice edge northward, contributing to the observed nega-

tive sea-ice anomaly. Also, the SLP anomaly centered over Greenland produces northerly geostrophic winds over the Labrador Sea, contributing to its positive sea-ice anomalies for the same reasons. The SLP anomalies and corresponding winds weaken substantially over the summer months, as do the sea-ice anomalies in each of these regions. In October, the SLP anomalies begin to reappear with the same sign and a similar spatial pattern to the previous winter. This coincides with the beginning of the sea-ice growth season and the reemergence of ice anomalies from the previous spring. In December, we observe a strong dipole SLP anomaly, and, again, observe sea-ice anomalies in the Bering, Barents-Kara and Labrador Seas, which are physically consistent with this pattern.

Besides explaining the observed teleconnection in sea-ice anomalies, these SLP patterns also suggest an SLP–sea-ice reemergence mechanism via their winter-to-winter regime persistence. L_3^{SLP}, the low-frequency SLP mode of $\mathcal{F}_1^M$, has a strong one-year autocorrelation of 0.70. Because SLP anomalies produce a significant sea-ice response, recurring SLP patterns will produce recurring sea-ice patterns. Thus, the observed winter-to-winter persistence of the SLP patterns of $\mathcal{F}_1^M$ provides a candidate mechanism for sea-ice reemergence.

As mentioned earlier in section 4c, the SLP patterns of $\mathcal{F}_1^M$ represent a low-pass filtered version of the full atmospheric signal. The SLP patterns of $\mathcal{F}_1^M$ should be thought of as a slowly evolving atmospheric circulation regime, rather than a snapshot of the full SLP field at each point in time. For example, the temporal evolution of the full SLP field is similar to the time series of $\mathrm{PC}_1^{\mathrm{SLP}}$ in Fig. 4.11, whereas the SLP patterns of $\mathcal{F}_1^M$ are similar to the low-pass filtered PC (red curve in Fig. 4.11). It is the persistence of the atmospheric circulation regime of $\mathcal{F}_1^M$ that provides a plausible mechanism for sea-ice reemergence. Sea-ice anomalies

are known to have a persistence of 2-5 months (Blanchard-Wrigglesworth et al., 2011a), therefore the sea-ice anomalies at a given time represent an integrated response to earlier atmospheric and oceanic forcing. Given this, one would expect that sea-ice anomalies are not strongly dependent on the chaotic month-to-month fluctuations of the atmosphere, but are more dependent on a temporally smoothed version of this fluctuating field. Therefore, the low-pass filtered SLP patterns of $\mathcal{F}_1^M$ provide a plausible physical link between atmospheric and sea-ice variability. The study of Blanchard-Wrigglesworth et al. (2011a) dismisses SLP persistence as a source of sea-ice reemergence because of the low one-month autocorrelation of the SLP pattern that best explains changes in sea-ice extent. Here, we argue that the low-frequency component of similar SLP patterns may play an important role in sea-ice reemergence.

Similar relationships between sea-ice and SLP anomalies are also observed in family $\mathcal{F}_2^M$ (Fig. 4.17), which has an annular SLP pattern resembling the AO, and a one-year autocorrelation of 0.41. Similar to $\mathcal{F}_1^M$, these SLP patterns are strongly active over the winter months (October–March), and fairly inactive over the summer months. The geostrophic winds of this pattern are primarily zonal, but also have a meridional component, which affects sea ice via surface air temperature advection. In January–March, there are northeasterly winds over the Bering Sea, southeasterly winds over Labrador Sea, and northeasterly winds over the Barents-Kara Seas, with corresponding positive, negative, and positive sea-ice anomalies, respectively. The SLP anomalies become small over the summer months, and reappear during the fall months with the same sign as the previous winter. With the reappearance of these SLP anomalies, we observe an ice reemergence, which is particularly strong in the Bering and Labrador Seas.

The relationship between SLP and sea ice is somewhat less clear in the observations than in the model. Column three of Fig. 4.18 shows the $\mathcal{F}_1^O$ SLP patterns for 1991, a year when the family was active. In January–March, there is an AO-like SLP pattern producing northerly winds over the Labrador Sea and southerly winds over the Barents-Kara Seas. We observe corresponding positive and negative sea-ice anomalies in these seas, analogous to what was observed in $\mathcal{F}_2^M$. However, the SLP patterns differ in the North Pacific. There is minimal advection over the Bering Sea, as a high-pressure anomaly is centered directly over it. This anomaly produces southerly winds over the Sea of Okhotsk, which are consistent with the negative sea-ice anomaly. On the other hand, the SLP patterns do not provide a clear explanation, in terms of meridional wind, for the positive Bering sea-ice anomalies. Compared to $\mathcal{F}_2^M$, these SLP patterns do not decorrelate as strongly over the summer months, and a negative SLP anomaly is retained over the pole, which also shifts onto the Eurasian continent over the summer months. The anomaly strengthens during the fall, producing similar winds and sea-ice patterns to the previous winter. One notable difference between the observational and model SLP families is the spatial stationarity of the SLP patterns. The SLP patterns of $\mathcal{F}_1^M$ and $\mathcal{F}_2^M$ are relatively fixed in space and pulse on and off with the annual cycle. The $\mathcal{F}_1^O$ SLP patterns also pulse with the annual cycle, yet are transient in space. The SLP centers-of-action advect substantially over the course of a year.

Given the seemingly similar sea-ice anomalies of $\mathcal{F}_1^M$ and $\mathcal{F}_1^O$, a natural question is why these families have such different atmospheric patterns. A closer analysis of the sea-ice variability of each family reveals clear differences between the two. For each family, we compute the proportion of sea-ice variance in a given region,

relative to the variance of the full Arctic domain. We find that $\mathcal{F}_1^M$ contains 24% of its variance in the Bering Sea, 22% in the Barents-Kara Seas, and 8% in the Labrador Sea. Conversely, $\mathcal{F}_1^O$ contains 5% of its variance in the Bering Sea, 35% in the Barents-Kara Seas, and 14% in the Labrador Sea. Therefore, the dominant sea-ice feature of $\mathcal{F}_1^M$ is the dipole between the Bering and Barents-Kara Seas, whereas the dominant feature of $\mathcal{F}_1^O$ is the dipole between the Labrador and Barents-Kara Seas. The corresponding atmospheric circulation patterns of each family act to reinforce these dominant sea-ice anomalies, and have significantly different spatial patterns.

It should be noted that the data analysis approach employed here is capable of identifying correlation, but not causality. In particular, we have not quantified the relative importance of the ocean and the atmosphere in producing sea-ice reemergence. Also, we have identified SLP modes with interannual to decadal variability, but have not provided a mechanism for this observed variability. We speculate that, rather than intrinsic atmospheric variability, this low-frequency variability of the atmosphere results from SST or sea-ice forcing. The generation of low-frequency atmospheric variability has been widely studied, with many authors suggesting that extratropical and tropical SST anomalies are capable of driving low-frequency variability in the atmosphere (Lau and Nath, 1990; Latif and Barnett, 1994; Trenberth and Hurrell, 1994; Weng and Neelin, 1998; Selten et al., 1999; Robertson et al., 2000; Kushnir et al., 2002; Czaja and Frankignoul, 2002). Other authors (e.g., Mysak and Venegas, 1998), have suggested that sea-ice anomalies could drive low-frequency atmospheric patterns, but modeling studies have suggested that the atmospheric response is quite weak compared with the typical magnitude of atmospheric anomalies (Alexander et al., 2004; Magnusdottir

et al., 2004). Therefore, we speculate that anomalous SST forcing is the most likely candidate for the observed low-frequency SLP patterns, but more study is required on this problem. These unanswered questions could be investigated in a future study involving a hierarchy of GCM experiments.

4.6.3 Metrics for sea-ice reemergence

We now establish a set of reemergence metrics for sea ice, SST, and SLP, by which one can judge the activity of sea-ice reemergence and associated mechanisms in different regions. These metrics, computed for the reconstructed fields of each family, quantify the intensity and sign of ice reemergence events. We focus on the values of these metrics in the Bering, Barents-Kara, and Labrador Seas. The sea-ice metric is defined as the integrated (area-weighted) SIC anomaly in a given region. We define the SLP metric as the maximum value of the meridional geostrophic wind over a given region. This is a proxy for the amount of warm/cold air advection and northward/southward ice advection over a given region. The SST metric is defined as the integrated (area-weighted) SST anomalies in the portion of the seas that are imprinted by summer SST anomalies. Specifically, we compute the integrated SST anomalies in the Kara sea (75°E – 100°E and 65°N – 80°N), the northern Bering Sea (165°E – 160°W and 60°N – 65°N), and the northern Labrador Sea (70°W – 40°W and 60°N – 80°N). It is helpful to compare the metrics, plotted in Figs. 4.19–4.21, to Movies 12–14 which show the dynamical evolution of the corresponding fields for the same time period.

Figure 4.19 shows $\mathcal{F}_1^M$ metrics for 100 years of model output. We observe a number of reemergence events, characterized by periods in which the sea-ice metric is large, with consistent sign, over a number of successive winters. For example,

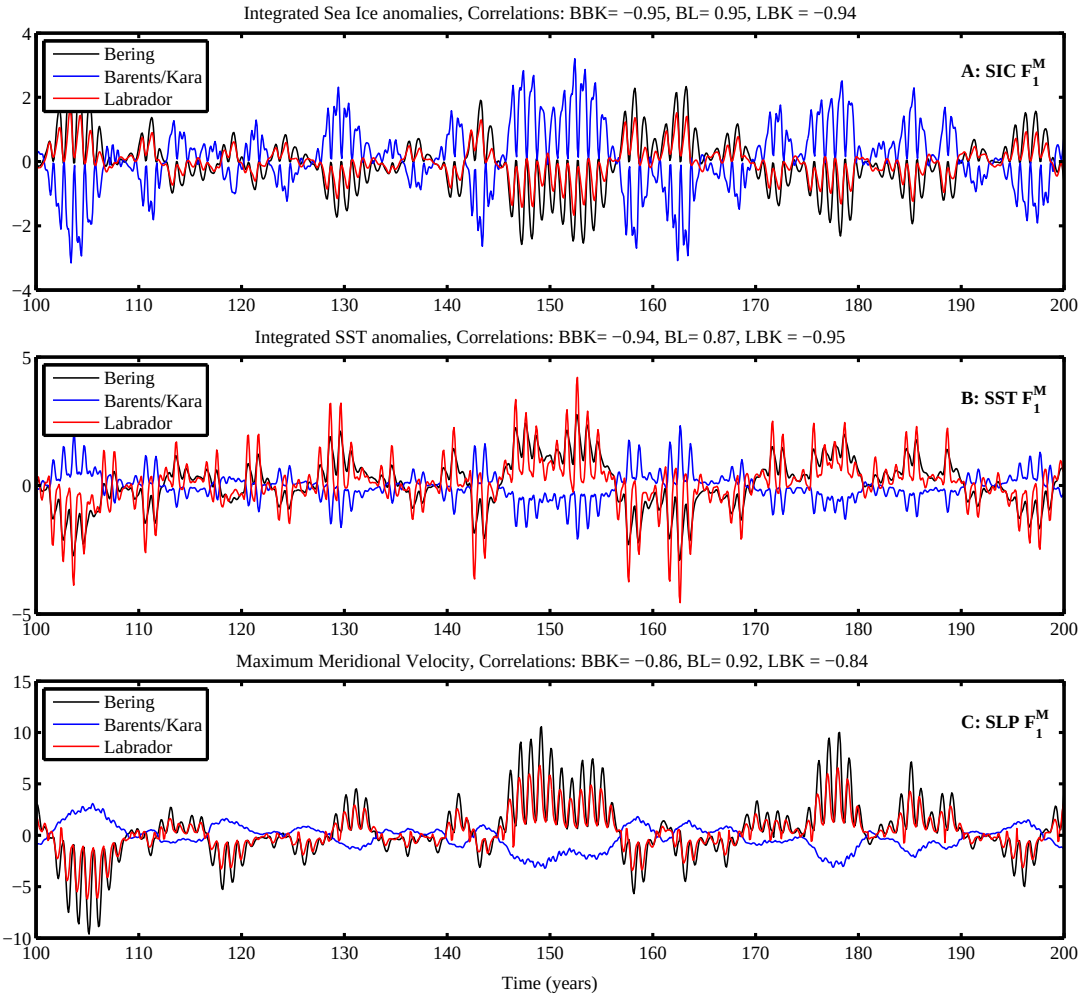

Figure 4.19: Reemergence metrics for ice, SST and wind of family $\mathcal{F}_1^M$ in the Barents/Kara, Bering, and Labrador Seas, by which we judge the activity of ice reemergence. Active periods of reemergence are characterized by repeated years in which these metrics are large (either positive or negative). Note that the SIC and SST metrics have been normalized by their respective standard deviations. The SLP metric is reported in m/s.

notable periods of active reemergence occur during years 101–106, 128–131, 146–155, and 175–179. The sea-ice phase relationships for this family are striking, with strong positive correlation (0.95) between the Bering and the Labrador Seas and strong anti-correlation (-0.95) between the Bering and Barents-Kara Seas. The SST metric reveals the SST-sea-ice reemergence mechanism, as years with large ice metrics have large SST metrics of the opposite sign (note the anti-correlation of like-colored curves in panels A and B). During reemergence events, the SST metrics are close to zero in the winter months and grow large in the summer months as the sea-ice anomalies imprint the SST field. These SST metrics also show a clear in-phase relationship between the Bering and Labrador Seas and out-of-phase relationship between the Bering and Barents-Kara Seas. The SLP metric is clearly out-of-phase with the sea-ice metric, which illustrates the sea ice-SLP reemergence mechanism, since positive (negative) meridional wind anomalies produce negative (positive) sea-ice anomalies. During reemergence events, in the Bering and Labrador Seas, we observe that the SLP metric is large over the winter and close to zero over the summer. In the Barents-Kara Sea, we observe more persistence, as the family maintains its wind anomalies throughout an entire reemergence event.

Figure 4.20 shows the metrics for family $\mathcal{F}_2^M$. Again, we observe very strong phase relationships in sea-ice anomalies, with in-phase anomalies between the Barents-Kara and Bering Seas and out-of-phase anomalies between the Bering and Labrador Seas. The SST metric displays strong SST–sea-ice reemergence mechanisms in the Labrador and Bering Seas. Also, as noted in section 5c, there is not a clear SST–sea-ice mechanism in the Barents-Kara Sea. The SLP metric has a strong signal in the Labrador Sea, which is large in winter and small in summer, and out-of-phase with the sea-ice anomalies. The SLP–sea-ice mechanism is less

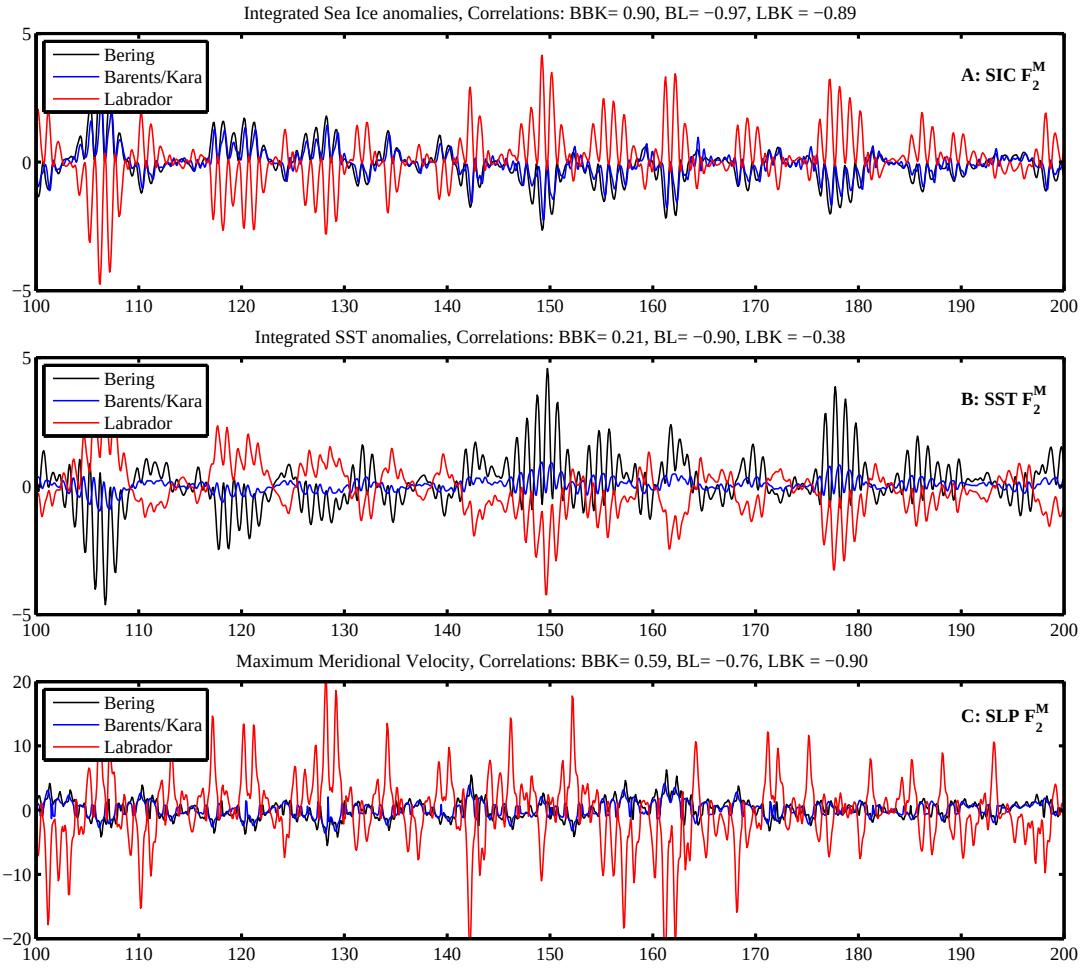

Figure 4.20: Reemergence metrics for ice, SST and wind of family $\mathcal{F}_2^M$ in the Barents/Kara, Bering, and Labrador Seas, by which we judge the activity of ice reemergence. Active periods of reemergence are characterized by repeated years in which these metrics are large (either positive or negative).

strong in the Barents-Kara and Bering Seas, yet we do observe persistent wind anomalies which are out-of-phase with the sea-ice anomalies.

We show metrics for $\mathcal{F}_1^O$ in Fig. 4.21. This family exhibits a strong SST–sea-ice reemergence mechanism in the Barents-Kara Sea. The SST signal is very weak in the Bering Sea, and in the Labrador Sea it tends to persist over periods of reemergence, rather than being imprinted each summer. The wind anomalies in the Labrador and Barents-Kara Seas are consistent with the sea ice-SLP reemergence mechanism. As noted earlier, the Bering Sea wind anomalies are not consistent with the sea-ice anomalies. Rather, we observe that the wind anomalies are inconsistent (in-phase) with the sea-ice anomalies.

4.6.4 Regional sea-ice relationships conditional on SLP modes

The reemergence families suggest a number of sea-ice teleconnections which are related to large-scale SLP patterns. Are these regional teleconnections visible in the raw SIC data? Are the teleconnections strengthened by conditioning on certain low-frequency SLP modes being active? To answer these questions, we select pairs of regions and compute lagged cross-correlations in total sea-ice area anomalies of the raw data between these regions. Note that the cross-correlations are obtained by computing a time series of sea-ice area anomalies for each region, and performing lagged correlations between these two time series. Our choice of regions and SLP modes is guided by the reemergence families. We consider the regions and SLP pattern that display the strongest teleconnection for each family.

The results are shown in Fig. 4.22, for months of the year with sea-ice coverage in the marginal ice zones (December–May) and for lags of -23 to 23 months. Panels A and B show lagged cross-correlations between the Barents-Kara and Bering Seas

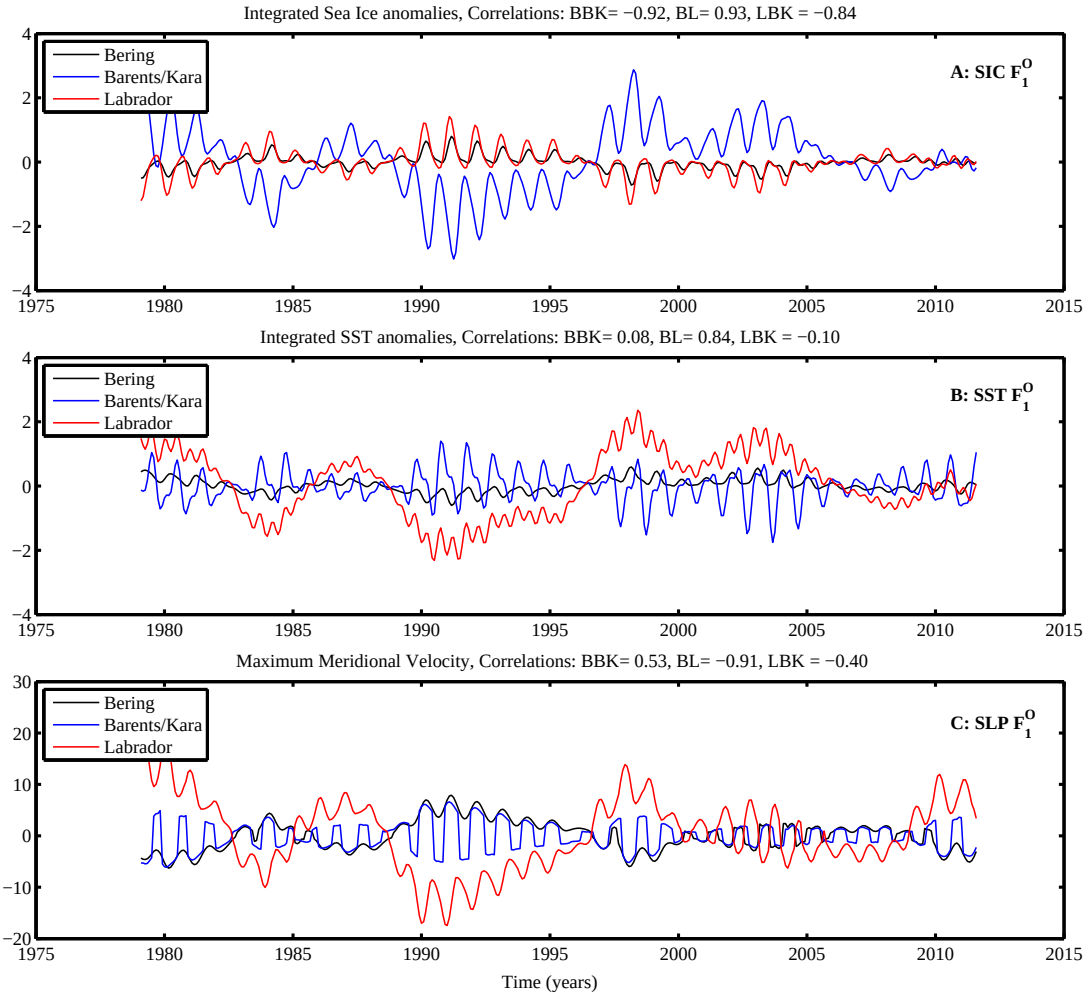

Figure 4.21: Reemergence metrics for ice, SST and wind of family $\mathcal{F}_1^O$ in the Barents/Kara, Bering, and Labrador Seas, by which we judge the activity of ice reemergence. Active periods of reemergence are characterized by repeated years in which these metrics are large (either positive or negative).

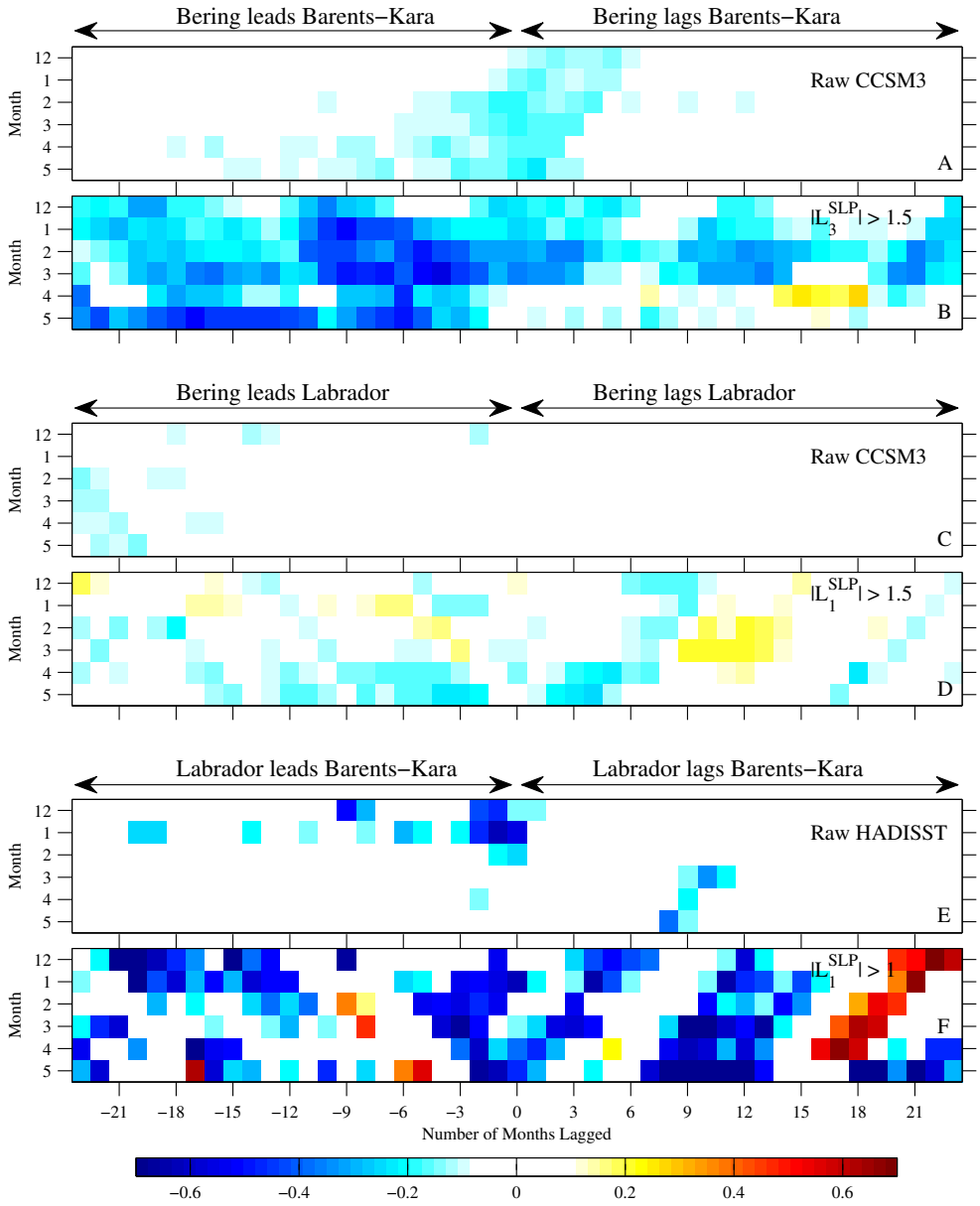

Figure 4.22: Lagged correlations in sea-ice area anomalies between different seas. (A) and (B) show CCSM3 correlations between the Barents-Kara and Bering Seas for the raw data and conditional on $|L_3^{\mathrm{SLP}}| > 1.5$, respectively. (C) and (D) show CCSM3 correlations between the Bering and Labrador Seas for the raw data and conditional on $|L_1^{\mathrm{SLP}}| > 1.5$, respectively. (E) and (F) show HadISST correlations between the Barents-Kara and Labrador Seas for the raw data and conditional on $|L_1^{\mathrm{SLP}}| > 1$, respectively.

for the raw CCSM3 data and conditional on $|L_3^{\mathrm{SLP}}| > 1.5$ (corresponds to 14% of the data), respectively. This corresponds to the primary teleconnection of $\mathcal{F}_1^M$. All correlations plotted in color are significant at the 95% level, based on a t-distribution statistic. In the raw data, we observe negative correlations between the Bering and Barents-Kara Seas, which are strongest at lags of -6 to 6 months. There is a dramatic strengthening of these negative correlations when conditioned on an active L_3^{SLP} mode (the DA mode). We also observe that the correlations are more persistent when the DA mode is active. Another interesting feature is the clear bias in correlations towards lags in which Bering anomalies lead Barents-Kara anomalies. The analogous correlations, corresponding to family $\mathcal{F}_2^M$, are shown in panels C and D for the Labrador and Bering Seas and for SLP mode L_1^{SLP} (the AO mode). These correlations are very small compared with panels A and B. The raw data displays very little correlation structure and weak correlations, that are primarily negative, emerge after conditioning on the AO mode. It should be noted that the limb of negative correlations, with Bering lagging Labrador, corresponds to summer sea-ice anomalies in the Bering Sea, which are extremely weak. Therefore, this limb has questionable significance.

Panels E and F show cross-correlations between the Barents-Kara and Labrador Seas for the HadISST dataset, conditional on $|L_1^{\mathrm{SLP}}| > 1$ (corresponds to 35% of the data). Note that we use a value of 1 rather than 1.5 for the conditional correlations because of the shortness of the observational time series. Also, the shortness of the time series implies a higher 95% significance level for correlations. We plot correlations using the same colorbar as CCSM3 and simply white-out all correlations which are not significant at the 95% level. The raw data displays some negative correlation, but a dramatic strengthening is observed when conditioning

on an active AO mode. The limb of white in panel F, extending from (May, +3) to (Dec, +9) corresponds to lagged correlations with summer months. At lags beyond this limb, we observe strong negative correlations. This feature is a reemergence of anti-correlation between the Barents-Kara and Labrador Seas. The reemergence structure is less clear for negative lags, where the Labrador leads the Barents-Kara, however we generally observe anti-correlation between the two seas, which is significantly stronger than the raw data.

4.7 Conclusions

We have studied Arctic sea-ice reemergence (Blanchard-Wrigglesworth et al., 2011a) in a comprehensive climate model and observations. This study has documented the regional and temporal details of sea-ice reemergence and illustrated two potential reemergence mechanisms, involving SST and SLP persistence, respectively. We have used coupled NLSA (Chapter 2), a nonlinear data analysis technique for multivariate timeseries, to analyze the co-variability of Arctic SIC, SST, and SLP. Coupled NLSA was applied to a 900-year equilibrated control integration of CCSM3, yielding spatiotemporal modes, analogous to EEOFs, and temporal patterns, analogous to PCs. Modes were also extracted from 34 years of observational data, using SIC and SST observations from HadISST and SLP reanalysis from ERA-Interim. In both the model and observations, these NLSA modes capture three distinct types of temporal behavior: periodic, low-frequency, and intermittent variability. The low-frequency modes have spatial patterns that closely resemble the leading EOFs of each variable. In particular, the low-frequency SLP modes correlate strongly with the well-known Arctic Oscillation (AO, Thomp-

son and Wallace, 1998) and Arctic Dipole Anomaly (DA, Wu et al., 2006) patterns of SLP variability. The temporal patterns of the low-frequency SLP modes, obtained here without any preprocessing of the raw data, closely resemble a low-pass filtered version of the corresponding PCs obtained via EOF analysis.

Performing time-lagged pattern correlations, we have found clear pan-Arctic sea-ice reemergence signals in the model and observations. The lagged pattern correlation approach employed in this study reveals a stronger reemergence signal in observations than previous studies on reemergence (Blanchard-Wrigglesworth et al., 2011a; Day et al., 2014b). Using coupled NLSA modes, we have found low-dimensional families that are able to reproduce the reemergence signal of the raw SIC data. Intriguingly, these families explain a relatively small portion of the raw SIC variance, yet when removed from the raw data the resulting signal exhibits significantly weaker reemergence. Moreover, the associated SST and SLP patterns of these families demonstrate two possible reemergence mechanisms, consistent with those proposed by Blanchard-Wrigglesworth et al. (2011a) and Deser et al. (2002). The SST–sea-ice reemergence mechanism, in which spring sea-ice anomalies are imprinted and stored as summer SST anomalies, is clearly active in the Barents-Kara, Bering, and Labrador Seas. The SLP–sea-ice mechanism, in which sea-ice anomalies reemerge due to the winter-to-winter persistence of low-pass filtered SLP anomalies (atmospheric regimes), is also observed in these regions, with the exception of the Bering Sea in the observational record.

A key finding of this study is that these reemergence patterns are part of a pan-Arctic scale organization involving SLP teleconnection patterns. In particular, we have found strong phase relationships between sea-ice reemergence events in geographically distinct regions. Unable to explain this teleconnection in terms

of purely local SST anomalies, we find clear relationships between regional sea-ice anomalies and large-scale SLP variability. In CCSM3, an out-of-phase relationship between the Bering/Labrador and Barents-Kara Seas is found to be consistent with the phase and amplitude of the DA mode. Similarly, an out-of-phase relationship between the Bering/Barents-Kara and Labrador Seas is found to be consistent with the phase and amplitude of the AO mode. In observations, the AO mode is able to explain the strong out-of-phase anomalies of the Barents-Kara and Labrador Seas, but cannot explain the weaker anomalies of the Bering Sea. These regional phase relationships are weakly visible in the raw SIC data, and are significantly strengthened by conditioning on an appropriate SLP mode (the AO or DA) being active.

Another key aspect of this study is the regional and temporal characterization of sea-ice reemergence. We have identified significant regional differences in reemergence between the model and observations, particularly in the Labrador Sea and the North Pacific sector, despite their pan-Arctic agreement. We have also found that reemergence events and mechanisms have significant temporal variability, and that the low-frequency modes of the reemergence families act as effective predictors of periods of active or quiescent reemergence. A set of reemergence metrics has been created, by which one can judge the strength and sign of sea-ice reemergence events, and the associated SST and SLP mechanisms.

In this study, we have demonstrated two plausible mechanisms for sea-ice reemergence, involving the atmosphere and the ocean, but which mechanism is most crucial in producing ice reemergence? Is sea-ice reemergence a fully coupled phenomenon, or does it also occur in more idealized situations? This data analysis study has identified correlation, but not causation. In Chapter 5, we analyze a

hierarchy of coupled model experiments to study these questions.

Chapter 5

Sea-Ice Reemergence in a Model Hierarchy

5.1 Introduction

The study of Chapter 4 identified an atmospheric role in spring-to-fall reemergence, relating reemerging sea-ice concentration (SIC) patterns to pan-Arctic scale sea-level pressure (SLP) teleconnection patterns. These patterns closely resemble the Arctic Dipole Anomaly (DA, Wu et al., 2006) and Arctic Oscillation (AO, Thompson and Wallace, 1998) patterns of SLP variability. This study also corroborated earlier findings on an SST–SIC spring-to-fall reemergence mechanism, and suggested a possible SLP–SIC mechanism, in which SIC anomalies reemerge due to winter-to-winter regime persistence of large-scale atmospheric circulation patterns. Chapter 4 did not quantify the relative importance and possible inter-dependence of these two mechanisms. In the present work, we explore a model hierarchy to gain insight into the relative roles of the ocean and the atmosphere in producing

sea-ice reemergence. Our main finding is that the SST–SIC mechanism can exist as a stand-alone process, while the SLP–SIC mechanism cannot. Nevertheless, the atmosphere is found to a play a crucial role in setting SIC patterns of reemergence, particularly in models that have full coupling between the atmosphere and the ocean.

Sea-ice reemergence requires two elements: (1) a source of sea-ice variability to create initial sea-ice anomalies and (2) a source of memory, which allows these anomalies to reemerge at some time in the future. Reemergence has been studied in observations and comprehensive climate models, both of which involve full-physics and fully-coupled ocean, atmosphere, and sea-ice components. In this study, we analyze a hierarchy of models using the Community Climate System Model version 4 (CCSM4; Gent et al., 2011), designed to probe different aspects of oceanic and atmospheric variability and memory. Summarized in Figure 5.1, these models consist of a fully-coupled control run, a slab ocean model (SOM) which has reduced oceanic memory, and two coordinated ocean-ice reference experiments (COREs) which have active sea-ice–ocean components forced by a specified atmosphere and lack ocean-to-atmosphere coupling. Using this model hierarchy, we perform a cross-model comparison with particular focus on: (1) the pan-Arctic, regional, and temporal aspects of sea-ice reemergence; (2) the relationship between sea-ice reemergence and SLP teleconnections; and (3) the representation of SST–SIC and SLP–SIC reemergence mechanisms.

5.2 Model hierarchy and methods

5.2.1 CCSM4 model hierarchy

We examine a hierarchy of global climate model (GCM) experiments from CCSM4, summarized in Figure 5.1. The fully-coupled CCSM4 successfully simulates many aspects of Arctic climate, including the SIT distribution and SIC field (Jahn et al., 2012). CCSM4 has known Arctic SLP biases, particularly a Beaufort high which is too weak and an SLP field that is generally biased low relative to reanalysis data (de Boer et al., 2012). The CCSM4 control run (b40.1850.track1.1deg.006) is 1300 years long, is forced with 1850 greenhouse gas levels, and has a grid of 1° nominal resolution for the ocean, sea-ice, and atmosphere components.

The SOM is the "CCSM4-NEWSOM", as described in Bitz et al. (2012). The SOM has full atmosphere and sea-ice components, a mixed-layer ocean, and is forced with 1850 greenhouse gas levels. The mixed-layer depth, computed from an ocean general circulation model (OGCM) control run, is spatially-varying but fixed in time. The SOM also includes a "Q-flux" term, which accounts for changes to mixed-layer heat content due to ocean heat transport convergence. The Q-flux term, computed offline using the OGCM control run, is spatially-varying and has a seasonal cycle. The SOM run is 60 years long and shares the same grid as the control run.

Note that in the SOM run SST was not explicitly stored as an output variable. We use the "surface temperature" variable stored in the atmospheric model output, which is equal to SST for fully ocean-covered gridpoints. For gridpoints that are fully covered by sea ice (we define this as SIC $>$ 70%), we set SST equal to -

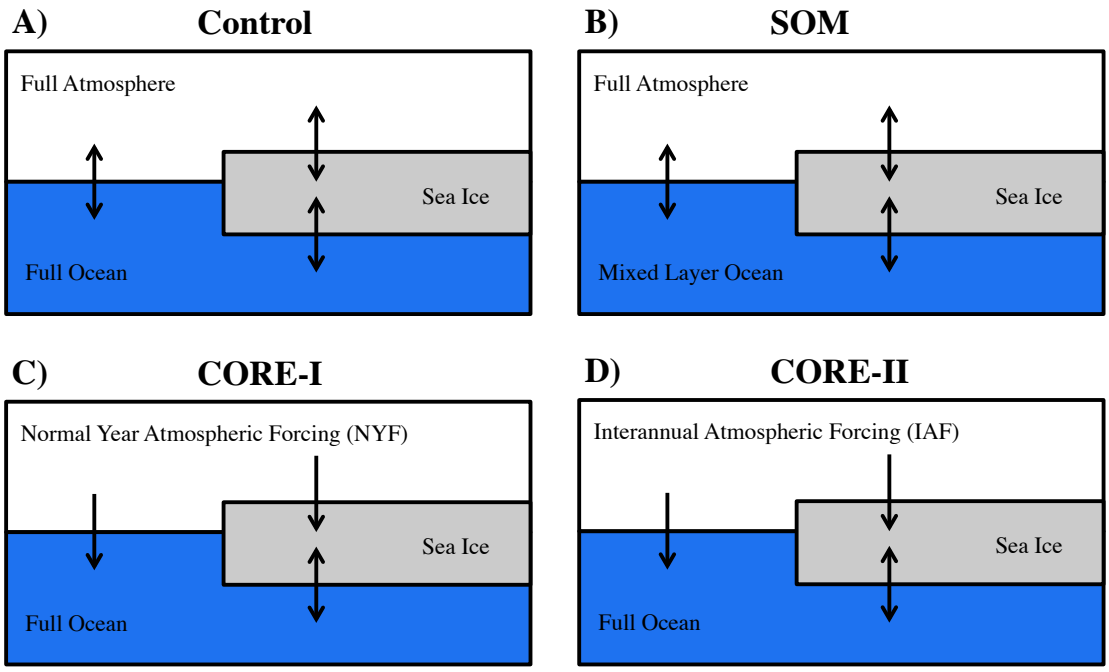

Figure 5.1: Schematic of the different CCSM4 runs analyzed in this study. Arrows indicate coupling between different components of the atmosphere–ocean–sea-ice system.

1.8C, the freezing point of saltwater at a salinity of 35 parts per thousand. SST at gridpoints with partial ice coverage was obtained by performing a bilinear (2-D) interpolation between the ice-covered and ocean-covered gridpoints. We also produced data using a newer version of the CCSM4 SOM with an updated code base. With this dataset, we reached the same qualitative conclusions, but observed some differences in the spatial patterns of the leading modes of variability. In particular, the leading SIC and SST modes have a stronger signal in the Sea of Okhotsk. Correspondingly, the high pressure center in Figure 5.4, ahead, is shifted further West over the Bering Sea, which is consistent with the modified SIC field. In this study, we present the data from the "CCSM4-NEWSOM", as it provides better contact with the earlier literature of Bitz et al. (2012).

The CORE runs have identical ice-ocean components to the control run, and are forced using the atmospheric data product developed in Large and Yeager (2004) and subsequently updated in Large and Yeager (2009). We analyze CCSM4 ice-ocean runs that are forced with phase I (CORE-I; Griffies et al., 2009) and phase II (CORE-II; Danabasoglu et al., 2014) of the CORE forcing. The 950-yr CORE-I run is forced by normal year forcing (NYF) version 2 (Large and Yeager, 2009), which is a repeated climatological mean annual cycle of atmospheric state variables and fluxes. The CORE-II run is forced by interannnually varying forcing (IAF) version 2 (Large and Yeager, 2009), which is an estimate of the atmospheric state over the 60 year period from 1948–2007. This run is 300-yrs long, consisting of five repetitions of the 60-yr CORE-II forcing cycle. We analyze the last 60-yrs of this run to minimize issues related to spin up. Figure 2 of Danabasoglu et al. (2014) shows that by the fifth forcing cycle, the CCSM4 CORE-II experiment has equilibrated. Both CORE-I and CORE-II atmospheric fields are defined on a T62 grid (1.875° resolution). In order to focus on internal variability, we detrend the CORE-II data by subtracting the monthly linear trend from each month.

We also compare CCSM4 results to 35-years of SIC satellite observations from the Met Office Hadley Center Sea Ice and Sea Surface Temperature (HadISST; Rayner et al., 2003) dataset. As with the CORE-II run, we detrend the HadISST data by subtracting monthly linear trends. All data is monthly averaged and the seasonal cycle is not removed. Retaining the seasonal cycle is crucial for our analysis of reemergence using nonlinear Laplacian spectral analysis (NLSA) modes, ahead.

5.2.2 Data analysis methods

In this work we utilize coupled NLSA, a unit-independent data analysis algorithm that extracts spatiotemporal modes of variability in multivariate datasets (Chapter 2). Coupled NLSA is a multivariate extension of the original NLSA algorithm, which is a nonlinear data analysis technique designed to identify intrinsic timescales and spatiotemporal patterns in dynamical systems (Giannakis and Majda, 2012c,a, 2013). Here, we follow the approach of Chapter 4 and study the co-variability of SIC, SST, and SLP in the CCSM4 model hierarchy. For each model, we recover sets of temporal and spatiotemporal modes, and use these modes to investigate the representation of sea-ice reemergence. We refer the reader to Chapters 2 and 4 for more details on the coupled NLSA methodology and implementation.

Coupled NLSA captures periodic modes, which represent the seasonal cycle, low-frequency modes, which capture interannual-to-decadal variability, and intermittent modes, which reflect the interaction of this periodic and low-frequency variability, in both space and time. Following Chapter 4, reemergence mode families are constructed as the minimal set of modes able to qualitatively reproduce the reemergence signal of the raw SIC data. For each model, we identify a five-mode reemergence family, consisting of a low-frequency mode, and degenerate pairs of annual and semiannual intermittent modes. The modes were computed truncation levels of $l = 21, 24$, and 23 eigenfunctions and Gaussian locality parameters of $\epsilon =$ 0.8, 1.0 and 1.0 for the control, CORE-II, and SOM runs, respectively.

5.3 Results

5.3.1 Sea-ice reemergence in CCSM4

We begin with a comparison of the regional sea-ice reemergence characteristics in the CCSM4 model runs and HadISST observations, shown in Figure 5.2. We assess sea-ice reemergence by computing time-lagged pattern correlations of the raw SIC anomaly field via the methodology of Chapter 3 and Chapter 4. For each initial month (from Jan–Dec) and lag (from 0–23 months), we report the time-mean pattern correlation, taken over all (month, month+lag) pairs in the SIC time series.

Over a pan-Arctic domain (0°–360° and 45°N–90°N), we find that the control and CORE-II experiments closely match the HadISST reemergence signal. Each of these displays a clear spring-to-fall reemergence, with spring SIC anomalies positively correlated with fall anomalies, despite a loss of correlation over the intervening summer months. The fall-to-spring reemergence is quite weak in each of these experiments. Note that if one performs time-lagged total area correlations via the methodology of Blanchard-Wrigglesworth et al. (2011a), the fall-to-spring reemergence is more prominent, yet still significantly weaker than the spring-to-fall reemergence.

Consistent with earlier CCSM3 findings (Blanchard-Wrigglesworth et al., 2011a), the SOM spring-to-fall reemergence signal is significantly weaker than the control run. This suggests the crucial importance of a full-depth ocean in obtaining a realistic representation of spring-to-fall reemergence. Ahead, we will argue that the fall-to-spring reemergence is not as severely affected in the SOM.

The CORE-I run exhibits substantial sea-ice persistence and an unrealistically

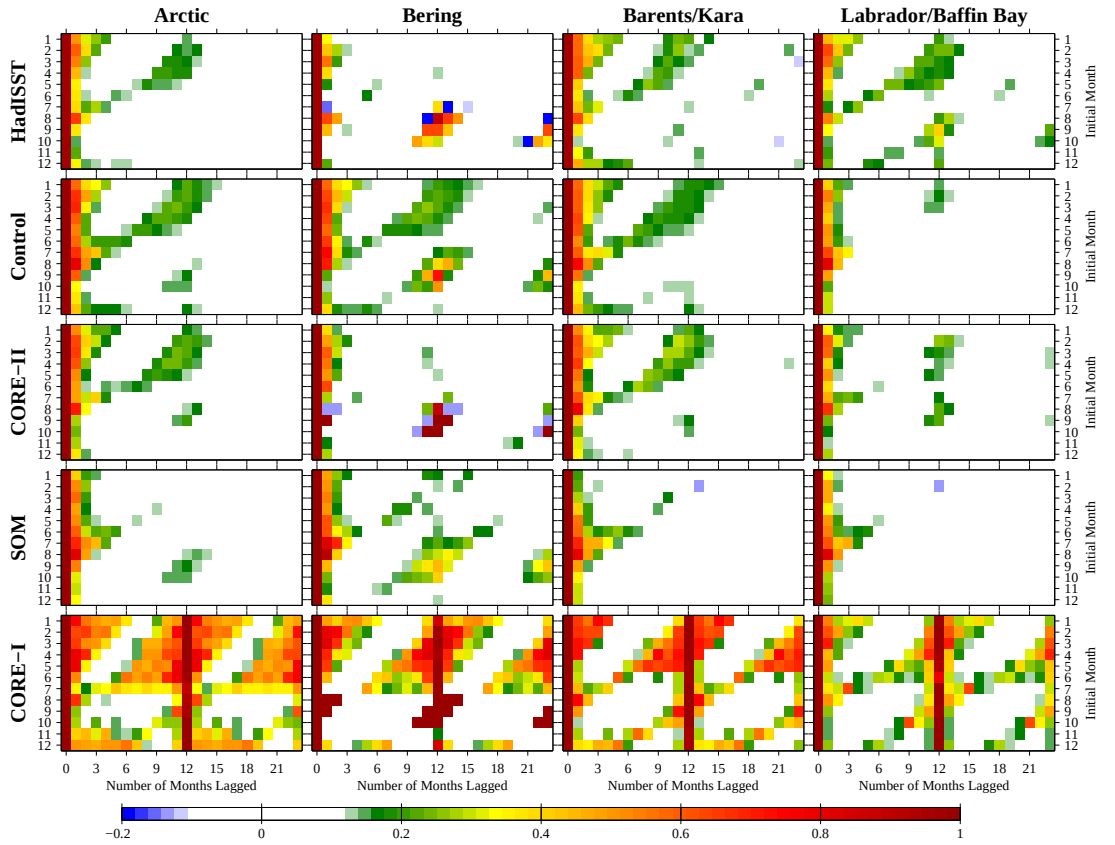

Figure 5.2: Time-lagged pattern correlations of SIC anomalies, computed for HadISST observations and various CCSM4 model runs, over different regions of the Arctic.

strong reemergence signal, likely due to the absence of atmospheric variability in this model. This suggests that internal ocean variability alone is insufficient to produce a realistic reemergence signal. Also, the SIC variability of CORE-I dramatically underestimates that of observations. The ratio of area-integrated variance in CORE-I vs HadISST is 0.01. As a comparison, the ratios are 0.72, 0.53, and 0.56 for the control, CORE-II, and SOM runs, respectively. This indicates that a reasonable representation of atmospheric variability is essential to producing reasonable sea-ice variability and reemergence.

Next, we examine the regional reemergence signals in the Bering (165°E–

160°W and 55°N–65°N), Barents-Kara (30°E–90°E and 65°N–80°N), and Labrador (70°W–40°W and 45°N–80°N) seas. The CORE-I reemergence signal is too strong in all regions, relative to observations. The SOM reemergence signals are consistently weaker than the control run, and are slightly enhanced in the Bering Sea.

We find that the CORE-II run is a better match with observations than the control. Specifically, matching observations, CORE-II has a weak reemergence signal in the Bering Sea and Sea of Okhotsk (not shown), whereas the control has strong reemergence signals in these regions. CORE-II qualitatively agrees with observations in all regions, except the Labrador Sea/Baffin Bay region, where it has a weak reemergence signal. This weak reemergence signal in the Labrador Sea/Baffin Bay is a robust feature across all CCSM3 and CCSM4 runs that we have analyzed, likely related to the challenges of accurately modeling deep ocean convection in the Labrador sea (Danabasoglu et al., 2012). Interestingly, Blanchard-Wrigglesworth and Bitz (2014) note strong SIT biases in the CORE-II run. Despite these biases in SIT, the CORE-II SIC reemergence signal is very realistic.

Next, informed by the NLSA reemergence families, we investigate the temporal variability of sea-ice reemergence across these CCSM4 models. We compute time-lagged pattern correlations of the raw SIC data, both for the full time-series, and conditional on times in which the low-frequency SIC mode (L_1^{SIC}) of each reemergence family is active. In all three models, we find that the conditional correlations display enhanced spring-to-fall and fall-to-spring reemergence (see Figure 5.3). This indicates substantial temporal variability in the strength of reemergence events across all three models. This also demonstrates that the low-frequency NLSA modes are effective predictors of these periods of enhanced reemergence.

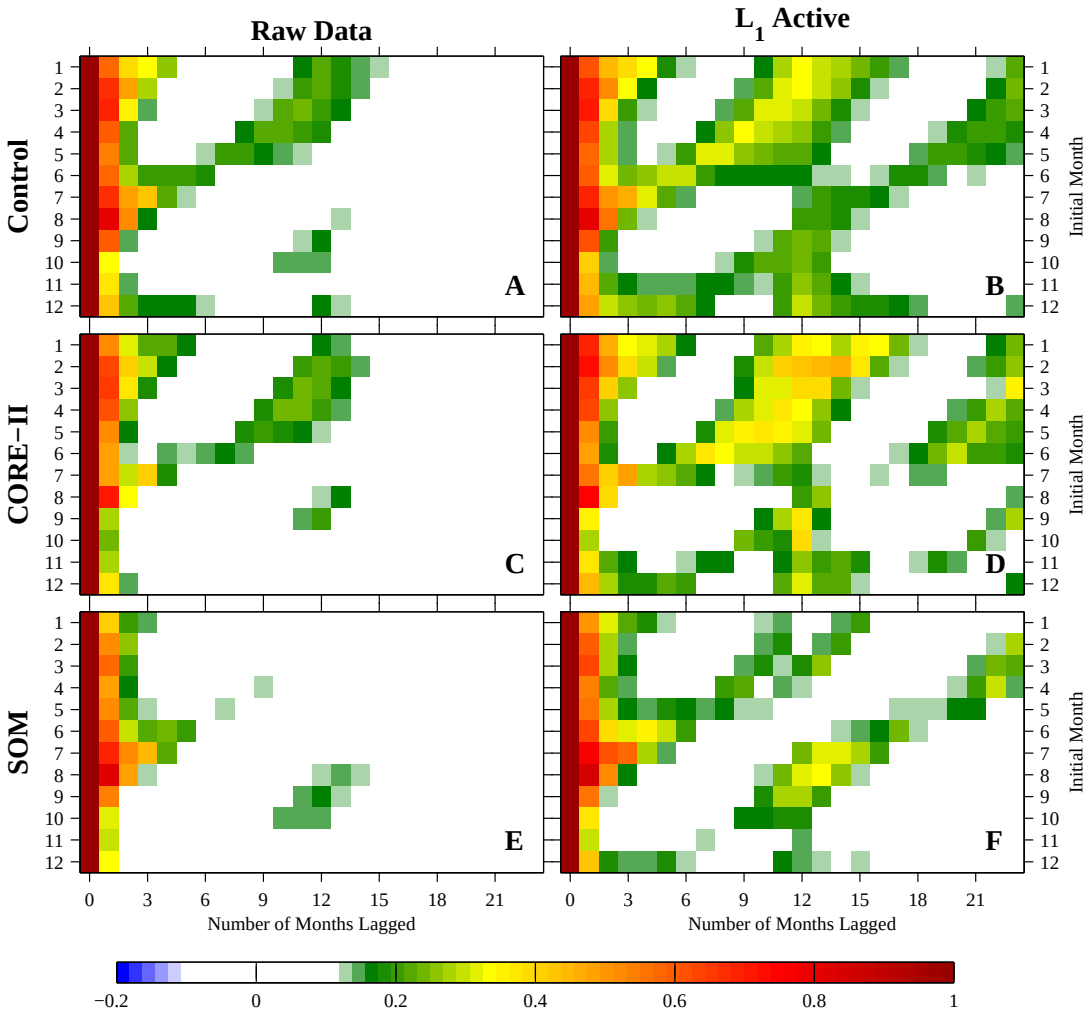

Figure 5.3: Time-lagged pattern correlations for different CCSM4 model runs, computed for the raw SIC anomaly data (left column) and conditional on the L_1^{SIC} mode of each reemergence family being active (right column). We condition on $\left|L_1^{\text{SIC}}\right| > 2$ for the control run and $\left|L_1^{\text{SIC}}\right| > 1.5$ for the CORE-II and SOM runs.

In the SOM, the conditional correlations show a fall-to-spring reemergence of similar strength to the control and CORE-II models, but a significantly weaker spring-to-fall reemergence. The fall-to-spring reemergence occurs in regions of the central Arctic that are fully ice-covered during winter, where SSTs are unable to retain the memory of earlier SIC anomalies. Since the ocean does not participate in the fall-to-spring reemergence mechanism involving persistence of SIT anomalies, one would expect that the simplified ocean of the SOM would not impact the representation of this mechanism. Conversely, the spring-to-fall reemergence mechanism depends crucially on ocean heat storage below the mixed layer (Holland et al., 2013). Therefore one would expect decreased fidelity of this mechanism in the SOM. The conditional lagged correlations of Figure 5.3 are consistent with both of these expectations.

5.3.2 Reemergence mechanisms and SLP–SIC teleconnections

We now examine the spatiotemporal evolution of the NLSA reemergence families, with a particular focus on winter SIC–SLP teleconnections. Figure 5.4 shows winter means (January–March) of the reconstructed SIC, SST, and SLP fields of each reemergence family. These patterns are composites, computed over all times in which L_1^{SIC} of each family is active, in positive phase. The negative phase composites are similar, with opposite sign. Movie 15 of the online supplementary material shows the monthly evolution of these fields.

The winter SIC patterns are quite similar between the control and SOM runs, with an SIC dipole pattern between the Bering and Barents-Greenland-Iceland-Norwegian (Barents-GIN) Seas. The SIC pattern of CORE-II is dominated by

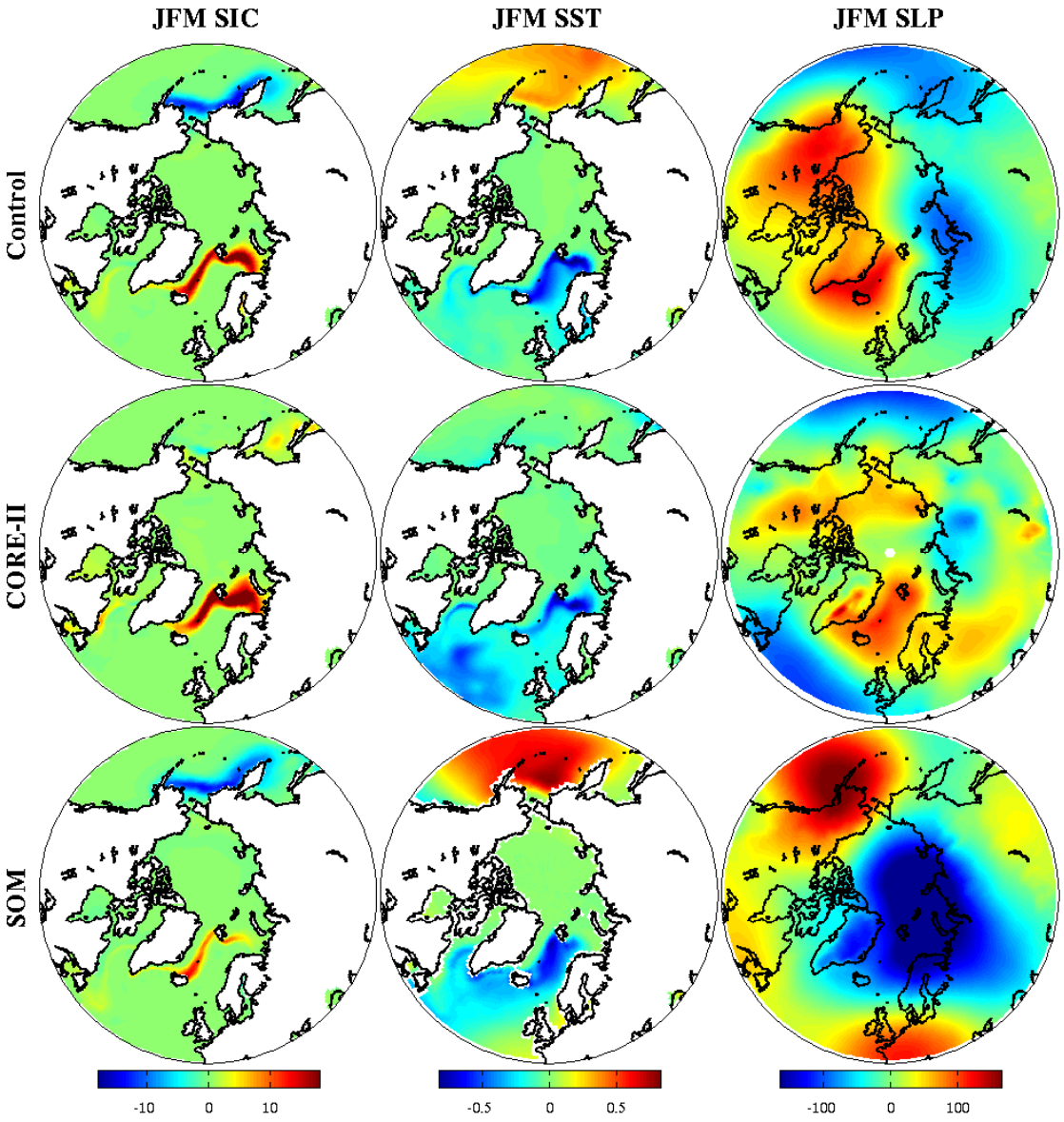

Figure 5.4: Winter mean (Jan–Mar) composites of SIC, SST, and SLP shown for reemergence families of the control, CORE-II, and SOM. The composites are computed over all times in which L_1^{SIC} of each family is active, in positive phase.

anomalies in the Barents-GIN Seas, and lacks the North Atlantic–North Pacific dipole that characterizes the control and SOM. It should also be noted that despite being forced by a realistic atmosphere, the CORE-II SIC pattern differs substantially from the leading observational SIC mode, whether this mode is derived via EOF analysis (Deser et al., 2000) or via NLSA (Chapter 4). The SST patterns of each family have opposite sign to the local SIC anomalies, and generally reflect the spring-to-fall SST–SIC reemergence mechanism (see Movie 15). One exception to this is the Barents region of the SOM, which does not display the summer imprinting of SST anomalies seen in the Bering Sea of the SOM and in the other models. A possible reason for this is the shallow depth of the Bering Sea, meaning the mixed layer ocean is a reasonable approximation to the true ocean dynamics of this region, and therefore provides a reasonable representation of the SST–SIC mechanism. Conversely, the Barents-GIN seas are deeper, and are likely poorly represented by the SOM.

The SLP patterns of each reemergence family provide a physical explanation for the inter-model differences in winter SIC. The SOM and control run have somewhat different SLP patterns, but share a key common feature: a transpolar advective pathway defined via geostrophic winds. This pathway creates communication between the North Atlantic and North Pacific basins, providing an SLP–SIC teleconnection between these disconnected regions. The geostrophic winds of these SLP patterns, and their associated surface air temperature advection, tend to create SIC anomalies of opposite sign in the Bering and Barents-GIN Seas. In contrast, the CORE-II run does not exhibit this transpolar advective pathway, and, correspondingly, does not display a North Atlantic–North Pacific teleconnection.

To examine this winter SLP–SIC interaction more precisely, we next consider

the relationship between meridional wind and SIC in the Bering, GIN, and Barents-Kara Seas (see Figure 5.5). Using the reemergence families, we create indices for these regions based on spatial-mean meridional winds and spatial-mean SIC anomalies, and normalize these indices by the maximum standard deviation over the three regions. In regions where there is strong SLP–SIC co-variability, we expect a negative correlation between these indices, since positive meridional winds create negative SIC anomalies, and vice versa. The control run shows this negative correlation clearly in the Bering, GIN, and Barents-Kara Seas, all regions of significant SIC variability in this model. Similarly, the SOM shows negative correlations in the Bering and GIN seas, which dominate the winter SIC variability of this model, and no relationship in the Barents-Kara Seas, which have little winter SIC variability. CORE-II shows a clear negative relationship in the Barents-Kara Seas, a weak positive relationship in the GIN Seas, and a low-variance SIC signal in the Bering Sea. The SLP–SIC relationships in CORE-II are weaker than the other models, as they can explain the Barents-Kara anomalies, but not the GIN anomalies.

A necessary condition for an SIC–SLP teleconnection is a clear negative correlation between mean meridional wind and mean SIC in at least one region of both the North Atlantic and North Pacific. The control and the SOM clearly satisfy this necessary condition, but CORE-II does not. Why is this the case? A key difference between these three models is the lack of ocean-to-atmosphere coupling in CORE-II (see Figure 5.1). In particular, CORE-II ocean heat anomalies are unable to feedback on the atmosphere and modify the atmospheric state. These results suggest that this ocean-to-atmosphere coupling is essential in creating coherent pan-Arctic-scale co-variability of SIC and SLP.

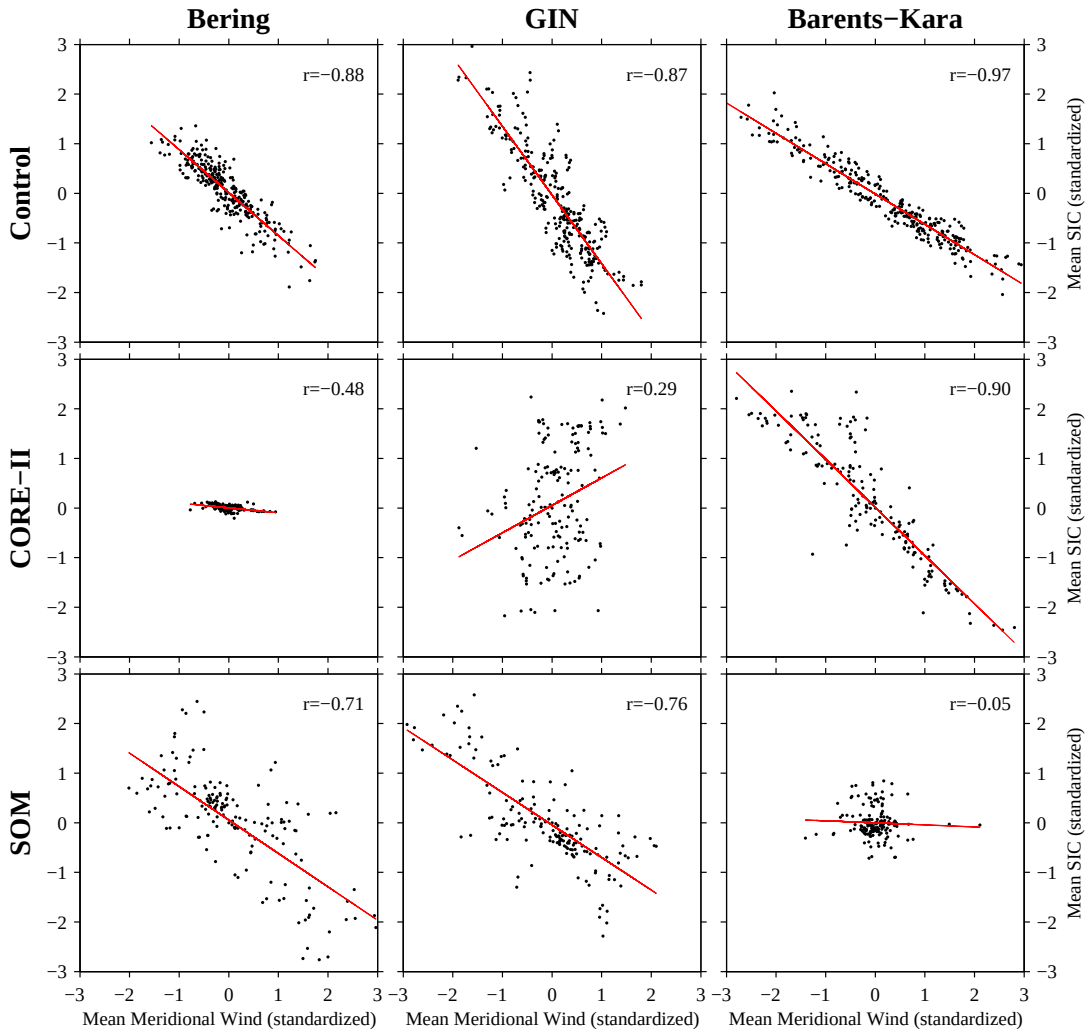

Figure 5.5: Scatterplots of standardized mean SIC vs mean meridional wind for the control, CORE-II, and SOM. These values are computed over winter months (Jan–March) in the Bering, GIN, and Barents-Kara Seas.

Movie 15 shows that the reemergence families of the control and SOM display the previously mentioned SLP–SIC reemergence mechanism, due to their winter-to-winter SLP regime persistence. This SLP–SIC mechanism is not well represented in the CORE-II run, as the SLP patterns are quite transient in space (Movie 15) and do not correlate as clearly with SIC anomalies (Figure 5.5). Conversely, the CORE-II and control runs display the SST–SIC reemergence mechanism, whereas this mechanism is not as robustly represented in the SOM. Given CORE-II's stronger and more realistic reemergence signal compared with the SOM, this suggests that the SST–SIC mechanism can operate as a stand-alone reemergence mechanism. In contrast, the SLP–SIC mechanism cannot operate as a stand-alone process, in the sense that it crucially depends on the full-depth dynamics and persistence of the ocean. This suggests that oceanic persistence is the key source of memory for sea-ice reemergence. However, this does not preclude an atmospheric role in reemergence. Given the observed pan-Arctic scale organization of SIC anomalies in the control and SOM, the atmosphere is the most likely driver of this variability, as oceanic variability does not provide a direct method of communication between different ocean basins. In the runs with ocean-to-atmosphere coupling, the atmosphere provides an important dynamical linkage, setting the spatial patterns of SIC reemergence.

5.4 Conclusions

We have assessed the representation of sea-ice reemergence and associated SST and SLP-based mechanisms in a hierarchy of CCSM4 models. The primary conclusions of this study are:

1. There is good quantitative agreement of pan-Arctic reemergence between observations, the control, and CORE-II. On regional scales, CORE-II matches the reemergence signal of observations better than the control.

2. Relative to observations, the reemergence signals of the SOM and CORE-I are too weak and too strong, respectively. The weak SOM reemergence signal indicates the crucial role of ocean heat anomalies stored below the mixed layer in providing memory for reemergence. The unrealistically strong reemergence in CORE-I indicates the necessity of atmospheric variability in providing a realistic representation of reemergence.

3. The control, CORE-II and SOM all exhibit substantial temporal variability in the strength of reemergence events. The low-frequency SIC modes of the NLSA reemergence families are effective predictors of periods of enhanced reemergence activity.

4. The SIC patterns of the reemergence families of the control and SOM runs exhibit a winter sea-ice teleconnection between the Bering and Barents-GIN Seas. The SLP patterns of the families are physically consistent with the SIC patterns, and allow communication between the North Pacific and North Atlantic sectors via a transpolar advective pathway. The CORE-II winter SIC pattern is dominated by anomalies in the Barents-GIN Seas, and does not exhibit this teleconnection. This suggests that dynamical feedback from the ocean to the atmosphere is essential in creating large-scale organized patterns of SIC–SLP co-variability.

5. The control run exhibits both the SST–SIC and the SLP–SIC reemergence mechanisms. The representation of the SST–SIC and SLP–SIC mechanism

is degraded in the SOM and CORE-II runs, respectively. CORE-II has a more realistic reemergence signal than the SOM, suggesting that the SST–SIC mechanism is able to operate as a stand-alone mechanism. In models with ocean-to-atmosphere coupling, atmospheric variability plays a key role in reemergence, setting the spatial patterns of SIC reemergence.

In this chapter, we have attempted to gain insight into the coupled nature of sea-ice reemergence, by exploring models with active sea-ice components, but different physics and coupling of the atmosphere and the ocean. Because of the nonlinear, coupled dynamics of the atmosphere-ocean-ice system it is challenging to properly address notions of causality in this framework. Additional work, involving idealized model experiments and analysis of other GCMs is required to further test the conclusions presented in this chapter.

Chapter 6

Fall-to-Spring Sea-Ice Reemergence Mechanisms

6.1 Introduction

In addition to the well-known decline of Arctic sea-ice extent over the satellite era, submarine and satellite measurements indicate that Arctic sea ice has also thinned over this time period (Rothrock et al., 1999; Kwok and Rothrock, 2009). This reduction in sea-ice thickness (SIT) has important implications for Arctic climate, as it modifies heat and momentum fluxes between the atmosphere and the ocean, which, in turn, affects the large-scale mean state and variability of the atmosphere-ice-ocean system (Holland et al., 2006a). SIT also plays an important role in Arctic feedback mechanisms such as the negative ice thickness–ice growth rate feedback (Bitz and Roe, 2004), the positive sea-ice albedo feedback (Budyko, 1969; Curry et al., 1995), and the negative ice thickness–ice strength feedback (Owens and Lemke, 1990).

Owing to its persistence, SIT provides a potential source of predictability for the Arctic climate system (Chevallier and Salas-Mélia, 2012; Guemas et al., 2014). This is a property that could be exploited by operational sea-ice prediction systems. Indeed, recent studies have shown improved predictions in model experiments that assimilate SIT data (Yang et al., 2014) and in experiments that are initialized using knowledge of the SIT state (Day et al., 2014a). Perfect model predictability studies have shown that sea-ice volume has potential predictability at lead times up to roughly 36 months, which is significantly longer than the analogous estimates for sea-ice extent (Tietsche et al., 2014). The SIT state also has important implications for sea-ice predictability, as GCM studies show that thin sea-ice states are inherently less predictable than thick states (Holland et al., 2011; Germe et al., 2014). A related challenge for GCM-based predictability studies is that the mean state and variability of SIT varies substantially across models (Blanchard-Wrigglesworth and Bitz, 2014).

Chapters 3–5 of this thesis have focused on the spring-to-fall variety of sea-ice reemergence and associated reemergence mechanisms involving SST and SLP. In this chapter, we examine the fall-to-spring variety of reemergence, focusing on a mechanism proposed by Blanchard-Wrigglesworth et al. (2011a) in which growth season (fall) SIC anomalies reemerge the following melt season (spring) due to persistent SIT anomalies in the central Arctic. This fall-to-spring reemergence is an example of a process in which SIT acts as a crucial source of predictability for SIC anomalies. In this chapter, we study the co-variability of Arctic SIC, sea-surface temperature (SST), sea-level pressure (SLP), and SIT using coupled nonlinear Laplacian spectral analysis (NLSA). We specifically focus on (1) the representation of fall-to-spring reemergence by coupled NLSA modes; (2) the ability of these

modes to capture an SIT-based reemergence mechanism; and (3) the relation of this SIT mechanism to other reemergence mechanisms.

6.2 Datasets and methods

6.2.1 Datasets

This study is based on analysis of a 1300-year control run (b40.1850.track1.1deg.006) of the Community Climate System Model version 4 (CCSM4; Gent et al., 2011). This run is forced with 1850 greenhouse gas levels and has 1° nominal resolution for the ocean, sea ice, and atmosphere components. CCSM4 successfully simulates many aspects of Arctic climate and has a number of improvements compared to CCSM3 (Jahn et al., 2012). Of particular note for the present study is the significantly improved SIT representation in CCSM4, which motivates its use in our examination of the role of SIT in fall-to-spring sea-ice reemergence. All data is monthly averaged and the seasonal cycle has not been removed.

6.2.2 Data analysis methods

In this study, we utilize the coupled NLSA algorithm, as developed in Chapter 2, to investigate the co-variability of SIC, SST, SLP, and SIT in the Arctic sector. We use coupled NLSA to extract modes of co-variability for these datasets, and utilize these modes to study low-dimensional representations of sea-ice reemergence. We employ the methodology of Chapter 4 to construct "reemergence families" of NLSA modes: small mode subsets that are able to reproduce the lagged correlation structure of the raw SIC data.

We compute the coupled NLSA kernel using SIC, SST, and SLP as input variables and a Gaussian locality parameter of $\epsilon = 0.8$. NLSA modes are computed using a truncation level of $l = 21$ eigenfunctions. Note that the SIT modes are obtained by projecting the SIT data onto these eigenfunctions, and performing a singular value decomposition of the projected SIT data. This is analogous to our method for finding modes for the other variables. As in earlier chapters, coupled NLSA produces periodic, low-frequency, and intermittent modes of variability. We identify a reemergence family consisting of a low-frequency mode and pairs of annual and semiannual intermittent modes. Lagged correlations computed using this family display both a spring-to-fall and a fall-to-spring reemergence of correlation. Note that the SIC, SST, and SLP modes of this reemergence family are the same as those discussed for the CCSM4 control run in Chapter 5.

We also performed computations using SIC, SST, SLP, and SIT as input variables to the coupled NLSA kernel. We find that the inclusion of SIT significantly modifies the kernel values, as the term corresponding to SIT tends to dominate over the other variables. This is likely the result of the relatively weak seasonal cycle of SIT compared to the other fields. This weak seasonal cycle implies that the ratio of the phase velocity to the variance is generally lower for SIT than for other variables, meaning that the SIT term makes a more substantial contribution to the coupled NLSA kernel. For example, the ratio of non-periodic variance to periodic variance is 0.36 for SIC, 0.08 for SST, 1.63 for SLP, and 2.31 for SIT. SIT has the largest ratio, indicating its dominant influence on the kernel values. SLP also has a high ratio; however, the SLP field typically decorrelates over a 1–2 month timescale (see Chapter 4, Figure 11). This rapid decorrelation implies that the SLP field takes on many different states within a given 24-month embedding win-

dow, generally reducing the covariability between different 24-month lag-embedded samples. SIT, conversely, decorrelates over a 3–4 year timescale, meaning that each lag-embedded SIT vector represents a single coherent SIT state. This combination of a high non-periodic to periodic variance ratio and substantial autocorrelation over the embedding window gives SIT a dominant influence in the coupled NLSA kernel.

We find that the non-periodic NLSA modes from the four-variable kernel have spatial patterns that are dominated by SIT variability. Moreover, the intermittent–low-frequency envelope relationships that were used extensively in earlier chapters are substantially degraded when using the four-variable kernel. This makes it significantly more difficult, and in some cases impossible, to find low-dimensional mode families that capture sea-ice reemergence. For these reasons, we choose to use the three-variable coupled NLSA kernel for this study. Future work is needed to allow for inclusion of SIT in the coupled kernel, without dominating the other variables of interest.

6.3 Results

6.3.1 Fall-to-spring sea-ice reemergence

In this study, we focus on the fall-to-spring (growth season to melt season) reemergence of Arctic SIC anomalies. We characterize reemergence via the time-lagged pattern correlation methodology of Chapters 3–5. We compute time-mean pattern correlations for all initial months (Jan–Dec) and for all lags from 0–23 months. These time-lagged pattern correlations are reported in Figure 6.1. The left column shows correlations computed using the raw SIC data and the right

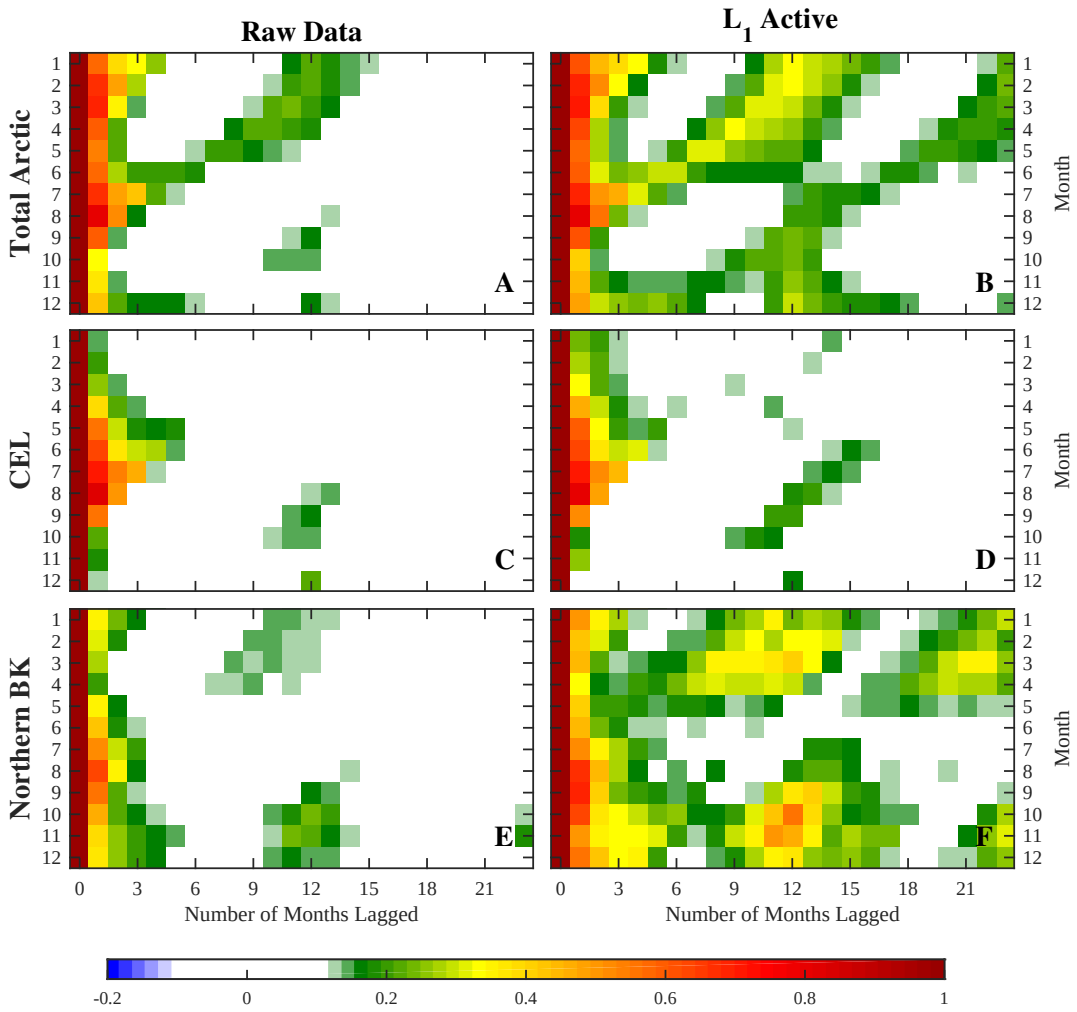

Figure 6.1: Time-lagged pattern correlations of SIC anomalies for the CCSM4 control run, computed over a pan-Arctic domain, the Chukchi, East Siberian and Laptev (CEL) Seas and the northern Barents-Kara (BK) Seas. (A), (C), and (E) show correlations computed using the raw SIC data. (B), (D), and (F) show conditional correlations computed over all times in which $\left|L_1^{\mathrm{SIC}}\right| > 2$. All correlations are significant at the 95% level, based on a t-test.

column shows conditional correlations computed during times in which the low-frequency SIC mode of the reemergence family is active ($\left|L_1^{\mathrm{SIC}}\right| > 2$).

Time-lagged pattern correlations computed over a pan-Arctic domain (0°–360° and 45°N–90°N), show a clear spring-to-fall reemergence and a relatively weak

fall-to-spring reemergence (Figure 6.1a). Both types of reemergence are substantially enhanced when conditioning on the low-frequency SIC mode being active (Figure 6.1b). Of particular interest in this study is the clear fall-to-spring reemergence displayed during times in which the reemergence mode family is active. Correlations were also computed using the time-lagged total area methodology of Blanchard-Wrigglesworth et al. (2011a). The fall-to-spring reemergence is more prominent in the total-area lagged correlations, yet remains substantially weaker than the spring-to-fall reemergence.

The fall-to-spring reemergence occurs in regions of the central Arctic that are fully sea-ice covered, and hence sea-ice anomaly free, during the winter months. We compute time-lagged pattern correlations for two regions of the central Arctic: the Chukchi, East Siberian and Laptev (CEL) Seas and the northern Barents-Kara (BK) Seas. These regions will be focussed on throughout this study. We define the CEL domain as 105°E–160°W and 65°N–80°N and define the northern BK domain as 10°E–90°E and 78°N–85°N. In both of these regions, we observe a weakened spring-to-fall reemergence in both the raw data and in the conditional correlations. The fall-to-spring reemergence, however, appears clearly in the conditional lagged correlations in both the CEL and the northern BK domains. The northern BK domain shows a particularly enhanced fall-to-spring reemergence signal compared with the Arctic conditional lagged correlations. The emphasized fall-to-spring reemergence in these regions motivates us to focus on them in this study.

6.3.2 SIT–SIC reemergence mechanism

We next examine the spatiotemporal evolution of the NLSA reemergence family, with particular focus on the role of SIT in fall-to-spring (growth season to melt

season) reemergence. Figure 6.2 shows reconstructed SIC and SIT fields from the reemergence family for different months of the year. These are composite patterns, obtained by averaging over all times in which the low-frequency SIC mode of the reemergence family is active, in positive phase. The yearly evolution and interplay of these fields reveals an SIT–SIC fall-to-spring reemergence mechanism, in which the memory of growth season (fall) SIC anomalies is retained by SIT anomalies in the central Arctic.

In September, we observe negative SIC anomalies in the CEL Seas and positive SIC anomalies in the northern BK and Greenland Seas. Roughly spatially coincident with these anomalies are like-signed SIT anomalies. After reaching its minimum extent in September, the sea-ice cover enters the growth season, characterized by southward migration of the sea-ice edge. The SIC anomalies tend to move with the sea-ice edge, eventually vacating the CEL and northern BK domains, whereas the SIT anomalies are spatially-persistent and insensitive to the sea-ice edge position. By March, the growth season (fall) SIC anomalies of the CEL and northern BK seas have been lost, as these seas are fully ice covered, and hence SIC anomaly free, during winter. Conversely, the SIT anomalies have persisted, retaining anomalies that are spatially coincident with the September anomalies. The melt season begins in April, and during this season the SIC anomalies begin to retreat northward, vacating the Bering Sea and the southern portion of the Barents Sea. Eventually, the SIC anomalies move far enough northward that they begin to interact with the SIT anomalies. In the CEL domain, the ice is anomalously thin, and melts out faster than normal, creating a negative SIC anomaly in this region. Conversely, the northern BK Seas have anomalously thick ice, meaning that the ice melts out more slowly than normal, creating a positive SIC anomaly.

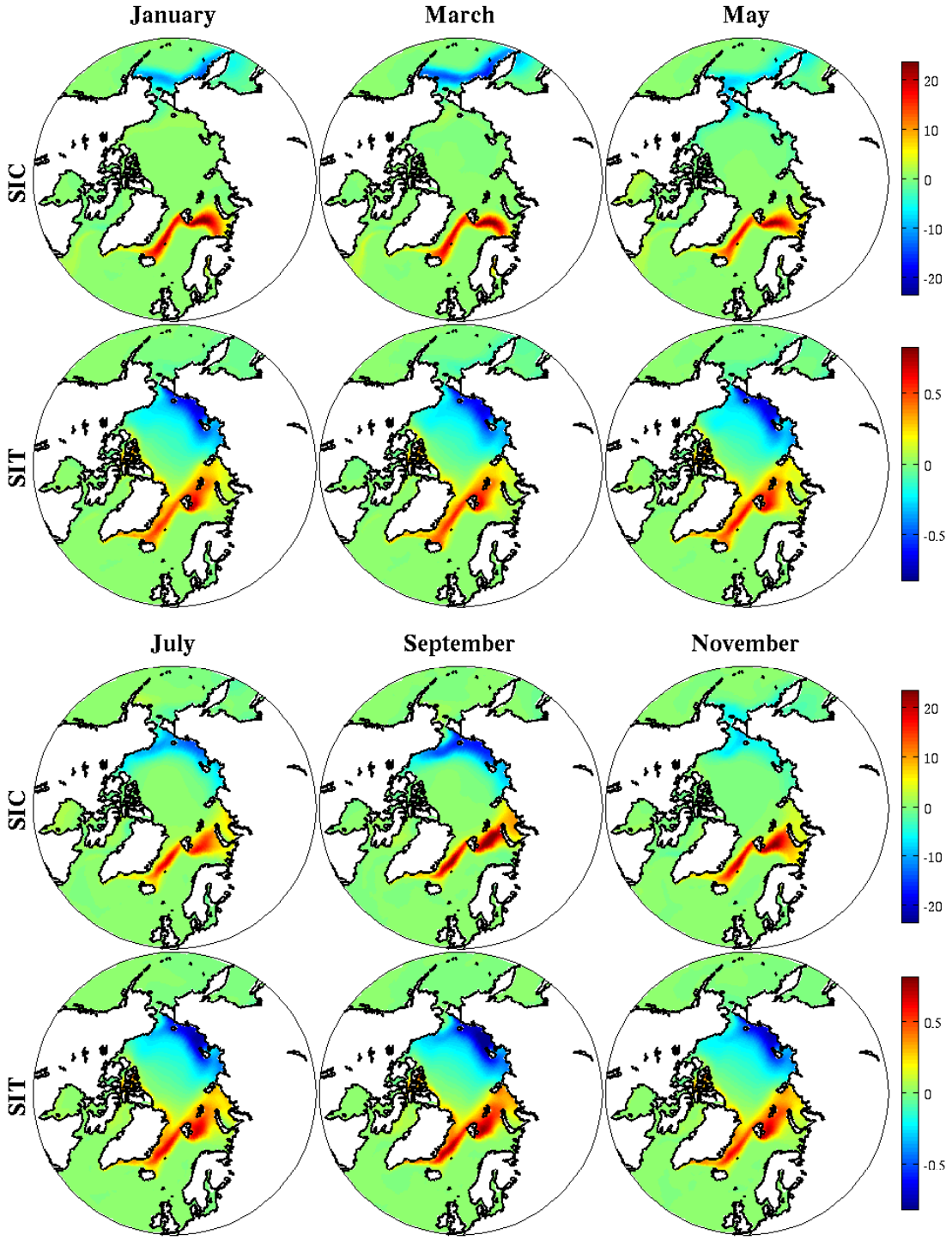

Figure 6.2: Spatial pattern composites of SIC and SIT, computed using the NLSA reemergence family. Movie 16 of the supplementary material shows the spatiotemporal evolution of these fields.

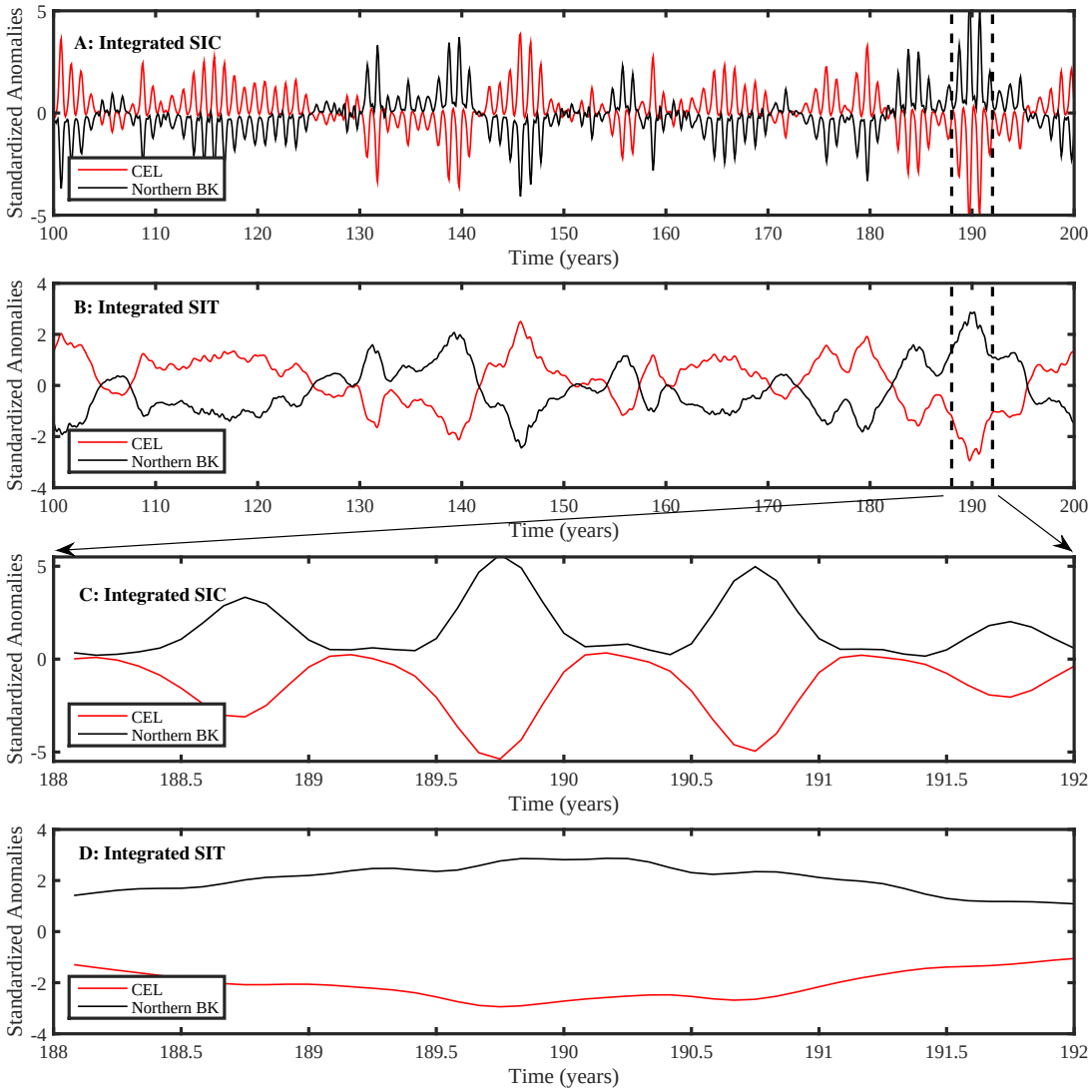

Figure 6.3: SIC and SIT reemergence metrics computed using the NLSA reemergence family. (A) and (B) show a 100-year portion of the time series; (C) and (D) show a four-year portion.

By this mechanism, growth season (fall) SIC anomalies tend to reemerge the following melt season (spring). After reemerging, the anomalies are maintained up to the September sea-ice minimum. This cycle roughly repeats again the following year, and these "reemergence events" tend to recur over 3–10 year time periods.

Next, we introduce a set of reemergence metrics, by which one can judge the

amplitude and phase of reemergence events, and assess the activity of the SIT–SIC reemergence mechanism. We define SIC and SIT metrics as the integrated SIC and SIT anomalies, respectively, over a region of interest. These metrics, computed using the NLSA reemergence family over the CEL and northern BK domains, are shown in Figure 6.3. Note that the metrics have been normalized by their standard deviation.

Fall-to-spring reemergence events can be identified as periods of time during which the SIC reemergence metrics (Figure 6.3a) have large amplitude and consistent sign over a number of consecutive years. The SIC metrics pulse with an annual cycle, with large amplitude in summer months and small amplitude in winter months. These metrics also display a clear anti-phase relationship between SIC anomalies in the CEL and northern BK domains. The SIT reemergence metrics (Figure 6.3b) have the same sign as the SIC metrics, but do not display an annual pulsing. Rather, the SIT metrics persist with the same sign for a number of years and closely resemble modulating envelopes for the SIC metrics. This relationship reflects the SIT–SIC reemergence mechanism described above, with SIT retaining memory that allows for SIC anomalies to reemerge in successive summers. Figures 6.3c and 6.3d display a zoom-in of these metric values for a four-year period of active reemergence. We observe that the SIC metric is small over the winter months and large over summer months. The SIT metric maintains a persistent sign over this four-year time period, matching the sign of the SIC anomalies.

6.3.3 Relation to other reemergence mechanisms

The identified reemergence family captures both fall-to-spring as well as spring-to-fall reemergence of SIC anomalies. In the previous section, we have demon-

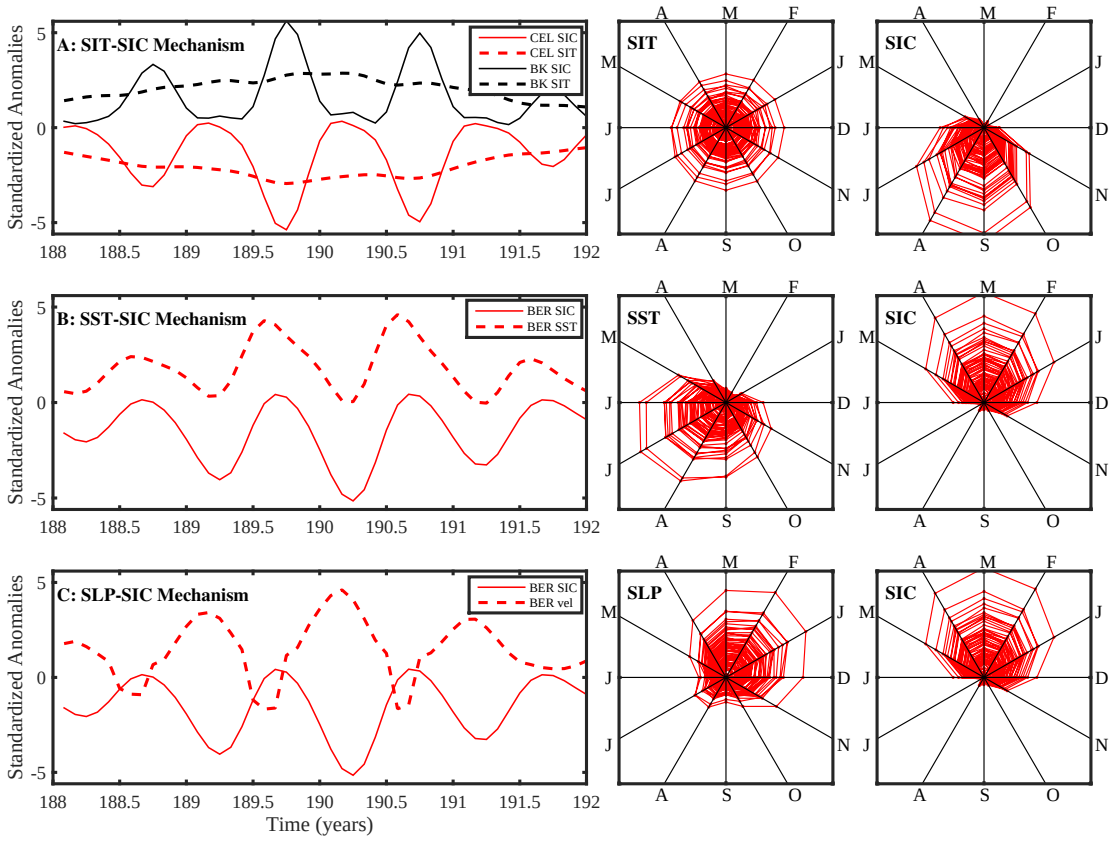

Figure 6.4: Time series and phase evolution of reemergence metrics for SIC, SST, SLP, and SIT. These metrics are computed using the NLSA reemergence family.

strated that the family describes an SIT–SIC mechanism for fall-to-spring reemergence. Additionally, the SST and SLP patterns of this family reflect the SST–SIC and SLP–SIC mechanisms for spring-to-fall reemergence discussed earlier in Chapters 3-5. This motivates a simultaneous comparison of all four fields of the reemergence family. In Figure 6.4, we investigate the seasonality and phase relationships of these three reemergence mechanisms. We find that each reemergence mechanism displays a clear relation to the seasonal cycle, involving interaction between SIC anomalies and a second physical variable of the ice-ocean-atmosphere system.

The left column of Figure 6.4 shows reemergence metrics plotted for a four-year

time period of active reemergence (the same four-year period as used in Figure 6.3). In all panels, SIC metrics are plotted as solid lines, and the metrics for the field that provides the reemergence mechanism are plotted as dashed lines. The two right columns show the phase evolution of these metrics with respect to the seasonal cycle. Specifically, for each metric $M(t)$, the phase evolution is given by $(x(t), y(t)) = (|M(t)|\cos(2\pi t/12), |M(t)|\sin(2\pi t/12))$, where t is the time measured in months. We plot these values for an 80-year portion of the timeseries. The phase plots are qualitatively similar for other 80-year portions of the 1300-year timeseries. The SIC and SIT metrics are defined as in section 3.2 of this chapter. The SST metric, as defined in Chapter 4, is the integrated SST anomaly computed over the region that experiences summer imprinting of SST anomalies. The SLP metric, as defined in Chapter 4, is the maximum value of the meridional geostrophic wind computed over a region of interest.

Figure 6.4a shows the SIT and SIC metrics computed for the CEL and northern BK domains. The four-year snapshot is that of Figure 6.3c and 6.3d, illustrating the SIT–SIC reemergence mechanism with persistent SIT anomalies providing the memory for fall SIC anomalies to reemerge the following spring. The phase evolution of these metrics clearly illustrates the persistence of the SIT anomalies and the seasonality of the SIC anomalies. The SIT metric tends to be active during all months of the year, with relatively circular trajectories in phase space, whereas the SIC metric tends to be strongly active in summer, peaking in September, and weakly active during the winter months.

In Figure 6.4b, we plot SST and SIC metric values for the Bering Sea. As in Chapter 4, the Bering SIC metrics are computed over 165°E – 160°W and 55°N – 65°N and the Bering SST metrics are computed over 165°E – 160°W and 60°N –

65°N. For visual clarity we do not plot metrics from the Barents-Kara Seas. The Barents-Kara metrics display similar qualitative behavior and are out of phase with the Bering Sea metrics. The four-year snapshot shows that the SIC metric is large in winter and small in summer. The SST metric has opposite sign to the SIC metric, and is large in summer and small in winter. These metrics illustrate the trade-off between SST and SIC, in which summer SST anomalies store the memory of spring SIC anomalies. This SST memory allows for SIC anomalies to reemerge the following fall, as illustrated by the metrics. The phase evolution also demonstrates this SST–SIC trade-off, as the SIC metric is strongly active in winter months and the SST metric is strongly active in summer months. Indeed, the sum of these two phase portraits would yield a result with relatively circular trajectories in phase space.

Finally, in Figure 6.4c we plot SLP and SIC metrics for the Bering Sea. Again, the Barents-Kara metrics display similar behavior, which we choose not to plot for visual clarity. The meridional winds have opposite sign to the SIC anomalies, and have largest amplitude during the winter months. This anti-correlation suggests a physical SLP–SIC interaction, as positive meridional winds correspond to negative SIC anomalies, and vice versa. The physical consistency of the SIC and SLP fields, along with the winter-to-winter persistence of the SLP patterns provides an SLP–SIC mechanism for reemergence. The phase diagrams illustrate that the wind anomalies generally lead the SIC anomalies, as the winds are maximal in January and February, whereas the SIC anomalies peak in March. This relationship, with wind anomalies leading and SIC anomalies lagging, is consistent with the physical expectation that these SIC anomalies are forced by atmospheric circulation anomalies. Additional work, investigating the causality of this SLP–SIC lead-lag

relationship, is required.

6.4 Conclusions

In this work, we have examined the fall-to-spring (growth season to melt season) reemergence of Arctic SIC anomalies in a CCSM4 control integration. Using modes of variability obtained via coupled NLSA, we have constructed a reemergence family of NLSA modes that captures both the fall-to-spring and spring-to-fall reemergence of Arctic SIC anomalies. This reemergence family captures the spatiotemporal evolution of SIC, SST, SLP, and SIT, allowing us to simultaneously study these fields in relation to sea-ice reemergence.

Lagged correlations of raw SIC data from CCSM4 display spring-to-fall and fall-to-spring reemergence of SIC anomalies. The fall-to-spring reemergence is most active in regions of the central Arctic, such as the CEL and northern BK Seas. Both types of reemergence are enhanced during periods of time in which the reemergence mode family is active. This low-dimensional reemergence family reveals an SIT–SIC fall-to-spring reemergence mechanism. In this mechanism, fall SIC anomalies imprint like-signed SIT anomalies in the central Arctic. These SIT anomalies persist over the winter months when the central Arctic becomes fully ice-covered and loses its fall SIC anomalies. As ice melts the following spring, the ice edge moves northwards, interacts with the SIT anomalies, and reinherits SIC anomalies of the same sign as the fall.

We have introduced SIC and SIT reemergence metrics, by which one can judge the amplitude and phase of reemergence events and the SIT–SIC reemergence mechanism. These metrics display interannual-to-decadal variability in the

strength and sign of reemergence events. They also clearly display the SIT–SIC mechanism described above. Consideration of SST and SLP reemergence metrics demonstrates that the reemergence family additionally captures SST and SLP-based mechanisms for spring-to-fall sea-ice reemergence. Phase diagrams reveal that each of these mechanisms has a clear relationship to the seasonal cycle. The SIT–SIC mechanism has large SIC anomalies in summer, small SIC anomalies in winter, and SIT anomalies of similar amplitude in all months. The SST–SIC mechanism has large winter SIC anomalies, which trade off with the ocean to produce large summer SST anomalies. The SLP–SIC mechanism has large SIC and SLP anomalies in winter, with the SLP anomalies leading SIC by about one month.

Chapter 7

Conclusions

7.1 Summary of findings

In this thesis, we have introduced a novel approach for data analysis of high-dimensional multivariate timeseries and applied it to climate data from comprehensive climate models and observations. Described in Chapter 2, Coupled NLSA provides a unit-independent analysis of multiple physical fields without requiring any initial normalization of the input data. We have used this technique as a tool throughout the thesis to study the statistical and dynamical properties of Arctic sea-ice reemergence, a phenomenon in which spring sea-ice anomalies tend to recur the following fall and fall sea-ice anomalies tend to recur the following spring. In Chapter 3, we studied coupled modes of variability of SST and SIC in the North Pacific sector. These modes were found in three distinct varieties: (1) periodic modes which reflect the periodic variability of the system; (2) low-frequency modes, which reflect interannual to decadal variability; and (3) intermittent modes, which reflect the interaction of the periodic and low-frequency variability of the system, in both

space and time. The intermittent temporal modes have an important relationship with the low-frequency modes, in the sense that the low-frequency modes provide a modulating envelope for the intermittent modes. This relationship was found to be crucially important in constructing "reemergence families" of modes, which are low-dimensional and capture the lagged correlation structure of the raw SIC data. The reemergence families reflect an SST–SIC reemergence mechanism in which the memory of spring SIC anomalies is stored as SST anomalies, allowing the SIC anomalies to reemerge the following fall. These families are connected to the NPGO mode of North Pacific SST variability, which emerges as the leading low-frequency mode in the coupled NLSA analysis. When conditioning the raw SIC data on times when the NPGO is active, we observed an enhanced reemergence signal. We also identified a second reemergence family, related to the PDO, capturing SST reemergence in the North Pacific. This chapter also presented the first use of NLSA on a timeseries with a relatively small number of samples. Somewhat surprisingly, the coupled NLSA algorithm performs quite well on the short observational dataset, successfully extracting periodic, low-frequency, and intermittent modes of variability.

In Chapter 4, we applied the methodology developed in Chapter 3 to an Arctic domain and added SLP to our analysis. We identified pan-Arctic agreement in reemergence signals between CCSM3 output and HadISST observations. However, the two datasets exhibit substantial regional differences in reemergence. The time-lagged pattern correlation methodology for assessing reemergence provides similar pan-Arctic results for the model and observations, whereas the total-area lagged correlation approach shows more substantial reemergence in the model. We also identified substantial temporal variability in the strength of reemergence events,

which may have important implications for sea-ice predictability. Low-dimensional reemergence families were constructed, and reflect the SST–SIC reemergence mechanism, particularly in the Bering, Barents-Kara, and Labrador Seas. These regions also exhibit clear phase relationships in SIC anomalies, which can be explained by the SLP teleconnection patterns of each family. These SLP patterns provide a method of communication between geographically separated regions of SIC variability. The SLP patterns have a natural interpretation as low-passed filtered versions of the full SLP field. These atmospheric circulation regimes suggest another potential sea-ice reemergence mechanism, via their winter-to-winter persistence.

The work of Chapter 4 identified an atmospheric role in reemergence, but did not quantify the relative role and importance of the atmosphere and the ocean in producing sea-ice reemergence. In Chapter 5, we investigated this question using a hierarchy of climate models with differing atmospheric and oceanic formulation. Lagged correlations across these datasets indicate the crucial role of oceanic memory and atmospheric variability in producing reasonable representations of reemergence. SLP–SIC teleconnections, analogous to those identified in Chapter 4, are found to exist in models with full coupling between the atmosphere and the ocean. This suggests that dynamical feedback of ocean anomalies on atmospheric circulation is essential in creating large-scale organized patterns of SIC and SLP variability. The reemergence families of these models reflect the SST–SIC and SLP–SIC reemergence mechanisms to varying degrees, and suggest that the SST–SIC mechanism can exist as a stand-alone process, while the SLP–SIC mechanism requires interaction with the ocean to produce memory in sea ice.

In Chapter 6, we studied the role of SIT in fall-to-spring Arctic sea-ice reemergence, adding SIT to the analyses of Chapters 4 and 5. We found that a low-

dimensional family of NLSA modes is able to capture both the spring-to-fall and fall-to-spring reemergence. The SIT and SIC fields of this family reveal an SIT–SIC mechanism for reemergence in which persistent winter SIT anomalies in the central Arctic allow fall SIC anomalies to reemerge the following spring. This family also captures the SST–SIC and SLP–SIC spring-to-fall reemergence mechanisms of Chapters 3–5. We introduced reemergence metrics for these fields, and studied their relation to the seasonal cycle. The spring-to-fall reemergence is characterized by SLP–SIC interactions in which wind anomalies tend to lead SIC anomalies by roughly one month. Additionally, this spring-to-fall reemergence exhibits a clear tradeoff between summer SST and winter SIC anomalies. Finally, the fall-to-spring reemergence is characterized by SIC anomalies that are large in summer and small in winter, and SIT anomalies that are persistent through all months of the year.

7.2 Future work

The work in this thesis has motivated a number of related questions, which could form the basis for future work. We briefly summarize some of these questions here.

In Chapters 3–5 all observational datasets and the CORE-II model runs were detrended by subtracting the monthly linear trend from each month. This was done with the intention of focusing on the internal variability of these systems. This assumption of a linear response to changes in external forcing is ad-hoc and may introduce biases. A research problem of interest is using NLSA to study signals with strong trends. We have done preliminary work analyzing the observational SIC dataset without any detrending, finding that NLSA and SSA effectively sepa-

rate a single "trend" mode and associated intermittent modes. This lies in contrast to EOF analysis, which mixes the trend signal over a large number of modes. The spatial reconstruction of the NLSA and SSA trend modes in space captures the long-term changes in sea-ice, along with the seasonality of this trend. More work is required to understand the conditions in which NLSA and SSA are able to capture trend-based variability. If successful, this could be a useful technique to provide a physically-based detrending of data.

The results of Chapter 4, regarding the temporal variability of reemergence events, suggest that predictability resulting from reemergence may also be a function of time. Are high reemergence years intrinsically more predictable than low reemergence years? In ongoing work with Ed Blanchard-Wrigglesworth, we are investigating this question by producing ensembles of GCM integrations initialized in high and low reemergence states. We plan to analyze the predictability in these two regimes to assess the influence of sea-ice reemergence on intrinsic predictability of Arctic sea ice.

The results of Chapter 5 suggest that the dynamics and persistence associated with a full-depth ocean are a crucial element of reemergence. Holland et al. (2013) investigated the role of heat storage below the mixed layer, but additional work regarding this is needed. An NLSA-based study investigating the vertical oceanic structure of sea-ice reemergence could help shed light on the oceanic mechanisms that contribute to oceanic memory storage.

The emphasis of reemergence signals when conditioning on low-frequency NLSA modes (Figure 12 of Chapter 3, Figure 15 of Chapter 4, Figure 3 of Chapter 5, Figure 1 of Chapter 6) suggests that these modes may have value in the context of statistical sea-ice prediction models. An interesting future direction would be

to develop statistical prediction methods based on these modes.

Bibliography

Alexander, M. A., U. S. Bhatt, J. E. Walsh, M. S. Timlin, J. S. Miller, and J. D. Scott, 2004: The atmospheric response to realistic Arctic sea ice anomalies in an AGCM during winter. *J. Climate*, **17 (5)**, 890–905.

Alexander, M. A., C. Deser, and M. S. Timlin, 1999: The reemergence of SST anomalies in the North Pacific Ocean. *J. Climate*, **12**, 2419–2433.

Ambaum, M. H., B. J. Hoskins, and D. B. Stephenson, 2001: Arctic oscillation or North Atlantic oscillation? *J. Climate*, **14 (16)**, 3495–3507.

Aubry, N., W.-Y. Lian, and E. S. Titi, 1993: Preserving symmetries in the proper orthogonal decomposition. *SIAM J. Sci. Comput.*, **14**, 483–505.

Barnes, E. A., 2013: Revisiting the evidence linking Arctic amplification to extreme weather in midlatitudes. *Geophys. Res. Lett.*, **40 (17)**, 4734–4739.

Belkin, M. and P. Niyogi, 2001: Laplacian eigenmaps and spectral techniques for embedding and clustering. *NIPS*, Vol. 14, 585–591.

Belkin, M. and P. Niyogi, 2003: Laplacian eigenmaps for dimensionality reduction and data representation. *Neural computation*, **15 (6)**, 1373–1396.

Belkin, M. and P. Niyogi, 2004: Semi-supervised learning on riemannian manifolds. *Machine learning*, **56 (1-3)**, 209–239.

Berry, T., R. Cressman, Z. Greguric-Ferencek, and T. Sauer, 2013: Time-scale separation from diffusion-mapped delay coordinates. *SIAM J. Appl. Dyn. Sys.*, **12**, 618–649.

Bitz, C., M. Holland, E. Hunke, and R. Moritz, 2005: Maintenance of the sea-ice edge. *J. Climate*, **18 (15)**, 2903–2921.

Bitz, C. and G. Roe, 2004: A mechanism for the high rate of sea ice thinning in the Arctic Ocean. *J. Climate*, **17 (18)**, 3623–3632.

Bitz, C., K. Shell, P. Gent, D. Bailey, G. Danabasoglu, K. Armour, M. Holland, and J. Kiehl, 2012: Climate sensitivity of the Community Climate System Model, Version 4. *J. Climate*, **25 (9)**, 3053–3070.

Blanchard-Wrigglesworth, E., K. C. Armour, C. M. Bitz, and E. DeWeaver, 2011a: Persistence and inherent predictability of Arctic sea ice in a GCM ensemble and observations. *J. Climate*, **24**, 231–250.

Blanchard-Wrigglesworth, E., C. Bitz, and M. Holland, 2011b: Influence of initial conditions and climate forcing on predicting Arctic sea ice. *Geophys. Res. Lett.*, **38 (18)**.

Blanchard-Wrigglesworth, E. and C. M. Bitz, 2014: Characteristics of Arctic sea-ice thickness variability in GCMs. *J. Climate*, **27 (21)**, 8244–8258.

Broomhead, D. S. and G. P. King, 1986: Extracting qualitative dynamics from ex-

perimental data. *Phys. D*, **20 (2–3)**, 217–236, doi:10.1016/0167-2789(86)90031-x.

Budyko, M., 1969: The effect of solar radiation variations on the climate of the earth. *Tellus*, **21**, 611–619.

Cavalieri, D. J. and C. L. Parkinson, 1987: On the relationship between atmospheric circulation and the fluctuations in the sea ice extents of the Bering and Okhotsk Seas. *J. Geophys. Res.*, **92(C7)**, 7141–7162.

Cavalieri, D. J. and C. L. Parkinson, 2012: Arctic sea ice variability and trends, 1979-2010. *The Cryosphere*, **6 (4)**, 881–889, doi:10.5194/tc-6-881-2012.

Chapman, W. L. and J. E. Walsh, 1993: Recent variations of sea ice and air temperature in high latitudes. *Bulletin of the American Meteorological Society*, **74 (1)**, 33–47.

Chevallier, M. and D. Salas-Mélia, 2012: The role of sea ice thickness distribution in the Arctic sea ice potential predictability: A diagnostic approach with a coupled GCM. *J. Climate*, **25 (8)**, 3025–3038.

Chevallier, M., D. Salas y Mélia, A. Voldoire, M. Déqué, and G. Garric, 2013: Seasonal forecasts of the pan-Arctic sea ice extent using a GCM-based seasonal prediction system. *J. Climate*, **26 (16)**, 6092–6104.

Coifman, R. R. and S. Lafon, 2006: Diffusion maps. *Appl. Comput. Harmon. Anal.*, **21(1)**, 5–30, doi:10.1016/j.acha.2006.04.006.

Collins, W. D., et al., 2004: Description of the NCAR Community Atmosphere

Model (CAM 3.0). Tech. Rep. TN-464+STR, National Center for Atmospheric Research, 226 pp.

Collins, W. D., et al., 2006: The Community Climate System Model version 3 (CCSM3). *J. Climate*, **19**, 2122–2143.

Curry, J. A., J. L. Schramm, and E. E. Ebert, 1995: Sea ice-albedo climate feedback mechanism. *J. Climate*, **8**, 240–247.

Czaja, A. and C. Frankignoul, 2002: Observed impact of Atlantic SST anomalies on the North Atlantic Oscillation. *J. Climate*, **15 (6)**, 606–623.

Danabasoglu, G., S. C. Bates, B. P. Briegleb, S. R. Jayne, M. Jochum, W. G. Large, S. Peacock, and S. G. Yeager, 2012: The CCSM4 ocean component. *J. Climate*, **25 (5)**, 1361–1389.

Danabasoglu, G., et al., 2014: North Atlantic simulations in coordinated ocean-ice reference experiments phase II (CORE-II). Part I: mean states. *Ocean Modelling*, **73**, 76–107.

Day, J., E. Hawkins, and S. Tietsche, 2014a: Will Arctic sea ice thickness initialization improve seasonal forecast skill? *Geophys. Res. Lett.*, **41 (21)**, 7566–7575.

Day, J., S. Tietsche, and E. Hawkins, 2014b: Pan-Arctic and regional sea ice predictability: Initialization month dependence. *J. Climate*, **27 (12)**, 4371–4390.

de Boer, G., W. Chapman, J. E. Kay, B. Medeiros, M. D. Shupe, S. Vavrus, and J. Walsh, 2012: A characterization of the present-day Arctic atmosphere in CCSM4. *J. Climate*, **25 (8)**, 2676–2695.

de Cotlogon, G. and C. Frankignoul, 2003: On the persistence of winter sea surface temperature in the North Atlantic. *J. Climate*, **16**, 1364–1377.

Dee, D. P., et al., 2011: The ERA-Interim reanalysis: configuration and performance of the data assimilation system. *Q.J.R. Meteorol. Soc.*, **137**, 553–597, doi:10.1002/qj.828.

Deser, C., M. Holland, G. Reverdin, and M. S. Timlin, 2002: Decadal variations in Labrador sea ice cover and North Atlantic sea surface temperatures. *J. of Geophys. Res.*, **107**, C5, doi:10.1029/2000JC000683.

Deser, C., R. Knutti, S. Solomon, and A. S. Phillips, 2012a: Communication of the role of natural variability in future North American climate. *Nature Climate Change*, **2 (11)**, 775–779.

Deser, C., A. Phillips, V. Bourdette, and H. Teng, 2012b: Uncertainty in climate change projections: the role of internal variability. *Climate Dynamics*, **38 (3-4)**, 527–546.

Deser, C., J. E. Walsh, and M. S. Timlin, 2000: Arctic sea ice variability in the context of recent atmospheric circulation trends. *J. Climate*, **13**, 617–633.

Di Lorenzo, E., et al., 2008: North Pacific Gyre Oscillation links ocean climate and ecosystem change. *Geophys. Res. Lett*, **35**, L08 607, doi:10.1029/2007GL032838.

Eisenman, I. and J. Wettlaufer, 2009: Nonlinear threshold behavior during the loss of Arctic sea ice. *Proceedings of the National Academy of Sciences*, **106 (1)**, 28–32.

Fang, Z. and J. Wallace, 1994: Arctic sea ice variability on a timescale of weeks and its relation to atmospheric forcing. *J. Climate*, **7**, 1897–1914.

Francis, J. A. and E. Hunter, 2007: Drivers of declining sea ice in the Arctic winter: A tale of two seas. *Geophys. Res. Lett.*, **34 (17)**, doi:10.1029/2007GL030995.

Francis, J. A. and S. J. Vavrus, 2012: Evidence linking Arctic amplification to extreme weather in mid-latitudes. *Geophys. Res. Lett.*, **39 (6)**.

Gent, P. R., et al., 2011: The Community Climate System Model Version 4. *J. Climate*, **24 (19)**, 4973–4991.

Germe, A., M. Chevallier, D. S. y Mélia, E. Sanchez-Gomez, and C. Cassou, 2014: Interannual predictability of Arctic sea ice in a global climate model: regional contrasts and temporal evolution. *Climate Dynamics*, **43 (9-10)**, 2519–2538.

Ghil, M., et al., 2002: Advanced spectral methods for climatic time series. *Rev. Geophys.*, **40(1)**, 3.1–3.41.

Giannakis, D., 2015: Dynamics-Adapted Cone Kernels. *SIAM J. Appl. Dyn. Sys.*, in press.

Giannakis, D. and A. J. Majda, 2012a: Comparing low-frequency and intermittent variability in comprehensive climate models through nonlinear Laplacian spectral analysis. *Geophys. Res. Lett*, **39**, L10 710, doi:10.1029/2012GL051575.

Giannakis, D. and A. J. Majda, 2012b: Limits of predictability in the North Pacific sector of a comprehensive climate model. *Geophys. Res. Lett*, **39**, L24 602, doi: 10.1029/2012GL054273.

Giannakis, D. and A. J. Majda, 2012c: Nonlinear Laplacian spectral analysis for time series with intermittency and low-frequency variability. *Proc. Natl. Acad. Sci.*, **109**, 2222–2227.

Giannakis, D. and A. J. Majda, 2013: Nonlinear Laplacian spectral analysis: Capturing intermittent and low-frequency spatiotemporal patterns in high-dimensional data. *Stat. Anal. Data Min.*, **6 (3)**, 180–194, doi: 10.1002/sam.11171.

Giannakis, D. and A. J. Majda, 2015: Data-driven methods for dynamical systems: Quantifying predictability and extracting spatiotemporal patterns. *Mathematical and Computational Modeling: With Applications in Engineering and the Natural and Social Sciences*, R. Melnik, Ed., Wiley, Hoboken, 288.

Giannakis, D., W.-w. Tung, and A. J. Majda, 2012: Hierarchical structure of the Madden-Julian oscillation in infrared brightness temperature revealed through nonlinear Laplacian spectral analysis. *Intelligent Data Understanding (CIDU), 2012 Conference on*, IEEE, 55–62.

Griffies, S. M., et al., 2009: Coordinated ocean-ice reference experiments (COREs). *Ocean Modelling*, **26 (1)**, 1–46.

Groth, A. and M. Ghil, 2011: Multivariate singular spectrum analysis and the road to phase synchronization. *Physical Review E*, **84 (3)**, 036 206.

Guemas, V., et al., 2014: A review on Arctic sea ice predictability and prediction on seasonal-to-decadal timescales. *Quarterly Journal of the Royal Meteorological Society*.

Holland, M. M., D. A. Bailey, and S. Vavrus, 2011: Inherent sea ice predictability in the rapidly changing Arctic environment of the Community Climate System Model, version 3. *Climate Dynamics*, **36 (7-8)**, 1239–1253.

Holland, M. M., C. Bitz, E. Hunke, W. Lipscomb, and J. Schramm, 2006a: Influence of the sea ice thickness distribution on polar climate in CCSM3. *J. Climate*, **19**, 2398–2414.

Holland, M. M. and C. M. Bitz, 2003: Polar amplification of climate change in coupled models. *Climate Dynamics*, **21 (3-4)**, 221–232.

Holland, M. M., C. M. Bitz, and B. Tremblay, 2006b: Future abrupt reductions in the summer Arctic sea ice. *Geophys. Res. Lett.*, **33 (23)**.

Holland, M. M., E. Blanchard-Wrigglesworth, J. Kay, and S. Vavrus, 2013: Initial-value predictability of Antarctic sea ice in the Community Climate System Model 3. *Geophys. Res. Lett.*, **40 (10)**, 2121–2124.

Jahn, A., et al., 2012: Late-twentieth-century simulation of Arctic sea ice and ocean properties in the CCSM4. *J. Climate*, **25 (5)**, 1431–1452.

Johnson, M. A., A. Y. Proshutinsky, and I. V. Polyakov, 1999: Atmospheric patterns forcing two regimes of Arctic circulation: A return to anticyclonic conditions? *Geophys. Res. Lett.*, **26 (11)**, 1621–1624.

Jones, P. W., M. Maggioni, and R. Schul, 2008: Manifold parametrizations by eigenfunctions of the Laplacian and heat kernels. *Proceedings of the National Academy of Sciences*, **105 (6)**, 1803–1808.

Kay, J. E., M. M. Holland, and A. Jahn, 2011: Inter-annual to multi-decadal Arctic sea ice extent trends in a warming world. *Geophys. Res. Lett.*, **38**, L15 708, doi: 10.1029/2011GL048008.

Koenigk, T. and U. Mikolajewicz, 2009: Seasonal to interannual climate predictability in mid and high northern latitudes in a global coupled model. *Climate dynamics*, **32 (6)**, 783–798.

Kushnir, Y., W. Robinson, I. Bladé, N. Hall, S. Peng, and R. Sutton, 2002: Atmospheric GCM response to extratropical SST anomalies: Synthesis and evaluation*. *J. Climate*, **15 (16)**, 2233–2256.

Kwok, R. and D. Rothrock, 2009: Decline in Arctic sea ice thickness from submarine and ICESat records: 1958–2008. *Geophys. Res. Lett.*, **36 (15)**.

Large, W. and S. Yeager, 2009: The global climatology of an interannually varying air–sea flux data set. *Climate Dynamics*, **33 (2-3)**, 341–364.

Large, W. G. and S. G. Yeager, 2004: Diurnal to decadal global forcing for ocean and sea-ice models: the data sets and flux climatologies. Tech. Rep. TN-460+STR, National Center for Atmospheric Research, 105 pp.

Latif, M. and T. P. Barnett, 1994: Causes of decadal climate variability over the North Pacific and North America. *Science*, **266 (5185)**, 634–637.

Lau, N.-C. and M. J. Nath, 1990: A general circulation model study of the atmospheric response to extratropical SST anomalies observed in 1950-79. *J. Climate*, **3 (9)**, 965–989.

L'Heureux, M. L., A. Kumar, G. D. Bell, M. S. Halpert, and R. W. Higgins, 2008: Role of the Pacific-North American (PNA) pattern in the 2007 Arctic sea ice decline. *Geophys. Res. Lett.*, **35 (20)**, doi:10.1029/2008GL035205.

Lindsay, R. and J. Zhang, 2005: The thinning of Arctic sea ice, 1988-2003: Have we passed a tipping point? *J. Climate*, **18 (22)**, 4879–4894.

Liu, J., Z. Zhang, R. M. Horton, C. Wang, and X. Ren, 2007: Variability of North Pacific sea ice and East Asia-North Pacific winter climate. *J. Climate*, **20**, 1991–2001.

Lorenz, E. N., 1963: Deterministic nonperiodic flow. *J. Atmos. Sci.*, **20 (2)**, 130–141.

MacFarling Meure, C., D. Etheridge, C. Trudinger, P. Steele, R. Langenfelds, T. Van Ommen, A. Smith, and J. Elkins, 2006: Law dome co2, ch4 and n2o ice core records extended to 2000 years bp. *Geophys. Res. Lett.*, **33 (14)**.

Magnusdottir, G., C. Deser, and R. Saravanan, 2004: The effects of North Atlantic SST and sea ice anomalies on the winter circulation in CCM3. Part I: Main features and storm track characteristics of the response. *J. Climate*, **17 (5)**, 857–876.

Mantua, N. J. and S. Hare, 2002: The Pacific Decadal Oscillation. *J. Oceanogr.*, **58**, 35–44, doi:10.1023/A:1015820616384.

Mantua, N. J., S. R. Hare, Y. Zhang, J. M. Wallace, and R. C. Francis, 1997: A pacific interdecadal climate oscillation with impacts on salmon production. *Bulletin of the american Meteorological Society*, **78 (6)**, 1069–1079.

Maslanik, J., S. Drobot, C. Fowler, W. Emery, and R. Barry, 2007: On the Arctic climate paradox and the continuing role of atmospheric circulation in affecting sea ice conditions. *Geophys. Res. Lett.*, **34 (3)**, doi:10.1029/2006GL028269.

Moritz, R. E., C. M. Bitz, and E. J. Steig, 2002: Dynamics of recent climate change in the Arctic. *Science*, **297 (5586)**, 1497–1502.

Msadek, R., G. Vecchi, M. Winton, and R. Gudgel, 2014: Importance of initial conditions in seasonal predictions of Arctic sea ice extent. *Geophys. Res. Lett.*, **41 (14)**, 5208–5215.

Mysak, L. A. and S. A. Venegas, 1998: Decadal climate oscillations in the Arctic: A new feedback loop for atmosphere-ice-ocean interactions. *Geophys. Res. Lett.*, **25 (19)**, 3607–3610.

North, G. R., T. L. Bell, R. F. Cahalan, and F. J. Moeng, 1982: Sampling errors in the estimation of empirical orthogonal functions. *Monthly Weather Review*, **110 (7)**, 699–706.

Overland, J. E. and M. Wang, 2005: The third Arctic climate pattern: 1930s and early 2000s. *Geophys. Res. Lett.*, **32 (23)**, doi:10.1029/2005GL024254.

Overland, J. E. and M. Wang, 2010: Large-scale atmospheric circulation changes are associated with the recent loss of Arctic sea ice. *Tellus A*, **62 (1)**, 1–9, doi:10.1111/j.1600-0870.2009.00421.x.

Overland, J. E. and M. Wang, 2013: When will the summer Arctic be nearly sea ice free? *Geophys. Res. Lett.*, **40 (10)**, 2097–2101.

Owens, W. B. and P. Lemke, 1990: Sensitivity studies with a sea ice-mixed layer-pycnocline model in the Weddell sea. *J. Geophys. Res: Oceans (1978–2012)*, **95 (C6)**, 9527–9538.

Parkinson, C. L., 1990: The impacts of the Siberian high and Aleutian low on the sea ice cover of the Sea of Okhotsk. *Ann. Glaciology*, **14**, 226–229.

Polyakov, I. V. and M. A. Johnson, 2000: Arctic decadal and interdecadal variability. *Geophys. Res. Lett.*, **27 (24)**, 4097–4100.

Proshutinsky, A. Y. and M. A. Johnson, 1997: Two circulation regimes of the wind-driven Arctic Ocean. *Journal of Geophysical Research: Oceans*, **102 (C6)**, 12 493–12 514, doi:10.1029/97JC00738.

Rayner, N. A., D. E. Parker, E. B. Horton, C. K. Folland, L. V. Alexander, D. P. Rowell, E. C. Kent, and A. Kaplan, 2003: Global analyses of sea surface temperature, sea ice, and night marine air temperature since the late nineteenth century. *J. Geophys. Res.*, **108**, 4407, doi:10.1029/2002JD002670.

Rigor, I. G. and J. M. Wallace, 2004: Variations in the age of Arctic sea-ice and summer sea-ice extent. *Geophys. Res. Lett.*, **31 (9)**, doi:10.1029/2004GL019492.

Rigor, I. G., J. M. Wallace, and R. L. Colony, 2002: Response of sea ice to the Arctic Oscillation. *J. Climate*, **15**, 2648–2663, doi:10.1175/1520-0442.

Robertson, A. W., C. R. Mechoso, and Y.-J. Kim, 2000: The Influence of Atlantic Sea Surface Temperature Anomalies on the North Atlantic Oscillation*. *J. Climate*, **13 (1)**, 122–138.

Rothrock, D. A., Y. Yu, and G. A. Maykut, 1999: Thinning of the Arctic sea-ice cover. *Geophys. Res. Lett.*, **26 (23)**, 3469–3472.

Sasaki, Y. N. and S. Minobe, 2006: Seasonally dependent interannual variability of sea ice in the Bering Sea and its relation to atmospheric fluctuations. *J. Geophys. Res.*, **110**, C05 011.

Sauer, T., J. A. Yorke, and M. Casdagli, 1991: Embedology. *Journal of statistical Physics*, **65 (3-4)**, 579–616.

Schröder, D., D. L. Feltham, D. Flocco, and M. Tsamados, 2014: September Arctic sea-ice minimum predicted by spring melt-pond fraction. *Nature Climate Change*.

Screen, J. A. and I. Simmonds, 2010: The central role of diminishing sea ice in recent Arctic temperature amplification. *Nature*, **464 (7293)**, 1334–1337.

Screen, J. A. and I. Simmonds, 2013: Exploring links between Arctic amplification and mid-latitude weather. *Geophys. Res. Lett.*, **40 (5)**, 959–964.

Screen, J. A., I. Simmonds, and K. Keay, 2011: Dramatic interannual changes of perennial Arctic sea ice linked to abnormal summer storm activity. *Journal of Geophysical Research: Atmospheres*, **116 (D15)**, doi:10.1029/2011JD015847.

Selten, F. M., R. Haarsma, and J. Opsteegh, 1999: On the mechanism of North Atlantic decadal variability. *J. Climate*, **12 (7)**, 1956–1973.

Serreze, M. C., 2011: Climate change: Rethinking the sea-ice tipping point. *Nature*, **471 (7336)**, 47–48.

Serreze, M. C. and J. A. Francis, 2006: The Arctic amplification debate. *Climatic Change*, **76 (3-4)**, 241–264.

Serreze, M. C., M. M. Holland, and J. Stroeve, 2007: Perspectives on the Arctic's shrinking sea-ice cover. *Science*, **315 (5818)**, 1533–1536, doi: 10.1126/science.1139426.

Serreze, M. C., et al., 2003: A record minimum arctic sea ice extent and area in 2002. *Geophys. Res. Lett.*, **30 (3)**, doi:10.1029/2002GL016406.

Sigmond, M., J. Fyfe, G. Flato, V. Kharin, and W. Merryfield, 2013: Seasonal forecast skill of Arctic sea ice area in a dynamical forecast system. *Geophys. Res. Lett.*, **40 (3)**, 529–534.

Smith, R. and P. Gent, 2004: Reference manual for the Parallel Ocean Program (POP): Ocean component of the Community Climate System Model (CCSM2.0 and 3.0). Tech. Rep. LAUR-02-2484, Los Alamos National Laboratory, 75 pp.

Stephenson, S. R., L. C. Smith, and J. A. Agnew, 2011: Divergent long-term trajectories of human access to the Arctic. *Nature Climate Change*, **1 (3)**, 156–160.

Stocker, T., et al., 2013: Climate change 2013: The physical science basis. contribution of working group i to the fifth assessment report of the intergovernmental panel on climate change. Tech. rep., National Center for Atmospheric Research, 1535 pp. doi:10.1017/CBO9781107415324.

Stroeve, J., L. C. Hamilton, C. M. Bitz, and E. Blanchard-Wrigglesworth, 2014: Predicting September sea ice: Ensemble skill of the SEARCH sea ice outlook 2008–2013. *Geophys. Res. Lett.*, **41 (7)**, 2411–2418.

Stroeve, J., M. M. Holland, W. Meier, T. Scambos, and M. Serreze, 2007: Arctic sea ice decline: Faster than forecast. *Geophys. Res. Lett.*, **34 (9)**, doi: 10.1029/2007GL029703.

Stroeve, J. C., V. Kattsov, A. Barrett, M. Serreze, T. Pavlova, M. Holland, and W. N. Meier, 2012: Trends in Arctic sea ice extent from CMIP5, CMIP3 and observations. *Geophys. Res. Lett.*, **39 (16)**, doi:10.1029/2012GL052676.

Swart, N. C., J. C. Fyfe, E. Hawkins, J. E. Kay, and A. Jahn, 2015: Influence of internal variability on Arctic sea-ice trends. *Nature Climate Change*, **5 (2)**, 86–89.

Takens, F., 1981: *Detecting strange attractors in turbulence*. Springer.

Teng, H. and G. Branstator, 2011: Initial value predictability in prominent modes of North Pacific subsurface temperature in a coupled GCM. *Climate Dyn.*, **36**, 1813–1834.

Thompson, D. W. and J. M. Wallace, 2000: Annular modes in the extratropical circulation. Part I: month-to-month variability*. *J. Climate*, **13 (5)**, 1000–1016.

Thompson, D. W. J. and J. M. Wallace, 1998: The Arctic oscillation signature in the wintertime geopotential height and temperature fields. *Geophys. Res. Lett*, **25**, 1297–1300, doi:10.1029/98GL00950.

Tietsche, S., D. Notz, J. Jungclaus, and J. Marotzke, 2011: Recovery mechanisms of Arctic summer sea ice. *Geophys. Res. Lett.*, **38 (2)**.

Tietsche, S., D. Notz, J. H. Jungclaus, and J. Marotzke, 2013: Predictability of

large interannual arctic sea-ice anomalies. *Climate dynamics*, **41 (9-10)**, 2511–2526.

Tietsche, S., et al., 2014: Seasonal to interannual Arctic sea ice predictability in current global climate models. *Geophys. Res. Lett.*, **41 (3)**, 1035–1043.

Timlin, M. S., M. A. Alexander, and C. Deser, 2002: On the reemergence of North Atlantic SST anomalies. *J. Climate*, **15**, 2707–2712.

Trenberth, K. E. and J. W. Hurrell, 1994: Decadal atmosphere-ocean variations in the Pacific. *Climate Dynamics*, **9 (6)**, 303–319.

Tsukernik, M., C. Deser, M. Alexander, and R. Tomas, 2010: Atmospheric forcing of Fram Strait sea ice export: A closer look. *Climate Dynamics*, **35 (7-8)**, 1349–1360, doi:10.1007/s00382-009-0647-z.

Vautard, R. and M. Ghil, 1989: Singular Spectrum Analysis in nonlinear dynamics, with applications to paleoclimatic time series. *Phys. D*, **35**, 395–424, doi:10.1016/0167-2789(89)90077-8.

von Storch, H. and F. W. Zwiers, 1999: *Statistical Analysis in Climate Research*. Cambridge University Press, 484 pp., doi:10.1017/CBO9780511612336.

Walsh, J. E., W. L. Chapman, and T. L. Shy, 1996: Recent decrease of sea level pressure in the central Arctic. *J. Climate*, **9 (2)**, 480–486.

Wang, J., J. Zhang, E. Watanabe, M. Ikeda, K. Mizobata, J. E. Walsh, X. Bai, and B. Wu, 2009: Is the Dipole Anomaly a major driver to record lows in Arctic summer sea ice extent? *Geophys. Res. Lett.*, **36 (5)**, doi:10.1029/2008GL036706.

Wang, W., M. Chen, and A. Kumar, 2013: Seasonal prediction of Arctic sea ice extent from a coupled dynamical forecast system. *Mon. Wea. Rev.*, **141 (4)**, 1375–1394.

Watanabe, E., J. Wang, A. Sumi, and H. Hasumi, 2006: Arctic Dipole Anomaly and its contribution to sea ice export from the Arctic Ocean in the 20th century. *Geophys. Res. Lett.*, **33 (23)**, doi:10.1029/2006GL028112.

Weng, W. and J. D. Neelin, 1998: On the role of ocean-atmosphere interaction in midlatitude interdecadal variability. *Geophys. Res. Lett.*, **25 (2)**, 167–170.

Wettstein, J. J. and C. Deser, 2014: Internal variability in projections of twenty-first-century Arctic sea ice loss: Role of the large-scale atmospheric circulation. *J. Climate*, **27**, 527–550, doi:10.1175/JCLI-D-12-00839.1.

Winton, M., 2006: Does the Arctic sea ice have a tipping point? *Geophys. Res. Lett.*, **33 (23)**.

Wu, B., J. Wang, and J. E. Walsh, 2006: Dipole Anomaly in the winter Arctic atmosphere and its association with sea ice motion. *J. Climate*, **19**, 210–225, doi:10.1175/JCLI3619.1.

Yang, Q., S. N. Losa, M. Losch, X. Tian-Kunze, L. Nerger, J. Liu, L. Kaleschke, and Z. Zhang, 2014: Assimilating SMOS sea ice thickness into a coupled ice-ocean model using a local SEIK filter. *J. Geophys. Res: Oceans*, **119 (10)**, 6680–6692.

Yi, D., L. A. Mysak, and S. A. Venegas, 1999: Decadal-to-interdecadal fluctuations of Arctic sea-ice cover and the atmospheric circulation during 1954–1994. *Atmosphere-Ocean*, **37 (4)**, 389–415.

Yuan, X., D. Chen, and C. Li, 2014: A Markov model for seasonal forecast of Arctic sea ice. In prep.

Zhang, J., M. Steele, D. A. Rothrock, and R. W. Lindsay, 2004: Increasing exchanges at Greenland-Scotland Ridge and their links with the North Atlantic Oscillation and Arctic sea ice. *Geophys. Res. Lett.*, **31 (9)**.

Zhang, Y., J. M. Wallace, and D. S. Battisti, 1997: Enso-like interdecadal variability: 1900-93. *J. Climate*, **10 (5)**, 1004–1020.